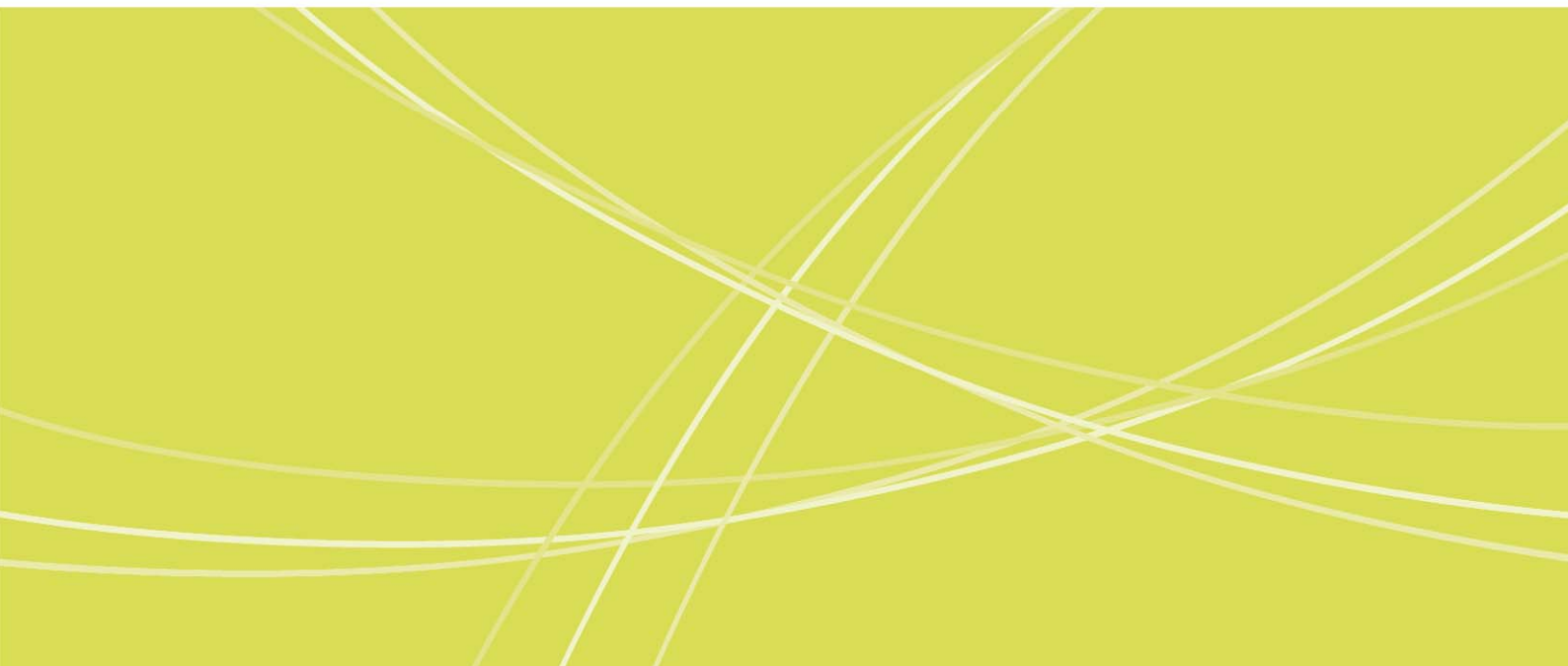




# South Eastern Australian **Climate Initiative**

**Program Annual Report 2011/12**

**September 2012**



## **Citation**

CSIRO (2012) South Eastern Australian Climate Initiative Program Annual Report 2011/12. CSIRO, Australia, September 2012, 151 pp.

## **Research Team**

*Program Director* David Post

*Theme Leaders* Bertrand Timbal (Theme 1), Francis Chiew (Theme 2), Harry Hendon (Theme 3)

*Project Leaders* Bertrand Timbal (Project 1.1), Peter Briggs and Mike Raupach (Project 1.2),  
Dewi Kirono (Project 2.1), Nicholas Potter (Project 2.2), Harry Hendon (Project 3.1), QJ Wang (Project 3.2)

*Additional Project Team Members (by organisation)*

CSIRO: James Bennett, Wenju Cai, Tim Cowan, Warrick Dawes, Marie Ekstrom, Vanessa Haverd, Sandra Hawthorne, David Kent, Yun Li, Matt Paget, Cuan Petheram, Prafulla Pokhrel, Ariaan Purich, Arthur Read, David Robertson, Jin Teng, Jai Vaze, Biao Wang, Quan Wang, Ziyuan Wang, Kirien Whan, Lu Zhang

Bureau of Meteorology: Oscar Alves, Alex Evans, Morwenna Griffiths, Eun-Pa Lim, Guo Liu, Chris Lucas, Hanh Nguyen, Guomin Wang, Yang Wang, Griffith Young

## **Program Governance**

*Steering Committee* Campbell Fitzpatrick (Chair, Victorian Department of Sustainability and Environment), Jody Swirepik (Murray–Darling Basin Authority), Jo Mummery (Department of Climate Change and Energy Efficiency), Neville Smith (Bureau of Meteorology), and Ian Prosser (CSIRO)

*Science Panel* Graeme Pearman (Independent Chairperson), Michael Manton (Independent Expert),  
Jason Alexandra (Murray–Darling Basin Authority), Rae Moran (Victorian Department of Sustainability and Environment), Alison McMorrow (Department of Climate Change and Energy Efficiency), Peter May (Bureau of Meteorology), and Glen Walker (CSIRO)

## **Administration**

*Program Coordinator* Therese McGillion (to April 2012)

*Program Communicator* Bec Jennings

*Finance Officer* Suzanne Blankley

*Data Manager* Steve Marvanek

*Administration Officer* Ben Wurcker

## **Report production**

*Editor* Karin Hosking

*Production Assistants* Rachel von Gerhardt, Simon Gallant

© Copyright Commonwealth Scientific and Industrial Research Organisation (CSIRO Australia), 2012

## **Important notice:**

All rights are reserved and no part of this publication covered by copyright may be reproduced or copied in any form or by any means except with the written permission of CSIRO.

The results and analyses contained in this report are based on a number of technical, circumstantial or otherwise specified assumptions and parameters. The user must make its own assessment of the suitability for its use of the information or material contained in or generated from the report. To the extent permitted by law, CSIRO excludes all liability to any party for expenses, losses, damages and costs arising directly or indirectly from using this report.

## **Address and contact details:**

CSIRO Water for a Healthy Country Flagship

Ph (+61 2) 62465617

Email: seaci@csiro.au

## EXECUTIVE SUMMARY

The South Eastern Australian Climate Initiative (SEACI) was established in 2006 to investigate the causes, impacts and prediction of climate variability and change in south-eastern Australia. The first three years of SEACI made progress in characterising and explaining the nature and causes of the recent drought, produced climate and runoff projections out to 2030, and improved seasonal forecasts of rainfall and runoff across south-eastern Australia. These research findings are summarised in CSIRO (2010a).

Research in Phase 2 of SEACI builds on the findings of Phase 1. It is a three year, \$9 million research partnership between the Murray–Darling Basin Authority, the Victorian Department of Sustainability and Environment, CSIRO Water for a Healthy Country Flagship, the Bureau of Meteorology, and the Australian Government Department of Climate Change and Energy Efficiency. The SEACI study area incorporates the Murray–Darling Basin, the state of Victoria and southern South Australia, including the Eyre Peninsula.

Research in Phase 2 of SEACI has been conducted through three related themes. This report summarises the progress made in the third and final year (2011/12) of Phase 2 of SEACI. Progress made in the first year of Phase 2 was summarised in the Program Annual Report 2009/10 (CSIRO, 2010b), progress in the second year was summarised in the Program Annual Report 2010/11 (CSIRO, 2011), and an overall synthesis of research findings from SEACI Phase 2 can be found in CSIRO (2012).

### Theme 1: Understanding past hydroclimate variability and change in south-eastern Australia

*Research in Theme 1 is contributing to a better understanding of the factors that influence climate and streamflow within south-eastern Australia*

Work in Project 1.1 reconstructed key climate variables back to the 1860s. This showed that the lack of intensification of the sub-tropical ridge which accompanied relatively low levels of global warming in the 1950s to 1970s was also seen in the 1860s to 1890s. Additionally, preliminary results suggest that the sub-tropical ridge over south-eastern Australia is affected not only by the extent of the Hadley circulation, but also its intensity. It is suggested that intensification of the Hadley circulation in summer and expansion throughout the year may have contributed to the observed decline in rainfall over south-eastern Australia. Interestingly, these patterns are seen only in global climate model runs with anthropogenic inputs; however the influence of greenhouse gases is difficult to distinguish from the influence of stratospheric ozone depletion. The relationship between observed trends in mean sea level pressure and rainfall across south-eastern Australia suggests that local pressure increases could account for much of the autumn rainfall decrease since the 1950s. These trends in mean sea level pressure are not well captured in global climate models however, perhaps explaining why these models have not been able to reproduce the observed rainfall trends, particularly in autumn (March, April, May).

Research in Project 1.2 studied the impact of climate variability and change on the water balance in south-eastern Australia using the CABLE land surface model, applied to Australian terrestrial carbon and water cycles, and constrained by multiple observation types including streamflow. The major impacts of key variables on total outflow (Q) from the SEACI region are as follows. A 10 percent change in mean annual rainfall was found to lead to a 29 percent change in runoff. A 1 °C rise in temperature led to a 5.2 percent decrease in runoff. This decrease was largely due to changes in transpiration, with changes in soil evaporation having a smaller impact. Translating these elasticities to likely changes by 2050, the largest effect of climate change on SEACI region runoff occurs through decreased precipitation, where a 5 percent decrease (typical of a number of climate projections) would lead to a 15 percent decrease in outflow. A warming of 1 °C (typical of climate projections for approximately 2050) would cause an additional runoff decrease of 5 percent. The response to a likely CO<sub>2</sub> increase of 100 ppm would lead to a runoff increase of 9 percent (because of increased plant water use efficiency). For elasticities of outflow to precipitation and temperature in selected catchments, there is fair agreement with results from Project 2.2. Modelled elasticities of

outflow to precipitation were typically slightly higher than empirical estimates, while modelled and empirical elasticities of outflow to temperature agreed within the uncertainty bounds.

## Theme 2: Long-term hydroclimate projections in south-eastern Australia

*Research in Theme 2 is improving long-term projections of climate and streamflow for south-eastern Australia*

Research in Project 2.1 shows that the global climate models used in the IPCC Fourth Assessment Report are much better at simulating the regional coarse-scale rainfall (and climate variables) than they are at representing the large-scale climatic conditions that affect south-eastern Australia. None of the 25 models are consistently better than all the other models for all the measures, but there are a couple of models that consistently perform poorly against most of the measures. Despite this, practically all the models project a decline in future rainfall (particularly cool season rainfall) across the southern part of south-eastern Australia. Using only the best models or putting more weight on the better models does not reduce the range of projections. Thus for now, projections of climate change are probably best developed using all available models (aside from perhaps excluding the consistently poor models). The projections and range of results for CSIRO-Mk3.6 and ACCESS are similar to those of previous CSIRO models. Analogue downscaling and dynamical downscaling using the Weather Research and Forecasting (WRF) model provides finer resolution projections of changes to rainfall than the projections from the coarse-scale global climate models. However, the daily rainfall sequences are not sufficiently similar to historical rainfall for direct input into hydrological models. More research is required to improve the daily rainfall simulations and to bias-correct the outputs so they can be used directly in water availability studies. However, at the very least, empirical scaling of the outputs from the downscaled models is likely to give more reliable projections of future rainfall than empirical scaling informed by global climate model simulations. Statistical downscaling approaches like the non-homogeneous hidden Markov model (NHMM) can potentially be fitted to match the daily rainfall characteristics important for hydrological modelling; however, NHMM's use is limited to smaller regions because of the difficulty calibrating to large numbers of points.

Results from Project 2.2 indicate that results from empirical regression-based methods for estimating the effect of temperature on runoff are dependent on the spatial scale of the data used. A spatial scaling effect is observed for areas larger than about 100,000 km<sup>2</sup> where temperature becomes increasingly more important to runoff generation in larger, drier parts of the Murray–Darling Basin. As a result, the inclusion of the very large dry areas of the Murray–Darling Basin can bias temperature elasticity estimates. This is one reason why several previous large-scale studies showed very large effects on runoff as a result of changes in temperature. Calculated at catchment scale, we estimate that of the observed runoff reduction during the Millennium drought, 67 percent was due to reductions in rainfall, 4 percent was due to the higher maximum temperatures associated with this reduced rainfall, and 7 percent was due to a residual temperature increase, with the remainder due to changes in rainfall characteristics (lack of high rainfall years and proportionally higher rainfall declines in autumn and winter). Hydrological modelling with a semi-distributed process model shows a non-linear response to surface saturation during extremely dry periods with rainfall replenishing the near-surface and groundwater stores rather than becoming runoff. Runoff production is directly connected to the surface saturation of a catchment. Adapting conceptual rainfall-runoff models to represent farm dams improved the runoff modelling slightly during the Millennium drought, suggesting a larger proportional influence of farm dams on runoff interception during droughts. It was found that calibrating against different objective functions (focusing on low flows, for example) was not able to significantly improve the representation of hydrologic response in different periods. The bias in runoff estimates (at least during dry periods) appears to be model dependent.

## Theme 3: Seasonal hydroclimate prediction in south-eastern Australia

*Research in Theme 3 is exploring the potential for improved seasonal forecasts of climate and streamflow*

Research in Project 3.1 showed that the record rainfall in 2010 occurred largely as a result of a record-strength La Niña event. Warmer sea-surface temperatures across northern Australia may have contributed about 15 percent of the total rainfall anomaly averaged across eastern Australia (up to 25 percent of the total in the north). The Southern Annular Mode, which exhibited record high polarity in spring 2010, may have contributed about 8 percent of the total rainfall anomaly over eastern Australia (up to 50 percent in central NSW). To the degree that the rainfall was tied to La Niña, the record rainfall in spring 2010 was largely predictable given the demonstrated capability to predict sea temperature variations associated with El Niño/La Niña. However, even after accounting for the behaviour of the Southern Annular Mode and sea-surface temperatures trends, the rainfall received in 2010 was at the upper limit of what would typically be expected for a La Niña event of the magnitude that occurred in 2010. Seasonal prediction of the 2010 rainfall anomaly was demonstrated with a lead time of three months with the POAMA2.4 model. Interestingly, the Southern Annular Mode appears to be a source of longer lead predictability than first thought.

To further improve seasonal streamflow forecasts, research in Project 3.2 investigated the use of outputs from dynamical hydrological and climate models as predictors to represent catchment wetness and climate condition, as well as the use of multiple models to produce merged forecasts. The Water Partition and Balance monthly hydrological model has been used to make a prediction of streamflow in the upcoming season under mean seasonal climate conditions. This prediction reflects the influence of the initial catchment condition only and is used as a predictor in the seasonal forecast model. This new forecast model produces more skilful forecasts than the current operational seasonal forecast model, for most of the catchments tested in eastern Australia. The best index of the large-scale state of the climate for use in the operational forecast model has also been investigated. A Bayesian model averaging technique is used to merge forecasts from multiple models, each with a different climate index. The merged forecasts are more skilful in many situations and they also appear to moderate the errors of poorly forecast events relative to those made using only the best climate index.

# CONTENTS

<b>Executive Summary .....</b>	<b>i</b>
<b>Contents.....</b>	<b>iv</b>
<b>Figures.....</b>	<b>v</b>
<b>Tables .....</b>	<b>xii</b>
<b>Acronyms .....</b>	<b>xiii</b>
<b>Chapter 1: Introduction .....</b>	<b>1</b>
<b>Chapter 2: Project 1.1.....</b>	<b>4</b>
<b>Chapter 3: Project 1.2.....</b>	<b>44</b>
<b>Chapter 4: Project 2.1.....</b>	<b>63</b>
<b>Chapter 5: Project 2.2.....</b>	<b>80</b>
<b>Chapter 6: Project 3.1.....</b>	<b>117</b>
<b>Chapter 7: Project 3.2.....</b>	<b>133</b>
<b>Chapter 8: Next steps .....</b>	<b>139</b>
<b>List of SEACI publications for 2011/12 .....</b>	<b>140</b>
<b>References.....</b>	<b>143</b>

## FIGURES

- Figure 1. The study area of the South Eastern Australian Climate Initiative ..... 1
- Figure 2. Map of the locations of mean surface-level pressure observations used to reconstruct the sub-tropical ridge intensity from 1860 to 2009 (L. Ashcroft, personal communication, 2012) thus extending the previous reconstruction from Drosdowsky (2005) back prior to 1890. The latitudinal extent of the climatological position of the STR is indicated in red, while the longitudinal band used by Drosdowsky (2005) is shown in blue ..... 6
- Figure 3. Monthly correlations computed between the between the intensity of the sub-tropical ridge (STR-I) and SEA rainfall using different datasets and different periods; in addition the correlations between the two STR-I reconstructions are indicated (blue line with reverse sign to fit on the graph) ..... 7
- Figure 4. Eleven year running means for SEA rainfall (upper graph: annual, left Y-axis and for March to November, right Y-axis) and for global temperature anomalies (in degree, left Y-axis) (HadCRUT2v dataset) with the two STR-I reconstructions (in hPa, right Y-axis) (lower graph). Epochs 1 and 3 correspond to periods of no global warming, no intensification of the STR and high SEA rainfall. By comparison, Epochs 2 and 4 correspond to periods of global warming, STR intensification and low decadal SEA rainfall ..... 8
- Figure 5. Maps of the thirty-year (1981–2011) deviations of rainfall from the long-term average: Top left, for the annual mean and three distinctive parts of the annual cycle; top right, for late autumn–early winter (April to July); bottom left, for the latter part of winter and early part of spring (August to October); and bottom right, for the warm part of the year (November to March) ..... 9
- Figure 6. Histograms (number of systems per decade, for each one degree of latitude from 43° S to 18° S) showing the position of centres for all entities (left) and only those entities having rainfall greater than 200 mm/day (right). The red line shows 1910–1960, green shows 1981–2011 and the black line shows the entire time period from 1910–2011 ..... 10
- Figure 7. As per Figure 6 but for summer (December, January, February) rainfall entities only ..... 11
- Figure 8. As per Figure 6 but for winter (June, July, August) rainfall entities only; right graph shown entities with rainfall above 100 mm); bottom left graph shows all entities in autumn (March, April, May) and bottom right in spring (September, October, November) ..... 11
- Figure 9. Annual cycle of the mean latitude of daily rainfall entity centres for all systems (solid lines) and for systems with rainfall above 100 mm (dashed line) for the entire Australian continent. The red line shows 1910–1960, green shows 1981–2011 and the black line shows the entire time period from 1910–2011. The shifts (measured as the difference between the red and green curves in the middle of the transition season) during the transition seasons are highlighted using a bold dashed vertical line ..... 12
- Figure 10. Relationship between Hadley cell expansion and sub-tropical ridge shift (a) and intensification (b) across a range of global datasets: 8 reanalyses (green circle), 2 climate model simulations (NCAR CCSM3 and CSIRO Mk 3.6) of the 20th century using different external forcings (natural only: yellow symbols, anthropogenic: pink symbols and full forcings: blue symbols). In all instances, individual model runs are shown as well as ensemble means (bold) ..... 14
- Figure 11. Correlation between mean sea level pressure (SLP) and southern hemisphere Hadley cell intensity (top) and extent (bottom) from the ERAI reanalysis dataset ..... 15
- Figure 12. Seasonal correlation between AWAP rainfall and ERA-I southern hemisphere Hadley cell intensity (contours) and extent (shading). Only values significant at the 90% level are shown ..... 16

Figure 13. Positions of the ‘relative’ global contours where the number of tropical tropopause days exceeds 200 from the radiosondes and four reanalyses. The zero line is the long-term average which, as part of the calculation process, is made to be equal for all products ..... 17

Figure 14. Relationship between global warming and Hadley cell expansion across a range of global datasets: 8 reanalyses (green circle), 2 climate model simulations (NCAR CCSM3 and CSIRO Mk 3.6) of the 20th century using different external forcings (natural only: yellow symbols, anthropogenic: pink symbols and full forcings: blue symbols). In all instances, individual model runs are shown as well as ensemble means (bold) ..... 19

Figure 15. Relationship between global warming and STR-P (top) and STR-I (bottom) across a range of global datasets: observation (black circle for the last 30 years and black square for the 20th century) 8 reanalyses (green circle), 2 climate model simulations (NCAR CCSM3 and CSIRO Mk 3.6) of the 20th century using different external forcings (natural only: yellow symbols, anthropogenic: pink symbols and full forcings: blue symbols). In all instances, individual model runs are shown as well as ensemble means (bold) ..... 20

Figure 16. Trends in degrees C for annual mean sea-surface temperature. Linear trends are computed over the period 1950–2008 (Hurrell et al., 2008) ..... 23

Figure 17. Sea-surface temperature (SST) perturbation experiments: +1 °C in the tropics (top, to+1) and –1 °C in the southern ocean (bottom, so–1)..... 24

Figure 18. Annual cycle (months of the year are indicated by their first letter) of the intensity ( $\times 10^9 \text{ kg s}^{-1}$ ) vs. extent (degrees of latitude) of the Hadley cells in both hemispheres. Determined from the mean of eight reanalyses (black cross with the size of the cross indicating the range from all reanalyses) and from the ACCESS global climate model experiments (CTL: red, so–1: green, to+1: blue). ..... 26

Figure 19. Hadley cell intensity (top) and extent (bottom) showing the difference between southern ocean cooling and the control experiments (left) and between the tropical warming and control experiments (right) for annual and seasonal means, derived using the ACCESS climate model. The Northern Hemisphere is shown by orange open bars and the Southern Hemisphere by grey solid bars ..... 27

Figure 20. Zonal mean annual cycle of tropopause height in latitude-time space in the three simulations. Contours are plotted every 1 km from 9–15 km. Colours denote the simulation; Control=red, to+1=blue and so–1=green 28

Figure 21. Summary of tropical and extra-tropical responses to the perturbation experiments in the tropics (15 km contour) and extra-tropics (11 km contour). Responses are separated by hemisphere and broken down into annual and seasonal means. Expansion in this context means that the contour moves towards its respective pole ..... 29

Figure 22. Average annual cycle of tropopause height over Eastern Australia (135°–155° E) from the radiosondes (black), ERA Interim (red) and experiments using the ACCESS climate model 1.0 CMIP5 historical run (blue) ..... 31

Figure 23. Zonal mean tropopause height trends from radiosondes (black), ERA Interim (red) and ACCESS 1.0 historical CMIP5 simulation (blue). Units are  $\text{m dec}^{-1}$ . Trends calculated from 1979–2010 (2005 for ACCESS) ..... 32

Figure 24. Spatial pattern of ERA-I tropopause trends from 1979–2010. Greens and oranges are positive values, blues and purple are negative values..... 33

Figure 25. As in Figure 24, except for the ACCESS 1.0 historical CMIP5 simulation ..... 33

Figure 26. CMIP5 multi-model mean rainfall trends of the first run of all available models for 1950–2005 (left panels), and corresponding observational (based on GPCP v2.2) rainfall trends for 1979–2005 (right panels) over the Southern Hemisphere. Trends are shown for all seasons: March, April, May; June, July, August; September, October, November; and December, January, February. Rainfall trends are shown as a percentage of climatology, and trends from individual models have been interpolated to a standard  $4^\circ \times 4^\circ$  grid. .... 35

Figure 27. March, April, May rainfall trends for 1950–2005 in individual CMIP5 models over Australia. Trends in observations (AWAP, 1950–2005) are included for reference (bottom right panel). Rainfall trends are shown as a change in percentage from climatology (1950–2005). Trends for each model are an ensemble average of all available ensemble members in the historical experiment and the number of ensemble members for each model is indicated in brackets after the model name. .... 38

Figure 28. March, April, May MSLP trends for 1950–2005 in individual CMIP5 models over the Southern Hemisphere. Trends in NCEP/NCAR reanalysis are included for reference. MSLP trends are shown in hPa/yr. Trends for each model are an ensemble average of all available ensemble members in the historical experiment and the number of ensemble members for each model is indicated in brackets after the model name..... 39

Figure 29. Atmospheric circulation patterns obtained by regressing detrended anomalies onto a detrended DMI using: (a) all samples, implying a linear relationship; (b) samples with a positive DMI value (positive IOD events); and (c) samples with a negative DMI value (negative IOD events). The regression coefficients (colour) and correlation coefficient (green contours, greater than that required for the 95 % confidence level) are plotted. The coefficients shown are associated with: outgoing longwave radiation (left,  $W m^{-2} °C^{-1}$ ); 200-hPa geopotential height (centre,  $m °C^{-1}$ ); and Australian rainfall (right,  $mm^{-1} season^{-1} °C^{-1}$ ). Figure reproduced from Cai et al., (in press.)..... 41

Figure 30. Map shows continental total evaporation E from BIOS2 (1990–2011 mean). Panels show mean monthly E at 12 Ozflux sites providing multi-year eddy covariance measurements of water and carbon fluxes. Red points are observations of E, red lines are BIOS2 predictions (both keyed to left axis). Blue lines show monthly mean precipitation (right axis) ..... 47

Figure 31. Mean water balance fluxes in 34 unimpaired catchments. Stacked bars represent soil evaporation  $E_s$  (brown), transpiration  $E_t$  (yellow), wet-canopy evaporation  $E_w$  (sky blue) and outflow Q (dark blue). The long-term water balance is  $P = E_t + E_s + E_w + Q$ , so the total height of the stacked bars gives the precipitation (P) in each catchment. Stars give potential (Priestley-Taylor) evaporation in each catchment. Catchments are ordered as in Potter et al. (2011), based on a dryness index, with drier catchments on the right ..... 48

Figure 32. (Upper panel) sensitivity of outflow (Q) to precipitation (P), denoted  $\eta(Q,P)$ , for UC34 catchments. (Lower panel) sensitivity of outflow (Q) to temperature (T), denoted  $\eta(Q,T)$ . Orange points: BIOS2 model results; green points: empirical results (SEACI Project 2.2; Potter et al., 2011)..... 49

Figure 33. Breakdown of contributions to sensitivity of outflow to temperature,  $\eta(Q,T)$ , for 34 unimpaired catchments ..... 50

Figure 34. BIOS2 predictions of the cumulative probability distribution function of soil-column outflow Q ( $mm y^{-1}$ ), spatially averaged across the whole SEACI region, over 100 years. This is the fraction of years for which the outflow is less than a value Q, plotted against Q. Red curve is the CDF for present conditions; green, blue and black curves give the CDF at warmings of 1, 2 and 4 °C ..... 54

Figure 35. Comparison between humidity estimated from daily minimum temperature as in BIOS2 (red line) and direct hourly observations at the Tumbarumba Ozflux site (blue) for 2009..... 55

Figure 36. Monthly time series of the (spatial) median difference within the SEACI region for the solar radiation forcing used for AWAP WaterDyn runs 26h and 26c is given in panel a). The spatial median is used to minimise the impact of differences related to the coastal and inland water buffering, which may be large but involve small areas. The resulting differences in b) upper and c) lower layer soil moisture starting in March 2007 are due almost entirely to changes in the solar radiation surfaces related to fixing the bias correction. The inference is that for the SEACI region, AWAP run 26c contains a spuriously large negative trend in soil moisture from March 2007 to 2010. The bias in upper layer soil moisture is most pronounced in the winter months. Differences in 1989 solar radiation (panel a) reflect differences between the climatologies used to fill the period 1900–1989, which are from 1990–2008 for 26c and 1990–2011 for 26h. The lack of bias in 26c in November 2009 is accidental: positive bias from sensor drift in the first half of the month was balanced by negative bias in the second half of the month from the use of climatology for 13 missing days in what was a notably hot and dry November in the region ..... 58

Figure 37. Correlation matrix (at zero time lag) between spring (September, October, November, SON) rainfall in the whole MDB and several climate indices: Niño 3.4 (n34), Indian Ocean Dipole Mode Index (dmi), sub-tropical ridge intensity (stri), Tripole Index (tpi) and ENSO Modoki Index (emi). Signs and magnitudes of correlation coefficients are indicated by colours, colour densities and sizes of circles ..... 60

Figure 38. Comparison of the skill of linear-regression model (left) and random-forest model (right) in predicting whether spring (September, October, November, SON) rainfall in the MDB will fall into wet, medium and dry terciles, using 5 climate indices as predictor variables with forecast lead times from zero (nowcast) to 6 months. Each colour block represents the fraction of a test data set predicted by the model to be wet (blue), medium (green) or dry (red), when the true outcome (known from the test data) is respectively wet (lower band), medium (middle band) and dry (upper band). A prediction with 100% skill would appear as a completely blue lower band, a completely green middle band and a completely red upper band ..... 61

Figure 39. Modelling components for estimating climate change impact on future streamflow with the main sources of uncertainty shown in red ..... 64

Figure 40. Examples of spatial patterns of the observed (upper panels) and modelled (lower panels) long-term average (1950–1999) of the first empirical orthogonal function (EOF) of annual sea-surface temperature over the Pacific and Indian oceans. The model skill score (M-statistic) is also indicated. An M-statistic of 1 indicates a perfect match between the GCM modelled and observed values and an M-statistic of 0 indicates a very poor match ..... 67

Figure 41. Examples of spatial patterns of the observed and modelled relationship between the spring (September, October, November ENSO index (NINO3.4) and SEA rainfall. The model skill score (M-statistic) is also indicated . 68

Figure 42. M-Statistic summarising the GCMs’ ability to simulate the observed spatial pattern of mean seasonal Tripole Index and Tripole Index-SEA rainfall relationship for 1950–1999 ..... 69

Figure 43. Observed and modelled temporal pattern of winter (June, July, August) ENSO index (Left: variability during 1860 to 2020. Middle: histogram of the time series. Right: power spectrum)..... 69

Figure 44. Range of M-statistic summarising the 25 CMIP3-GCMs ability to simulate the observed historical (1961–2000) characteristics ..... 70

Figure 45. Range of projected change in mean annual precipitation averaged across the Murray–Darling Basin for a 1 °C global warming based on all 24 GCMs (first column) and based on the best five GCMs assessed against the different measures (columns 2 to 10) ..... 71

Figure 46. Annual mean rainfall, mean sea level pressure and temperature in each model along with the observed pattern for 1950–2000..... 71

Figure 47. M-statistic and  $\Delta_{SS}$  skill scores for the mean annual rainfall, coefficient of variation of annual rainfall (CV), and linear trend of the annual rainfall simulated by each model for 1950–2000. Higher M-statistic and lower  $\Delta_{SS}$  indicate better performance ..... 72

Figure 48. The projected 21st century change in rainfall over eastern Australia for each model (bottom) along with the spatial distribution of the projected changes (top) ..... 72

Figure 49. Flowchart showing modelling experiments. The modelling components are shaded in grey. Circles with crosses indicate calculated differences; numbered circles indicate points of comparison as referred to in the text 73

Figure 50. 28 rainfall sites (black circles), 91 grid cells (blue squares), and 38 (nine pink filled catchments are used for hydrological simulations) catchments in the Murray headwaters used for NHMM downscaling (Fu et al., submitted.) ..... 74

Figure 51. Daily runoff distribution (1985–2000) for eight catchments in the Murray headwaters, with hydrological modelling using daily rainfall from observation (SILO) and analogue, NHMM and WRF downscaling methods. The mean annual runoff from the various methods is shown at the end of the legend label..... 76

Figure 52. (a) Percentage change in future mean annual runoff for 2046–2065 according to 10 GCMs using the analogue downscaling method (top 10 plots) and the daily scaling (following 10 plots); and (b) percentage change in mean annual runoff averaged across the SEACI region (Teng et al., 2012) modelled using rainfall downscaled from 10 GCMs using the analogue downscaling method (triangles) and the daily scaling method (squares) .....	77
Figure 53. Mean annual rainfall (a) and runoff (b) for 34 study catchments in south-eastern Australia .....	84
Figure 54. Rainfall elasticities of streamflow (a) and temperature elasticities of streamflow (b) for the 34 catchments in south-eastern Australia .....	85
Figure 55. Runoff sensitivities to rainfall and maximum temperature. Note these are expressed as a mm change in annual runoff due to a 1 mm increase in annual rainfall, and a mm change in runoff due to an increase in annually averaged maximum temperature resulting in a 1 mm increase in potential evapotranspiration. X-axis is mean annual dryness index .....	86
Figure 56. Water and energy budgets for a water-limited (arid) catchment: a) long-term water budget, b) drought water budget, c) long-term energy budget, and d) drought energy budget .....	89
Figure 57. Water and energy budgets for an energy-limited (humid) catchment: a) long-term water budget, b) drought water budget, c) long-term energy budget, and d) drought energy budget.....	89
Figure 58. Change in actual evapotranspiration against observed, expected and residual temperature anomalies ( $T_a$ ; $E(T_a)$ ; $R(T_a)$ ) since 1997 for 34 catchments in SE Australia .....	90
Figure 59. Mean annual rainfall and runoff (mm and GL) for increasingly drier partial areas of the MDB .....	91
Figure 60. Rainfall and temperature elasticities of runoff (a) – note the reversed right hand axis; sensitivities to rainfall and potential evaporation (b); and proportion of the observed runoff reduction ( $\delta Q$ ) in the MDB explained by the reduction in rainfall and the temperature anomaly during the Millennium drought (c) for increasing partial area of the Murray–Darling Basin .....	92
Figure 61. Daily observed and streamflow prediction from TOPOG; stream option activated.....	95
Figure 62. Daily observed and predicted streamflow with and without stream option in TOPOG. Y-axis has logarithmic scale to show better differentiation of individual lines.....	95
Figure 63. Annual summary of streamflow; simulations start 1951 while observations start 1973.....	96
Figure 64. Observed relationship between annual rainfall (x-axis; mm) and streamflow (y-axis; mm), Brankeet Creek, 1973–2011 .....	97
Figure 65. Annual average TOPOG catchment storage and percentage saturated area .....	97
Figure 66. Annual average TOPOG modelled catchment saturated area versus streamflow, 1974–2011 .....	98
Figure 67. Modification of SIMHYD to include a farm dam component .....	104
Figure 68. Number of catchments exceeding Nash-Sutcliffe Efficiency scores during the validation period (1997–2008).....	105
Figure 69. Number of catchments exceeding mean daily runoff bias (modelled minus observed) during the validation period (1997–2008) .....	105
Figure 70. Farm dams (red) and their catchments (grey) for an example catchment in south-eastern Australia..	107
Figure 71. Location of the ten catchments used in this activity .....	108
Figure 72. Calibration and simulation results for the Sacramento model.....	110
Figure 73. Calibration and simulation results for the GR4J model.....	112

Figure 74. Projected median and range (10th and 90th percentiles) of change for (a) mean annual precipitation (% change); (b) mean annual runoff (% change); and (c) mean annual runoff (mm change) for a 1 °C global warming 115

Figure 75. Standardised eastern Australian area averaged rainfall anomaly (east of 135° E; blue) and the SOI (green) calculated with respect to the 30 year reference period 1961–1990 (Jones et al., 2009)..... 119

Figure 76. (a) Seasonal mean sea-surface temperature (SST) anomaly for September, October, November 2010 based on the Hurrell SST analysis (Hurrell et al., 2008), (b) reconstruction of September, October, November 2010 SST anomaly based on regression of SST onto the SOI index for 1960–2009 and then scaled by the magnitude of 2010 SOI in September, October, November, and (c) as in (b) but regression of SST onto a time series of eastern Australian rainfall (mean rainfall east of 135E) for 1960–2009 and then scaled by the magnitude of the observed eastern Australian rainfall anomaly in September, October, November 2010 ..... 120

Figure 77. Time series (grey bars) of (a) SST PC1, (b) SST PC2, (c) the DMI, (d) SSTnAU and (e) the SAM index overlaid with trend lines (red) computed over the period of 1960–2010. The total change attributed to the trend over the 51 years is indicated along with its statistical significance of the trend on the upper right of each graph..... 121

Figure 78. (a) Global MSLP anomaly in 2010 September, October, November (SON) from NCEP reanalyses. (b) Reconstruction of 2010 September, October, November MSLP anomaly based on the regressed relationship with the SOI during 1960–2009 and then scaled by the SOI anomaly in September, October, November 2010. (c) As in (b) except for regression onto the SAM. Colour shading interval is 1 hPa..... 122

Figure 79. Composites of MSLP anomalies in September, October, November for negative ( $\leq -0.5$ ), neutral ( $-0.5 < < 0.5$ ) and positive ( $\geq 0.5$ ) events of SOI and SAM. MSLP data are from NCEP-NCAR reanalyses 1960–2010. Colour shading indicates MSLP anomalies with 0.5 hPa interval. The number of samples in each category is shown in the upper right of each map..... 123

Figure 80. Composites of rainfall anomalies in September, October, November for negative ( $\leq -0.5$ ), neutral ( $-0.5 < < 0.5$ ) and positive ( $\geq 0.5$ ) events of SOI and SAM. Rainfall anomalies are from the AWAP analyses 1960–2010. Colour shading indicates rainfall anomalies with 0.4 mm/day shading interval. The number of samples in each category is shown in the upper right of each map. The mean amplitudes of standardised SAM and SOI and raw eastern Australia area averaged rainfall for each category are displayed at the bottom left in each map..... 124

Figure 81. Observed (blue bars) and predicted (orange and green bars) time series of SOI and eastern Australia area averaged rainfall (EAU) in September, October, November. (a) Prediction of SOI was made using multiple linear regression onto SST PC1, PC2, DMI and SSTnAU index including trend (orange) and detrended (green). Predictions/regressions were formed with leave-one-out cross-validation. The correlation of the prediction including the trend with the observed values (using cross validation) is displayed in upper right of the panel. Red dotted lines indicate 95% prediction interval. (b) As in (a) except for eastern Australia rainfall predicted using SST PC1 and PC2, the DMI, SSTnAU and the SAM indices. Prediction of eastern Australia area averaged rainfall was made in the same manner as that of SOI but with the SAM index as an additional predictor ..... 125

Figure 82. Top row (a) to (e): Values of the individual multiple linear regression coefficients when multiplied by the magnitudes of each predictor in September, October, November 2010. Bottom row (f) to (g): Values of the bivariate regression coefficients in 2010 for (f) PC1 and (g) PC2. The partial regression coefficients after removing the influence of SST PC1 and PC2 are shown for (h) DMI, (i) SSTnAU, and (j) the SAM. Colour shading interval is 0.2 ..... 127

Figure 83. The same as Figure 81 except for December, January, February..... 128

Figure 84. Observed (red bars) and predicted (lead time 0 months in dark blue, lead time 3 months in light blue) anomalies of various climate indices for spring 2010. From left to right: south-eastern Australia rainfall index (rainfall averaged over south-eastern Australia), and the NINO3, IOD, SOI and SAM indices. Magnitudes of the indices are in respective standard deviations ..... 129

Figure 85. (a) Initial land surface wetness anomaly for 1 September 2010. Shading interval is 0.4 mm, (b) Lead time 0 predictions of standardised anomalies of key climate drivers and SEA rainfall from POAMA24 (blue bars), the experiment with randomised atmospheric initial conditions (green bars) and the experiment with random land surface initial conditions (yellow bars) ..... 130

Figure 86. SAM (red and orange bars) and NINO3 (dark and light blue bars) predicted from POAMA and the forecast experiment initialised with random ocean conditions. The atmosphere and land surface for both POAMA and the experiment were initialised with observed 2010 conditions..... 130

Figure 87. Composites of observed (upper panels) and 2 month lead POAMA forecast (lower panels) September, October, November rainfall anomalies in extreme wet years (1964,1973,1975,1998,2000, 2010) and extreme dry years (1963,1965,1967,1977,1982,1990,2002,2006) in eastern Australia. The numbers on the upper left corners indicate the number of sample years. The colour shading interval is 0.4 mm/day ..... 131

Figure 88. Location of the 20 catchments used in the study ..... 135

Figure 89. Skill improvement in percentage for 12 overlapping seasons (a) Method 2 over Method 1, (b) Method 3 over Method 2, and (c) Method 4 over Method 3. The skill improvement score used is based on root mean squared error in probability (RMSEP) ..... 136

Figure 90. Skill score calculated across all the catchments but for individual seasons over time. Blue is for Method 2 and red for Method 3. The skill score used is based on root mean squared error in probability (RMSEP) ..... 137

Figure 91. Overall skill score achieved using Method 4 relative to climatology for the 12 overlapping seasons (columns) and 22 catchments (rows). The skill score used is based on root mean squared error in probability (RMSEP) ..... 137

## TABLES

Table 1. CMIP5 models, institutions and the number of simulations from the historical experiments (precipitation and MSLP) used in this study.....	36
Table 2. Sensitivity $\eta(Q,X)$ of outflow $Q$ (spatially averaged over whole SEACI region) to key variables $X$ , calculated using runs over 1911–2011 at 200 randomly chosen points across the SEACI region.....	51
Table 3. Fractional changes in SEACI region outflow ( $\Delta Q/Q$ ) in response to assumed changes in driving variables, assessed as plausible over the period 2012–2050.....	53
Table 4. Bureau of Meteorology AWAP meteorology used to force recent AWAP WaterDyn historical runs 26h (due for release June 2012), and 26c (released March 2011). Download dates are colour-coded by age, from red (oldest) to green (newest). Green date ranges in the upper panel show the changes from run 26c to 26h, including complete new solar radiation, replacement of all 2010 and 2011 data, and an extension of the series from Feb 2011 to the end of 2011. Synthetic parts of the temperature and solar radiation series are constructed from data with a currency indicated by the cell colour .....	56
Table 5. Area-weighted estimates (mm of runoff) of the average relative effects of changes in rainfall and maximum temperatures on the study catchments during the Millennium drought (1997–2008). Bracketed values are percentage of the observed reduction during the drought compared to the pre-1997 averages .....	87
Table 6. Climate data summary for Brankeet Creek including streamflow where available. Note that streamflow from 1951 to 1973 is estimated from a quadratic relationship between annual rainfall and runoff.....	96
Table 7. Average rainfall for decades between 1974–83 and 2002–11 .....	98
Table 8. Decadal average streamflow (mm/a), % saturated area and catchment-average leaf area index for three historic climate series .....	99
Table 9. Annual summary of water balance and leaf area index for comparison years 1990 and 2003.....	100
Table 10. Monthly simulated water balance and leaf area index for the years 1990 and 2003.....	101
Table 11. Number of land elements with various depths of water table for the years 1990 and 2003 .....	103
Table 12. Modelling experiments carried out in this activity .....	109

## ACRONYMS

ACCESS	Australian Community Climate and Earth-System Simulator
AWAP	Australian Water Availability Project
BJP	Bayesian joint probability
BoM	Bureau of Meteorology
CABLE	CSIRO Atmosphere Biosphere Land Exchange model
CART	Classification and Regression Trees
CAWCR	Centre for Australian Weather and Climate Research
DDD	drought depth duration
DEM	digital elevation model
DJF	December, January, February
DMI	Indian Ocean Dipole Mode Index
EMI	El Niño Modoki Index
ENSO	El Niño – Southern Oscillation
EOF	empirical orthogonal function
FDC	flow duration curve
GCM	global climate model
GHG	greenhouse gases
GL	gigalitres
HC	Hadley circulation
hPa	hectoPascals
IOD	Indian Ocean Dipole
IPCC	Intergovernmental Panel on Climate Change
JAS	July, August, September
JJA	June, July, August
LAI	Leaf area index
MAM	March, April, May
MDB	Murray–Darling Basin
MMC	mean meridional circulation
MMM	multi-model mean
MSLP	mean sea level pressure
NCAR	National Center for Atmospheric Research
NCEP	National Center for Environmental Prediction

NHMM	non-homogenous hidden Markov Model
NSE	Nash-Sutcliffe efficiency
NWP	numerical weather prediction
PET	potential evapotranspiration
POAMA	Predictive Ocean Atmosphere Model for Australia
SAM	Southern Annular Mode
SEA	south-eastern Australia
SEACI	South Eastern Australian Climate Initiative
SLP	sea level pressure
SOI	southern oscillation index
SON	September, October, November
SST	sea-surface temperature
STR	sub-tropical ridge
STR-I	sub-tropical ridge intensity
STR-P	sub-tropical ridge position
TIO	tropical Indian Ocean
Tmax	maximum temperature
TTD	tropical tropopause days
WAPABA	Water Partition and Balance monthly hydrological model
WRF	Weather Research Forecasting
WIRADA	Water Information Research and Development Alliance

## CHAPTER 1: INTRODUCTION

### The South Eastern Australian Climate Initiative

Phase 2 of the South Eastern Australian Climate Initiative (SEACI) is a three year, \$9 million research program investigating the causes and impacts of climate change and climate variability across south-eastern Australia. The SEACI geographical study area incorporates the Murray–Darling Basin, the state of Victoria and southern South Australia, including the Eyre Peninsula, as shown in Figure 1.

Planning for future management of Australia’s water resources requires an understanding of the future state of Australia’s climate. This program aims to deliver a holistic and better integrated understanding of climate change and climate variability across south-eastern Australia to support water managers and policy makers.

The research program includes studies of the nature and causes of climate variability, on time scales from weeks to decades. This range of scales is relevant to the stakeholders. Issues on short-term time scales (weeks and months) arise in the operational management of water, while horizons for water resources and infrastructure planning and policy are of a long-term nature (years and decades).

SEACI is a partnership between CSIRO Water for a Healthy Country Flagship, the Australian Government Bureau of Meteorology, the Murray–Darling Basin Authority, the Victorian Department of Sustainability and Environment, and the Australian Government Department of Climate Change and Energy Efficiency. CSIRO is the managing agency.

A Steering Committee, comprising representatives of each partner agency, sets and monitors the strategic direction of SEACI. In 2011–12 a representative from the Murray–Darling Basin Authority (Jody Swirepik) chaired the Steering Committee. The Steering Committee is supported by a Science Panel, which provides advice on implementation of the initiative. The Science Panel is chaired by an independent expert, Dr Graeme Pearman.

In 2011–12, Dr David Post from CSIRO continued his role as SEACI Program Director.

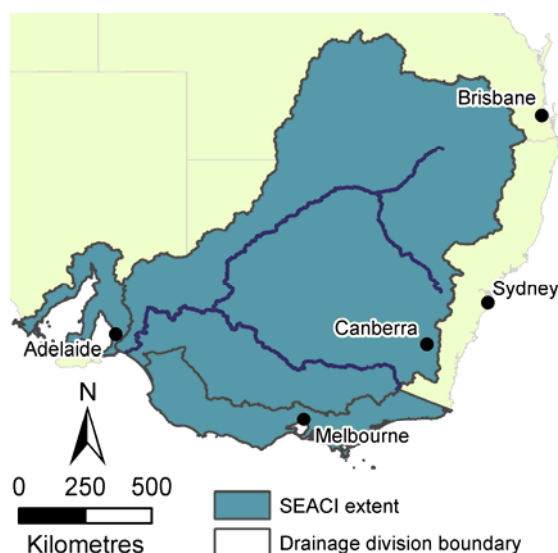


Figure 1. The study area of the South Eastern Australian Climate Initiative

## Research context

The variability of Australia's climate has always been a challenge for water management and agricultural industries. Global climate change is now recognised as a threat to water resources, agriculture and natural ecosystems in many parts of the world. In south-eastern Australia, temperatures have been rising steadily and with the exception of 2010 and 2011, rainfall has been low since the late 1990s. Similar rainfall declines started in the mid-1970s in south-west Western Australia, prompting the establishment of the Indian Ocean Climate Initiative (IOCI) in 1997. IOCI research focused on understanding variability and change in the region's climate, and showed that climate change is likely to be a significant factor in observed changes in the region. The clear benefits of IOCI motivated the establishment of SEACI.

## Findings from Phase 1 of the South Eastern Australian Climate Initiative

Research in Phase 1 of SEACI included an investigation into the nature and causes of the Millennium drought which occurred from 1997 to 2009 in south-eastern Australia (SEA). The research concluded that this drought was unprecedented with regards to its extent, the low degree of inter-annual rainfall variability, and the seasons in which the rainfall declined. In particular, SEACI research found that throughout the drought the rainfall decline was greatest in the autumn months, unlike in previous droughts where rainfall decline was greatest in winter and spring.

The sub-tropical ridge (STR) is a band of high pressure which affects rainfall across southern Australia. SEACI research found a strong relationship between increased pressures along the STR and recent rainfall decline. Further modelling studies conducted within SEACI showed that this observed intensification of the STR could only be reproduced when human influences on atmospheric greenhouse gas and particle (i.e. aerosol) concentrations were included. This suggests a link between global warming and the recent rainfall decline in SEA.

Research throughout Phase 1 of SEACI also showed that the 13 percent decline in rainfall in the southern Murray–Darling Basin during the Millennium drought led to a 44 percent reduction in streamflow. The magnitude of this reduction in streamflow was greater than expected. This is thought to be due to the absence of wet years over the decade, and to the seasons in which the rainfall has declined. The decline in autumn rainfall has meant that winter rains must moisten the soil before any useful streamflow can begin. It is expected that in the future this effect will be amplified as average temperatures across the region continue to increase due to climate change.

Phase 1 of SEACI also achieved improvements to the coupled atmosphere–ocean–land climate model (POAMA) to increase the accuracy of seasonal forecasting, especially for south-eastern Australia. Ongoing research efforts further refined POAMA, with the aim of increasing the accuracy of prediction at longer lead times.

Research in Phase 2 of SEACI built upon the findings and progress made in Phase 1. Phase 2 addressed key research questions through three linked research themes, described below.

Details of the findings of Phase 1 of SEACI can be found in CSIRO (2010a; 2010b).

# Research themes

## Theme 1: Understanding past hydroclimate variability and change in south-eastern Australia

Research in Theme 1 is leading to a better understanding of the factors that drive changes in both climate and streamflow within the region. The projects aim to understand and attribute causes of observed climate change in SEA, as well as diagnose the relationships between climate variability and the water balance.

The projects in Theme 1 are:

Project 1.1: Understanding and attributing climate change in SEA.

Project 1.2: Impact of climate variability and change on the water balance.

## Theme 2: Long-term hydroclimate projections in south-eastern Australia

Research in Theme 2 is leading to improved hydroclimate projections for SEA. The research aims to identify the most suitable global climate models, to assess methods for downscaling projections from these models to obtain catchment scale climate series, and to adapt hydrological models to represent changed rainfall–temperature–streamflow relationships and dominant hydrological processes in a warmer, drier environment with increased levels of CO<sub>2</sub>.

The projects in Theme 2 are:

Project 2.1: Climate change projections.

Project 2.2: Hydroclimate impacts for SEA.

## Theme 3: Seasonal hydroclimate prediction in south-eastern Australia

Theme 3 is aiming to improve predictions of rainfall and streamflow on timescales of around 1 to 12 months in SEA, extending to the development of operational products. It assesses the skill of models in producing useful predictions of streamflow. Additionally, it is further developing modelling approaches and assessing the utility of seasonal forecasts in improving the skill of hydrological modelling for SEA.

The projects in Theme 3 are:

Project 3.1: Advancing seasonal predictions for SEA.

Project 3.2: Hydrological application of seasonal predictions.

## About this report

This report provides detailed information about the progress made in each of the six SEACI research projects in the 2011/12 financial year. Publications arising from the year's research are listed at the end of the document. A synthesis of findings from the whole three years of SEACI Phase 2 can be found in CSIRO (2012).

## CHAPTER 2: PROJECT 1.1

### Understanding and attributing climate change in south-eastern Australia

Bertrand Timbal, Hanh Nguyen, Chris Lucas and Morwenna Griffiths (BoM/CAWCR)

Tim Cowan, Wenju Cai, and Ariaan Purich (CSIRO/CAWCR)

Linden Ashcroft (Melbourne Uni), Julie Arblaster (BoM/CAWCR and NCAR)

## Executive summary

- Historical reconstruction of both south-eastern Australian (SEA) rainfall and sub-tropical ridge (STR) intensity allowed us to explore the interactions between these two measures and the global average temperature as far back as the 1860s. The 1860s to 1890s provide another example alongside the 1950s to 1970s of an extended period where, in the absence of noticeable global warming, no STR intensification was observed in conjunction with strong decadal variability of SEA rainfall with a very wet decade (the 1870s was as wet as the 1970s).
- Departures from the long-term climatology across Australia observed during the last 30 years show a continent which is getting wetter in terms of mean annual rainfall, with the exception of south-eastern and south-western Australia and Tasmania. While there has been a slight reduction in the number of systems affecting the tropical part of the continent, there has been a sizeable increase in the size of the larger systems, resulting in an increase in rainfall, particularly in the warm season. On the contrary, drying trends have been observed in south-eastern and south-western Australia, particularly in autumn and winter. This reflects the facts that during the cool season, fewer extra-tropical systems have been observed, and the reduction in rainfall has been strongest for the more intense systems.
- The addition of new climate reanalysis products further confirms our findings from last year. The addition of the CSIRO Mk3.6 climate model simulations of the 20th century further highlights the strong linear relationship between the expansion of the Hadley Circulation and the STR. It also reinforces the role of human-related activity in these changes.
- Preliminary results from research on the role of the Hadley cell on local STR and rainfall suggest that the local STR at the longitudes of SEA is likely to be affected not only by the extent of the Hadley circulation, but also the Hadley cell intensity. These preliminary results further hint at the likely influence of the Hadley cell on SEA rainfall. It is suggested that Hadley cell intensification in summer and expansion throughout the year may contribute to the observed SEA rainfall decline.
- Global warming is shown to be strongly associated both with the expansion of the Hadley circulation and poleward shift and intensification of the STR. These relationships are observed only in the model simulations containing anthropogenic inputs. Other factors may be important too. The role of stratospheric ozone depletion in driving such changes is also uncertain, based on CMIP3 model results and individual forcing runs using the CSIRO Mk3-6-0 model (CMIP5).
- Climate reanalysis products may not be fully reliable for the investigation of long-term climate trends due to some changes in the observational data through time.
- The ACCESS global climate model shows some potential as a research tool, but work remains to be done in order to understand its strengths (ability to reproduce realistic mean meridional circulations) and limitations (sizeable biases for various quantities of interest). In this model, warming the tropical sea-surface temperature results in a greater impact on the mean meridional circulation than cooling the southern ocean.

- CMIP3 and CMIP5 models poorly simulate the observed late 20th century decrease in autumn (March, April, May) rainfall across SEA. This is despite the CMIP5 multi-model mean broadly simulating the observed winter (June, July, August) rainfall reduction across south-west Western Australia, and the model simulation of increasing mean sea level pressure, albeit too far south.
- The relationship between observed trends in mean sea level pressure and rainfall across SEA suggests that local pressure increases could account for much of the autumn rainfall decrease since 1950. The inability of CMIP5 models to simulate increasing trends in mean sea level pressure in the correct location may be one of the factors limiting the ability of CMIP5 models to reproduce observed rainfall trends. This result confirms work completed during Phase 1 of SEACI (using CCSM3 with external forcings) which showed that in order to obtain realistic rainfall trends across SEA, the climate model needed to be downscaled.

## Background

Phase 1 of SEACI made substantial progress in documenting recent climate change in SEA and identifying the large-scale circulations that control the regional climate of SEA including the El Niño – Southern Oscillation (ENSO), the Indian Ocean Dipole (IOD), and the Southern Annular Mode (SAM). Key findings were that the recently observed decline in rainfall in SEA has occurred predominantly in the autumn and early winter, and that much of this decline is accounted for by an increased intensity of the STR. In addition, it was established that the rise in the STR-I followed the rise of global temperature. Although the STR-I and STR-position are convenient diagnostics closely linked to rainfall in SEA, the causality of the global temperature–STR relationship remains to be established and requires further investigation.

During the first year of Phase 2 of SEACI, further progress was made in better understanding and attributing the ongoing rainfall deficiency in SEA. The characterisation of the severity of the recent drought was improved by analysis of a longer set of data from the instrumental record. This provided a better comparison of the severity of the rainfall deficiency in the Millennium drought relative to that of the Federation drought. The annual cycle of the natural variability of rainfall in SEA and its relationship with the annual cycle of the ongoing rainfall deficiency was analysed, identifying the amount of natural variability which is not due to large-scale forcings but rather, weather noise. Finally, an important contribution was to review the existing literature regarding the mean meridional circulation (MMC) of the atmosphere, its observed changes, and likely response to global warming with a focus on relevant features for climate in SEA.

### Objectives

The objectives for 2011–12 were to:

1. Update the evaluation of the ongoing climate anomalies with a focus on daily rainfall;
2. Analyse the characteristics of the meridional circulation, and its trends in the observations in all available climate reanalyses products (now eight in total);
3. Analyse existing climate simulations to evaluate the ability of models to reproduce the meridional circulation changes and to explore the possible attribution of these changes;
4. Perform numerical experiments to test hypotheses about the relationship between the large-scale states of the ocean and atmospheric circulations and the mean meridional circulation;
5. Examine whether climate models (both CMIP3 and CMIP5) could simulate the observed autumn rainfall reduction across SEA in the late 20th century with a focus on models with and without ozone depletion in the 20th century experiments; and
6. Examine whether the impact pathway whereby the IOD and ENSO influence SEA's climate, is symmetric with respect to positive and negative phases of the IOD and ENSO.

# Objective 1

## Update the evaluation of the ongoing climate anomalies with a focus on daily rainfall

### Historical reconstruction of STR intensity and SEA rainfall from 1860

Following on the development of a SEA rainfall reconstruction as far back as 1865 (Timbal and Fawcett, in press) reported in CSIRO (2011), a new reconstruction (Ashcroft, 2012, personal communication) of the sub-tropical ridge intensity (STR-I) has been developed using Bureau of Meteorology Mean Sea Level Pressure (MSLP) stations in the vicinity of the regions used in the original work by Drosdowsky (2005). The long-term monthly 9 am mean sea level pressure data were obtained for ten stations in south-eastern Australia (Figure 2) for 1860–2009.

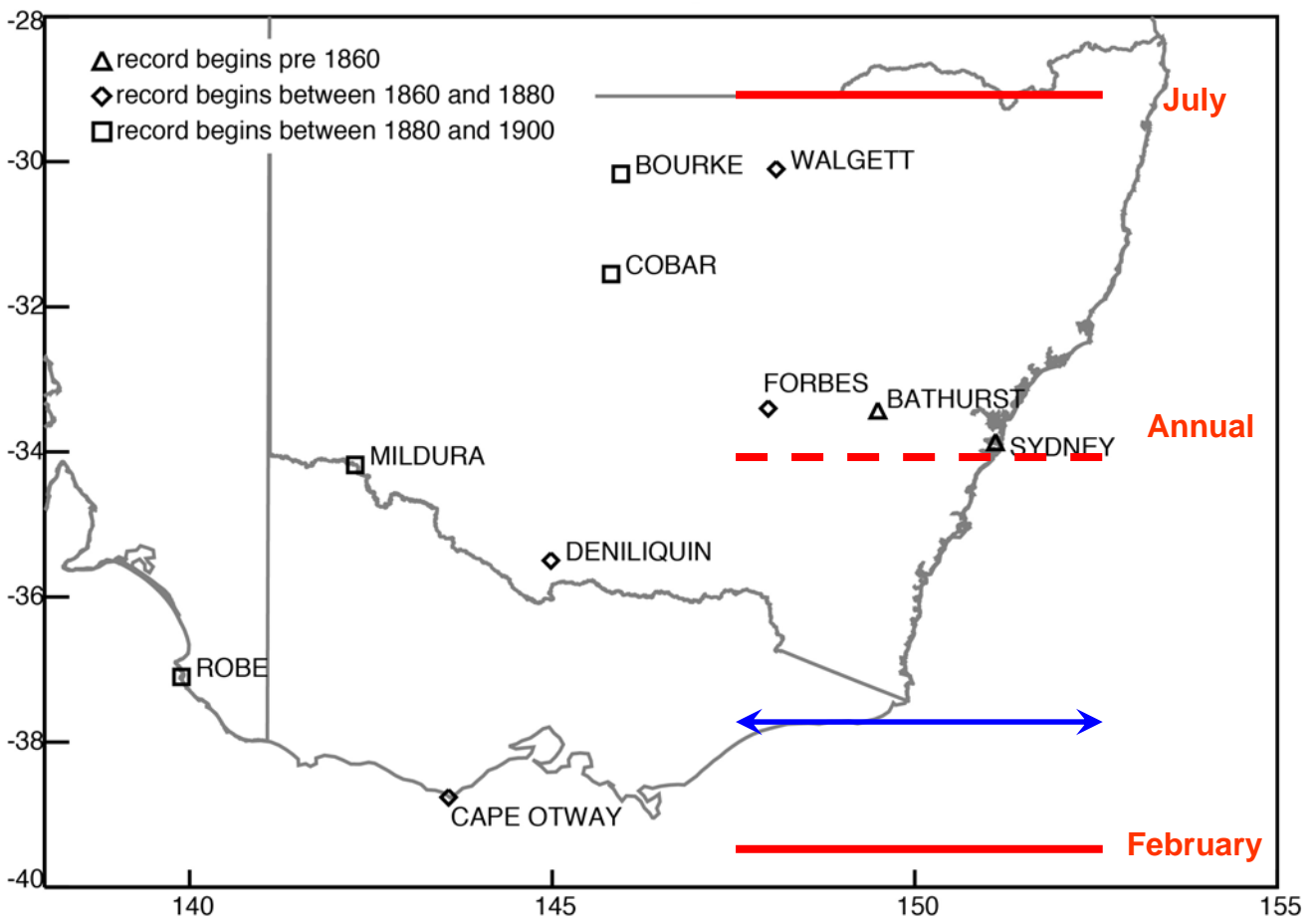


Figure 2. Map of the locations of mean surface-level pressure observations used to reconstruct the sub-tropical ridge intensity from 1860 to 2009 (L. Ashcroft, personal communication, 2012) thus extending the previous reconstruction from Drosdowsky (2005) back prior to 1890. The latitudinal extent of the climatological position of the STR is indicated in red, while the longitudinal band used by Drosdowsky (2005) is shown in blue

Data were homogenised to ensure that no data issues affect the long-term climate signal. This was done by using the penalised maximal  $F$  and  $t$  tests from the RHtestsV3 homogenisation package (Wang, 2008; Wang et al., 2007; Wang and Feng, 2010), similar to the method of Ashcroft et al. (submitted). Inhomogeneities were first identified for each station by comparing the data to a reference series built from highly correlated neighbouring stations and applying

the penalised maximal  $t$  test. Additional inhomogeneities were then identified in the adjusted data for each individual station using the maximal  $F$  test and detailed station history information.

The STR-I reconstruction appears very similar to the Drosdowsky (2005) one, with monthly correlations for the overlapping period (1890 to 2009) at or in excess of 0.9 for autumn, winter and spring and dropping to a value close to 0.8 in summer (Figure 3).

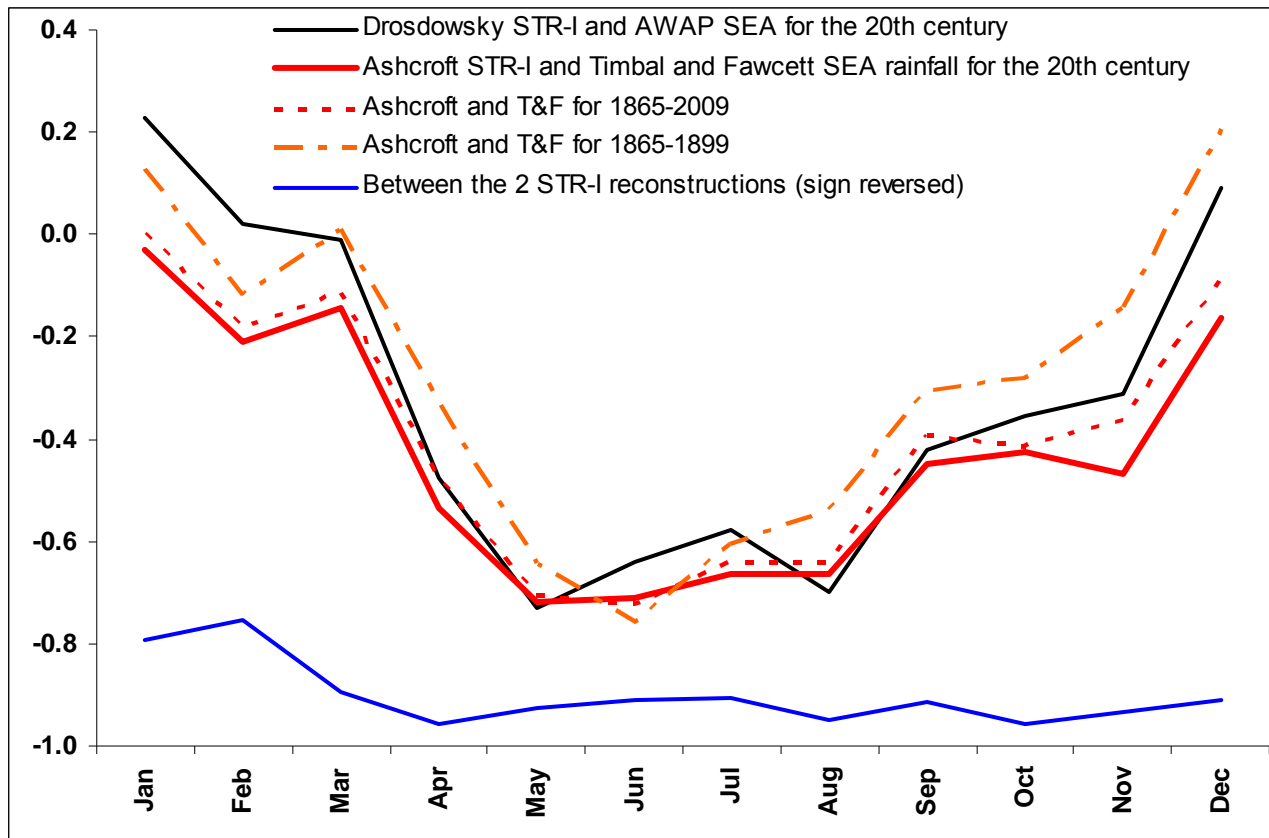


Figure 3. Monthly correlations computed between the between the intensity of the sub-tropical ridge (STR-I) and SEA rainfall using different datasets and different periods; in addition the correlations between the two STR-I reconstructions are indicated (blue line with reverse sign to fit on the graph)

Using the new reconstruction, the relationship between SEA rainfall (using the Timbal and Fawcett (in press) reconstruction) and the STR-I is very similar to what was found by Timbal and Drosdowsky (2012) using the Drosdowsky (2005) series. Correlations for the entire 20th century are moderate to large and significant for the period from April to November with the largest values observed between May and August depending on the dataset used (Figure 3). For the newly available period (1865 to 1899), the correlation coefficients are very similar to those for the long-term averages confirming that (over sufficiently long periods to avoid a high level of noise) the relationship between STR-I and SEA rainfall is very stable as reported by Timbal and Drosdowsky (2012) for the 1900 to 2010 period.

In addition, the extension back in time of both the SEA rainfall and STR-I series alongside the global temperature of the planet from the hadCRUYT2v dataset (a reconstruction of historical global temperatures made by the Hadley Centre in the U.K.) provide an opportunity to extend the identification of epochs proposed in Timbal et al. (2009). This was to identify periods (1910 to 1945 and 1975 to now) where the planet has been warming, and both the STR is intensifying and the SEA rainfall is lower than the long-term mean. In contrast it was noted that during the 1950s to 1970s, there was an extended period where no warming was observed and at the same time no STR intensification was apparent. During the same period, SEA rainfall had a strong decadal variability including the wettest decade (1950s) on record. The 1860s to 1890s provide a second example of such a period with no warming, no STR intensification and strong decadal variability with an equally very wet decade (1870s) (Figure 4).

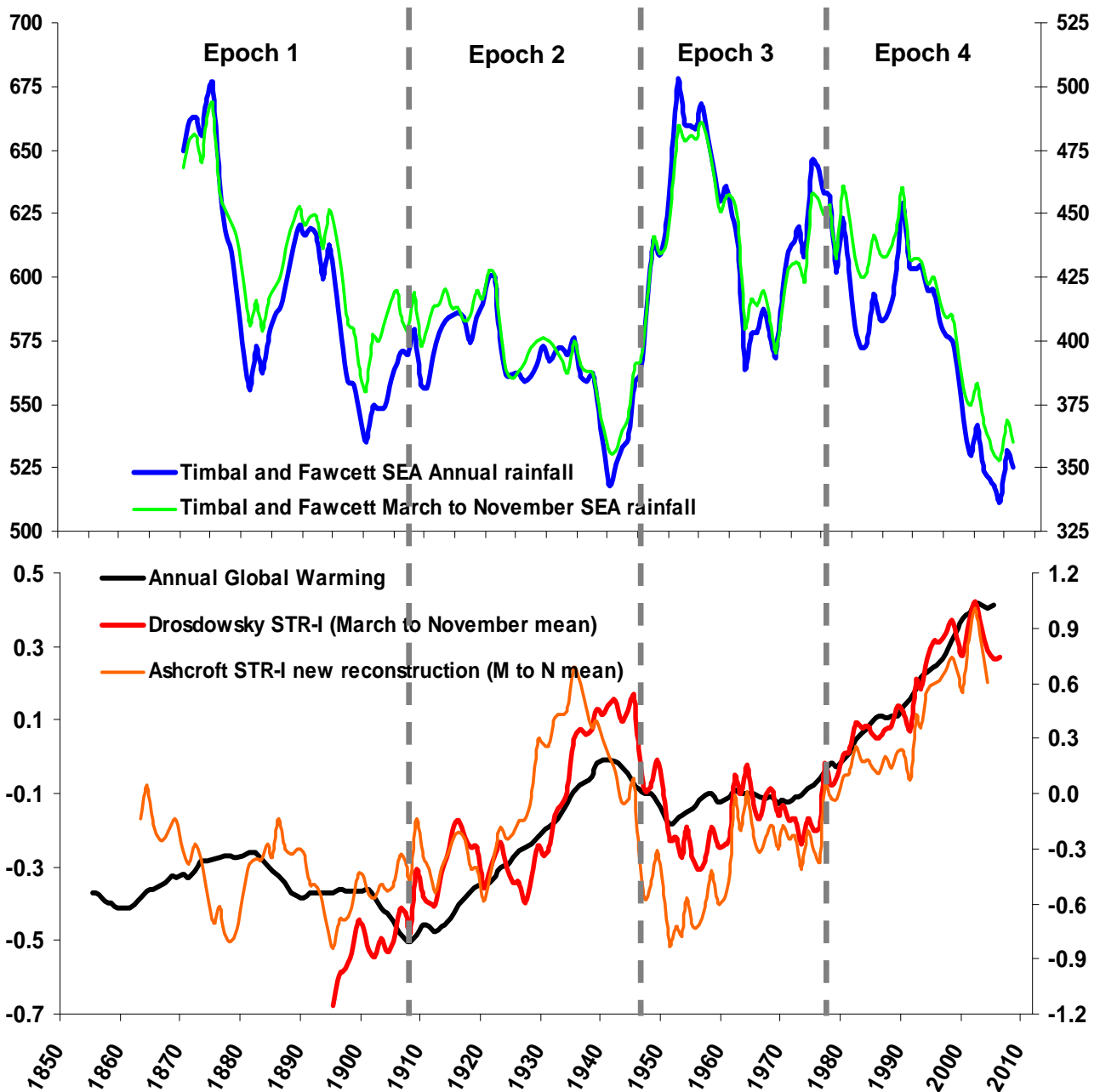
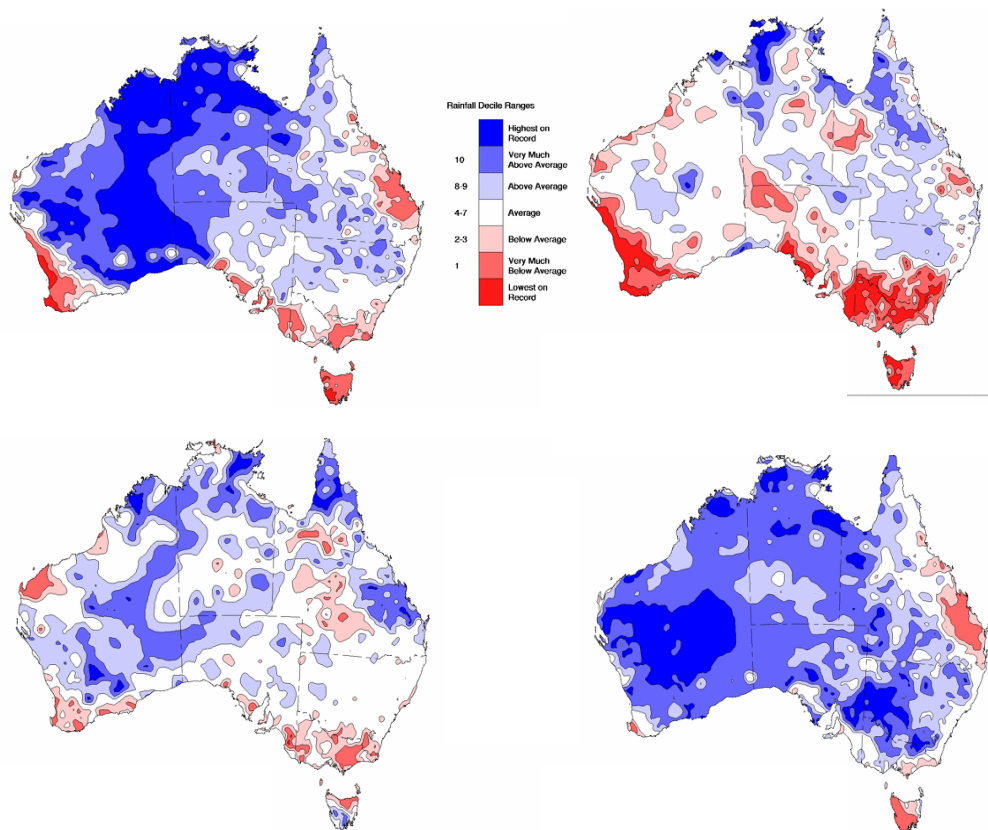


Figure 4. Eleven year running means for SEA rainfall (upper graph: annual, left Y-axis and for March to November, right Y-axis) and for global temperature anomalies (in degree, left Y-axis) (HadCRUT2v dataset) with the two STR-I reconstructions (in hPa, right Y-axis) (lower graph). Epochs 1 and 3 correspond to periods of no global warming, no intensification of the STR and high SEA rainfall. By comparison, Epochs 2 and 4 correspond to periods of global warming, STR intensification and low decadal SEA rainfall

### **Describing the changing nature of Australian rainfall**

Additional work on Australian rainfall was carried out using the Australian Water Availability Project (AWAP) rainfall data. It has been observed that the rainfall across Australia during the last 30 years is in places (and in particular for SEA) a marked departure from the long-term (1900–2011) average (Figure 5).



*Figure 5. Maps of the thirty-year (1981–2011) deviations of rainfall from the long-term average: Top left, for the annual mean and three distinctive parts of the annual cycle; top right, for late autumn–early winter (April to July); bottom left, for the latter part of winter and early part of spring (August to October); and bottom right, for the warm part of the year (November to March)*

Across Australia, variations of rainfall from the long-term average for the last 30 years (Figure 5) depict a continent which is getting wetter in terms of mean annual rainfall (Figure 5) with the exception of south-eastern and south-western Australia and Tasmania. Rainfall in these regions is primarily linked to frontal storm tracks and is dominated by cool season (e.g. April to October) precipitation. The reductions in rainfall across these regions are predominantly a late autumn-early winter phenomenon. The rest of the cool part of the year (August to October) does not show such a strong signal across these regions. In fact, averaged across the Australian continent, there has been a slight increase in rainfall. This is the time of the year when the variability of indicators of the state of the climate system, such as ENSO and IOD, are at their peak, suggesting a weak but positive contribution to rainfall over the last 30 years counteracting the rainfall reduction seen in the earlier part of the cool season. Finally, the map for the warm part of the year (November to March) shows a continent which has become overwhelmingly wetter, although that signal is much diminished along the southern edge of the continent.

The purpose of this analysis was to determine the causes of that rainfall departure in terms of rain systems ('entities' – or areas of contiguous rainfall most likely associated with the same larger scale atmospheric circulation pattern/feature). A database has been generated using daily AWAP rainfall maps from 1900 to the present. Here we analyse how these rainfall entities and their characteristics (position of the centre, numbers, volume of rain, spatial extent and density) have evolved over time and contributed to the rainfall anomalies observed across Australia during the last 30 years. Although the AWAP dataset starts in 1900, a sizeable portion of the Australian continent is affected by missing daily data until 1906. This missing data decreased rapidly to around 1910, and has barely changed since that time. The early missing data unduly biased the results, and thus only data after 1910 are used in this analysis.

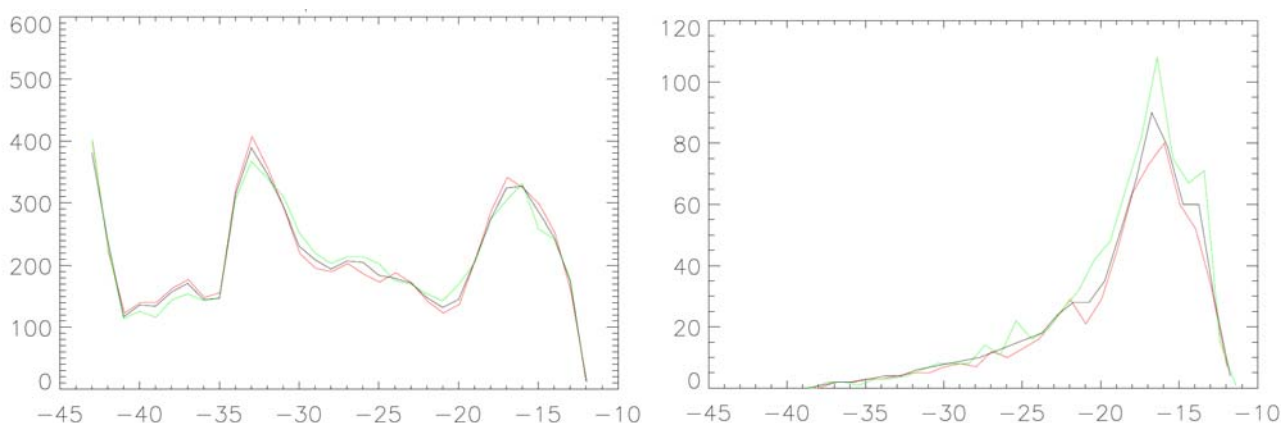


Figure 6. Histograms (number of systems per decade, for each one degree of latitude from 43° S to 18° S) showing the position of centres for all entities (left) and only those entities having rainfall greater than 200 mm/day (right). The red line shows 1910–1960, green shows 1981–2011 and the black line shows the entire time period from 1910–2011

The average latitude of the centre of the rainfall entities shows a double peak structure, with a preference for centres to be located in the tropics between 15° and 20° S or in the extra-tropics around 33° S when all entities are considered (Figure 6 left). For more intense systems (registering daily rainfall above 200 mm), only the tropical peak is visible (Figure 6 right). The last 30 years (green lines) show a decrease of extra-tropical centres (between 40° S and 30° S) consistent with the reduced rainfall in the southern part of the continent (Figure 5 top left). In contrast, the earlier part of the record 1910 to 1960 (red) has the opposite behaviour suggesting a long-term trend. The tropical peak is also reduced when all systems are considered, which is inconsistent with the observed increased in rainfall across most of northern Australia but, the overall decrease in numbers is compensated by a large increase of the larger systems (with rainfall above 200 mm). The symmetry between the red (prior to 1960) and green curves on both sides of the long-term mean is again suggestive of a long-term trend.

The tropical peak in Figure 6 is primarily due to summer systems (Figure 7). All the characteristics observed using annual statistics are confirmed when only the summer systems are considered (NB: the Y-axis differs, with about half of the systems from the annual plots accounted for during summer). This result is the strongest indication that the summer rainfall increase across northern Australia is made up in large part by more intense rainfall systems.

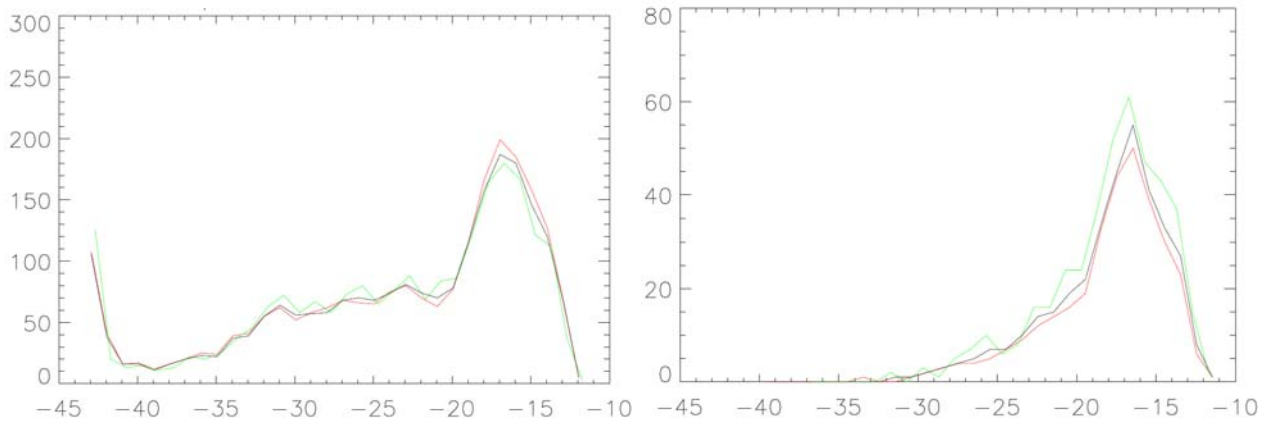


Figure 7. As per Figure 6 but for summer (December, January, February) rainfall entities only

The extra-tropical peak in Figure 6 is primarily made of winter (June, July, August) systems; the total number of these systems is fewer during the last 30 years compared to the long-term mean and early part of the record (Figure 8 top left). In percentage terms, the reduction in the number of more intense systems (with rainfall above 100 mm) is even more pronounced (i.e. a reduction of nearly 50 percent between the early part of the record and the last 30 years, Figure 8, top right).

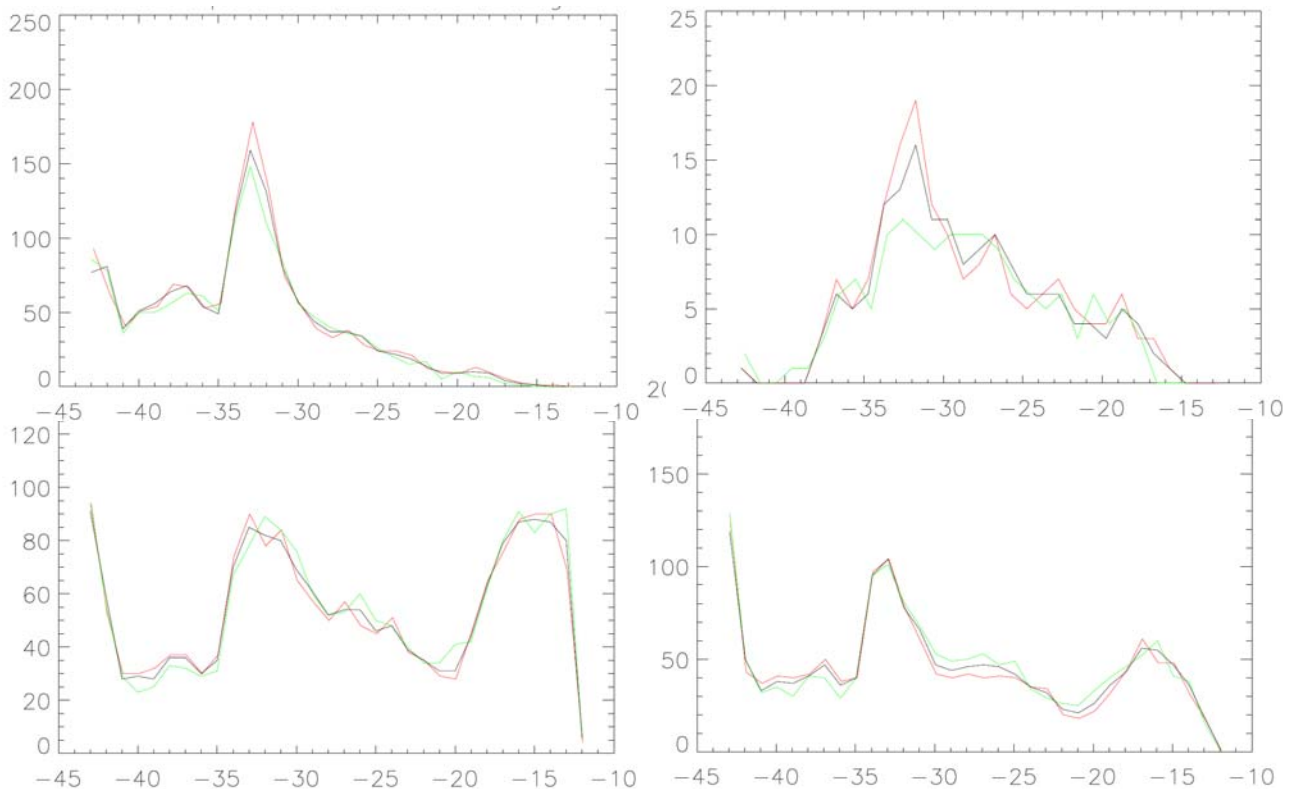


Figure 8. As per Figure 6 but for winter (June, July, August) rainfall entities only; right graph shown entities with rainfall above 100 mm; bottom left graph shows all entities in autumn (March, April, May) and bottom right in spring (September, October, November)

Particularly relevant for SEA is the result for autumn (Figure 8 lower left); across the Australian continent there has been a reduction of the number of systems south of 33° S compensated by an increase in systems further north. This result is consistent with the findings by Whan et al. (in press) that autumn rainfall may be either winter-like or

summer-like and while the winter-like types have reduced (centred further south), the summer-types have increased (centred further north). It is worth noting that while changes in spring (Figure 8 lower right) are very similar in terms of numbers of systems, this has not resulted in a significant reduction in the total rainfall in SEA as it did in autumn.

The annual cycle of the average position of all rainfall entities across the Australian continent has marked seasonality, consistent with the seasonality of the rainfall across the continent: that is, further tropical in summer and extra-tropical in winter (Figure 9). Noteworthy is the later shift to winter latitudes in autumn and earlier shift to summer latitudes in spring (by about 5 days in autumn and 15 days in spring) between the earlier part of the record (1910–1960) compared to the last 30 years (1981–2011), thus suggesting a shortening of the time of the year when cool season rainfall systems dominate. This is consistent with the result presented in the 2011 annual report, showing a trend toward an increased fraction of SEA rainfall coming from systems located further north. In addition, during the winter months, systems affecting SEA appear to be located further south. In between these two opposite trends, the shift from warm to cool season systems is more abrupt and occurring earlier in autumn. To a lesser extent this is also the case in spring for the shift from cool season to warm season systems. A possible explanation is that the strengthening of the STR prevents systems forming around the mean latitude of the ridge (around 33° S).

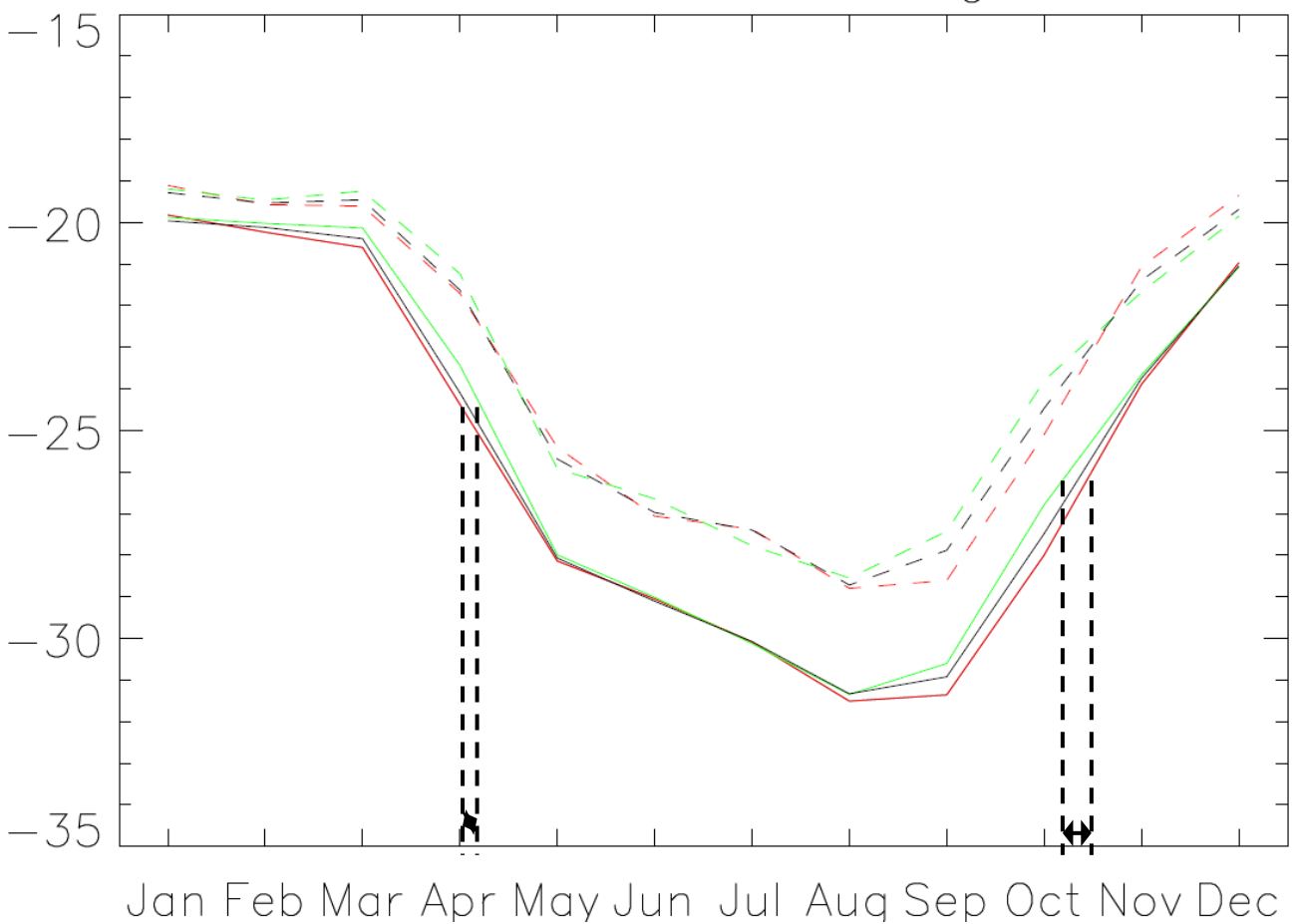


Figure 9. Annual cycle of the mean latitude of daily rainfall entity centres for all systems (solid lines) and for systems with rainfall above 100 mm (dashed line) for the entire Australian continent. The red line shows 1910–1960, green shows 1981–2011 and the black line shows the entire time period from 1910–2011. The shifts (measured as the difference between the red and green curves in the middle of the transition season) during the transition seasons are highlighted using a bold dashed vertical line

## Objective 2

### **Analyse the meridional circulation, and its trends in the observations in all available climate reanalyses**

#### ***Hadley circulation diagnosed from reanalyses***

Last year's results were updated as new reanalyses data became available. In particular, the ERA Interim product (produced by the European Centre for Medium-Range Weather Forecasts, ECMWF) is now available for the entire period of study (1979–2009). This enabled us to validate the multi-linear technique used to infill the missing data of some products. The addition of an 8th product (20<sup>th</sup> century reanalyses project) also enhances the robustness of the findings.

We also added a second ensemble of model simulations of the 20th century, from the CSIRO Mk3.6 model. The same external forcings were used as for CCSM3 and there were ten simulations for each ensemble. The calculations were done for the entire 20th century period.

The main results are:

- The expansion of the Hadley cell is still consistently observed in all eight reanalysis products over the last 30 years.
- The 1-to-1 linear relationship between the Hadley cell expansion and the poleward shift of the STR with a high correlation coefficient between annual means ( $r^2=0.8$ ) (Figure 10a) confirms the signature of the descending branch of the Hadley cell at the surface. There is a clear separation between the cloud of points associated with model simulations where only natural forcings are used characterised by zero change or even contraction equatorward, and the same model simulations when either anthropogenic or full forcing are used, characterised by the expansion poleward.
- The linear relationship between Hadley cell expansion and intensification of the STR has a relatively high correlation coefficient ( $r^2=0.35$ ) (Figure 10b). There is a notable distinction between the results obtained for experiments performed with the Mk3.6 and the CCSM3 anthropogenic and full forcing runs. In the former model, most of the points show STR-I weakening with Hadley cell expansion. By contrast, some points from the latter model show STR-I intensification with Hadley cell expansion. This difference may be due to the fact that Hadley cell expansion in the CCSM3 is more marked in all runs with values of expansion close to those inferred from the reanalyses in the last 30 years ( $\geq 0.3^\circ$  per decade). This is likely to induce a stronger response of the STR-I.

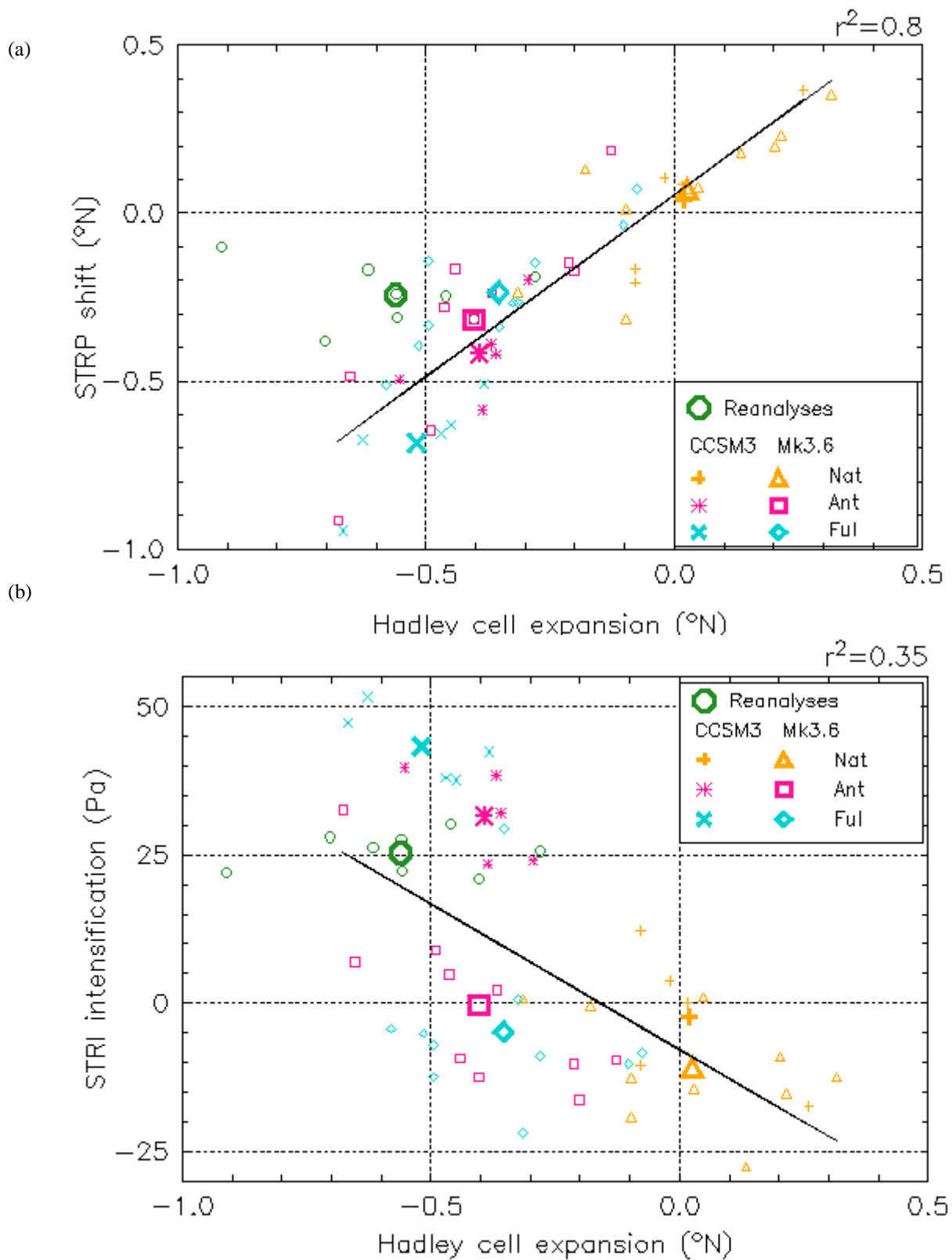


Figure 10. Relationship between Hadley cell expansion and sub-tropical ridge shift (a) and intensification (b) across a range of global datasets: 8 reanalyses (green circle), 2 climate model simulations (NCAR CCSM3 and CSIRO Mk 3.6) of the 20th century using different external forcings (natural only: yellow symbols, anthropogenic: pink symbols and full forcings: blue symbols). In all instances, individual model runs are shown as well as ensemble means (bold)

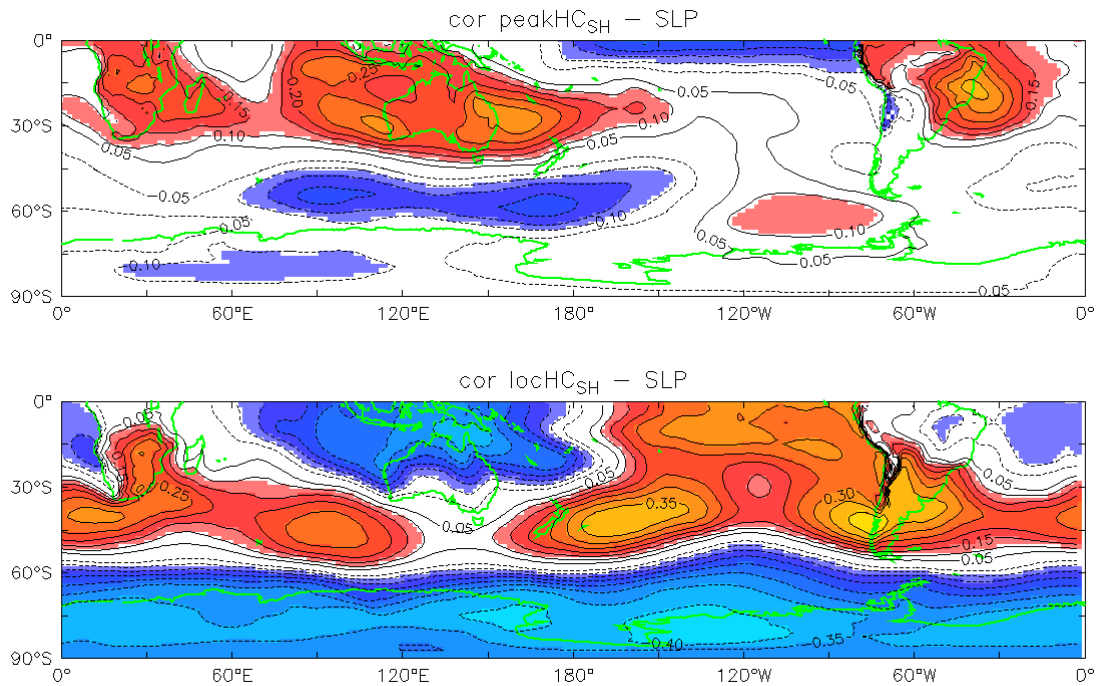


Figure 11. Correlation between mean sea level pressure (SLP) and southern hemisphere Hadley cell intensity (top) and extent (bottom) from the ERAI reanalysis dataset

To investigate how the global zonal mean meridional circulation affects the Australian continent, we show a spatial correlation between the Southern Hemisphere Hadley cell intensity and extent and the mean sea level pressure (MSLP) in Figure 11. This representation highlights the relationship between the Hadley cell (measured as a single entity across the Southern Hemisphere) for both intensity and extent and local MSLP including the belt of high pressure, the STR. The map correlation between the Hadley cell intensity and MSLP (Figure 11) shows a dipole characterised by strong positive values dominating the whole Australian continent and negative values south of it in a band between 45° S and 60° S. The correlation between the extent and MSLP is marked by strong negative values in the tropical part of Australia and positive values along the 30°–55° S band near the summer position of the STR. These preliminary results suggest that the Hadley cell is likely to influence the local STR at the longitudes of SEA and thus, by inference, SEA rainfall.

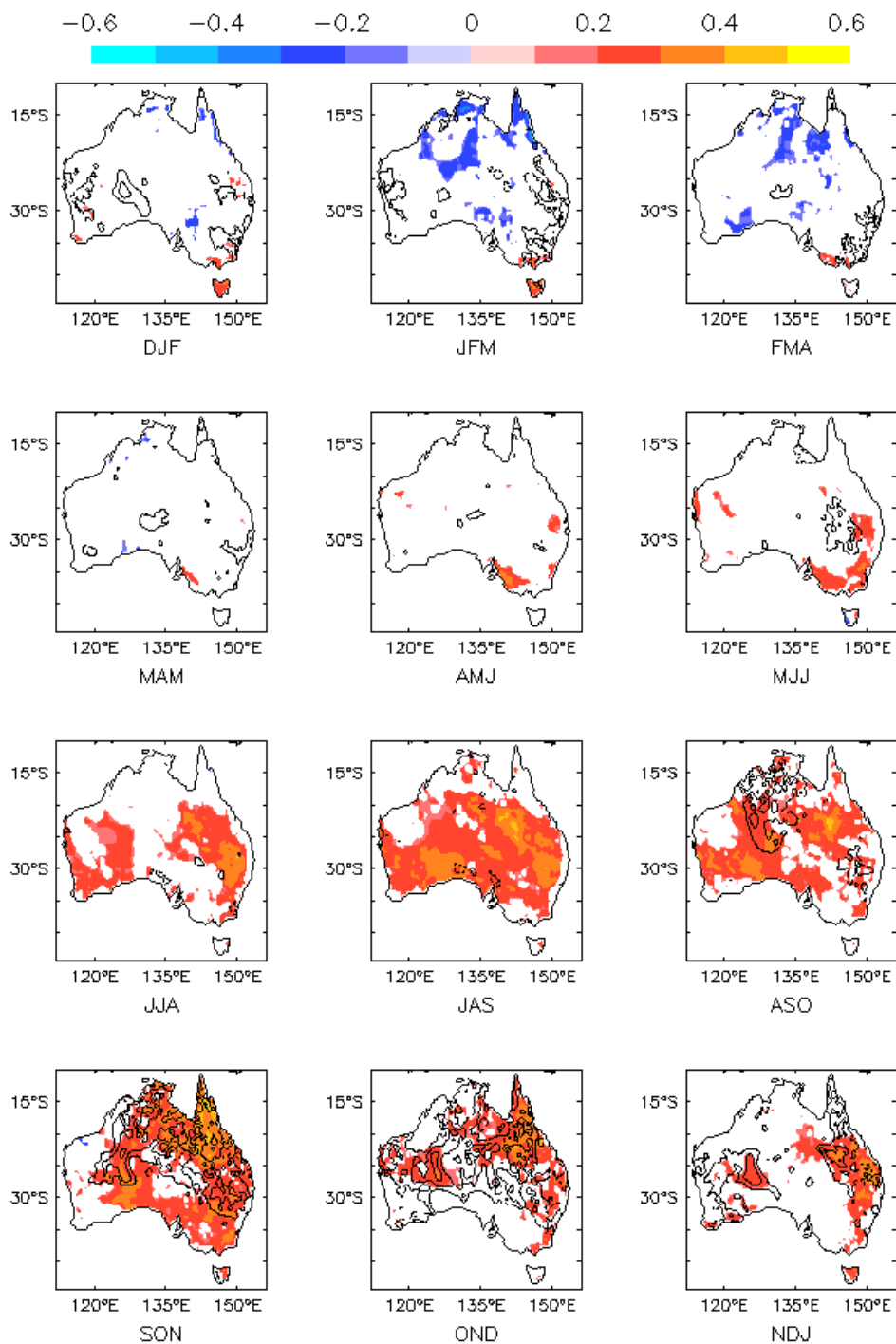


Figure 12. Seasonal correlation between AWAP rainfall and ERA-I southern hemisphere Hadley cell intensity (contours) and extent (shading). Only values significant at the 90% level are shown

Further interesting results include the maps of seasonal correlation between the Hadley cell and AWAP rainfall (Figure 12). These maps hint at a possible influence of the Hadley cell intensity on SEA rainfall during summer to early autumn, with positive correlations implying that an intensification of the Hadley cell is associated with rainfall decline at that time. Positive correlations were also found between the Hadley cell extent and rainfall throughout the year (except for autumn). This also reinforces the fact that SEA rainfall decline is associated with expansion of the Hadley cell.

### **Radiosonde studies of tropical expansion**

The goal of this work was to estimate the rate of tropical expansion in the Southern Hemisphere from radiosonde data, and to compare the results against similar calculations made using reanalysis data. This methodology allows for a comparison of the tropical expansion results from reanalysis data using a quasi-independent data source. An earlier part of this work was reported in CSIRO (2011); here, an update on the latest results obtained during this year is provided.

Tropical expansion was examined using the tropopause height frequency methodology first described by Seidel and Randel (2007). From the radiosonde data we created a time-latitude array of the number of tropical tropopause days (TTD), defined as having a tropopause above 14.5 km. Similar results were reported last year; and since then we have focused significantly on improving the quality assessment, removing biases from the results. Additionally, a further region (Africa) was added to the previous Australia–New Zealand and South America results, with some concerns about data quality in the new region. For the analysis, the time-latitude TTD array is contoured, and the change in the position of contours with time was used to estimate the expansion trend. An estimate of global expansion was made by averaging the results from three independent regions. The TTD=200 contour was taken as representative of the tropical edge (Figure 13). From this we estimated a tropical expansion trend of  $0.41 \pm 0.37 \text{ deg dec}^{-1}$ , significant at the 90 percent level. Strong decadal variability is apparent, although not statistically significant, with most of the expansion of the tropics occurring in the first half of the period of record (1979–2011).

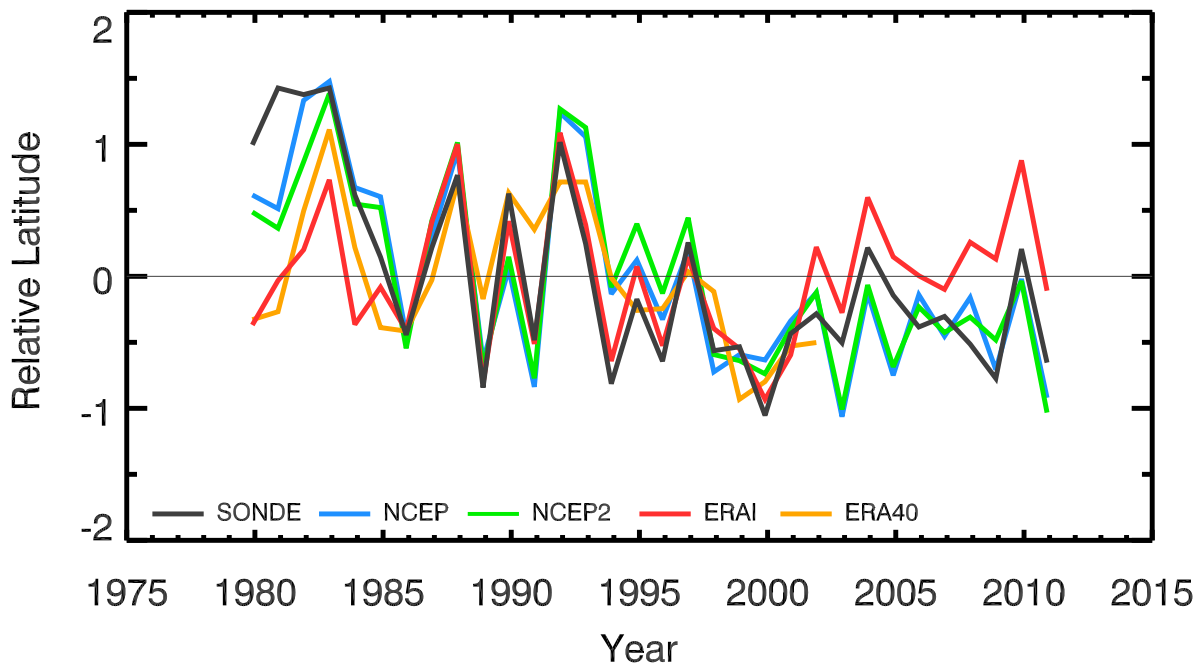


*Figure 13. Positions of the 'relative' global contours where the number of tropical tropopause days exceeds 200 from the radiosondes and four reanalyses. The zero line is the long-term average which, as part of the calculation process, is made to be equal for all products*

A similar analysis was performed using daily data from four reanalyses – the NCEP, NCEP2, ERA-40 and ERA-I. Time-latitude arrays of tropopause height were computed over similar areas and averaged to produce analogous results. One consistent feature identified across the reanalyses was a shift in the location of the contours. The reanalysis contours were displaced polewards relative to those derived from radiosonde data, indicating that too many days were identified as having a tropical tropopause. This results from the interpolation technique that Reichler et al. (2003) used to identify the tropopause in that data. On average, the tropical tropopause is identified too often in the winter months (see the next section).

The above issue results in a bias, the effects of which can mostly be removed when examining tropical expansion. Figure 13 shows the relative position (i.e. with the above bias removed) of the tropical edge from the radiosondes and the different reanalyses examined. In general, the inter-annual variations between the reanalyses are similar, but the resulting tendencies are different. NCEP-based products generally show a similar trend value. However, the ERA Interim (ERA-I) (red line) suggests a contraction of the tropics; notable differences from the radiosonde results and the other reanalyses are apparent both early in the record (before 1985) and at the end (after 2001). For the latter periods, we speculate that changes to the satellite observing system have created a significant inhomogeneity in the ERA-I data. As the ERA-I have been generated using the most advanced assimilation and prediction system developed by the ECMWF, and are therefore generally considered to be the 'best' reanalysis, this hypothesis requires more investigation, as do the discrepancies seen before 1985.

## Objective 3

### **Analyse existing climate simulations to evaluate the ability of models to reproduce meridional circulation changes and to explore the possible attribution of these changes**

#### ***The role of global warming***

Climate model simulations (CCSM3 and CSIRO Mk3.6) of the 20th century were analysed to determine possible causes of the Hadley cell expansion. Scatter plots of the 20th century trends (Figure 14) show a strong linear relationship ( $r^2 = 0.43$ ) between the Southern Hemisphere Hadley cell expansion and global warming. In the natural forcing runs, the cloud of points remains close to the zero point. As global temperature trends became positive in the anthropogenic and full forcing runs, they were all associated with expansion of the Hadley cell. The warming in these runs inferred from CCSM3 was twice as large as those from Mk3.6. This difference may explain the stronger expansion inferred from CCSM3 and by inference the poleward shift of the STR. As the Mk3.6 model also underestimates the magnitude of global warming compared to the CCSM3 model, it is possible that the tropical expansion and broadening of the Hadley circulation is related to global average temperature. In any case, the model results certainly indicate that the expansion of the Hadley cell is related to human-induced changes in atmospheric composition. Note that the Hadley cell expansion in the reanalyses for the last 30 years seems to be much more sensitive to global warming than in the model 20th century trends. Indeed, in the reanalyses a 0.25 °C warming was associated with a 0.5° expansion. It is unclear why even for a higher warming rate in the models the expansion rate would be lower; however these findings have possible implications for climate future projections which are based on the same models.

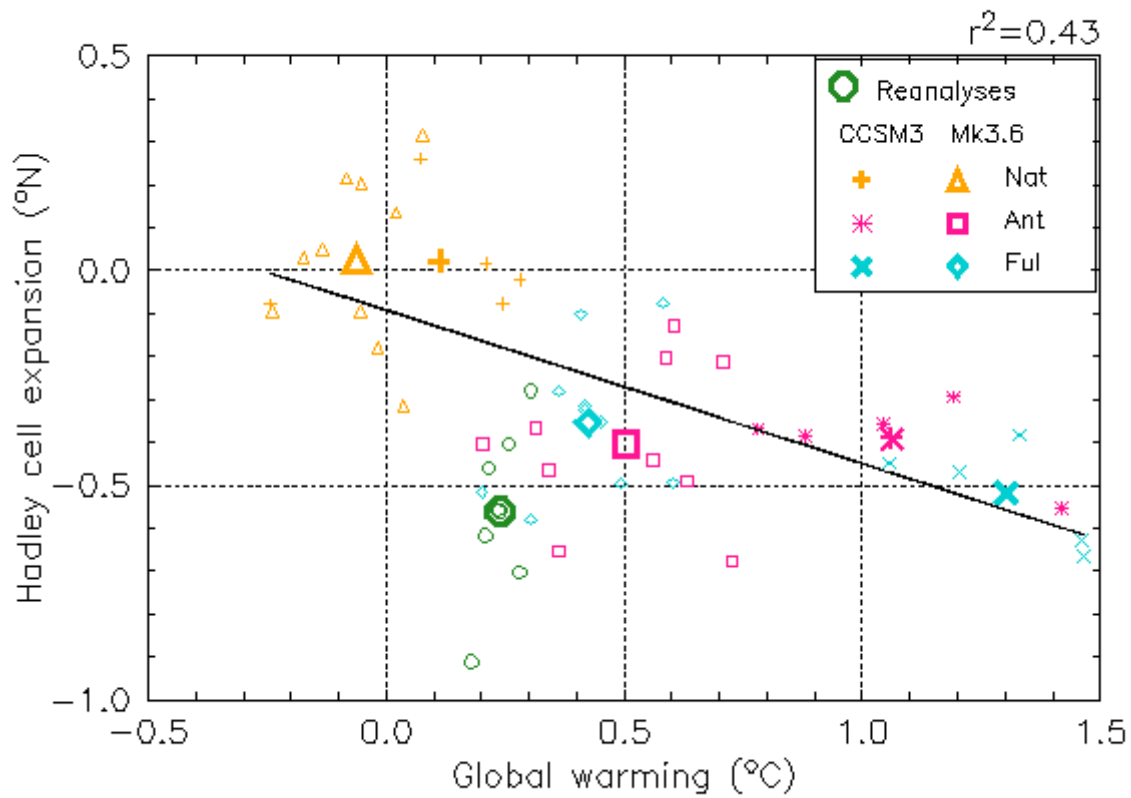


Figure 14. Relationship between global warming and Hadley cell expansion across a range of global datasets: 8 reanalyses (green circle), 2 climate model simulations (NCAR CCSM3 and CSIRO Mk 3.6) of the 20th century using different external forcings (natural only: yellow symbols, anthropogenic: pink symbols and full forcings: blue symbols). In all instances, individual model runs are shown as well as ensemble means (bold)

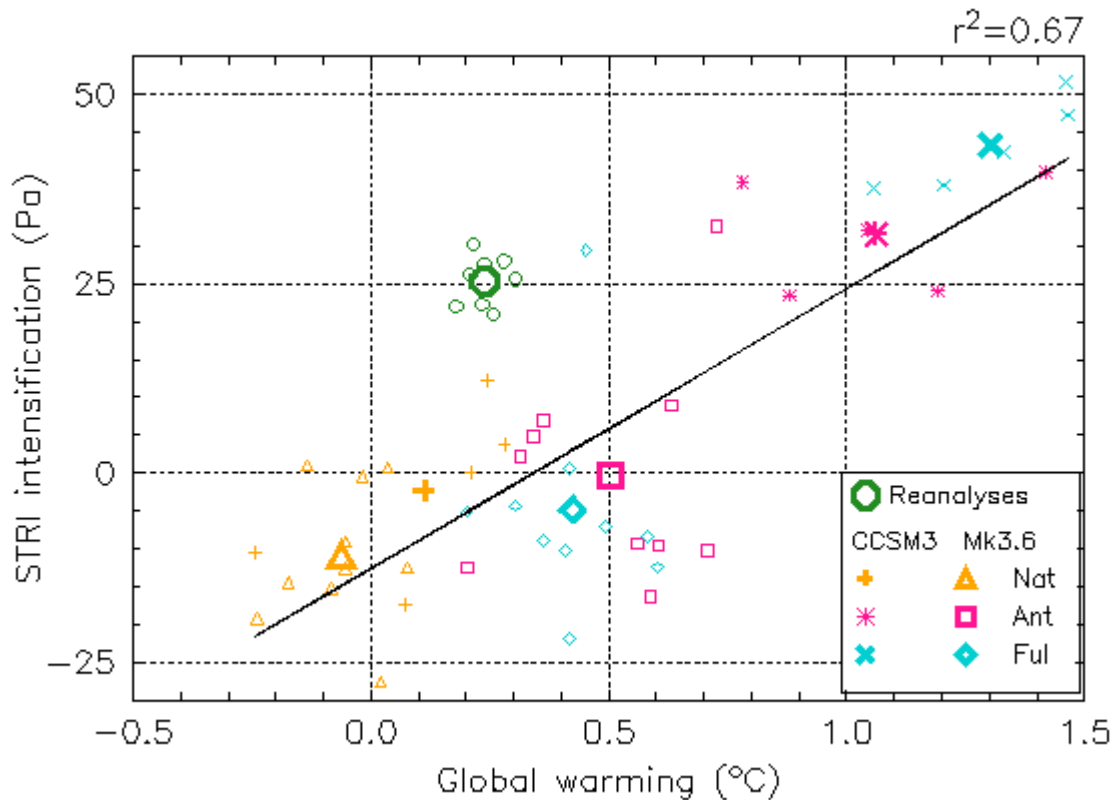
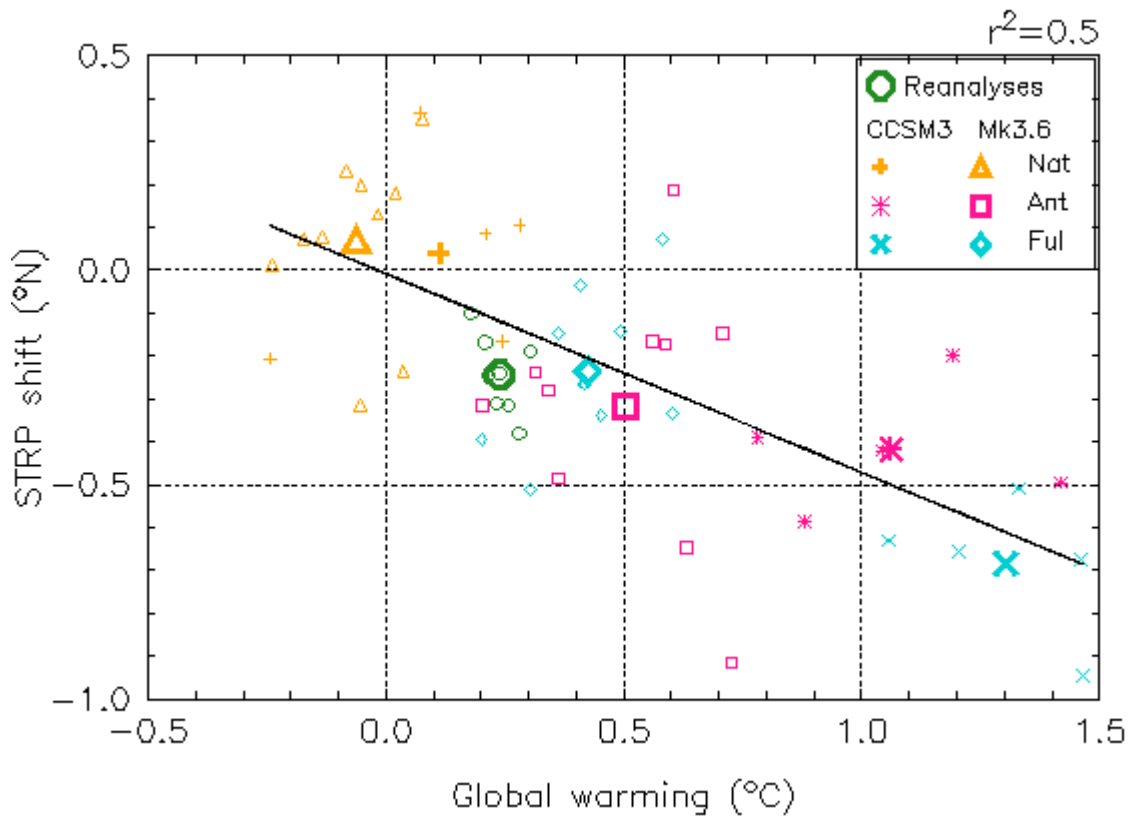


Figure 15. Relationship between global warming and STR-P (top) and STR-I (bottom) across a range of global datasets: observation (black circle for the last 30 years and black square for the 20th century) 8 reanalyses (green circle), 2 climate model simulations (NCAR CCSM3 and CSIRO Mk 3.6) of the 20th century using different external forcings (natural only: yellow symbols, anthropogenic: pink symbols and full forcings: blue symbols). In all instances, individual model runs are shown as well as ensemble means (bold)

It was shown in Objective 2 that the Hadley cell expansion is related to both global warming and changes in the STR. As expected, global warming is also associated with both intensification and the poleward shift of the STR (Figure 15). This scatter plot also shows observed changes for the 20th century which reinforce the model results. The response of the STR-P to global warming seems to be reasonably well reproduced in the models. The observed 0.51 ° poleward shift of STR-P associated with a 0.6 °C global warming was underestimated by the Mk3.6 anthropogenic and full forcing runs and overestimated by the CCSM3 runs (Figure 15). In contrast, the STR intensification associated with global warming in the models was far below that observed (Figure 15). Only CCSM3 was able to reproduce the observed STR intensification in the full forcing simulation, but for a surface warming rate twice as high as that observed. No STR intensification was inferred from Mk3.6 in the anthropogenic and full forcing runs, and a tendency for weakening was seen in the natural forcing runs.

The extent of the Hadley cell is associated with both the intensity and the position of the sub-tropical ridge. As such, it is perhaps surprising that the intensity of the sub-tropical ridge has only a weak association with the intensity of the Hadley circulation, but a stronger relationship with the Hadley cell expansion (see CSIRO, 2011). The mechanism behind this observation is yet to be investigated. Autumn is the critical season when both Hadley circulation broadening and the relationship between the sub-tropical ridge intensity and rainfall is observed. Earlier in summer the sub-tropical ridge does not have a major influence on rainfall, while later in winter the Hadley circulation expansion is far less pronounced. These observed changes involve complex interactions between the strengthening and displacement of the sub-tropical ridge in the transition season of autumn when the sub-tropical ridge shifts from south of the region in summer to north of the region in winter (Whan et al., in press).

### ***Other possible factors causing tropical expansion***

As part of the comprehensive review of the existing literature undertaken in the first year of Phase 2 of SEACI and continually updated during the program, the emphasis this year was on evaluating the growing body of research discussing the role of possible factors apart from the global warming of the planet driven by greenhouse gas emissions.

Modelling studies suggest that multiple factors can result in an expansion of the tropics. These include increasing greenhouse gas concentrations and associated changes to sea-surface temperatures, the impact of the Southern Hemisphere stratospheric ozone depletion and the effects of aerosols, both direct and indirect. Each of these forcings results in subtly different impacts on the tropical edge. Comparing these projections with the relevant climatological variables can provide a qualitative assessment of the relative importance of these factors.

Tropical expansion has been noted in both the Northern Hemisphere and the Southern Hemisphere, suggesting some degree of symmetry in the response. This suggests that the observed increase in increasing specific humidity (Willett et al., 2007; Dai, 2006; Lucas, 2010), associated with water vapour feedback in a warming climate, is playing a role in the tropics expanding. However, the observations of Hadley cell intensity, while highly uncertain, suggest no trend or a weak strengthening, which is inconsistent with this response. Vecchi and Soden (2007) and Ming and Ramaswamy (2011) suggest that this thermodynamic effect may affect the zonal Walker circulation more than the Hadley cell. The Walker circulation has weakened in recent decades, although Power and Kociuba (2011) indicate that internal climate variability accounts for a significant fraction of the observed weakening.

Many model-based studies have suggested that stratospheric ozone depletion has played a significant role in tropical expansion in the Southern Hemisphere. Multi-model averages of CMIP3 models with and without ozone (Son et al., 2009) have been used to qualitatively show that ozone has an impact on many aspects of the Southern Hemisphere circulation, including the location of the tropical edge. Son et al. (2010) used chemistry-climate models, which explicitly determine ozone depletion, to make this determination in a more quantitative fashion. McLandress et al. (in press) arrived at much the same conclusion using a coupled chemistry-climate model.

The role of stratospheric ozone depletion has also been investigated in global climate models (GCMs) with prescribed SST and individual radiative forcing using a 'time slice' modelling approach. Polvani et al. (2011) suggested that stratospheric ozone depletion was the main driver of 20th century Southern Hemisphere climate change. They found that ozone depletion resulted in a widening of the Hadley cell and an expansion of the Southern Hemisphere sub-tropical dry zones. They also suggest that future ozone recovery will approximately cancel the effects of greenhouse

gases on the mean meridional circulation in the first half of the 21st century. Kang et al. (2011) suggested that distinct effects of polar stratospheric ozone depletion could extend well into the subtropics, resulting in an increase in precipitation. Staten et al. (2011), using a similar methodology, indicated that as a whole the indirect SST changes have been the main driver of circulation change both from the pre-industrial (1870) to the present period and extending into the future. However, their simulations show that ozone depletion has a significant, albeit temporary, impact on the hemispheric circulation.

Modelling studies have also shown that aerosol effects, both direct and indirect, can affect the larger circulation. Aerosol forcing of the climate is complex, but quite significant. They can directly affect the radiative flux through scattering (primarily sulphate aerosol) or absorption (e.g. black carbon), contributing to surface cooling or atmospheric solar heating (see Ramanathan et al., 2001). Lohmann and Feichter (2005) reviewed the semi-direct and indirect impacts of aerosols on the climate. The semi-direct effect arises when the heating associated with absorbing aerosols changes relative humidity and affects the lifetime of clouds. The indirect effects of aerosols involve their interactions with cloud properties. Modelling studies (e.g. Ming and Ramaswamy, 2009) suggest that these indirect effects can be of approximately equal (but oppositely signed) magnitude to the forcing by GHG. These effects are generally not included in the simulations found in the CMIP3 multi-model ensemble. Further complicating the role of aerosols is their observed regional distribution, comparatively short lifetime and possible time evolution of their physical properties and radiative effect (e.g. Chung et al., 2005).

Several studies have examined the impact of aerosol forcing on the mean meridional circulation. Wang (2007) found that the direct effects of black carbon on the general circulation included a northward displacement of the Intertropical Convergence Zone, a strengthened (weakened) Hadley cell in the Northern (Southern) Hemisphere. Allen and Sherwood (2011) examined the direct effects of natural and anthropogenic aerosols on the mean meridional circulation in 'slab ocean' and climatological SST simulations. Allen et al. (2012) specifically identified a linkage between tropical expansion in the Northern Hemisphere and black carbon aerosol (and tropospheric ozone).

Ming and Ramaswamy (2011) modelled the response of the tropical circulation to both direct and indirect aerosol effects. Radiative cooling from aerosols is most prominent in the Northern Hemisphere, creating an inter-hemispheric radiative imbalance. The atmosphere attempts to moderate this asymmetry by altering the zonal mean circulation in the tropics, resulting in a weaker Hadley Circulation in the Northern Hemisphere (and stronger in the Southern Hemisphere). The asymmetrical portions of the circulation strengthen in both hemispheres. In the zonal mean, the subtropics (defined in their study as 20°–30° latitude) of both hemispheres have become wetter. However, the authors concluded that the atmospheric responses may be overestimated because of a lack of an interactive ocean model in these simulations.

These studies suggest that tropical expansion is a complex phenomenon, with multiple potential causes. More is going on than simply a response to global warming. Which of these causes is dominant now, and which will be dominant in the future, remains to be seen.

## Objective 4

### **Perform numerical experiments to test hypotheses about the sensitivity of the meridional circulation to oceanic and atmospheric factors**

#### ***Method***

The newly developed ACCESS global climate model has been used and tested to assess its ability to reproduce features which were identified in earlier SEACI work as being relevant to understanding the rainfall deficit across SEA (e.g. meridional circulation and tropopause height). During this year, the ACCESS model was developed further and hence it was difficult to use a unique and stable version. Most of the work done relied on simulations performed within CAWCR for other research programs. The work presented here focuses on three experiments performed by J. Arblaster and C. Chun. These 'SST perturbation experiments' used the Unified Model (UM) version 7.3 of the UM

modelling software with the HadGEM2-A configuration (HadGEM2 Development Team, 2011) at N96/L38 resolution (i.e. ACCESS version 0.9) with prescribed climatological sea-surface temperatures and sea ice from Hurrell et al. (2008). The HadGEM2-A configuration includes processes of the troposphere, land surface and hydrology and aerosols and is nearly equivalent to the atmospheric component used in the CMIP5 ACCESS1.0 simulations. HadGEM2 uses the MOSES II land surface scheme. More information on the model configuration can be found in Collins et al. (2011) and HadGEM2 Development Team (2011). Additional results were obtained from the first 'official' version of ACCESS, as provided to the CMIP5 database; ACCESS1.0.

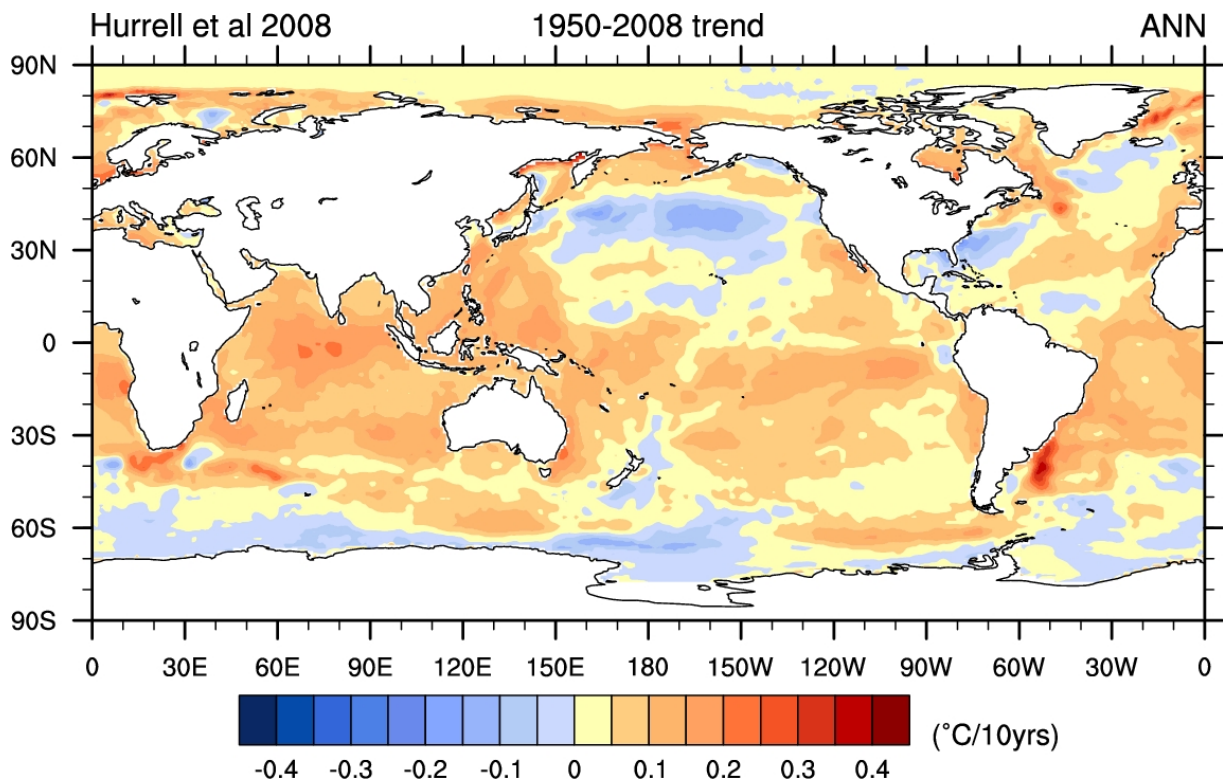


Figure 16. Trends in degrees C for annual mean sea-surface temperature. Linear trends are computed over the period 1950–2008 (Hurrell et al., 2008)

The primary experiments used in this study were designed to shed light on the role of changing SSTs on the characteristics of the mean meridional circulation. Annual mean SST trends from 1950 are shown in Figure 16.

Overall, a general warming was observed, strongest in the tropical band. The Northern Pacific between 30° N and 60° N and especially the whole southern ocean showed deviations from this global trend. These trends intensify the meridional temperature gradient, especially in the Southern Hemisphere, which in turn will likely affect the meridional circulation. However, temperature gradient changes arise from two sources – southern ocean cooling and tropical warming – which are hypothesised to affect the mean meridional circulation in different ways. Three idealised experiments were considered here.

1. CTL -- control simulation with no SST perturbations imposed. The run used 1961–1990 climatological sea-surface temperatures, which changed on a monthly time scale, but were fixed for the 30 years of the simulation.
2. to+1 -- a non-uniform tropical SST warming of 1 °C was imposed (Figure 17 top). Peak warming lay on the equator and decreases sinusoidally to zero at +/- 30° latitude.
3. so-1 -- a non-uniform cooling of the Southern Ocean of 1 °C was imposed (Figure 17 bottom). Peak cooling was located at 55° S, decreasing sinusoidally over 30° widths.

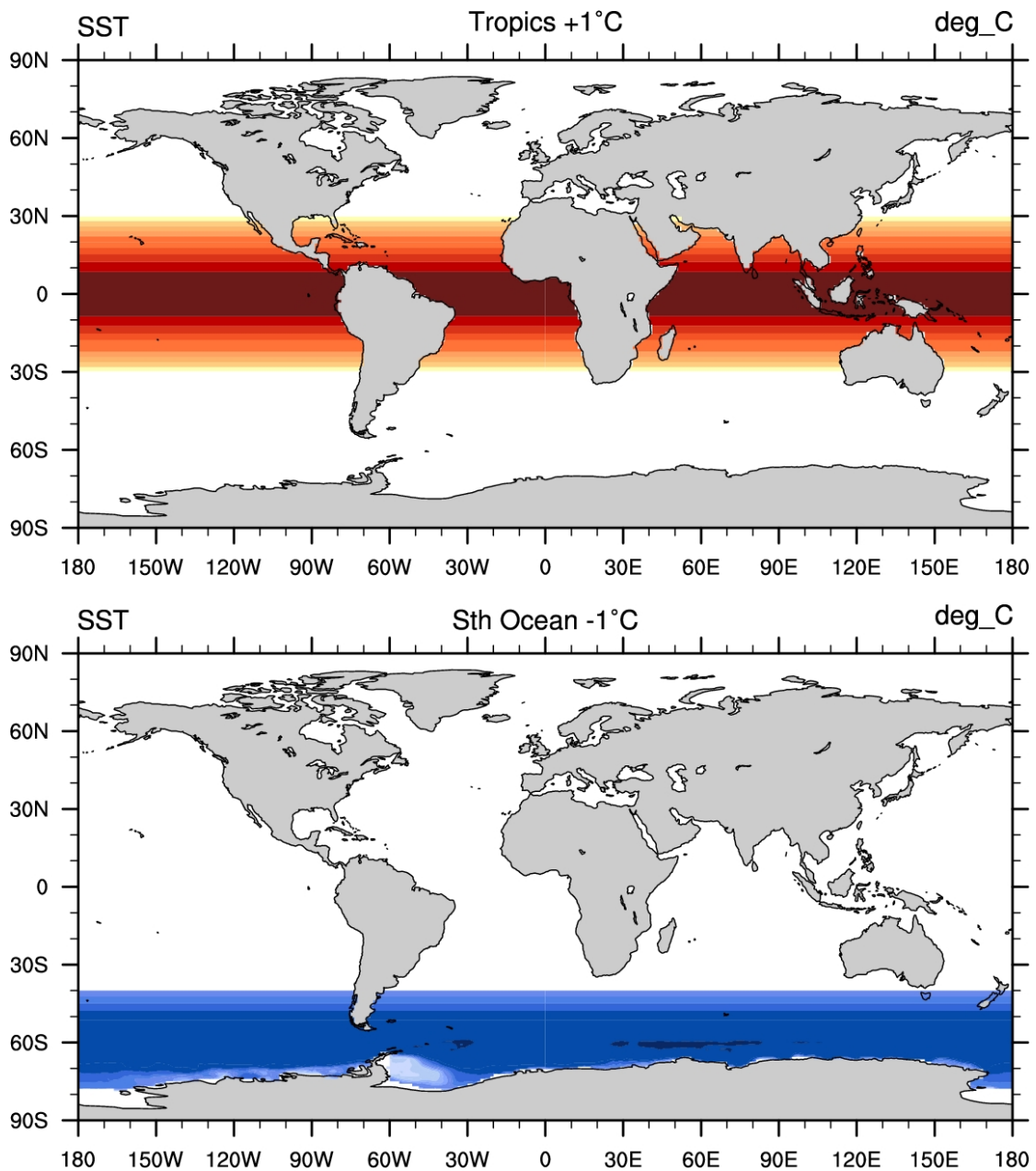


Figure 17. Sea-surface temperature (SST) perturbation experiments: +1°C in the tropics (top, to+1) and -1°C in the southern ocean (bottom, so-1)

Further details of the model experiment design are available in Marshall and Connolley (2006). The simulations were analysed to identify how the mean meridional circulation changes in response to these perturbations. The mean meridional circulation was analysed in two ways consistent with other studies performed in SEAC12; variations in the Hadley cell as identified by the isobaric mass stream function (e.g. Nguyen et al., submitted) and changes in the tropopause height.

The changes to the tropopause height were analogous but not identical to those presented by Lucas et al. (submitted) and others, owing to differences in the underlying data used. In earlier studies, we focused on the number of days within a given year that the tropopause was above a certain height threshold representative of conditions in the tropical air mass. Here we focused on the meridional position of a given zonal mean tropopause

height. This arose because of the lack of daily data with which to make the explicit frequency calculation. The two results should be analogous, but the exact relationship between them remains the subject of ongoing research.

Here, the height of the tropopause was estimated using the technique of Reichler et al. (2003) using the temperature and geopotential height fields from the ACCESS simulations. The input data available here was monthly with a vertical resolution of approximately 100 hPa at the relevant heights. The top layer saved was at 100 hPa, so the computation was limited to regions polewards of 25° in either hemisphere. There are known issues with the accuracy of tropopause heights using data with this coarse vertical resolution and temporal spacing. However, all of the perturbation experiments used this resolution, hence the comparison between the experiments should be relatively unaffected by this limitation. The accuracy of the ACCESS simulations in terms of this metric is addressed later.

Composite annual cycles with monthly resolution of the Hadley Circulation and the zonally averaged tropopause heights form the basis of the comparison here. These computations were performed for all three simulations examined here (control, to+1, so-1). For the Hadley circulation the (sub) tropical response was considered by examining the changes to the position of the poleward edge of the Hadley cell, defined by the zero isopleth at 500 hPa. Intensity was characterised by the peak value of the stream function within the cell. For the tropopause heights, we examined the change in position of two contours: those representing the tropical/sub-tropical edge (15 km) and the extra-tropics (11 km). This choice was somewhat arbitrary, and the exact details were somewhat sensitive to this choice. However, for any reasonable choices, the conclusions are qualitatively similar to those shown here.

### ***Hadley circulation response to sea-surface temperature perturbations***

Figure 18 shows the annual cycle of the Hadley cells from the model experiments. The mean from eight modern reanalyses, from Nguyen et al. (submitted) is also shown. In the ACCESS simulations, there is a consistent equatorward bias of 2–5° latitude in the position of the Hadley cell. This bias is more prominent in the Northern Hemisphere and during each hemisphere's warm seasons. Outside the positional bias, the annual cycle of the Hadley cell intensity matches the reanalyses very well (within the range obtained across all existing reanalyses).



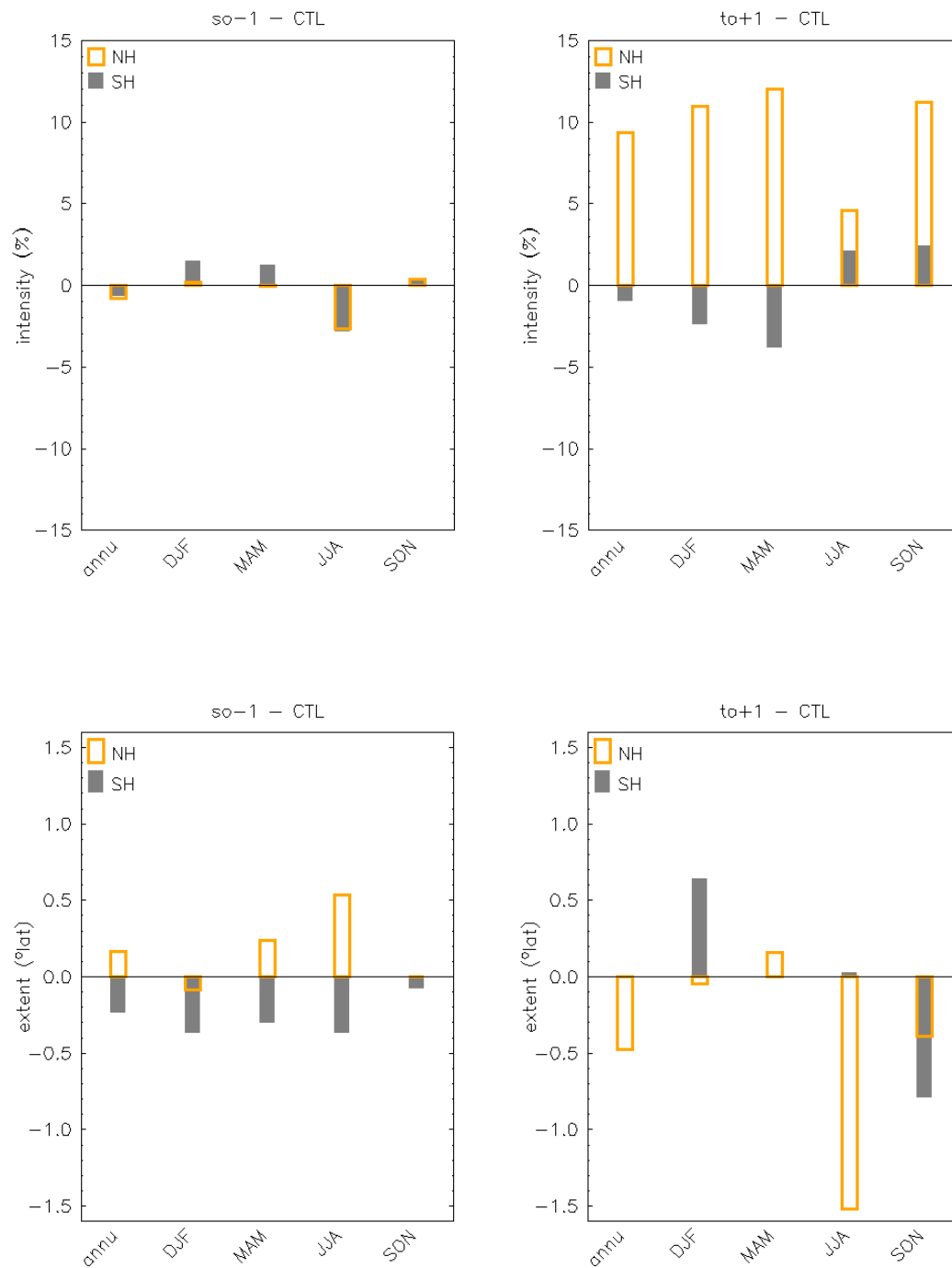


Figure 19. Hadley cell intensity (top) and extent (bottom) showing the difference between southern ocean cooling and the control experiments (left) and between the tropical warming and control experiments (right) for annual and seasonal means, derived using the ACCESS climate model. The Northern Hemisphere is shown by orange open bars and the Southern Hemisphere by grey solid bars

The changes to the Hadley cell extent were mixed in the simulations. In the tropical warming experiment, strong Northern Hemisphere contraction of the Hadley cell was seen in June, July, August and September, October, November with little change in other seasons. The Southern Hemisphere showed contraction in December, January,

February and expansion in September, October, November with little change in other seasons. In the southern ocean cooling experiment, a slight expansion was seen in both hemispheres during most seasons. This was generally less than 0.5° latitude, about half as large as the trends inferred from the reanalyses.

This contraction in association with intensification was also seen in the 20th century atmospheric model simulations (as shown in CSIRO, 2011). In many regards, the response is reminiscent of the response of the Hadley cell to the warm phase of ENSO, particularly in the Northern Hemisphere. As seen in Oort and Yienger (1996), the warm phase was seen to result in a contraction and intensification of the Hadley cell. However, care should be used as the changes imposed on the model were not ENSO-like, making the analogy limited. The extent of the anomalies seen here suggests a non-linear response with regard to the intensity anomalies.

**Tropopause height response to sea-surface temperature perturbations**

Figure 20 shows the monthly variation of tropopause height throughout the annual cycle for each of the three experiments. Overall, the annual cycle of tropopause height across all three experiments was broadly similar, with small differences introduced by the sea-surface temperature perturbations within the experiments. Between hemispheres, the annual cycles showed considerable variability.

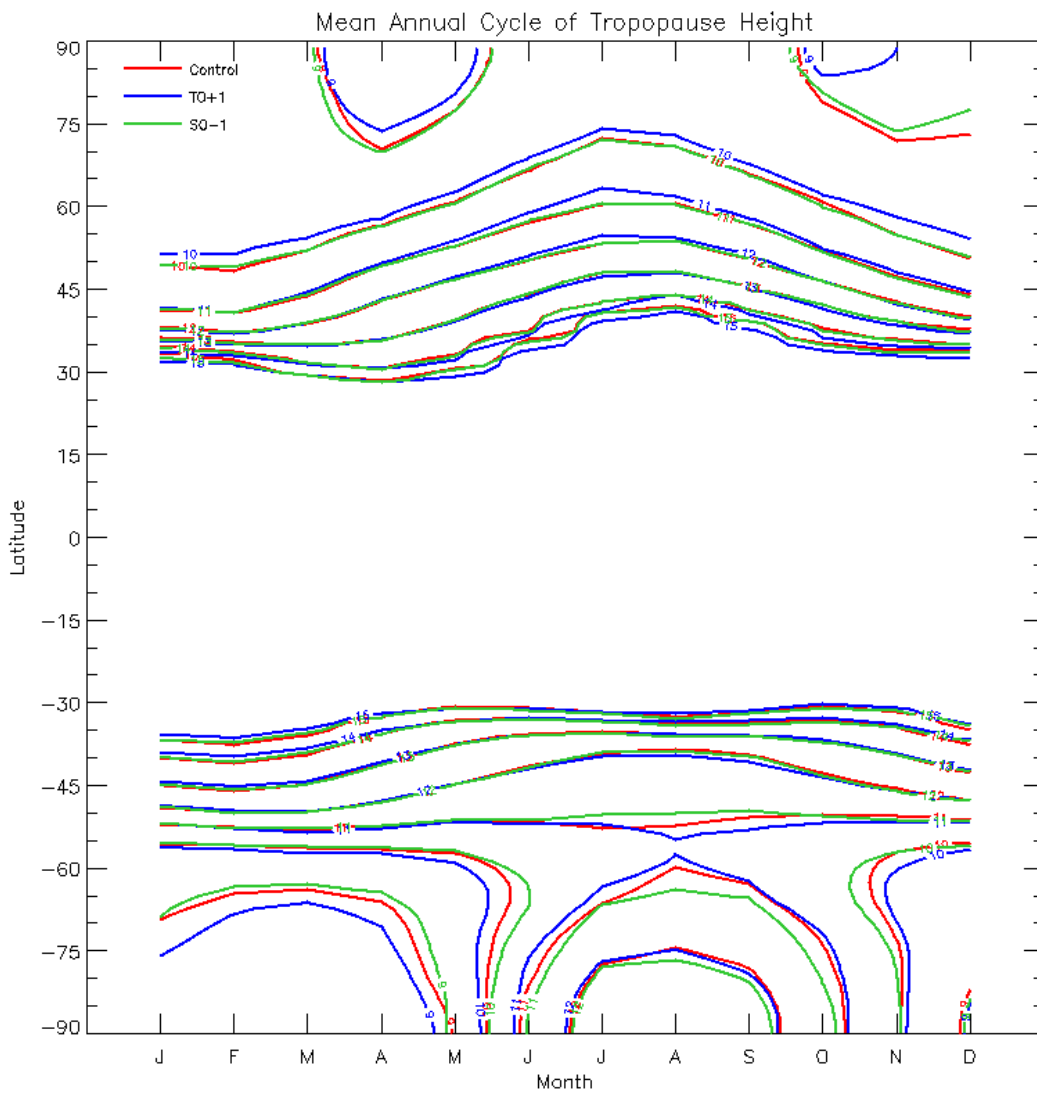


Figure 20. Zonal mean annual cycle of tropopause height in latitude-time space in the three simulations. Contours are plotted every 1 km from 9-15 km. Colours denote the simulation; Control=red, to+1=blue and so-1=green

In the Northern Hemisphere, tropopause height decreases monotonically towards the pole. Heights range from above 15 km around 30° N latitude to below 9 km near the poles during some seasons. The strength of the height gradient varies. Most contours are quasi-sinusoidal, reflecting the annual variability of tropopause height. The tropopause is highest in the Northern Hemisphere summer months (June, July, August), reflected by the more poleward positions of the contours during those seasons.

The Southern Hemisphere annual cycle of tropopause height is more complex. Tropopause height does not decrease monotonically towards the poles throughout the year. During late winter and early spring, tropopause heights above 12 km are indicated polewards of 75° S latitude. In the tropics, an annual cycle is seen in tropopause height, but the response is muted compared to the Northern Hemisphere, with hints of a weaker semi-annual component apparent on some contours.

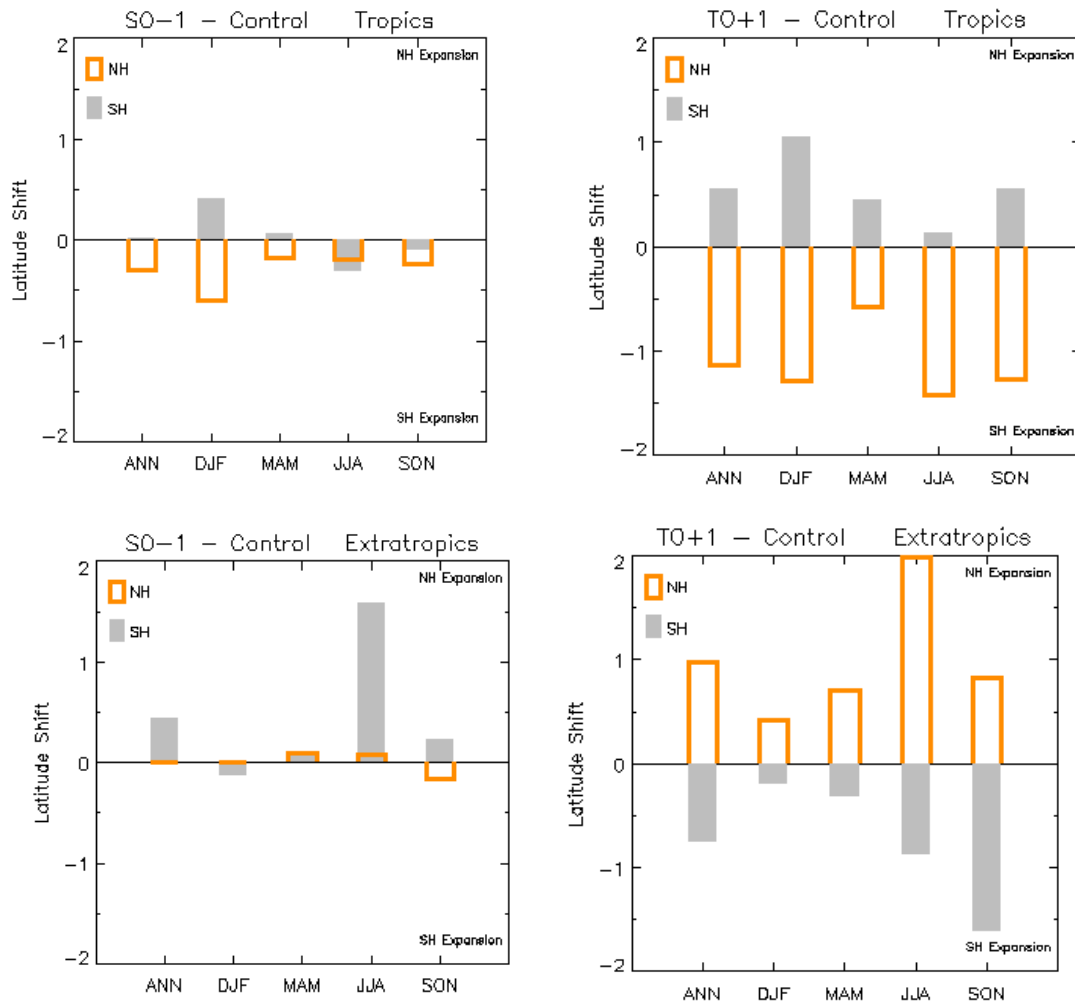


Figure 21. Summary of tropical and extra-tropical responses to the perturbation experiments in the tropics (15 km contour) and extra-tropics (11 km contour). Responses are separated by hemisphere and broken down into annual and seasonal means. Expansion in this context means that the contour moves towards its respective pole

Figure 21 summarises the broad response of the tropopause to the perturbations. The response varies by hemisphere and latitude. Overall, the tropical warming experiment had a larger effect. In that experiment, the response was larger in the Northern Hemisphere. Similar to the Hadley cell (Figure 19), a general contraction was seen in the tropics, although the response here had a consistent sign throughout the year. Changes are large in all Northern Hemisphere seasons, with March, April, May the smallest. The Southern Hemisphere shift is largest in December, January, February. In the extra-tropics, the opposite response is observed, with the extra-tropical contour moving poleward (i.e. expanding) throughout the year. The change from the tropics to the extra-tropics is ‘smooth’ with

some contours experiencing relatively little change. The changes are largest in June, July, August (Northern Hemisphere) and September, October, November (Southern Hemisphere).

The response to southern ocean cooling is significantly weaker than the tropical ocean forcing. In the tropics, a comparatively weak contraction is noted in the Northern Hemisphere, consistent across all seasons. The Southern Hemisphere response is generally small and weak, near zero on average. In the extra-tropics, a large change is noted in the Southern Hemisphere winter. Other seasons are weak, as is the response of the Northern Hemisphere.

### ***Reliability of tropopause heights in the ACCESS simulations***

The purpose of this section is to evaluate the reliability of the calculated tropopause heights in the model simulations. Because of the aforementioned data issues, we substituted an historical run of ACCESS 1.0 included in the CMIP5 dataset in place of the perturbation experiments. The atmospheric component is similar in the perturbation runs and the CMIP5 submission. The vertical data resolution is higher in the CMIP5 runs, with data reported approximately every 50 hPa at the relevant heights.

The results were compared to two further sources of data. The primary comparison was made with the tropopause heights determined from radiosonde observations, as described in Lucas et al. (submitted). These data have daily (or better) resolution, with tropopause heights averaged monthly to facilitate a more direct comparison. We also used results of tropopause height determined from the ERA Interim reanalysis. These data have monthly resolution, with a vertical spacing of approximately 25 hPa at the required heights. We limited this direct comparison to the region of eastern Australia, extending from roughly 135–155° E.

Figure 22 shows the results of the comparisons in the same format as in Figure 20. The ACCESS simulation is shown by the blue lines. It is qualitatively similar to the results presented in Figure 20. A low-amplitude annual cycle is apparent with a weak semi-annual component. The pattern in ACCESS 1.0 is generally shifted equatorward, perhaps a result of the increased vertical resolution.

The simulated cycles showed considerable differences between the direct observations and the reanalysis-based product, which are also different from one another. Both of the 'observational' datasets show a higher-amplitude annual cycle, which is more pronounced in the radiosonde-based data. Notable differences are apparent near 30° S, where reanalysis tropopause is considerably higher during the winter (June, July, August). A similar feature was noted in Lucas et al. (submitted) and was linked to a shift in the contours representing the tropical edge in that study. Apart from these important differences, the observational datasets largely agree on the evolution of the annual cycle across eastern Australia. Some of the differences may be due to differences in the underlying data sets (i.e. monthly vs. daily data) and the use of interpolation to identify the tropopause in the reanalysis.

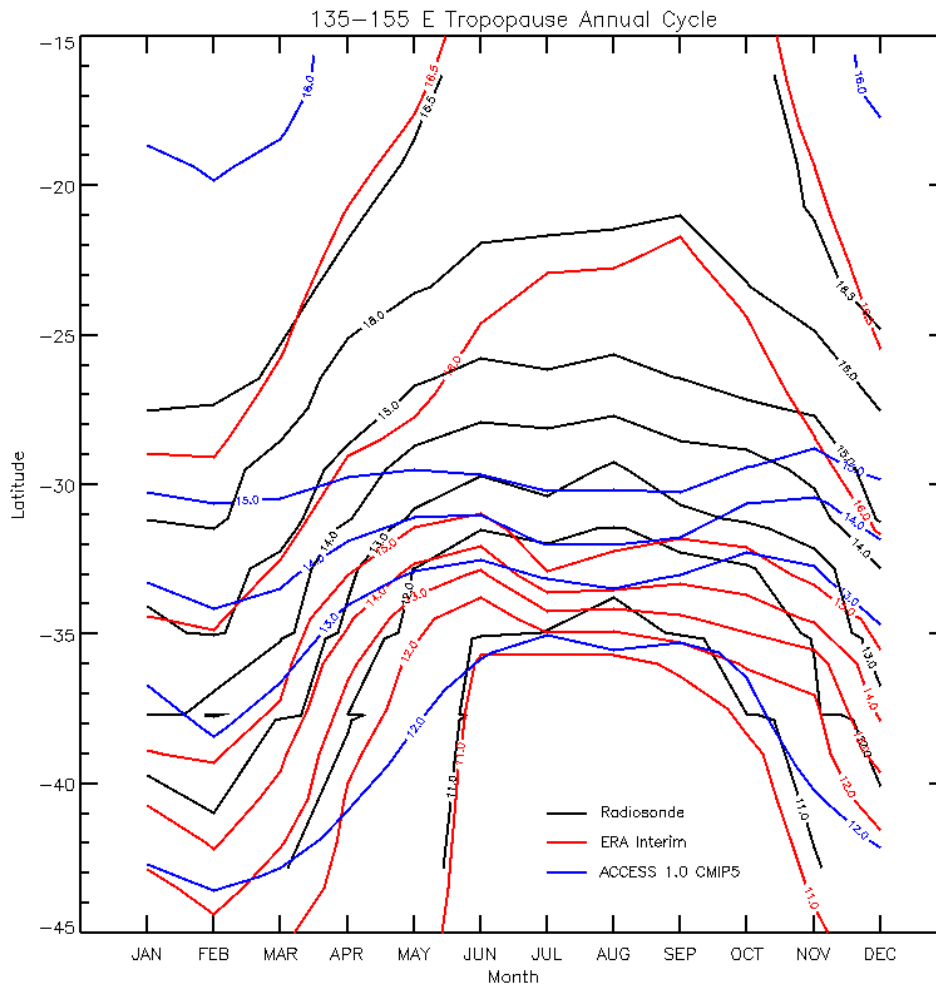


Figure 22. Average annual cycle of tropopause height over Eastern Australia (135°–155° E) from the radiosondes (black), ERA Interim (red) and experiments using the ACCESS climate model 1.0 CMIP5 historical run (blue)

Overall, the annual cycle of tropopause height in the ACCESS model is poorly reproduced. The origin of these shortcomings remains unclear. To some degree, the low vertical resolution and the monthly timescale of the data likely play a role as with the reanalysis. However, the problems with the ACCESS tropopause appear more significant than those in the reanalysis. The differences in annual cycle suggest that (at a minimum) the temperature and/or geopotential height fields in the sub-tropical upper troposphere are not accurately simulated. If the differences are due to the model itself, say through a poor representation of the relevant physics or dynamics, this suggests that any conclusions drawn from the model may be suspect and require careful validation. Further investigation is needed to identify the source of this apparent misrepresentation and its consequences.

Another method of examining model performance is by estimating the trend of tropopause height and comparing with observations. The use of trends in this manner is potentially problematic, as trends can be sensitive to things such as the choice of start and end points, but are useful in at least a qualitative sense. If the broader spatial patterns between models and observations are similar, then some degree of confidence can be achieved. The comparison here was done using the ACCESS 1.0 simulation noted above, the ERA-I Interim reanalysis and an estimate made from the Southern Hemisphere radiosonde data presented in Lucas et al. (submitted), suitably averaged into zonal bands. The trends in the observational sets were computed from 1979–2010, and the ACCESS model from 1979–2005 (the end of the simulation).

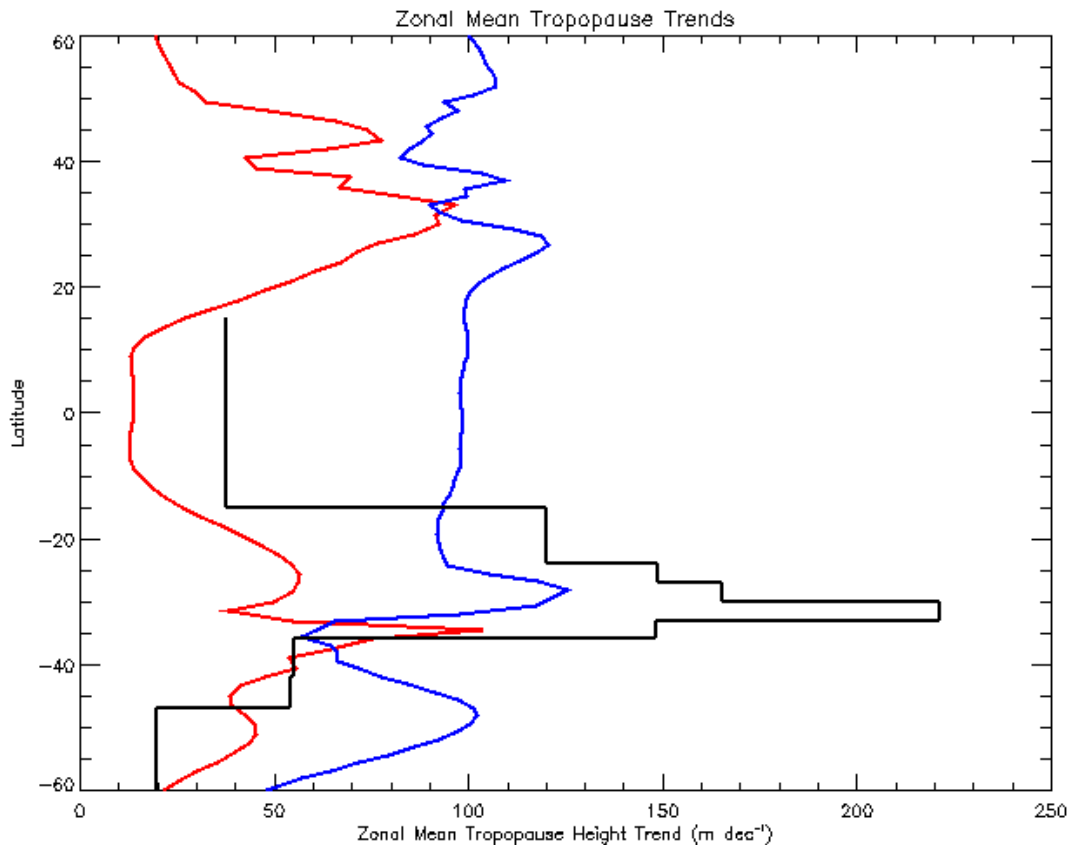


Figure 23. Zonal mean tropopause height trends from radiosondes (black), ERA Interim (red) and ACCESS 1.0 historical CMIP5 simulation (blue). Units are  $m\ dec^{-1}$ . Trends calculated from 1979–2010 (2005 for ACCESS)

Figure 23 summarises the results of this calculation in terms of the zonal mean. The radiosonde observations indicated a strong Southern Hemisphere trend between  $15^{\circ}\ S$  and  $30^{\circ}\ S$ , with lower values (but still positive) in the deep tropics and mid-latitudes. A similar pattern in the trends was noted by Seidel and Randal (2006) in the Southern Hemisphere. The ERA-I has a lower-valued peak in the Southern Hemisphere, but displaced further south and similar reductions in value outside this region. The ACCESS simulation also has a peak at  $30^{\circ}\ S$ , but this does not stand out as much from the considerably higher values found outside of the Southern Hemisphere subtropics. It is likely that this localised peak in the subtropics is to some degree associated with tropical expansion. It is likely that the region where tropopause height is observed more frequently at higher tropical heights would also see a strong upward trend in addition to whatever larger background trend exists.

Figure 24 shows the spatial pattern of the trends in the reanalysis. The band of high trend values in the subtropics of both hemispheres is readily apparent. However, a large region of negative trends in the eastern Pacific of both hemispheres offsets the general tendency in the subtropics. A closer examination of the trends in these regions (not shown) suggests an abrupt change in the tropopause characteristics around 2001/2002. A similar change in the characteristics of tropical expansion was noted in this reanalysis in Lucas et al. (submitted), who suggested the possibility of an inhomogeneity in that data source. The results here further highlight that possibility, and suggest particular locations where it may be more prominent. Few in situ observations exist in these regions of the world, suggesting that the reanalysis is less constrained and more sensitive to changes in the observing system. This also makes verification of this assertion difficult at this time.

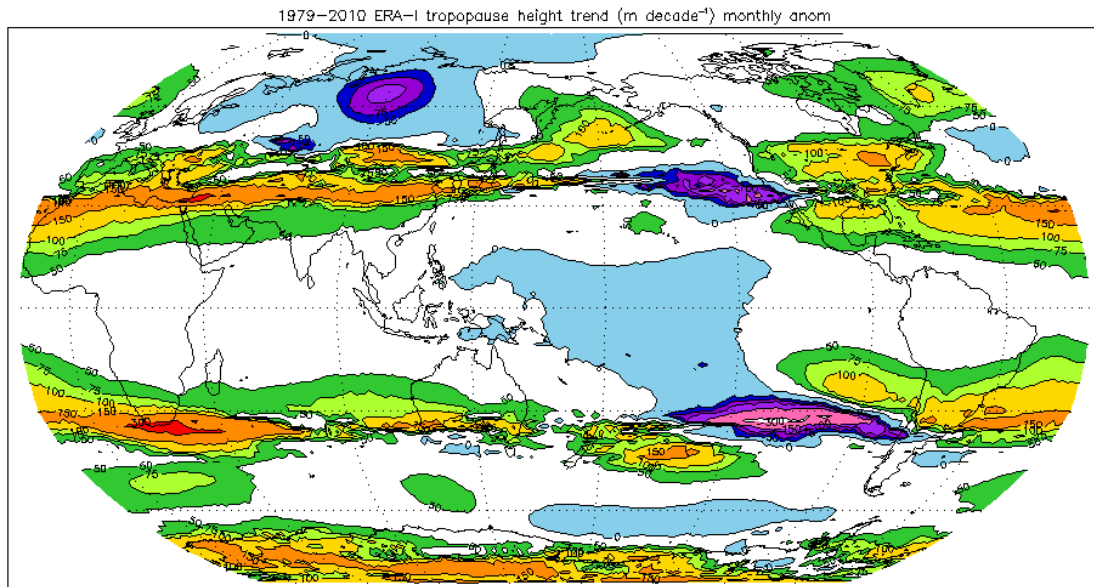


Figure 24. Spatial pattern of ERA-I tropopause trends from 1979–2010. Greens and oranges are positive values, blues and purple are negative values

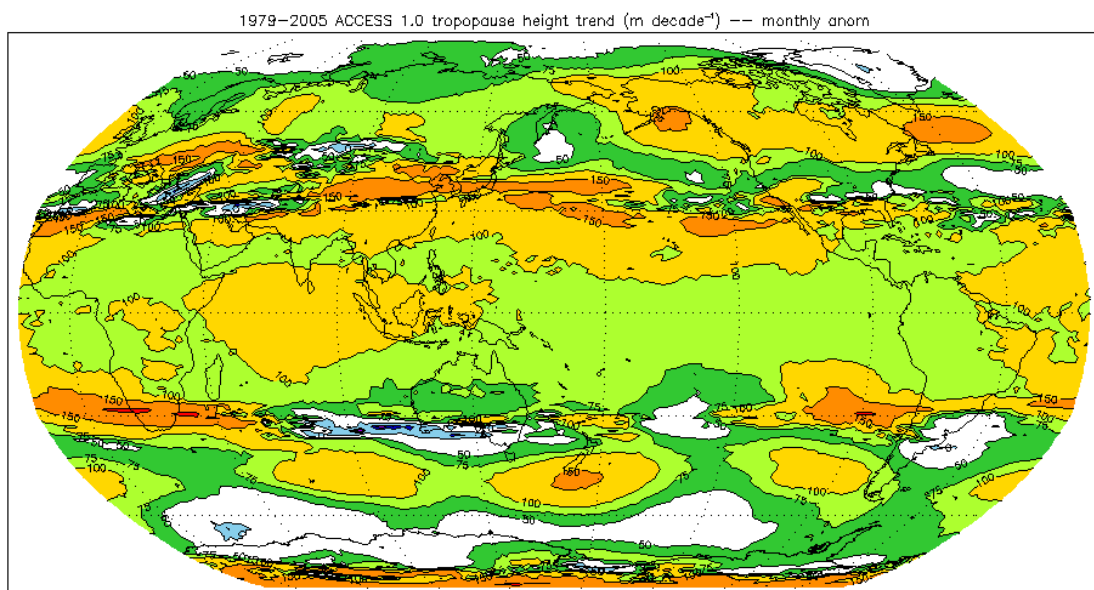


Figure 25. As in Figure 24, except for the ACCESS 1.0 historical CMIP5 simulation

Figure 25 shows the spatial pattern of trends in the ACCESS 1.0 CMIP5 historical simulation. The increase in trends in the subtropics is readily apparent, with a much higher background pattern. Trends computed from 1950–2005 (not shown) do not show this higher background, but maintain the enhancement in the subtropics. Examination of the time series at individual model grid points suggests that the higher background trends when using later start dates are a response to lower tropopause heights in the 1980s and 1990s associated with the volcanic eruptions of El Chichon and Pinatubo. Tropopause height was lowered significantly in the model following these eruptions, more than seen in observations. From this, we can speculate that the model/simulation may be overly sensitive to the significant volcanic aerosol forcing, creating the impression of a greater trend than actually exists. This hypothesis requires further investigation. Another feature of note is the region of slight decreasing trends south of Australia; these are also apparent in the ERA Interim trends (Figure 24). The reality of these trends is difficult to verify, as this region lacks in situ measurements. If these trends are accurate, then understanding their source could be important for interpreting recent climate change in south-eastern Australia.

## Objective 5

### **Examine whether climate models simulate the observed autumn rainfall reduction across south-eastern Australia in the late 20th century**

#### **Methods**

Rainfall and MSLP data from the historical experiments of 29 CMIP5 models were analysed (see Table 1 for model names and number of simulations examined). Multiple ensemble members of models were used where available. Model output was also compared to observational data sets: AWAP (Australian coverage), GPCC (global land coverage) and GPCP v2.2 (global coverage) for rainfall comparisons, and NCEP/NCAR (NCEP1), NCEP-DOE (NCEP2), ERA-40 and ERA-Interim reanalysis for MSLP comparisons. Model and observational climatologies were first assessed and then linear trends calculated using least square regression over 1950–2005 (56 years). For the multi-model mean, only one simulation from each model was used to equally represent each model. Results were interpolated onto a common grid ( $4^\circ \times 4^\circ$ ). An assessment of the proportion of the rainfall trend accounted for by changes in the MSLP was undertaken using observations and one run from each model. Firstly, the sensitivity was calculated through linear regression with the regression coefficient multiplied by the total MSLP trend to give to the pressure-induced rainfall changes.

To investigate the possible influence of Antarctic stratospheric ozone depletion on trends in rainfall, 'historical' and 'historical without ozone forcing' simulations from the CSIRO Mk3-6-0 model were compared.

#### **Historical trends in rainfall and mean sea level pressure for CMIP3 and CMIP5 experiments**

Compared to observations, CMIP5 models perform well in simulating the rainfall climatology in the Australian region (not shown). Most models simulate March, April, May rainfall climatology, although there is a slight wet bias in some models in central Australia. The models failed to simulate the orographic features along the east coast of Australia and western Tasmania, although they were able to generate the north-south gradient, with coastal regions of SEA being generally wetter than central and northern SEA regions. The CMIP5 models tended to simulate the June, July, August and December, January, February rainfall climatology quite well, although there was very little consistency in September, October, November, with some models showing wet and dry biases across SEA latitudes. For the March, April, May MSLP pattern, the zonally-oriented high pressure ridge that extends across southern Australia was well represented in nearly all of the models.

Although the majority of CMIP5 models simulate the mean climatology, most models do not reproduce the observed trends in SEA March, April, May rainfall. Trends in the CMIP5 multi-model mean (Figure 26) were much weaker than those in the observations, which is to be expected as a result of multi-model averaging, which cancels out the individual models interannual variability. However, compared to the CMIP3 mean of 24 models (not shown), the CMIP5 multi-model mean (Figure 26) exhibits large-scale spatial features in trends that show a greater similarity to observations. Analysing the individual CMIP5 model results for March, April, May in Australia (Figure 27), it can be seen that most models do not simulate the reduction in rainfall across SEA. Exceptions to this generalisation are the ACCESS1-0, MIROC-ESM, MIROC4h, MRI-CGCM3 and NorESM-ME models. However, of these models, only the ACCESS1-0 model was able to capture the north-west being wetter and south-east being drier across Australia. There was also a tendency for models to simulate an increase in rainfall across eastern Australia; in ten models that had five or more simulations, six showed an increase and four a reduction across southern SEA March, April, May rainfall from 1950–2005. Only in one of the 'drier' models did the reduction extend up to tropical north-east Australia (as seen in observations, bottom right hand panel in Figure 27; although this trend is a consequence of trends in March and not April, May – see Cai et al., in press). The inability of models to reproduce trends in March, April, May rainfall over SEA is not well understood. It should be noted that for March, April, May the CMIP5 models do simulate the increasing trend over central Western Australia (Figure 26, top panels), and the rainfall decrease across the south-western tip of South America.

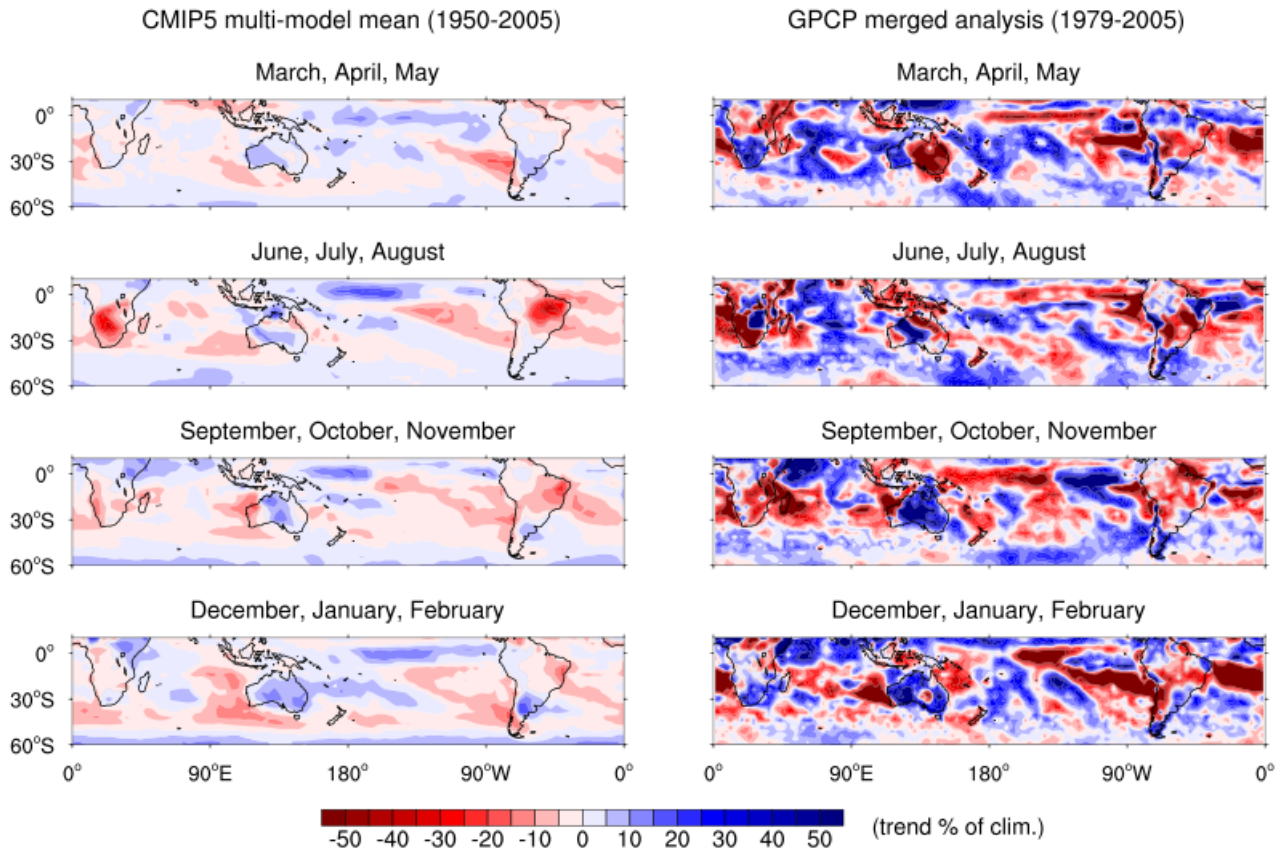


Figure 26. CMIP5 multi-model mean rainfall trends of the first run of all available models for 1950–2005 (left panels), and corresponding observational (based on GPCP v2.2) rainfall trends for 1979–2005 (right panels) over the Southern Hemisphere. Trends are shown for all seasons: March, April, May; June, July, August; September, October, November; and December, January, February. Rainfall trends are shown as a percentage of climatology, and trends from individual models have been interpolated to a standard  $4^{\circ} \times 4^{\circ}$  grid.

Table 1. CMIP5 models, institutions and the number of simulations from the historical experiments (precipitation and MSLP) used in this study.

<i>Model</i>	<i>Modelling group</i>	<i>Country</i>	<i>Simulations</i>
ACCESS1-0	Commonwealth Scientific and Industrial Research Organisation, and Bureau of Meteorology	Australia	1
ACCESS1-3	Commonwealth Scientific and Industrial Research Organisation, and Bureau of Meteorology	Australia	1
CCSM4	National Center for Atmospheric Research	United States	6
CNRM-CM5	Centre National de Recherches Meteorologiques / Centre Europeen de Recherche et Formation Avancees en Calcul Scientifique	France	10
CSIRO-Mk3-6-0	Commonwealth Scientific and Industrial Research Organisation, and Queensland Climate Change Centre of Excellence	Australia	10
CanCM4	Canadian Centre for Climate Modelling and Analysis	Canada	10 <sup>a</sup>
CanESM2	Canadian Centre for Climate Modelling and Analysis	Canada	5
FGOALS-g2	Institute of Atmospheric Physics, Chinese Academy of Sciences, and Tsinghua University	China	4
FGOALS-s2	Institute of Atmospheric Physics, Chinese Academy of Sciences	China	3
GFDL-CM3	National Oceanic and Atmospheric Administration Geophysical Fluid Dynamics Laboratory	United States	5 <sup>b</sup>
GFDL-ESM2G	National Oceanic and Atmospheric Administration Geophysical Fluid Dynamics Laboratory	United States	3
GFDL-ESM2M	National Oceanic and Atmospheric Administration Geophysical Fluid Dynamics Laboratory	United States	1
GISS-E2-H	National Aeronautics and Space Administration Goddard Institute for Space Studies	United States	5
GISS-E2-R	National Aeronautics and Space Administration Goddard Institute for Space Studies	United States	5
HadCM3	Met Office Hadley Centre	United Kingdom	4
HadGEM2-CC	Met Office Hadley Centre	United Kingdom	1
HadGEM2-ES	Met Office Hadley Centre	United Kingdom	4
IPSL-CM5A-LR	Institut Pierre-Simon Laplace	France	5
IPSL-CM5A-MR	Institut Pierre-Simon Laplace	France	1
MIROC-ESM	Japan Agency for Marine-Earth Science and Technology, Atmosphere and Ocean Research Institute (The University of Tokyo), and National Institute for Environmental Studies	Japan	3
MIROC-ESM-CHEM	Japan Agency for Marine-Earth Science and Technology, Atmosphere and Ocean Research Institute (The University of Tokyo), and National Institute for Environmental Studies	Japan	1
MIROC4h	Atmosphere and Ocean Research Institute (The University of Tokyo), National Institute for Environmental Studies, and Japan Agency for Marine-Earth Science and Technology	Japan	3
MIROC5	Atmosphere and Ocean Research Institute (The University of Tokyo), National Institute for Environmental Studies, and Japan Agency for Marine-Earth Science and Technology	Japan	4
MPI-ESM-LR	Max Planck Institute for Meteorology	Germany	3
MRI-CGCM3	Meteorological Research Institute	Japan	5
NorESM1-M	Norwegian Climate Centre	Norway	3
NorESM1-ME	Norwegian Climate Centre	Norway	1
bcc-csm1-1	Beijing Climate Center, China Meteorological Administration	China	3
inmcm4	Institute for Numerical Mathematics	Russia	1

<sup>a</sup> Precipitation and MSLP start at 1961, <sup>b</sup> MSLP ends at 2004

Next, we analysed MSLP trends across the Southern Hemisphere over 1950–2005 for each available CMIP5 model, shown in Figure 28. The majority of models showed a SAM-like pattern (trending towards a more positive phase; increasing pressure in the mid latitudes and decreasing pressure in the high latitudes) with models with more ensemble members showing weaker trends, likely a result of multi-member averaging. The magnitude of trends was generally underestimated by the models, regardless of the number of ensemble numbers, and the strong increase in MSLP seen over the entire Australian region during March, April, May was not reproduced in any of the models. Of the models that best captured the March, April, May rainfall trends across eastern Australia (ACCESS1-0, MIROC-ESM, MIROC4h, MRI-CGCM3 and NorESM-ME) only MIROC-ESM (three runs) and MIROC4h (three runs) simulated the increasing ridge of pressure across southern Australia. There was also a tendency for the models to simulate the increasing pressure belt too far south of Australia and New Zealand, although the models as a whole showed the climatological position of the sub-tropical high pressure ridge at the correct latitude (not shown). Two models generated strong MSLP trends (IPSL CM5A-LR, FGOALS-s2) that encapsulate southern Australia. In these models there was a drying trend over southern SEA (e.g., southern Victoria and Tasmania), which extended across the 40° – 45° S mid-latitude band, encompassing New Zealand and southwest South America (this was also seen in the IPSL CM5A-MR for one run), and a wetting trend further north in SEA. The positive SAM-like trend in these models allowed increased on-shore flow across eastern and north-eastern Australia, leading to strong rainfall increases in these areas, not seen in observations.

The relationships between trends in MSLP and trends in rainfall were also assessed. Observational results (not shown) suggested that across SEA the increasing trend in MSLP could have led to a large proportion of the trend in rainfall; however these results do not provide insight into the dynamics of such rainfall changes. As a consequence of CMIP5 models simulating the increasing trend in MSLP too far south of SEA, MSLP-induced trends in rainfall were correspondingly too far south (not shown). This may be one of the factors limiting the ability of CMIP5 models to reproduce observed rainfall trends across SEA during March, April, May.

The role of stratospheric ozone depletion in forcing Southern Hemisphere mid-latitude circulation changes is well established in the peer-reviewed literature (e.g., Polvani et al., 2011 and references therein), however the role of stratospheric ozone depletion in driving circulation and hence rainfall trends in March, April, May is not well understood. In CMIP3 historical simulations from 24 models, 14 were prescribed with stratospheric ozone depletion and ten were not. Rainfall and MSLP trends from CMIP3 models, with and without ozone, were calculated for each season for the period 1950–1999. The results (not shown) showed that there was no discernible difference between the two groups for March, April, May rainfall over SEA or the mid-latitude band, however the CMIP3 ozone depletion group (assumed to be more realistic) generated a stronger increase in pressure across the mid latitudes and reduction over the high latitudes (this was also true for December, January, February). Despite this increase in pressure, the location of the increase was too far south to force a rainfall change across SEA. This result suggests that the ozone depletion signal may carry through to March, April, May, shifting the storm tracks further south (as seen in observations in April, May; Cai and Cowan, in press); however, a decrease in rainfall as a result of this is not seen in the models, rather they simulate an increase in March, April, May rainfall across SEA in the late 20th century. This could mean that rainfall in this season is influenced by a dynamical process that the models are unable to capture, requiring further investigation. The same approach cannot be used with CMIP5 models as they all incorporate ozone depletion in their historical experiment design. Thus a multi-model comparison, grouping CMIP5 models into those with and without ozone depletion is not possible. Instead, the results of two experiments with the CSIRO Mk3-6-0 model (historical forcings, and historical forcings without ozone forcing) were analysed. The results were somewhat inconclusive, as ozone depletion does not necessarily correspond to a better representation of March, April, May rainfall trends: in fact, the ensemble average for the experiments without ozone forcing showed a weak decreasing trend over SEA, whilst the experiments with ozone depletion exhibited an increase over much of eastern Australia. Although inconsistent with rainfall observations, the trends were consistent with the CMIP3 ozone depletion multi-model mean.

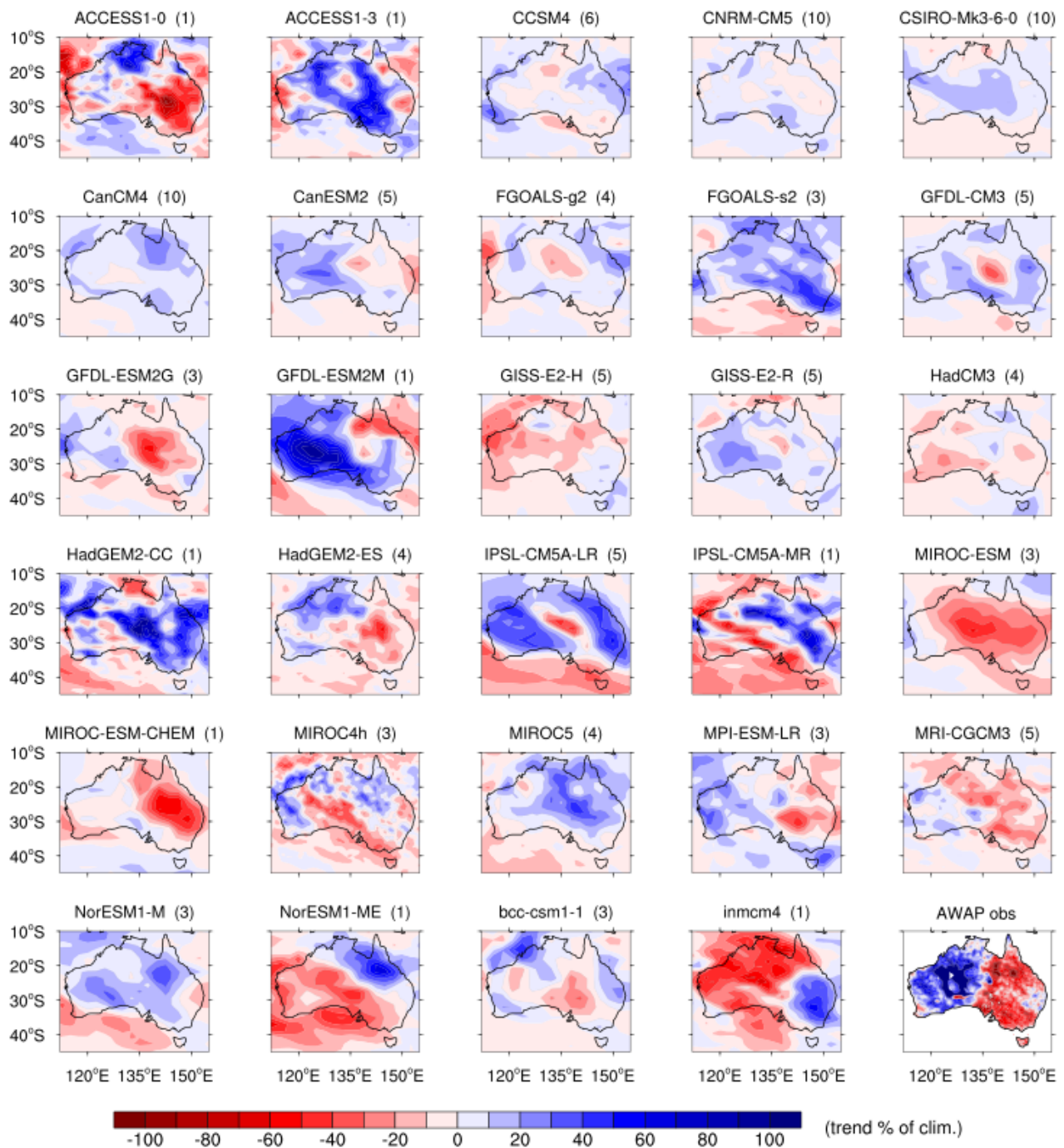


Figure 27. March, April, May rainfall trends for 1950–2005 in individual CMIP5 models over Australia. Trends in observations (AWAP, 1950–2005) are included for reference (bottom right panel). Rainfall trends are shown as a change in percentage from climatology (1950–2005). Trends for each model are an ensemble average of all available ensemble members in the historical experiment and the number of ensemble members for each model is indicated in brackets after the model name.

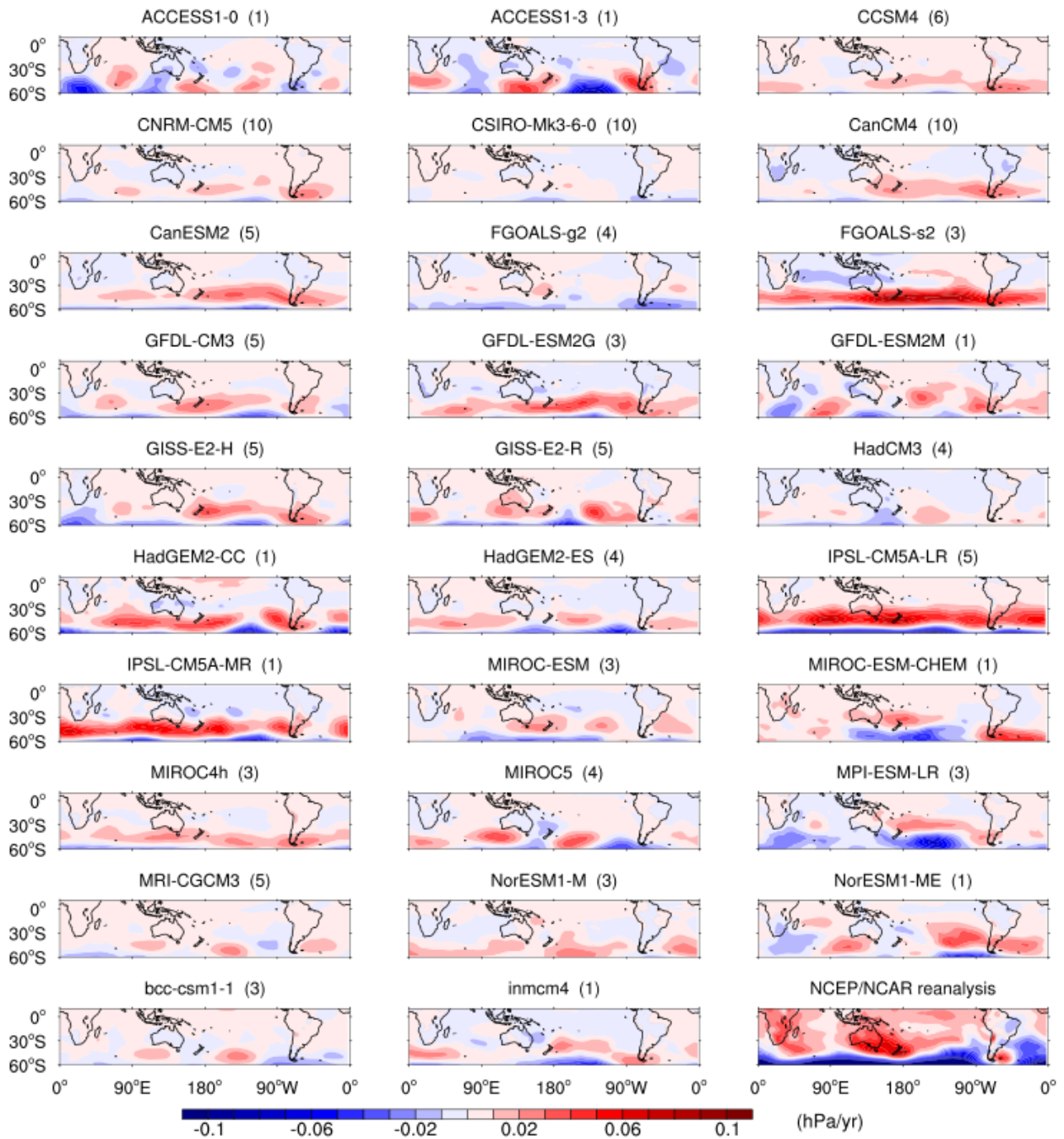


Figure 28. March, April, May MSLP trends for 1950–2005 in individual CMIP5 models over the Southern Hemisphere. Trends in NCEP/NCAR reanalysis are included for reference. MSLP trends are shown in hPa/yr. Trends for each model are an ensemble average of all available ensemble members in the historical experiment and the number of ensemble members for each model is indicated in brackets after the model name.

## Objective 6

**Examine whether the impact pathway whereby the IOD and ENSO influence SEA's climate, is symmetric with respect to positive and negative phases of the IOD and ENSO**

### *Method*

To analyse tropical influence pathways, data over the period 1950–2009 is analysed (rather than from during the post-1979 satellite era, as in Cai et al., 2011a) to increase the sample sizes of positive and negative phases of ENSO and the IOD. Hadley Centre global sea ice and SST reanalyses (Rayner et al. 2003) were used to monitor tropical SST variability in the tropical Indian and Pacific oceans. For the atmosphere, deep tropical convection and circulation anomalies were diagnosed using the mean outgoing longwave radiation, 200-hPa geopotential height, and upper-level divergence from NCEP/NCAR reanalyses (Kalnay et al. 1996). Definitions of ENSO and the IOD followed the standard NINO3.4 and Dipole Mode Index, respectively, as in Cai et al. (2011a). The NINO3.4 index describes the average of sea surface temperature anomalies over the equatorial Pacific Ocean (5°S–5°N, 170°–120°W) and the Dipole Mode index is the difference of the average sea surface temperature anomalies in the western (10°S–10°N, 50°–70°E) and eastern (10°S–Eq, 90°–110°E) tropical Indian Ocean.

### Asymmetry in the IOD and ENSO's influence on SEA climate

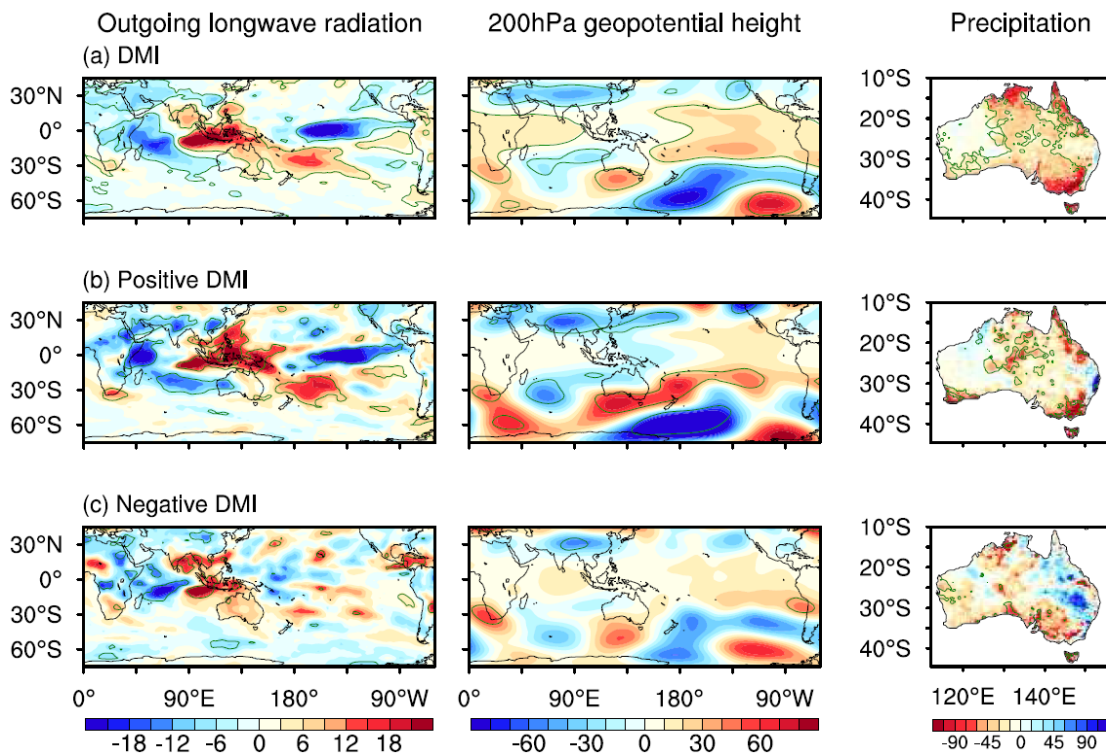


Figure 29. Atmospheric circulation patterns obtained by regressing detrended anomalies onto a detrended DMI using: (a) all samples, implying a linear relationship; (b) samples with a positive DMI value (positive IOD events); and (c) samples with a negative DMI value (negative IOD events). The regression coefficients (colour) and correlation coefficient (green contours, greater than that required for the 95 % confidence level) are plotted. The coefficients shown are associated with: outgoing longwave radiation (left,  $W m^{-2} \text{ } ^\circ C^{-1}$ ); 200-hPa geopotential height (centre,  $m \text{ } ^\circ C^{-1}$ ); and Australian rainfall (right,  $mm^{-1} \text{ season}^{-1} \text{ } ^\circ C^{-1}$ ). Figure reproduced from Cai et al., (in press.).

Previous studies have shown that the influence of the tropical Pacific and Indian Oceans on the climate of SEA in September, October, November stems from equivalent barotropic Rossby wavetrains that generate a high pressure centre anomaly over the Great Australian Bight (Timbal and Hendon, 2011; Cai et al., 2011b). These studies, however, focused on all data samples for their IOD and ENSO sea surface temperature indices, so the influence of each phase (e.g., El Niño, positive IOD, etc.) is not clear.

We performed our analysis using the DMI for 1950–2009, separating it into the two phases (positive and negative index values), and regressing anomalous outgoing longwave radiation (e.g., convection), 200-hPa geopotential height, and Australian rainfall onto the DMI samples. The resulting patterns are shown in Figure 29. Circulation anomalies associated with positive DMI samples were better defined than those associated with the negative DMI samples, with stronger tropical convection; in the eastern tropical Indian Ocean. The wavetrain response was also better defined for positive IOD events than for negative IOD events, translating into a greater rainfall response over southern Australia (including south-west Western Australia). The results suggest a strong asymmetry in the impact of the IOD on SEA in September, October and November. This IOD asymmetry impact is consistent with the positive skewness of the IOD, predominantly due to a negative skewness of SST anomalies in the eastern tropical Indian Ocean. This implies that the eastern Indian Ocean, which is important for generating the propagating wavetrain response to convection, is more sensitive to cold SST anomalies than warm SST anomalies that occur during negative IOD events.

The same analysis was undertaken for ENSO, separating the NINO3.4 index into El Niño and La Niña samples. The results (not shown) indicate that a similarly strong asymmetry also exists for ENSO. The impact of El Niño is conducted through the same wavetrain activity emanating from the tropical Indian Ocean, as the Pacific Southern

American pattern induced by ENSO events is too far east to influence Australia. In response to La Niña, northern Australian experiences increased rainfall associated with convection over the western Pacific, while some regions across eastern Australia are affected by the Pacific South American pattern-induced low pressure system. These results indicate that, as a result of a strong asymmetry, positive IOD events have a stronger impact on southern Australia than negative IOD events, whilst El Niño (La Niña) has a greater influence on SEA (central eastern Australia).

## Conclusions

The long-term rainfall deficiency over the last 30 years, which is predominately a late autumn/early winter phenomenon, was explored further. Following on from earlier SEACI work pointing toward the co-evolution of the STR-I and SEA rainfall, historical reconstruction of both SEA rainfall and STR-I allowed us to evaluate the interactions between these two quantities and the global average temperature as far back as the 1860s. The 1860s to 1890s provide another example (alongside the 1950s to 1970s) of an extended period where, in the absence of noticeable global warming, no STR intensification was observed, as well as strong decadal variability of SEA rainfall with a very wet decade (the 1870s was as wet as the 1970s). For the last 100 years, using daily rainfall maps across the Australian continent, it appears that the departure from the long-term climatology observed during the last 30 years consisted of a slight overall reduction in the number of systems affecting the tropical part of the continent but with a sizeable increase in the larger systems thus leading to an increase in rainfall. On the contrary, during the cool seasons fewer extra-tropical systems were observed and the reduction in rainfall was strongest for the more intense systems.

These observed changes across the Australian continent are explained in terms of changes in the mean meridional circulation. Based on radiosonde data, there has been significant tropical expansion over the last 30 years of  $0.41 \pm 0.37$  ° per decade. As part of that analysis, it was found that an inhomogeneity in the ERA-Interim reanalysis product exists, which gives incorrect trends in tropical expansion from that dataset. This raises the issue of the reliability of reanalyses for use in long-term climate studies. Similar trends were derived from all existing reanalyses for the Hadley circulation, which have been shown to control MSLP at the latitude of southern Australia. There is a very strong relationship between the Hadley cell expansion and both the position and the intensity of the STR. This behaviour was observed across all existing reanalyses as well as for climate model simulations of the last 50 years. Overall, the magnitude of these changes (Hadley cell widening and STR changes) appear closely related to global warming. Thus for 20th century simulations, only those models forced with anthropogenic inputs generated sufficient warming to produce these changes. However, the magnitude of the changes reproduced by climate models was not as large as those observed even if the model simulated a global warming of the same magnitude as that observed. Overall, many potential factors have been identified and implicated in tropical expansion. It appears to be more than a simple response to global warming/increasing GHG. Ozone and/or aerosol forcing are also likely to play a (perhaps significant) role. This has obvious implications for future projections of tropical expansion. This topic requires further investigation.

Some of the mechanisms driving the mean meridional circulation were investigated using the ACCESS model. The ACCESS model has some difficulty in correctly reproducing the annual cycle of tropopause height and has a bias in the extent of the Hadley cell, which may indicate potential issues with the model dynamics/physics within the subtropics. Encouragingly, ACCESS does qualitatively reproduce the observed meridional structure of tropopause trends, and the intensity of the Hadley cell is roughly correct. Careful evaluation of the model is required to improve the reliability of the conclusions that may be drawn from it. Taking into account these caveats, it was found that warming the tropical SST results in a greater impact on the mean meridional circulation than cooling the southern ocean. However, the trend produced is different from that observed. That is, increased tropical temperatures in the ACCESS model result in a stronger, narrower tropical width. There is, however, an opposite tendency in the mid-latitudes. Different metrics of tropical expansion were used. While generally similar in an annual sense, these produce different results when viewed at shorter time scales. This indicates important differences within the metrics, which need to be understood to strengthen any conclusions that may be drawn. Overall results from ACCESS suggest that while the intensification observed only in the Northern Hemisphere is controlled by the tropics, the expansion in the Southern Hemisphere might be controlled by the extra-tropics. The first assumption is consistent with Stachnik and

Schumacher (2011) who showed a similar response during warm phases of the ENSO. These results also support the findings from the reanalyses (CSIRO, 2011) that there was no statistically significant relationship between variability in the Hadley circulation intensity and its extent.

Using the CMIP database, it was found that, as a whole, the CMIP5 models were unable to capture the strong reduction in rainfall across SEA in March, April, May. While some models perform better than others, there is no overall consensus in the model tendencies (multi-model mean), unlike that simulated in June, July, August for south-west Western Australia. For MSLP, the CMIP5 models were able to simulate the high pressure ridge across southern Australia, however their trends exhibited an increase in surface pressure to the south of Australia, not over the continent as observed in reanalysis data. Analysis of MSLP-induced rainfall trends suggests that this may be one of the factors limiting the models' ability to simulate the observed rainfall trends. Furthermore, CMIP5 models that simulate a strong positive SAM-like pattern also simulate a strong increase in rainfall over eastern Australia, not seen in observations but most likely due to modelled on-shore flow and increased easterly-weather systems. The role of ozone depletion was also examined, although results from both CMIP3 models and the CSIRO Mk3-6-0 model were inconclusive.

For the September, October, November season, the asymmetry of ENSO and the impact of IOD on SEA's climate were examined. The findings suggest that both positive IOD and El Niño events affect SEA September, October, November rainfall more so than their counterparts; this is due to the strong positive skewness in these two phenomena. It also indicates that an increased positive IOD frequency is far more effective in generating a September, October, November rainfall reduction over SEA, as observed in the 2000s.

## Links to other projects

In 2011–12, the findings on the meridional circulation, sub-tropical-ridge and SEA rainfall relationships continued to underpin our current understanding of the rainfall decline in SEA and thus influenced all other projects within the SEACI program.

## CHAPTER 3: PROJECT 1.2

### Impact of climate variability and change on the water balance

Vanessa Haverd, Peter Briggs, Kirien Whan, James Barker, Michael Raupach

## Abstract

We studied the impact of climate variability and change on the water balance in south-eastern Australia using BIOS2, a model for water, energy, carbon and nutrient dynamics in the terrestrial biosphere in an environment that enables long model runs (from 1900 onward) at high spatial resolution (approximately 5 km) for the whole Australian continent, using gridded meteorological forcing data. BIOS2 consists of an enhanced version of CABLE (the Australian community terrestrial biosphere model), in the AWAP modelling environment. We applied BIOS2 to 'UC34', a group of 34 unimpaired catchments across south-eastern Australia (the same 34 catchments used in SEACI Project 2.2). We also applied BIOS2 over the whole SEA region (and in separate work over the whole of Australia). Major findings are as follows:

- As assessed with BIOS2, the sensitivity of SEACI region mean outflow to mean rainfall (the gain of the rainfall-runoff amplifier) is  $2.9 \pm 0.2$  percent (long-term mean, 1 standard deviation), implying that mean outflow decreases by 29 percent for each 10 percent decrease in mean rainfall (with all else constant).
- As assessed with BIOS2, the sensitivity of SEACI region mean outflow to temperature is  $-0.05 \pm 0.01$  °C<sup>-1</sup>. This value accounts for covariation of humidity with temperature. The implication is that outflow decreases by 5 percent (aggregated over the SEACI region) with each degree rise in temperature.
- The sensitivity of outflow to temperature is dominated by the sensitivity of transpiration to temperature, not the sensitivity of soil evaporation to temperature.
- Our model-based (BIOS2) determinations of the sensitivities of outflow to rainfall and temperature are in fair agreement with empirical determinations of the same sensitivities from SEACI Project 2.2 (where sensitivities were determined empirically using responses to natural variability in rainfall and temperature).
- The sensitivity of SEACI region outflow to CO<sub>2</sub> concentration is  $0.0009 \pm 0.0003$  ppm<sup>-1</sup>. This implies that a 100 ppm CO<sub>2</sub> increase would increase outflow by about 9 percent.
- We combined the above sensitivities with estimates of likely changes out to approximately 2050 in the major driving variables acting on outflow. The following picture emerged: there are three major contributors to likely long-term reductions in outflow. The largest single contributor is decreased precipitation, with an assumed 5 percent reduction in mean annual precipitation leading to a reduction of 15 percent in outflow. The next contributor is increased temperature, with a warming of 1 °C leading to an additional decrease in outflow of 5 percent. Third, the response to CO<sub>2</sub> (a likely increase 100 ppm) causes a 9 percent increase in outflow. Changes in other variables (radiation, wind, leaf area index) have much smaller likely effects.
- Linear-regression and tree-based (random-forest) analyses have been used to explore the relationship between spring rainfall in the Murray–Darling Basin and indices of large-scale modes of climate variability in preceding months. These two approaches have comparable skill at forecasting categories of Murray–Darling Basin spring rainfall from antecedent climate indices, when proper care is taken to avoid over-fitting and when both methods are applied to the same test problem.
- The availability of AWAP model products to the wider community continues to pay dividends for SEACI. A notable example is Webb et al. (2012), who found the signature of climate change in wine grape ripening driven by warming and declines in soil moisture, particularly in south-eastern Australia.

# Background

This project arose from the Australian Water Availability Project (AWAP), which aimed to monitor the state and trend of the terrestrial water balance of the Australian continent, including the past history and present state of soil moisture and all water fluxes contributing to changes in soil moisture (rainfall, transpiration, soil evaporation, surface runoff and deep drainage), across the entire Australian continent at a spatial resolution of 5 km. Past work in the AWAP has provided a 112 year (1900 to the present, and ongoing) record of soil moisture and all terrestrial water fluxes over the Australian continent at 5 km spatial and daily inter-annual resolution (with monthly archive).

As originally framed at the outset of Phase 2 of SEACI, the focus of Project 1.2 was to (i) maintain the AWAP data stream, (ii) apply it to model statistical climate–water relationships, and (iii) use the AWAP framework to understand the relationship between climatological drivers (precipitation, temperature, etc.) and hydrological responses (runoff, evaporation, etc.).

All of these lines of work have been delivered, but the priority and toolkit has evolved. We developed a modelling framework called BIOS2 (previously referred to as CableDyn). This is based on AWAP, and uses the same driving data and computational infrastructure, but replaces the simple (and robust) water balance model in AWAP (called WaterDyn) with an enhanced version of CABLE (Community Atmosphere-Biosphere-Land Exchanges). CABLE is the Australian community model for water, energy, carbon and nutrient dynamics in the terrestrial biosphere, describing not only energy and water exchanges but also carbon exchanges and carbon pool dynamics, and including far more sophisticated descriptions of critical biological processes (such as the effect of water stress, temperature changes and CO<sub>2</sub> changes on evapotranspiration) than WaterDyn. CABLE has been developed over many years in CSIRO, with more recent contributions from University colleagues. CABLE is the land surface scheme in most Australian atmospheric and climate models.

In the version used in BIOS2, CABLE has been greatly extended and improved in three major ways:

- i. A much improved soil-litter module (SLI; Haverd et al., 2010) has been added, leading to improvements in the treatment of soil evaporation and the effects of litter layers. The combined model is CABLE-SLI.
- ii. The implementation of CABLE-SLI in the AWAP modelling environment permits long model runs (from 1900 onward) at high spatial resolution (approximately 5 km) for the whole Australian continent, driven by gridded meteorological data.
- iii. We have undertaken a major program of rigorous model evaluation of CABLE-SLI (plus a biogeochemical model, CASAcnp) against multiple data on both the water and carbon cycles (eddy flux measurements of evapotranspiration and carbon exchanges, outflow data, ecological measurements of litterfall, soil carbon measurements).

The development of BIOS2 has created an important new toolkit that has been crucial to SEACI2 Project 1.2. However, it should be noted that BIOS2 was developed independently of funding and support by SEACI2. Rather, Project 1.2 has applied BIOS2 to answer basic questions about links between bioclimatic drivers and hydrological responses in south-eastern Australia.

Work in Project 1.2 on maintenance of the AWAP data stream has continued, because these data are essential for (and identical with) the driving data for BIOS2. We also continue to operate the existing AWAP website. AWAP (with WaterDyn) continues to be a respected and widely used modelling framework, which performs against independent benchmarks at least as well as other systems developed after AWAP.

# Objectives

In 2011–12, the objectives of Project 1.2 were:

- 1. Attribute observed trend and variability in SEACI region hydrology to variations in major drivers (temperature, CO<sub>2</sub>, wind, radiation, precipitation)**
  - Attribute observed hydrological responses in actual records (at scales from small catchments to whole SEACI region) to changes in major hydro-meteorological drivers (temperature, CO<sub>2</sub>, wind, radiation, precipitation).
  - Attribute the changes in the rainfall-runoff relationship found in Project 2.2, and characterise the 1997–2010 drought in these terms.
- 2. Explore the implication of temperature/humidity relationship for the sensitivity of the water balance to temperature**
  - Quantify the effect of the temperature/humidity relationship for sensitivity of water balance to temperature.
- 3. Evaluate feedbacks between meteorological drivers and hydrological responses that occur through biological and ecological processes (vegetation structure and functioning)**
  - Implement a dynamic carbon allocation scheme in BIOS2 based on optimisation of net primary production.
  - Use this scheme to investigate the response of leaf-root allocation ratios, and leaf area index, and root biomass, to decreasing moisture availability, increasing temperature and increasing CO<sub>2</sub>.
  - Use this scheme to investigate the water balance consequences of interactions between plant water use efficiency, transpiration, (likely) reduced leaf area, and (likely) increased fine root in water-stressed conditions.
- 4. Maintain and enhance the AWAP hydro-meteorological data stream. Create a more responsive connection between AWAP modelling and the BoM data stream**
  - Implement automated daily mirroring of the Bureau of Meteorology AWAP daily data archive so that Bureau quality control updates are immediately reflected in the CSIRO AWAP forcing data.
  - Implement automated dynamic modelling in response to changes in the meteorology.
  - Issue a revised and updated historical run in response to improvements in the Bureau AWAP meteorology.
  - Serve AWAP data to other users in SEACI; advise colleagues and the wider community of updates as they become available.

# Objective 1

**Attribute observed trend and variability in SEACI region hydrology to variations in major drivers (temperature, CO<sub>2</sub>, wind, radiation, precipitation)**

## *BIOS2 representation of hydrology in south-eastern Australia*

We are concerned with the water balance in a soil layer between the surface and some lower boundary (at depth 5 m in CABLE-SLI and BIOS2). The balance between soil water storage change, precipitation, total evaporation and outflow from the soil column (including both surface runoff and deep drainage) is

$$\underbrace{\frac{\Delta W}{\Delta t}}_{\text{Change in soil water store}} = \underbrace{P}_{\text{Precipitation}} - \underbrace{E}_{\text{Total Evaporation}} - \underbrace{Q}_{\text{Outflow}}$$

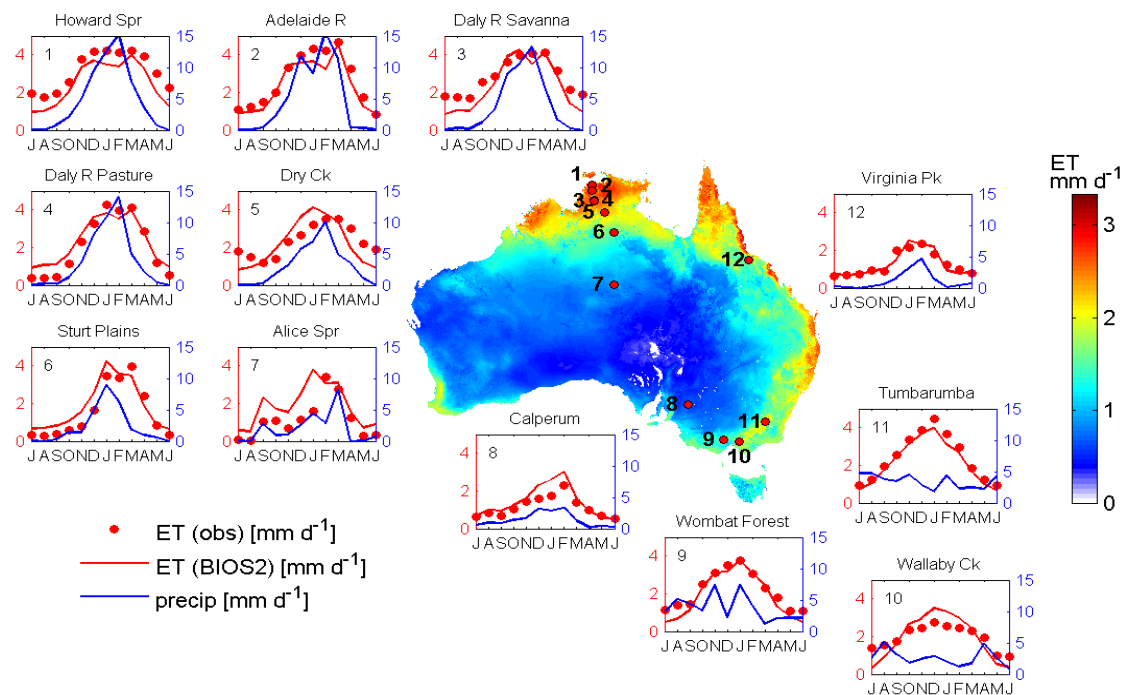


Figure 30. Map shows continental total evaporation  $E$  from BIOS2 (1990–2011 mean). Panels show mean monthly  $E$  at 12 Ozflux sites providing multi-year eddy covariance measurements of water and carbon fluxes. Red points are observations of  $E$ , red lines are BIOS2 predictions (both keyed to left axis). Blue lines show monthly mean precipitation (right axis)

BIOS2 represents the water balance well at monthly and longer time scales (as well as the carbon and energy balances, which are not a focus of this project). Here we give just one model-data comparison drawn from Haverd et al. (2012) (where many other comparisons are given). In Figure 30, the map shows the predicted continental total evaporation  $E$  from BIOS2 (1990–2011 mean). The 12 panels compare the predicted mean annual cycle of  $E$ , as mean monthly values, with eddy covariance measurements at 12 Ozflux sites (numbered). The agreement is very good.

Figure 31 shows the predictions of BIOS2 for the long-term water balance fluxes in 34 catchments unimpacted by significant diversions or landuse change used in this analysis (hereafter UC34). This group of catchments is the same group used in SEACI Project 2.2 (Potter et al., 2011).

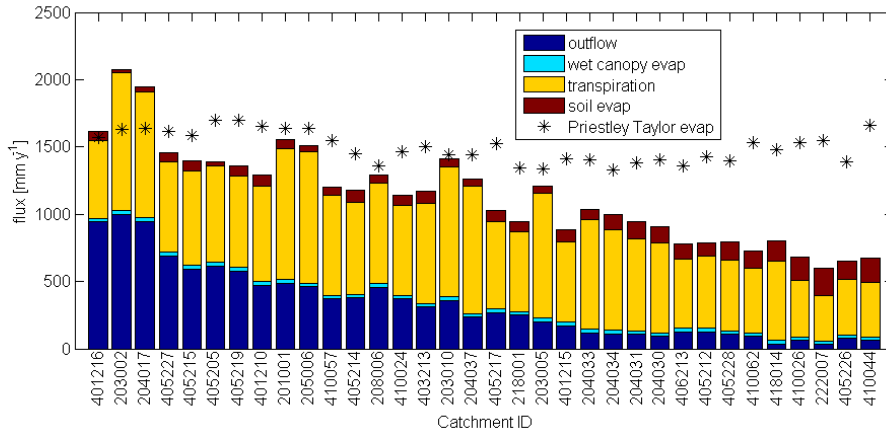


Figure 31. Mean water balance fluxes in 34 unimpaired catchments. Stacked bars represent soil evaporation  $E_s$  (brown), transpiration  $E_t$  (yellow), wet-canopy evaporation  $E_w$  (sky blue) and outflow  $Q$  (dark blue). The long-term water balance is  $P = E_t + E_s + E_w + Q$ , so the total height of the stacked bars gives the precipitation ( $P$ ) in each catchment. Stars give potential (Priestley-Taylor) evaporation in each catchment. Catchments are ordered as in Potter et al. (2011), based on a dryness index, with drier catchments on the right

The long-term water balance is  $P = E_t + E_s + E_w + Q$ , with precipitation  $P$ , transpiration  $E_t$ , soil evaporation  $E_s$ , wet-canopy evaporation  $E_w$  and outflow  $Q$  (storage change being negligible for a long-term balance). Figure 31 shows several features. First, all catchments in the UC34 group have precipitation ( $P$ ) greater than 700 mm, with a mean of around 1000 mm; this is much greater than the mean  $P$  for the SEACI region (around 450 mm), so UC34 represents wet parts of the SEACI region. Second, the outflow/precipitation ratio  $Q/P$  is more than 0.5 in the wettest catchments ( $P > 1500$  mm), falling to about 0.1 in drier UC34 catchments ( $P$  approximately 700 mm). Third, soil evaporation is relatively small in wet UC34 catchments with  $P > 1500$  mm (with  $E_s$  around 10 percent of total evaporation  $E$ ), but is relatively more significant in drier UC34 catchments with  $P$  approximately 700 mm, with  $E_s$  around 30 percent of  $E$ . Fourth, wet-canopy evaporation is insignificant everywhere. Fifth, there is little variation of mean potential (Priestley-Taylor) evaporation across the UC34 catchments.

### Sensitivity of outflow to rainfall: UC34 catchments

The sensitivity (or elasticity) of outflow ( $Q$ ) to precipitation ( $P$ ), denoted  $\eta(Q,P)$ , is defined as the fractional change in  $Q$  in response to a fractional change in  $P$ :

$$\eta(Q,P) = \frac{\text{fractional change in } Q}{\text{fractional change in } P} = \frac{\Delta Q/Q}{\Delta P/P} = \frac{P}{Q} \frac{\partial Q}{\partial P} = \frac{\partial \ln Q}{\partial \ln P}$$

The use of partial differentiation ( $\partial(\ln Q)/\partial(\ln P)$ ) indicates that all else but  $P$  is unchanged. The sensitivity  $\eta(Q,P)$  (a dimensionless quantity) can be thought of as the 'gain of the rainfall-runoff amplifier'; it is the amplification factor with which proportional changes in rainfall are reflected in proportional changes in outflow.

The upper panel of Figure 32 shows the sensitivity  $\eta(Q,P)$  as modelled by BIOS2 (orange points), for the UC34 unimpaired catchments. This was calculated as follows: a run of BIOS2 was performed for each catchment over a 48 year period (1960–2008) using observed meteorology. Each run was repeated using a uniform precipitation perturbation of –10 percent ( $\Delta P/P = -0.1$ ) so that conditions are perturbed to be 10 percent drier, with all other forcings (temperatures, radiation, etc.) held unchanged. The differences  $\Delta Q$  in outflows between the two runs were used to calculate  $\eta(Q,P)$  for each catchment.

Uncertainties (1 standard deviation) in BIOS2 predictions were evaluated by combining uncertainties in the  $P/Q$  and  $\partial Q/\partial P$  factors of  $\eta(Q,P)$ . The resulting uncertainty of 0.2 is dominated by the contribution of the 7 percent model error in  $P/Q$ , as quantified by analysing model/observation residuals of  $P/Q$  for each of the 34 catchments.

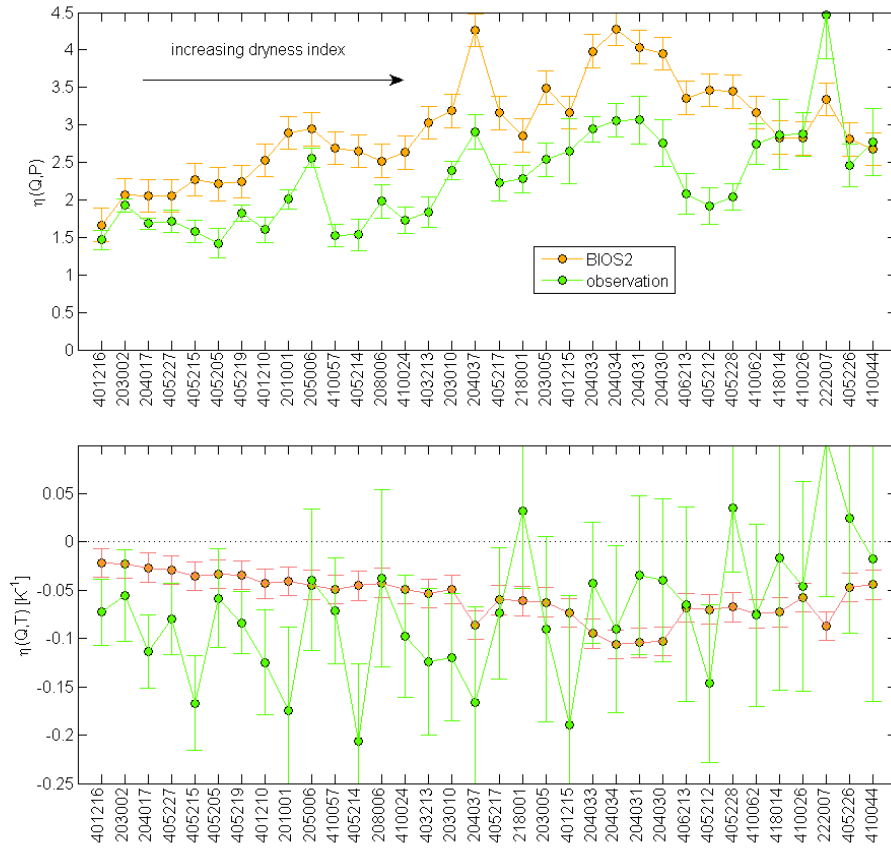


Figure 32. (Upper panel) sensitivity of outflow ( $Q$ ) to precipitation ( $P$ ), denoted  $\eta(Q,P)$ , for UC34 catchments. (Lower panel) sensitivity of outflow ( $Q$ ) to temperature ( $T$ ), denoted  $\eta(Q,T)$ . Orange points: BIOS2 model results; green points: empirical results (SEACI Project 2.2; Potter et al., 2011)

In wet catchments (left side of upper panel of Figure 32), the BIOS2 model estimates of  $\eta(Q,P)$  (orange points) were typically about 2, increasing to about 3.5 in dry catchments (right side). There was variability from catchment to catchment around this broad trend.

Figure 32 also shows empirical estimates of  $\eta(Q,P)$ , obtained in SEACI Project 2.2 by using responses of gauged streamflows to natural variability in rainfall (Potter et al., 2011). Modelled values were typically around 3. The agreement between modelled and empirical estimates of  $\eta(Q,P)$  was fair with similar magnitudes, trends and variability found by both methods. Estimates for the two wettest catchments agreed very closely. Modelled values were mostly higher elsewhere (typically by 0.5–1). Possible explanations for this are: (i) a limited ability of the empirical method to isolate the effect of changing precipitation from changes in other correlated variables; (ii) an underestimation of the modelled elasticity of transpiration to precipitation.

### Sensitivity of outflow to temperature in 34 unimpaired catchments (UC34)

The lower panel of Figure 32 shows the sensitivity (or elasticity) of outflow ( $Q$ ) to temperature ( $T$ ), denoted  $\eta(Q,T)$  and defined as

$$\eta(Q,T) = \frac{\text{fractional change in } Q}{\text{change in } T} = \frac{\Delta Q/Q}{\Delta T} = \frac{1}{Q} \frac{\partial Q}{\partial T} = \frac{\partial \ln Q}{\partial T}$$

This quantity has dimension  $^{\circ}\text{C}^{-1}$ . It is defined differently from  $\eta(Q,P)$ , with an absolute rather than fractional temperature change in the denominator, because fractional temperature changes are meaningless (unless absolute temperatures are used, and even then they are not intuitive).

The lower panel of Figure 32 shows the sensitivity  $\eta(Q,T)$  from BIOS2 (orange points) for the 34 unimpaired catchments, calculated as above for  $\eta(Q,P)$ . The same temperature perturbation ( $\Delta T = 1^\circ\text{C}$ ) was applied to both maximum and minimum daily temperatures. Vapour pressures were also adjusted in response to temperature changes, assuming that the daytime vapour pressure was constant and equal to the saturated vapour pressure at the minimum temperature. Uncertainties (1 standard deviation) in  $\eta(Q,T)$  of  $0.015^\circ\text{C}^{-1}$  from BIOS2 were dominated by uncertainties in the response of vapour pressure to temperature.

The resulting BIOS2 model estimates of  $\eta(Q,T)$  (orange points) were typically about  $-0.05^\circ\text{C}^{-1}$ . There was a tendency for  $\eta(Q,T)$  to increase in magnitude (become more negative) in drier catchments. The negative value of the sensitivity implies that outflow decreases with warming, with vapour pressures assumed to respond as above and all else held constant. Agreement with empirical estimates of  $\eta(Q,T)$  (SEACI Project 2.2 and Potter et al., 2011) was fair, with the BIOS2 estimates being smaller in magnitude in wetter catchments.

A significant issue is the relative contributions to the sensitivity  $\eta(Q,T)$  from the temperature responses of transpiration ( $E_t$ ) and soil evaporation ( $E_s$ ). From the steady-state water balance  $P = E_t + E_s + Q$ , neglecting wet-canopy evaporation) with constant  $P$ , it follows that Figure 33 shows the contributions to  $\eta(Q,T)$  from each term on the right hand side of this equation. In most catchments, particularly in wet environments (left hand side of Figure 33), the transpiration component dominates. An exception is Catchment 222007, which is sparsely vegetated and where soil evaporation constitutes a relatively high fraction of total evapotranspiration (Figure 31). In this catchment, the modelled contribution of transpiration is positive, because the increase in soil evaporation (associated with  $\Delta T = 1^\circ\text{C}$ ) leaves significantly less soil moisture available for transpiration.

$$\eta(Q,T) = -\frac{1}{Q} \left( \frac{\partial E_t}{\partial T} + \frac{\partial E_s}{\partial T} \right)$$

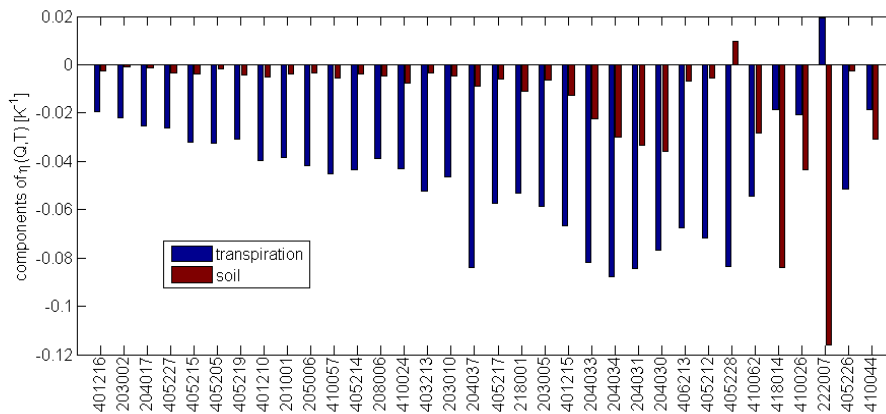


Figure 33. Breakdown of contributions to sensitivity of outflow to temperature,  $\eta(Q,T)$ , for 34 unimpaired catchments

### Sensitivities to multiple drivers: whole SEACI region

We extended the sensitivity studies above (for UC34 catchments) to examine the sensitivities of aggregate outflow to multiple drivers across the whole SEACI region, consisting of the MDB, the Victorian part of adjacent coastal Southeast Drainage Division, and the South Australian Gulf region.

The approach was to determine the average sensitivity  $\eta(Q,X)$  of aggregate outflow  $Q$  across the whole SEACI region to a set of drivers  $X$ , including precipitation (P), temperature (T), solar radiation (S), wind speed (U), CO<sub>2</sub> concentration (C) and leaf area index (L). Aggregate outflow is expressed in mm y<sup>-1</sup>, averaged across the area of the SEACI region (about 1.4 million km<sup>2</sup>). Average sensitivities were calculated by sub-sampling the SEACI region to a set of 200 randomly chosen representative points. The sensitivity  $\eta(Q,X)$  is defined as the fractional response to a fractional change in driver ( $\eta(Q,X) = \partial(\ln Q)/\partial(\ln X)$ ) when the driver  $X$  includes precipitation, radiation, wind speed or leaf area index, and as the fractional response to an absolute increment ( $\eta(Q,X) = \partial(\ln Q)/\partial X$ ) when  $X$  is temperature or CO<sub>2</sub>.

Table 2 gives the results, with interpretations as follows. The sensitivity of whole of region outflow to temperature (T) is  $-0.05 \pm 0.01$  °C<sup>-1</sup> for a temperature increment  $\Delta T = 1$  °C (Table 2, top row). Here and below, the range represents uncertainty in the long-term mean (1 standard deviation). We also calculated the sensitivity of whole-SEACI outflow to temperature,  $\eta(Q,T)$ , using larger temperature increments of  $\Delta T = 2$  and 4 °C. The resulting values (Table 2, second and third rows) are indistinguishable from the values with  $\Delta T = 1$  °C, suggesting that non-linear effects at high temperature perturbations are not significantly affecting the result.

*Table 2. Sensitivity  $\eta(Q,X)$  of outflow  $Q$  (spatially averaged over whole SEACI region) to key variables  $X$ , calculated using runs over 1911–2011 at 200 randomly chosen points across the SEACI region*

Driving variable (X)	$\eta(Q,X) =$ sensitivity of Q to X	Units of $\eta(Q,X)$	Definition of $\eta(Q,X)$	Inter- annual variability (1SD)	Long-term mean uncertainty (1SD)	Perturbation $\Delta X$ used to find $\eta(Q,X)$
Temperature (T)	-0.05	°C <sup>-1</sup>	$\partial(\ln Q)/\partial T$	0.01	0.01	1°C
Temperature (T)	-0.05	°C <sup>-1</sup>	$\partial(\ln Q)/\partial T$	0.01	0.01	2°C
Temperature (T)	-0.05	°C <sup>-1</sup>	$\partial(\ln Q)/\partial T$	0.01	0.01	4°C
Precipitation (P)	2.9	None	$\partial(\ln Q)/\partial(\ln P)$	0.2	0.2	-10%
Solar radiation (S)	-1.27	None	$\partial(\ln Q)/\partial(\ln S)$	0.07	-	5%
Wind speed (U)	-0.11	None	$\partial(\ln Q)/\partial(\ln U)$	0.01	-	+50%
CO <sub>2</sub> (C)	0.0009	ppm <sup>-1</sup>	$\partial(\ln Q)/\partial C$	0.0001	0.0003	10 ppm
Leaf Area Index (L)	-0.04	None	$\partial(\ln Q)/\partial(\ln L)$	0.01	-	20%

The whole SEACI region sensitivity of outflow to precipitation (P) is  $\eta(Q,P) = 2.9 \pm 0.2$  (Table 2, fourth line), is consistent with the dry catchment values in Figure 33 (upper panel).

The whole SEACI region sensitivity of outflow to changes in solar radiation (S) is  $-1.27 \pm 0.07$  (Table 2, fifth line). The negative value arises in the modelling because an increase in solar radiation boosts the total available energy at the surface and in turn increases both the latent and sensible heat fluxes to the atmosphere (through the surface energy balance). Since the latent heat flux is the total evaporation multiplied by the latent heat of vaporisation of water, an increase in solar radiation increases total evaporation and (because of the water balance) decreases outflow when precipitation held constant.

The whole SEACI region sensitivity of outflow to changes in wind speed (U) is small, at  $-0.11 \pm 0.01$  (Table 2, sixth line). Increasing wind speed increases aerodynamic conductance between the surface and the atmosphere, preferentially increasing latent heat flux at the expense of sensible heat flux in wet environments like the UC34 catchments, and vice versa in drier environments like most of the SEACI region; the crossover point, where the sensitivity of latent heat flux to wind speed is zero, occurs at the equilibrium evaporation rate. Water conservation

implies that the sensitivity of outflow to changes in any non-precipitation driver (including wind speed) is opposite in sign to the corresponding sensitivity of total evaporation, so outflow increases with wind speed in dry environments and decreases in wet environments. The overall balance leads to a sensitivity of outflow to wind speed that is small when outflow is aggregated to whole-SEACI scale.

The whole SEACI region sensitivity of outflow to changes in CO<sub>2</sub> concentration (C) is 0.0009 ± 0.0003 ppm<sup>-1</sup> (Table 2, seventh line). This implies a 9 percent increase in Q as CO<sub>2</sub> increases by 100 ppm, the likely increase over the next 40-50 years at the current rate of CO<sub>2</sub> growth of 2 ppm y<sup>-1</sup>. This is broadly consistent with hypotheses that plant water use efficiency increases with increasing CO<sub>2</sub>.

The whole SEACI region sensitivity of outflow to changes in leaf area index (L) is -0.04 ± 0.01 (Table 2, last line). Increasing leaf area index boosts transpiration and suppresses soil evaporation, and the low sensitivity is likely to result from the interplay between these two factors. The finding that the sensitivity is negative indicates that the effect on transpiration is larger, so that increasing leaf area index increases total evaporation over the SEACI region, therefore decreasing outflow.

### **Response of outflow to multiple drivers: whole SEACI region**

We now evaluate the implications of the sensitivities in Table 2 for the response of outflow (Q) across the SEACI region to simultaneous changes in multiple drivers: precipitation (P), temperature (T), solar radiation (S), wind speed (U), CO<sub>2</sub> concentration (C) and leaf area index (L). Taking Q to be a function of these six variables, the change in Q in response to simultaneous changes in all variables is (to first order):

$$\Delta Q(P, T, S, U, C, L) = \frac{\partial Q}{\partial P} \Delta P + \frac{\partial Q}{\partial T} \Delta T + \frac{\partial Q}{\partial S} \Delta S + \frac{\partial Q}{\partial U} \Delta U + \frac{\partial Q}{\partial C} \Delta C + \frac{\partial Q}{\partial L} \Delta L$$

Using the sensitivities  $\eta(Q, X)$  defined in Table 2, the fractional change in Q can be written as

$$\frac{\Delta Q}{Q} = \eta(Q, P) \frac{\Delta P}{P} + \eta(Q, T) \Delta T + \eta(Q, S) \frac{\Delta S}{S} + \eta(Q, U) \frac{\Delta U}{U} + \eta(Q, C) \Delta C + \eta(Q, L) \frac{\Delta L}{L}$$

To this point, the driving variables P, T, S, U, C and L have been treated as independent. However, at a larger scale than that of local or regional hydrological systems, these variables are actually strongly related. For example, climate change is driven by increases in concentrations of CO<sub>2</sub> (and other greenhouse gases), so changes in T and P are closely associated with changes in C.

For an illustrative assessment of the likely relative effects of all driving variables (P, T, S, U, C and L) on outflow, accounting for likely covariation among the driving variables, we take 2050 as a target year and make the following assumptions to estimate plausible changes in driving variables by 2050, relative to present (2012) values:

- CO<sub>2</sub> concentration:  $\Delta C \approx 100$  ppm. This is a simple extrapolation of the present CO<sub>2</sub> growth rate (2 ppm y<sup>-1</sup>) with a conservative allowance for acceleration in this growth rate in response to still-rising CO<sub>2</sub> emissions.
- Temperature:  $\Delta T \approx 1$  °C. This is a conservative estimate based on mid-range IPCC scenarios (and other lines of reasoning associating temperature rise with CO<sub>2</sub> increases, at a typical response rate of 0.01 °C ppm<sup>-1</sup>).
- Precipitation:  $\Delta P/P \approx -5$  percent. This is approximately consistent with findings from the MDB Sustainable Yields project where MDB-wide precipitation changes of approximately -3 percent by 2030 are suggested (CSIRO, 2008).
- Wind speed:  $\Delta U/U = -2$  percent. This assumes some ongoing stilling as a result of increasing surface roughness associated with ongoing reversals in deforestation and woody thickening in rangelands.
- Solar radiation:  $\Delta S/S = 0$  percent. Trends in solar radiation in the Australian and SEACI regions are small, so no change is assumed to 2050.

- Leaf area index:  $\Delta L/L = +10$  percent. Trends in leaf area index are uncertain, and different factors act in both directions. For instance, responses to likely decreasing precipitation would reduce leaf area index, while responses to environmentally aware land management (reductions in grazing pressure, conservation farming, etc.) are likely to increase it: For illustration, a 10 percent increase is assumed.

*Table 3. Fractional changes in SEACI region outflow ( $\Delta Q/Q$ ) in response to assumed changes in driving variables, assessed as plausible over the period 2012–2050*

Driving variable (X)	$\eta(Q,X) =$ sensitivity of Q to X	Definition of $\eta(Q,X)$	Assumed future perturbation ( $\Delta X$ )	Resulting fractional change in outflow ( $\Delta Q/Q$ )
Temperature (T)	$-0.05 \text{ } ^\circ\text{C}^{-1}$	$\partial(\ln Q)/\partial T$	$\Delta T = +1 \text{ } ^\circ\text{C}$	-5%
Precipitation (P)	2.9	$\partial(\ln Q)/\partial(\ln P)$	$\Delta P/P = -5\%$	-15%
Solar radiation (S)	-1.27	$\partial(\ln Q)/\partial(\ln S)$	$\Delta S/S = 0\%$	-
Wind speed (U)	-0.11	$\partial(\ln Q)/\partial(\ln U)$	$\Delta U/U = -2\%$	+0.2%
CO <sub>2</sub> (C)	0.0009 $\text{ppm}^{-1}$	$\partial(\ln Q)/\partial C$	$\Delta C = +100 \text{ ppm}$	+9%
Leaf area index (L)	-0.04	$\partial(\ln Q)/\partial(\ln L)$	$\Delta L/L = +10\%$	-0.4%

Table 3 shows the fractional changes in SEACI region outflow ( $\Delta Q/Q$ ) in response to these assumed changes in driving variables. The largest effect occurs through decreased precipitation, leading to a 15 percent decrease in outflow. Warming causes a significant additional decrease, of 5 percent. The response to CO<sub>2</sub> (+9 percent) more than offsets the decrease due to warming. Other variables have much smaller effects; in particular, the effect of a 10 percent increase in leaf area index is assessed as a small (–0.4 percent) change in outflow. Combining the effects of the three dominant driving variables (P, T and C), the resulting implication for SEACI region outflow is a decrease of 11 percent, somewhat less than the decrease due to precipitation alone.

#### **Effect of warming on the distribution of inter-annual variability in outflow**

Figure 34 provides a further illustration of the effect of temperature on SEACI region hydrology, by showing BIOS2 predictions of the cumulative probability distribution function (CDF) of outflow  $Q$  ( $\text{mm y}^{-1}$ ), under present conditions and at warmings of 1, 2 and 4 °C. The CDF is the fraction of years for which the outflow is less than a value  $Q$ , plotted against  $Q$ . The CDF was calculated by (1) sub-sampling the SEACI region to a set of 200 randomly chosen representative points (the same as the points used to calculate the SEACI region sensitivities in Table 2); (2) running BIOS2 at each point using 100 year forcing meteorology (1911–2011) with temperature increments  $\Delta T = 0, 1, 2$  or 4 °C applied to both daily maximum and daily minimum temperatures throughout the record; and (3) determining the CDF by sorting annual outflows  $Q$  (averaged spatially across the sample of points) into ascending order and plotting normalised rank (0 to 1) against  $Q$ .

For high warming (e.g.  $\Delta T = 4 \text{ } ^\circ\text{C}$ ), elasticities are consistent with those deduced from lower warming (e.g.  $\Delta T = 1 \text{ } ^\circ\text{C}$ ), as shown in Table 1. Responses at other points in the cumulative probability distribution than median (CDF = 0.5) are likewise consistent with the sensitivities  $\eta(Q,T)$  in Table 2. In other words, the sensitivity  $\eta(Q,T)$  describes not only the response of the SEACI region mean outflow to warming but also SEACI region-wide probability distribution for the inter-annual variation in outflow, as captured by the CDF in Figure 34.

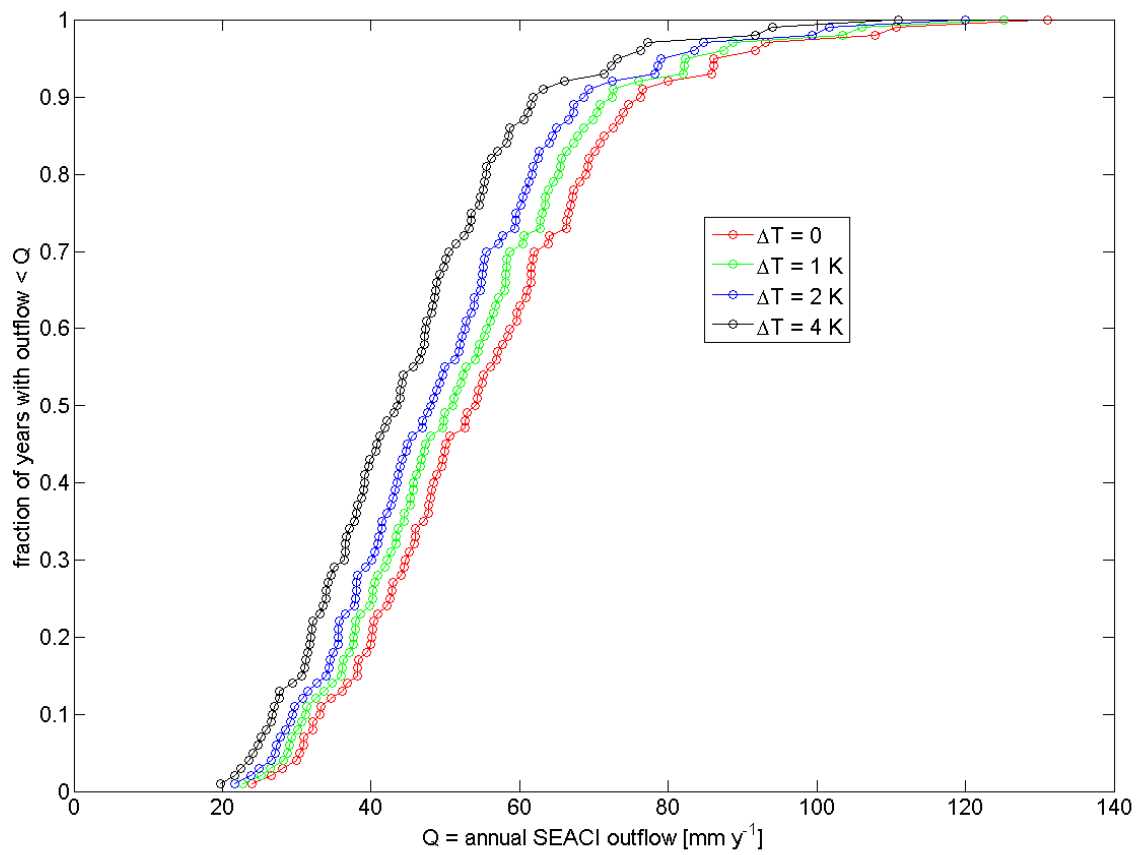


Figure 34. BIOS2 predictions of the cumulative probability distribution function of soil-column outflow  $Q$  ( $\text{mm y}^{-1}$ ), spatially averaged across the whole SEACI region, over 100 years. This is the fraction of years for which the outflow is less than a value  $Q$ , plotted against  $Q$ . Red curve is the CDF for present conditions; green, blue and black curves give the CDF at warmings of 1, 2 and 4 °C

## Objective 2

### Explore the implication of temperature/humidity relationship for the sensitivity of the water balance to temperature

The issue raised by this objective is minor. In estimating the sensitivity of outflow to temperature,  $\eta(Q,T)$ , it is necessary to account for the covariation of humidity and vapour pressure deficit with temperature. To do this, we used the simple assumption that the daytime vapour pressure is constant and equal to the saturated vapour pressure at the minimum temperature.

Figure 35 tests this assumption at the Tumbarumba Ozflux site (see Figure 30 for location). The blue line is the directly measured specific humidity (proportional to vapour pressure), and the red line is the estimate from the above assumption. Uncertainties in modelled humidity, and particularly its response to temperature, were propagated through to uncertainties in the elasticity of outflow to temperature (Table 1) and are the dominant contributor to this uncertainty. Agreement was good enough to justify continued use of the assumption.

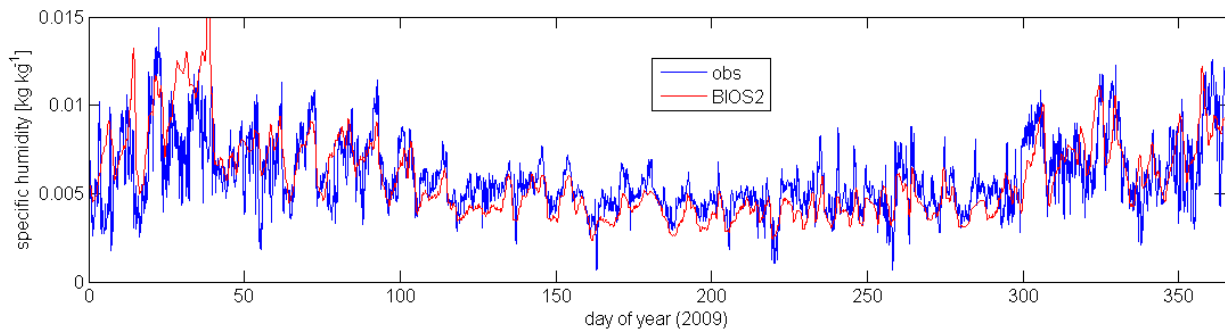


Figure 35. Comparison between humidity estimated from daily minimum temperature as in BIOS2 (red line) and direct hourly observations at the Tumbarumba Ozflux site (blue) for 2009

## Objective 3

### Evaluate feedbacks between meteorological drivers and hydrological responses that occur through biological and ecological processes (vegetation structure and functioning)

Work on this objective was combined with work on the first objective, particularly the evaluation of the sensitivity of outflow to leaf area index (L). The whole SEACI region sensitivity of outflow to changes in leaf area index is  $\eta(Q,L) = -0.04 \pm 0.01$  (inter-annual standard deviation) (see Table 2 and associated discussion). Increasing leaf area index boosts transpiration and suppresses soil evaporation, and the low sensitivity is likely to result from the interplay between these two factors.

Trends in leaf area index are uncertain, and are subject to several different drivers. For instance, responses to likely decreasing precipitation would reduce leaf area index, while responses to environmentally aware land management (reductions in grazing pressure, conservation farming, etc.) are likely to increase it. Assuming for illustration a change in leaf area index from 2012 to 2050 of 10 percent ( $\Delta\text{LAI}/\text{LAI} = +10$  percent), the resulting change in outflow would be a small  $-0.4$  percent.

We would like to investigate ecological feedbacks in much more detail using BIOS2, but the required model development is outside the scope of this project.

## Objective 4

### Maintain and enhance the AWAP hydro-meteorological data stream. Create a more responsive connection between the AWAP modelling and the BoM data stream

The Australian Water Availability Project (AWAP) data stream involves four main components:

- (1) operational acquisition of meteorological data (daily rainfall, solar radiation, maximum and minimum temperature, and 9 am and 3 pm vapour pressure) from the Bureau of Meteorology;
- (2) weekly operational production of near-real-time gridded hydro-meteorological quantities (soil moistures and water balance fluxes) with the WaterDyn model;
- (3) periodic production of historic gridded hydro-meteorological quantities by running WaterDyn from 1900 to present with best available gridded meteorological data; and

- (4) dissemination of both the gridded meteorological and hydro-meteorological data to a user community via ftp and in map form through a public website ([www.csiro.au/awap/](http://www.csiro.au/awap/)).

The BIOS2 results presented above are dependent on the meteorological data made available by the first of these four AWAP components.

### **Maintenance and enhancement of the AWAP hydro-meteorological data stream**

We continue to maintain the AWAP data stream through the operational system, with updated results available weekly via ftp, along with maintenance of the website ([www.csiro.au/awap/](http://www.csiro.au/awap/)), updating of graphical products, and improvement of the documentation.

The historical series of AWAP model outputs has been updated to the end of December 2011 using a combination of the existing CSIRO archive of Bureau data and updated data downloaded on February 16, 2012. At the completion of a quality control assessment the release announcement (to occur shortly) will be accompanied by updated documentation.

The updated run (26h) differs from the previous run (26c, released March 2011) only with respect to changes in the forcing meteorology. Nevertheless, some of these changes are significant. The currency of the meteorology for both runs is given in Table 3. No changes have been made to the WaterDyn model, which continues to be version 26M.

*Table 4. Bureau of Meteorology AWAP meteorology used to force recent AWAP WaterDyn historical runs 26h (due for release June 2012), and 26c (released March 2011). Download dates are colour-coded by age, from red (oldest) to green (newest). Green date ranges in the upper panel show the changes from run 26c to 26h, including complete new solar radiation, replacement of all 2010 and 2011 data, and an extension of the series from Feb 2011 to the end of 2011. Synthetic parts of the temperature and solar radiation series are constructed from data with a currency indicated by the cell colour*

#### **AWAP WaterDyn Release 26h Meteorology Download Dates (June 2012)**

	Date Range	1900-1910	1911-1949	1950-1989	1990-2008	2009	2010	2011
Solar radiation	daily	Synthetic	Synthetic	Synthetic	Feb-2012	Feb-2012	Feb-2012	Feb-2012
Recalibrated rainfall	daily	Mar-2010	Mar-2010	Mar-2010	Mar-2010	Nov-2010	Feb-2012	Feb-2012
Rainfall	monthly	Mar-2010	Mar-2010	Mar-2010	Mar-2010	Nov-2010	Feb-2012	Feb-2012
Temperature	daily	Synthetic	Jun-2009	Jun-2009	Jun-2009	Nov-2010	Feb-2012	Feb-2012

#### **AWAP WaterDyn Release 26c Meteorology Download Dates (March 2011)**

	Date Range	1900-1910	1911-1949	1950-1989	1990-2008	2009	2010
Solar radiation	daily	Synthetic	Synthetic	Synthetic	Jun-2009	Mar-2010	Mar-2011
Recalibrated rainfall	daily	Mar-2010	Mar-2010	Mar-2010	Mar-2010	Nov-2010	Mar-2011
Rainfall	monthly	Mar-2010	Mar-2010	Mar-2010	Mar-2010	Nov-2010	Mar-2011
Temperature	daily	Synthetic	Jun-2009	Jun-2009	Jun-2009	Nov-2010	Mar-2011

**Impact of changes to solar radiation:** As shown in Table 3, changes to the meteorology between runs 26c and 26h involved replacement of all existing data for 2010 and an update to 31 December 2011. In addition, the complete solar radiation data series was refreshed to take advantage of recent improvements including, in order of importance (Ian Grant, pers. comm., 8 May 2012):

- Correction of errors in modelled bias corrections applied to MTSAT-1R data from March 2007. Errors primarily affect lower exposure values. New bias corrections were performed using surface data.

- Filling of inland water locations and the creation of a 10 cell coastal buffer by extrapolation (applied to the whole archive).
- Removal of occasional negative values of solar radiation occurring in cloudy or low radiation conditions as a result of bias removal combined with uncertainties in the satellite model, applied from 2007 onwards.

Changes to the solar radiation have the following implications for AWAP results in the overlapping period of runs 26c and 26h (1900–2010):

- Due to the complete replacement of the solar radiation data, most modelled quantities will be at least slightly different. As shown in Figure 36, major differences, which are due to the correction of errors in earlier bias corrections (Grant, pers. comm., 8 May 2012), begin in March 2007 and increase through 2011. During this period, the size of the errors in the radiation forcing for run 26c are significant and propagate to the soil moisture surfaces. Changes in the earlier part of the solar radiation record are being investigated. Due to the significance of the bias from March 2007, run 26c should not be used for analysis of recent trends.
- A new monthly climatology for gap-filling the solar radiation was created using data from 1990–2011, replacing the previous one which used 1990–2008 data. Data for the full period were also used as the base for calculating percentile ranks of solar radiation, Priestley-Taylor potential evaporation, and open water (pan) evaporation for run 26h. The addition of the alternately dry and wet periods in 2009–2011 makes the climatology more representative of the range of conditions.
- Importantly, coastal and inland buffering by extrapolation removes the final dependence of the AWAP system on non-AWAP meteorology. Gaps in the model domain at coastal fringes and inland water bodies have previously been filled with legacy ground based SILO data from QDERM. This is no longer necessary.

**Impact of changes to recalibrated rainfall and temperature:** The impact of the replacement of the 2010 recalibrated rainfall and temperature data will be most visible in changes (improvements) to model surfaces in the later months of 2010, specifically within 6 months (rainfall) and 3 months (temperature) of the download date of the 26c meteorology (early March 2011). Six months and three months are the lengths of the Bureau of Meteorology data collection and quality control cycle for rainfall and temperature respectively.

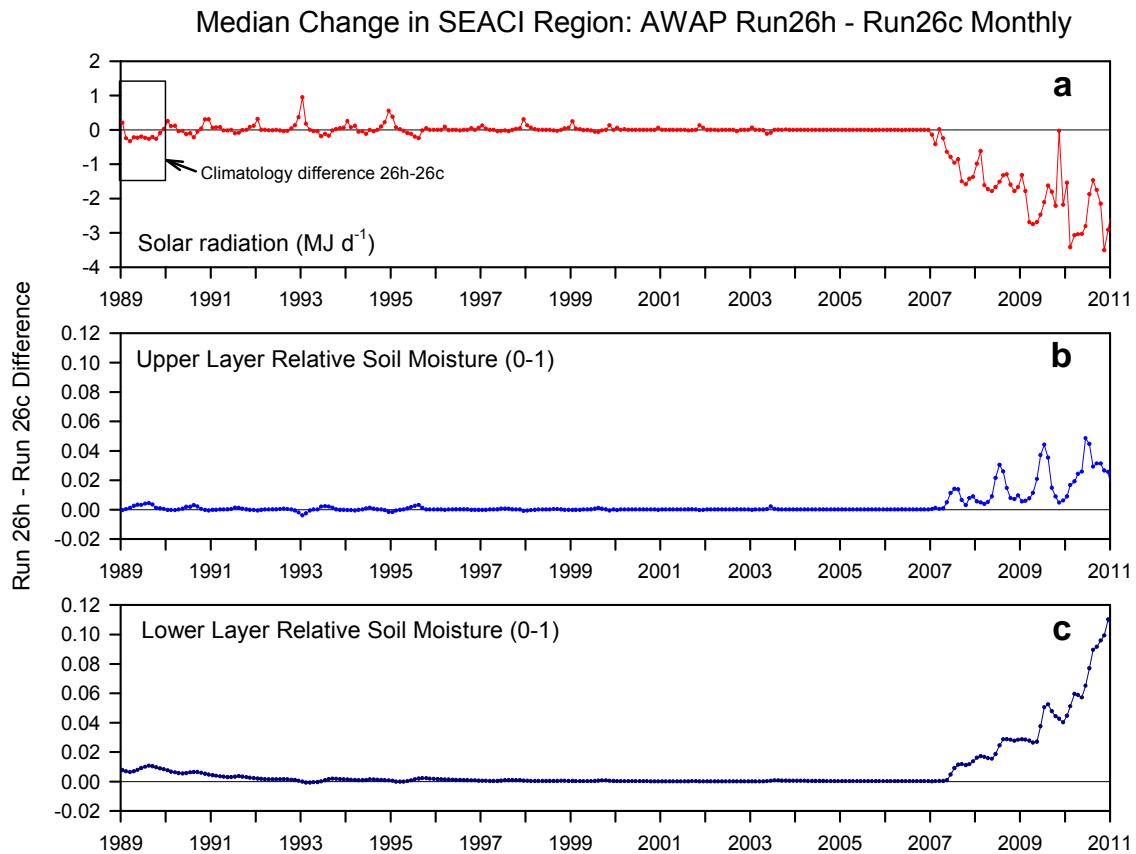


Figure 36. Monthly time series of the (spatial) median difference within the SEACI region for the solar radiation forcing used for AWAP WaterDyn runs 26h and 26c is given in panel a). The spatial median is used to minimise the impact of differences related to the coastal and inland water buffering, which may be large but involve small areas. The resulting differences in b) upper and c) lower layer soil moisture starting in March 2007 are due almost entirely to changes in the solar radiation surfaces related to fixing the bias correction. The inference is that for the SEACI region, AWAP run 26c contains a spuriously large negative trend in soil moisture from March 2007 to 2010. The bias in upper layer soil moisture is most pronounced in the winter months. Differences in 1989 solar radiation (panel a) reflect differences between the climatologies used to fill the period 1900–1989, which are from 1990–2008 for 26c and 1990–2011 for 26h. The lack of bias in 26c in November 2009 is accidental: positive bias from sensor drift in the first half of the month was balanced by negative bias in the second half of the month from the use of climatology for 13 missing days in what was a notably hot and dry November in the region

### **More responsive connection between AWAP modelling and the Bureau of Meteorology data stream**

This work involved a redesign of the AWAP operational system with benefits for model output quality, timeliness, and a reduced requirement for data management. There were two objectives: (1) to implement automated daily mirroring of the Bureau AWAP daily data archive so that Bureau quality control updates are immediately reflected in the CSIRO AWAP forcing data, and (2) to implement automated dynamic modelling in response to any changes in the meteorology. Any changes in the meteorology trigger an automated remodelling of the entire series starting from the date of the earliest meteorology change (which is necessary for current soil moisture stores to reflect earlier changes).

We expanded the scope of the objectives to include (3) recoding of the AWAP system infrastructure in a common scripting language (Python) for implementation on a single system under Linux, with an emphasis on portability; and (4) porting of the system to the High-Performance Computing Cluster supercomputing environment.

These additional objectives involve an overdue simplification of the AWAP system shell (which runs components in four scripting languages across two operating systems) and ensures the future of the AWAP infrastructure by making it easily portable to other systems including those run by external agencies. As part of the portability test, the new

system was being developed initially in the supercomputer environment, laying the groundwork for the eventual replacement of WaterDyn in the AWAP system by the more computationally-intensive BIOS2 model (Haverd et al., 2011) that has provided most of the results in this chapter of the report.

The first phase of the task is nearing completion, and has involved working closely with the Bureau of Meteorology to implement dynamic meteorology updates in a way that minimises their data transfer costs. The Bureau have expressed their intention to implement the Linux-based version of the AWAP as a Tier 3 operational system in the second half of this year, with funding provided by ABARES. In parallel activity, systems development work with the Bureau towards a NetCDF version of the AWAP meteorology archive has been completed. The system has been implemented at the Bureau of Meteorology.

### ***AWAP data services***

With the support of SEACI, the community of AWAP users has continued to grow. The CSIRO AWAP user list currently consists of over 120 people representing 47 government, university, and industry bodies, involving over 90 active, completed, or proposed projects. Three-quarters of these activities involve the use of CSIRO AWAP model products separately or in conjunction with Bureau of Meteorology AWAP meteorology.

## **Additional objective**

### **Modelling statistical climate-hydrology relationships using Australian Water Availability Project gridded data**

In the work reported here, linear (correlation-based) and regression tree (CART and random-forest) analyses were used to explore the relationship between spring rainfall in the MDB and indices of large-scale modes of climate variability in preceding months. The goal was to evaluate the relative skill levels, noise properties and other attributes of these two modelling approaches for predicting spring MDB rainfall from antecedent climate indices.

#### ***Correlation matrices between MDB rainfall and climate indices***

Figure 37 shows the correlation matrix (at zero time lag) between several climate indices and rainfall in the whole MDB in spring (September, October, November). The climate indices are: (1) Niño 3.4 (n34), an index of the ENSO (El Niño – Southern Oscillation) climate mode in the equatorial Pacific Ocean, derived from sea-surface temperatures in the central equatorial Pacific Ocean; (2) the Indian Ocean Dipole Mode Index (dmi), a comparable index for tropical modes in the Indian Ocean; (3) the sub-tropical ridge intensity (stri), an index of the intensity of the sub-tropical ridge over southern Australia; (4) the Tripole Index (tpi), a combined Pacific-Indian Ocean index reflecting the difference between SSTs north of Australia and the mean of central Pacific and central Indian equatorial SSTs; and (5) the ENSO Modoki Index (emi), a Pacific Ocean index reflecting north-south variations in SSTs near the equator.

In Figure 37, signs and magnitudes of correlation coefficients are indicated by colours, colour densities and sizes of circles. The indices giving the strongest zero-lag correlation with MDB spring rainfall are Niño 3.4, the Tripole Index and the ENSO Modoki index.

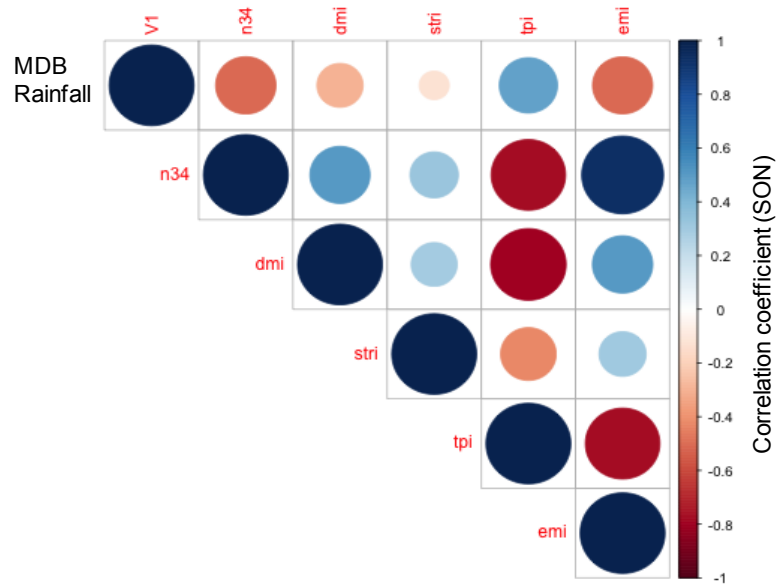


Figure 37. Correlation matrix (at zero time lag) between spring (September, October, November, SON) rainfall in the whole MDB and several climate indices: Niño 3.4 (n34), Indian Ocean Dipole Mode Index (dmi), sub-tropical ridge intensity (stri), Tripole Index (tpi) and ENSO Modoki Index (emi). Signs and magnitudes of correlation coefficients are indicated by colours, colour densities and sizes of circles

### Predictions of Murray–Darling Basin spring rainfall with random forests

In CSIRO (2011), CART (Classification and Regression Tree) methods were applied to obtain predicted MDB spring rainfall from antecedent climate indices. Skill scores of order 0.6–0.7 were obtained at forecast time intervals from 0 to 6 months. Subsequent work found that these scores were unrealistically high, because a single tree model constructed with the full dataset is prone to over-fitting. Such models have utility for diagnosis of relationships between rainfall and climate indices (e.g. Whan et al., in press), but care is needed in predictive applications to avoid over-fitting.

Several methods were tried to decrease over-fitting, based on various schemes for bootstrapping tree-based models (construction of models using randomly selected subsets of the total data set as training data, with testing against remaining data). A satisfactory solution was found to be the ‘random-forest’ method, a tree-based modelling approach that formalises this principle and also uses additional measures to reduce noise in the model (tree-based models being notoriously noisy).

A random-forest model was constructed to predict whether spring MDB rainfall will fall into ‘wet’, ‘medium’ and ‘dry’ terciles, each encompassing one-third of the rainfall probability distribution, on the basis of five antecedent climate indices (n34, dmi, stri, tpi, emi), observed from one to six months ahead, as predictor variables. This classification problem was used as a test case because tree-based methods are better suited to classification than prediction of continuous variables.

The skill of the random-forest model was compared with the skill of a linear-regression model in performing the same classification prediction with the same five climate indices as predictor variables. To do this, the output from the best-fit continuous linear-regression model (using a subset of the full data as training data) was reduced to categorical predictions of wet, medium and dry rainfall terciles.

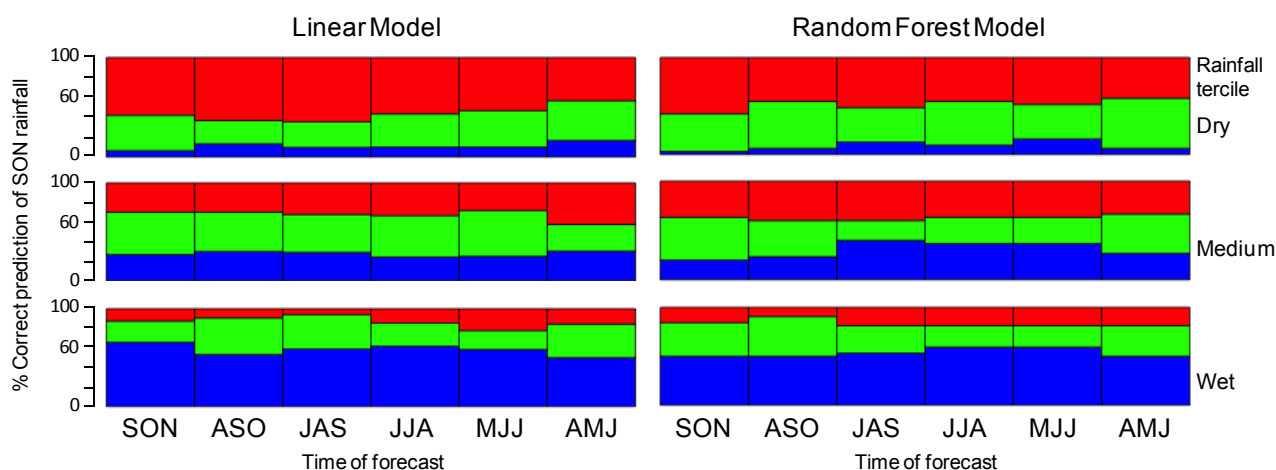


Figure 38. Comparison of the skill of linear-regression model (left) and random-forest model (right) in predicting whether spring (September, October, November, SON) rainfall in the MDB will fall into wet, medium and dry terciles, using 5 climate indices as predictor variables with forecast lead times from zero (nowcast) to 6 months. Each colour block represents the fraction of a test data set predicted by the model to be wet (blue), medium (green) or dry (red), when the true outcome (known from the test data) is respectively wet (lower band), medium (middle band) and dry (upper band). A prediction with 100% skill would appear as a completely blue lower band, a completely green middle band and a completely red upper band

Figure 38 compares the skill levels of the two kinds of model. Each colour block (blue-green-red) represents the fraction of a test data set predicted by the model to be wet (blue), medium (green) or dry (red), when the true outcome (known from the test data) is respectively wet (lower band), medium (middle band) and dry (upper band). A prediction with 100% skill would appear as a completely blue lower band, a completely green middle band and a completely red upper band.

The linear-regression model has a skill level of around 60 percent in 'now-casting' (forecasting at zero lead time) the dry and wet terciles of MDB rainfall from climate indices. The skill level for the medium tercile is lower because misclassification is likely in either direction. The skill of the linear-regression model for dry and wet terciles falls by 10 to 20 percent as the forecast lead time increases to 6 months.

For the random-forest model, skill levels are comparable with the linear-regression model but tend to be a little lower (by around 5 percent on average). The expected trend for skill levels to decrease with increasing forecast lead time is less evident for the random-forest than the linear-regression model.

We conclude from this analysis that tree-based (random-forest) methods and linear-regression methods have comparable skill at forecasting categories of MDB spring rainfall from antecedent climate indices, when proper care is taken to avoid over-fitting and when both methods are applied to the same test problem.

## Conclusions

- As assessed with BIOS2, the sensitivity of SEACI region mean outflow to mean rainfall (the gain of the rainfall-runoff amplifier) is  $2.9 \pm 0.2$  (1 standard deviation), implying that mean outflow decreases by 29 percent for each 10 percent decrease in mean rainfall (with all else constant).
- As assessed with BIOS2, the sensitivity of SEACI region mean outflow to temperature is  $-0.05 \pm 0.01 \text{ } ^\circ\text{C}^{-1}$ . This value accounts for covariation of humidity with temperature. The implication is that aggregated SEACI outflow decreases by 5 percent with each degree rise in temperature.

- The sensitivity of outflow to temperature is dominated by the sensitivity of transpiration to temperature, not the sensitivity of soil evaporation to temperature.
- Our model-based (BIOS2) determinations of the sensitivities of outflow to rainfall and temperature are in fair agreement with empirical determinations of the same sensitivities from SEACI2 Project 2.2 (where sensitivities were determined empirically using responses to natural variability in rainfall and temperature).
- The sensitivity of SEACI region outflow to CO<sub>2</sub> concentration is  $0.0009 \pm 0.0003 \text{ ppm}^{-1}$ . This implies that a 100 ppm CO<sub>2</sub> increase would increase outflow by about 9 percent.
- We combined the above sensitivities with estimates of likely changes out to 2050 in the major driving variables acting on outflow. The following picture emerged: there are three major contributors to likely long-term reductions in outflow. The largest single contributor is decreased precipitation, with 5 percent reduction in mean precipitation leading to a reduction of 15 percent in outflow. Second, increased temperature, with a warming of 1 °C, leads to an additional decrease in outflow of 5 percent. Third, the response to CO<sub>2</sub> (a likely increase 100 ppm) causes a 9 percent increase in outflow. Changes in other variables (radiation, wind, leaf area index) have much smaller likely effects. Combining the effects of the three dominant driving variables, the resulting implication for SEACI region outflow is a decrease of 11 percent, somewhat less than the decrease due to precipitation alone.
- Linear-regression and tree-based (random-forest) analyses have been used to explore the relationship between spring rainfall in the MDB and indices of large-scale modes of climate variability in preceding months. These two approaches have comparable skill at forecasting categories of MDB spring rainfall from antecedent climate indices, when proper care is taken to avoid over-fitting and when both methods are applied to the same test problem.
- The availability of AWAP model products to the wider community continues to pay dividends for SEACI. A notable example is the paper by Webb et al. (2012) which found the signature of climate change in wine grape ripening driven by warming and declines in soil moisture, particularly in south-eastern Australia.

## Links to other projects

We have illustrated the linkage with Project 2.2 in Figure 32, by comparing the sensitivities of outflow to precipitation and to temperature ( $\eta(Q,P)$   $\eta(Q,T)$ ) estimated from this work and from SEACI Project 2.2, where sensitivities were determined empirically using responses to natural variability in rainfall and temperature.

## CHAPTER 4: PROJECT 2.1

### Climate change projections

Dewi Kirono, Jin Teng, David Kent, Francis Chiew, Marie Ekstrom (CSIRO)

Bertrand Timbal, Yang Wang and Alex Evans (BoM)

## Abstract

Estimating future streamflow under a changed climate involves three main components: global climate modelling; downscaling; and hydrological modelling. The research in Project 2.1 builds on results from previous SEACI studies to improve global climate model (GCM) assessment and selection for hydrological applications (conducted through Activity 1) and to identify the most suitable downscaling method(s) for hydrological modelling in south-eastern Australia (conducted through Activity 2).

Research in Activity 1 showed that:

- Overall, the CMIP3 global climate models (used in the IPCC Fourth Assessment Report) are much better at simulating regional coarse-scale rainfall (and climate variables) than large-scale climate-ocean predictors/indices affecting south-eastern Australia rainfall and their relationship with rainfall. Among the indices investigated in this study, the mean seasonal ENSO index was best represented. None of the 25 models are consistently better than all the other models for all measures, but there are a couple of models that consistently perform poorly against most of the measures.
- Practically all the CMIP3 models project a decline in future rainfall (particularly cool season rainfall) across the SEACI region. The median rainfall projection is dependent on which measure is used to select or weight the better models. However, using the best models or putting more weight on the better models does not reduce the range of projections. Therefore, for now, climate change projections for hydrological application are probably best developed using all available CMIP3 models (apart from perhaps excluding the consistently poor models). The framework developed here can be easily used to assess the CMIP5 models (will be used in the IPCC Fifth Assessment Report) when they become fully available in 2013 and this will provide further insights.
- Simulations from the next generation of Australian global climate models (CSIRO-MK3.6 and ACCESS) represent the annual mean state of SEA rainfall (and climate) well, but their performance on variability and trend is not as strong. The projections and the range of results are relatively similar to the previous CSIRO models. The CSIRO-MK3.6 and ACCESS models also project a decline in future rainfall, but there is significant variability in the projections from the single (CSIRO-MK3.6) model (for example, the CSIRO-MK3.0 and CSIRO-MK3.5 runs fall within the bounds of the CSIRO-MK3.6 ensemble).

Research in Activity 2 showed that:

- The analogue downscaling and Weather Research and Forecasting (WRF) dynamic downscaling model can provide finer resolution projections of changes to seasonal and annual rainfall than the projections from coarse-scale global climate models. Therefore, at the very least, empirical scaling informed by outputs from downscaling models is likely to give more reliable projections of future rainfall than scaling informed by global climate model simulations.
- The daily rainfall sequences from the analogue and WRF models are not sufficiently reliable for direct input into hydrological models. More research is required to improve daily rainfall simulations and to develop and assess methods to bias-correct simulations of predictor variables from global climate models and daily rainfall outputs from downscaling models for hydrological modelling.

- Statistical downscaling models like the non-homogeneous hidden Markov model (NHMM) approach can be directly fitted or calibrated to match the daily rainfall distribution/characteristics important for hydrological modelling. However its use is limited to smaller regions because of the difficulty calibrating to large numbers of points, grid cells or catchments (compared to the direct gridded outputs from analogue downscaling and dynamic downscaling). Other issues arise related to the stochastic generation of multiple ensembles of outputs.

Future research efforts will focus on using CMIP5 GCM simulations (including transient simulations), and integrated consideration of GCMs, downscaling methods and hydrological models, for example, weighting the results from the different combinations of models based on their ability to reproduce historical streamflow characteristics.

## Background

Water resources are vulnerable to climate variability and climate change. Water managers use long historical climate and water data (to characterise hydroclimate variability) and projections of future water availability (to account for climate change impact) to guide water resources planning. Estimating future streamflow under a changed climate involves three main components: global climate modelling; downscaling; and hydrological modelling (Chiew and Prosser, 2011; Chiew et al., 2011) (see Figure 39). Project 2.1 carried out research in the global climate modelling and downscaling areas, while Project 2.2 focused on hydrological modelling. Both projects in Theme 2 were closely related to and used information from the projects in Theme 1.

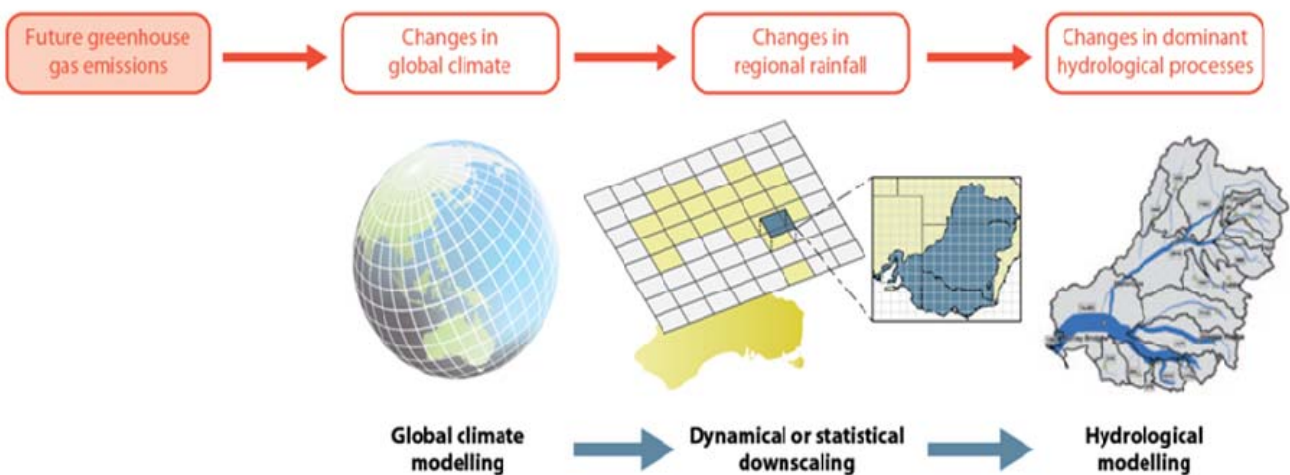


Figure 39. Modelling components for estimating climate change impact on future streamflow with the main sources of uncertainty shown in red

In climate modelling, there is uncertainty around future levels of greenhouse gas (GHG) emissions, how the global climate (in particular global temperature) will respond to the emissions, and how the regional climate will change in a warmer world. To quantify and reduce the uncertainty, SEACI research assessed a range of global climate models results with a view of placing more weight on projections from the better models. This was conducted through Activity 1.

Previous studies used different sets of GCMs and considered many different geographical foci and variables tested, or vastly different approaches. As a result, there is a lack of comparability among studies. This study assessed the GCMs' ability to reproduce observed climate variables and the atmospheric-oceanic drivers affecting rainfall over the SEA region using consistent evaluation skill scores. Such a consistent approach enables comparison of results from a variety of measures in order to develop a robust framework for GCM selection. For example, is there a model which consistently performs better than all the other models for all the measures, and therefore should be favoured in

developing the climate projection? Are rainfall projections based on the CMIP3 models dependent on the measures that the models are assessed against? Is the range of projections reduced when only better models considered?

To support this work, a tool for assessing and exploring GCM performance and projections was developed. The tool was also then used to conduct a preliminary investigation of the new sets of simulation from the IPCC AR5 (i.e. the CSIRO-Mk3.6 and ACCESS models).

Global climate models operate on a very coarse spatial resolution. For example, Victoria is typically represented by less than five grid cells. For regional and catchment hydrological modelling, SEACI research uses statistical and dynamic downscaling models to downscale the coarse resolution global climate model outputs to daily rainfall and other climate variables at the catchment scale. This was conducted through Activity 2.

Previous studies have suggested that although GCMs are generally considered to be the major source of uncertainty in quantifying climate change impacts on hydrology, the uncertainty associated with the choice of a downscaling method can also be significant. Many downscaling studies suggest that there is no single best downscaling model and the optimum model will depend on the application and region (Fowler et al., 2007; Chiew et al., 2010; Frost et al., 2011). To identify the most suitable downscaling method for south-eastern Australia, considerable effort was focused on the comparison of different downscaling techniques for hydrological impact studies across the region.

The simplest form of downscaling involves 'delta-change' or empirical scaling methods. These methods have frequently been used (eg. Chiew et al., 2009) to obtain future climate series to drive calibrated hydrological models to make future predictions. For example, the future climate series used for the current SEACI projections was obtained by scaling the historical daily climate series by the changes in seasonal means and daily precipitation distribution simulated by global climate models, often referred to as the 'daily scaling method' (Chiew et al., 2009). The daily scaling method is simple, therefore can be easily used with many models and global warming scenarios to represent the large range of uncertainty in future climate and water projections over very large regions. The main limitations of this method are (i) it relies on coarse-scale precipitation from GCMs and (ii) it does not consider potential changes to precipitation characteristics other than the seasonal means and daily distribution (that is, it does not consider changes in sequencing as it uses the same historical rainfall sequence to represent the future).

Recognising the limitations of empirical scaling, three additional downscaling methods were compared within this project: analogue statistical downscaling (Timbal et al., 2009), NHMM statistical downscaling (Charles et al., 1999) and dynamical downscaling with the Weather Research and Forecasting (WRF) model (Skamarock et al., 2008). These downscaling methods were assessed based on their ability to reproduce observed daily rainfall characteristics when downscaling from reanalysis data and then used to generate future runoff projections informed by various GCMs and compared with the daily scaling method as a benchmark.

In light of the diversity of the approaches, this activity aimed to explore the merits and limitations of each downscaling method in modelling climate change impact on runoff across south-eastern Australia in order to guide future applications.

# Objectives

The research in Project 2.1 was conducted through two activities.

## **Climate projections in the SEACI region, in the context of GCM assessment and selection**

The objectives were to:

1. Assess the ability of global climate models available in the Coupled Model Intercomparison Project 3 (CMIP3) database to reproduce observed large-scale factors (as identified in Theme 1) and their relationships with SEA rainfall using a consistent approach so that results could be compared.
2. Conduct a preliminary assessment on how the global climate model simulations developed for the IPCC Fifth Assessment Report IPCC (CMIP5) perform, compared to the older generation of the CSIRO's global climate models runs.
3. Explore how model assessment and weighting influence the range of future rainfall projections across SEA.

## **Downscaling for hydrological modelling**

The objectives were to:

1. Assess historical and future daily runoff as modelled using rainfall from the analogue method and compare them against results from the daily scaling method.
2. Assess NHMM statistical downscaling to site, catchment and gridded daily rainfall time series and the modelled runoff using the NHMM downscaled rainfall.
3. Validate the available WRF hindcast runs against AWAP recalibrated rainfall for the SEACI region, and assess the runoff modelled using WRF rainfall.
4. Compare the results from the different downscaling methods, and assess the merits and limitations of the downscaling methods in modelling climate change impact on runoff across south-eastern Australia.

# Activity 1

## **Climate projections in the SEACI region in the context of GCM assessment and selection**

### **Methods**

Twenty-five global climate models available in the CMIP3 database were assessed. Researchers examined the ability of these models to reproduce observed large-scale factors affecting rainfall in SEA (as identified in Theme 1) and their relationship with SEA rainfall. These include the El Niño – Southern Oscillation (ENSO), Indian Ocean Dipole (IOD), Southern Annular Mode (SAM), sub-tropical ridge (STR) and the tropical sea-surface temperature (tropical SST). The ENSO represents the effects of the Pacific Ocean, the IOD represents the Indian Ocean impacts, and the SAM represents the effects of the atmospheric circulation at high latitudes. The tropical SST is an alternative approach that combines key influences on SEA climate from variations in both the Indian and Pacific oceans, and it is represented by the Tripole Index (Timbal and Hendon, 2011).

In this study, the ENSO and IOD modes of variability were diagnosed as the first empirical orthogonal function (EOF) of SSTs over the Pacific and Indian oceans respectively while the SAM is the first EOF mode of mean sea level pressure

(MSLP) over the Southern Ocean (Cai et al., 2009a,b). The Tripole Index was computed as the difference between SST north of Australia (extending from the eastern Indian Ocean and across the Maritime Continent) minus the average of SSTs in two regions – across the central western Indian Ocean and across the central Pacific Ocean (Timbal and Hendon, 2011). The STR derivation followed that of Drosowsky (2005). The modelled climate driver indices from the GCMs were compared to the observations over the period 1950–1999. The observation data for the ENSO, IOD and tripole indices were obtained from the HadISST SST database, and the SAM data were obtained from NCEP-reanalysis MSLP data. Two datasets were used to compare the GCM simulations of STR: the BoM dataset (Drosowsky, 2005) which is based on station data; and the dataset derived from MSLP fields of the NCEP-reanalysis (see also Kent et al. (2011) for a more detailed assessment of the STR simulations). The M-statistic of Watterson (2008), the  $\Delta_{ss}$  of Pierce et al. (2009) and coefficient correlation (R) were used to quantify the ability of each of the GCMs in reproducing the spatial pattern of each of the indices. However, only the M-statistic is shown here. The same skill scores were also used to quantify the GCMs modelled teleconnection; the linear correlation between each of the indices and the SEA rainfall. Examples of observed and modelled spatial pattern of the first EOF and the associated M-statistic value are provided in Figure 40 while those of teleconnection are given in Figure 41. The ability of each model to reproduce the temporal pattern of each index was conducted qualitatively by plotting the time series, developing probability distributions and extracting the power spectrum of the observed and modelled time series (see results in Figure 43).

To examine the implications of selecting or weighting models based on their ability to reproduce historical observed characteristics, the researchers started by ranking the models according to their M-statistic and selected the top five models for a particular variable (e.g. ENSO). Secondly, the researchers calculated the range (10th, median and 90th percentile) of percent change in future mean annual rainfall over the Murray–Darling Basin (MDB) based on all models and based on the top five models (selected based on each variables performance) (see Kirono et al., 2011 for more details).

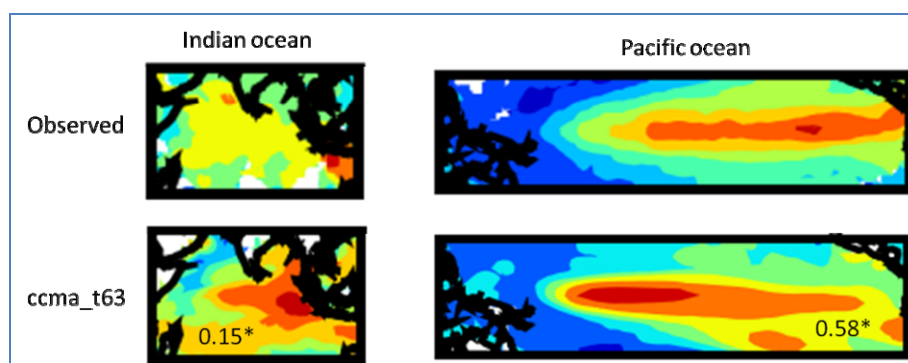


Figure 40. Examples of spatial patterns of the observed (upper panels) and modelled (lower panels) long-term average (1950–1999) of the first empirical orthogonal function (EOF) of annual sea-surface temperature over the Pacific and Indian oceans. The model skill score (M-statistic) is also indicated. An M-statistic of 1 indicates a perfect match between the GCM modelled and observed values and an M-statistic of 0 indicates a very poor match

The researchers also examined the ability of the Australian global climate models (i.e. CSIRO-Mk3.6 and ACCESS) in reproducing key climate variables over SEA, in comparison to the older CSIRO models (i.e. CSIRO-MK3.0 and CSIRO-Mk3.5) runs. Assessment of large-scale indices and their relationship with rainfall is yet to be conducted. The climate variables that were examined included mean sea level pressure (MSLP), air temperature (T) and rainfall (P), particularly for their annual mean climatology, coefficient of variability (CV) and linear trend. They were examined for both a historical period (1950–2000) and a projected period (2006–2100, using the SRESA1B and RCP4.5 experiments). The CSIRO-Mk3.6, in particular, has ten ensemble runs (see also Kent and Kirono, 2012).

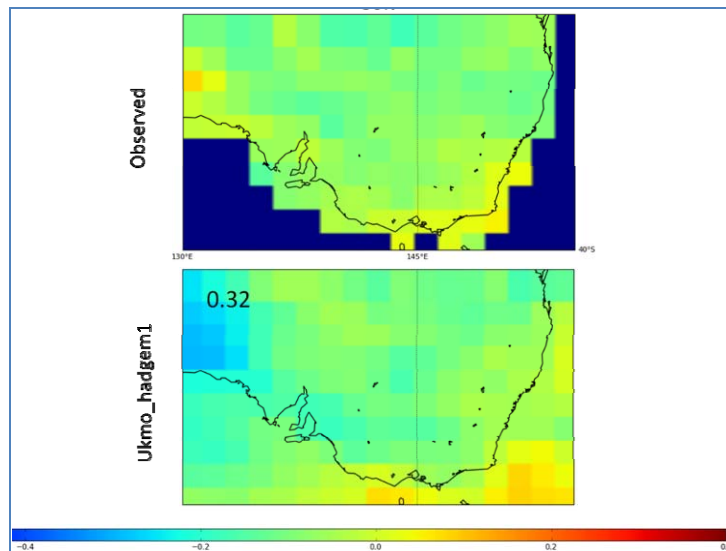


Figure 41. Examples of spatial patterns of the observed and modelled relationship between the spring (September, October, November) ENSO index (NINO3.4) and SEA rainfall. The model skill score (M-statistic) is also indicated

## Results

Figure 42 shows the ability of the GCMs to reproduce the spatial pattern of the observed seasonal Tripole Index. Overall, most GCMs represent the historical spatial mean of the Tripole Index relatively poorly, with an average M-statistic of 0.26. The results for the IOD, SAM and ENSO are not shown here, but in general the GCM representation of the ENSO index was better, while the IOD and SAM were similar to their respective tripole representation. For example, the average M-statistic of all models for the ENSO, IOD, and SAM indices were 0.59, 0.34, and 0.04 respectively. With regard to the GCMs' ability in representing the teleconnection between the seasonal tripole and SEA rainfall, most GCMs have a relatively low M-statistic ( $\leq 0.4$ ). The results for the teleconnection between ENSO, IOD, and/or SAM with the SEA rainfall were relatively similar to this (not shown here). Overall, there seems to be no single model that is consistently good across all the examined climate drivers, and their teleconnection with rainfall. For example, the MRI-CGCM2.3's averaged M-statistic for seasonal ENSO, IOD, SAM and tripole are 0.64, 0.36, 0.05 and 0.55, respectively while the GISS-AOM's are 0.20, 0.46, 0.06 and 0.14, respectively. Figure 43 also indicates that even though MRI-CGCM2.3 can reproduce the long-term mean of spatial pattern ENSO relatively well, the model poorly replicates the observed temporal characteristics of the ENSO index (results for other indices are not shown here, but they suggest relatively similar results). The GISS-AOM, on the other hand, shows poor performance in both the long-term mean as well as the temporal characteristic of ENSO index. All of these results suggest that identifying/rejecting models which are consistently poor might be more feasible than selecting those which are consistently good across examined variables.

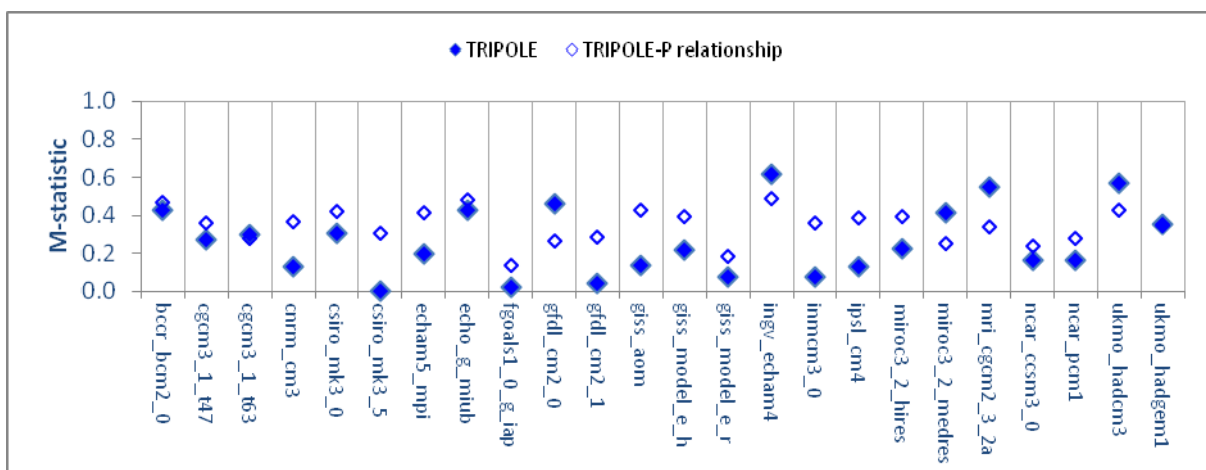


Figure 42. M-Statistic summarising the GCMs' ability to simulate the observed spatial pattern of mean seasonal Tripole Index and Tripole Index-SEA rainfall relationship for 1950–1999

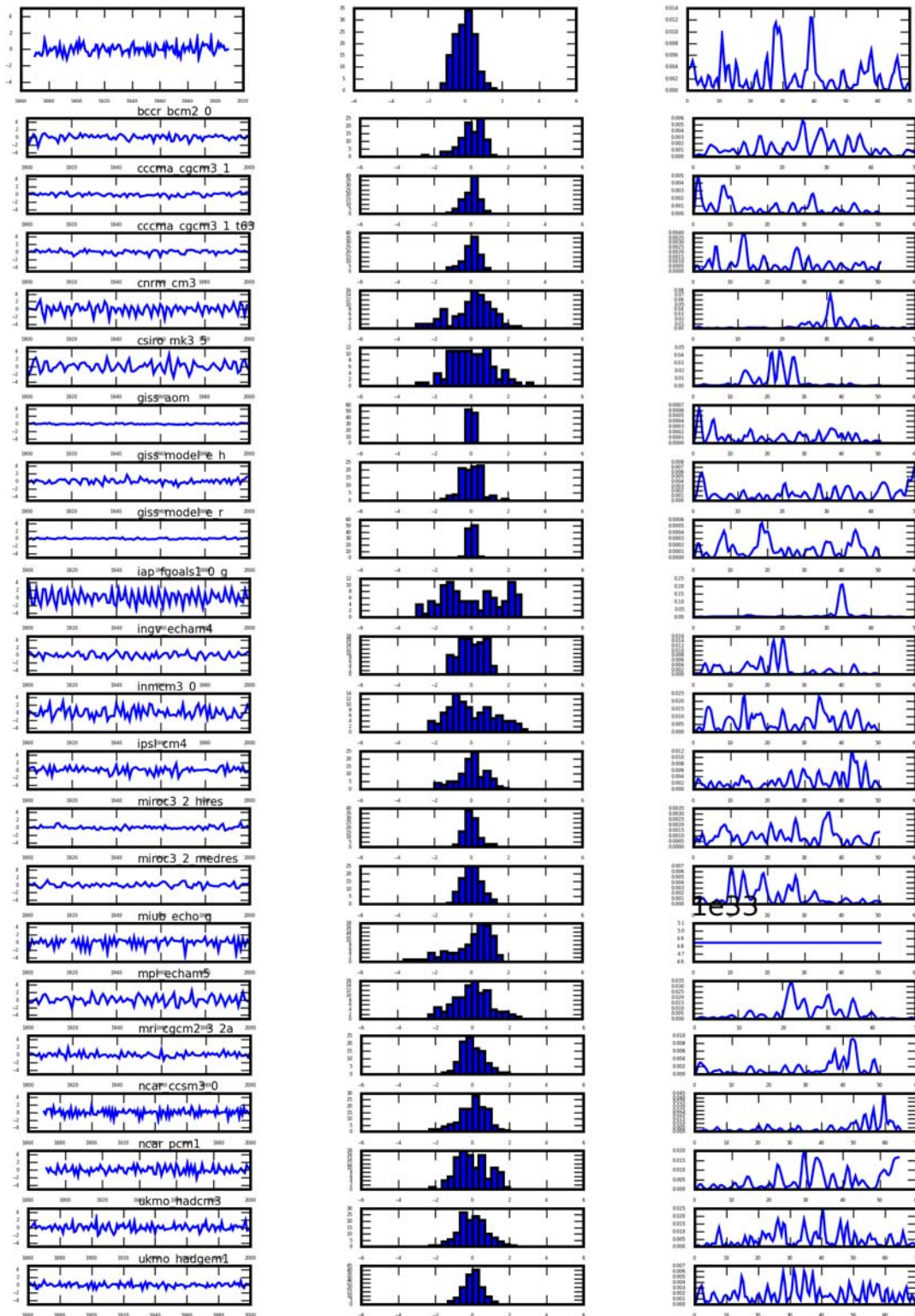


Figure 43. Observed and modelled temporal pattern of winter (June, July, August) ENSO index (Left: variability during 1860 to 2020. Middle: histogram of the time series. Right: power spectrum)

Figure 44 summarises the M-statistic of the 25 CMIP3 models' ability to reproduce the observed historical (1961–2000) climate across SEA, the atmospheric-oceanic drivers that affect rainfall in SEA and the correlation between their

indices and SEA rainfall. Overall, the CMIP3 models appear to be better at simulating the regional coarse-scale rainfall (and climate) than the atmospheric-oceanic drivers indices and their relationship with SEA rainfall.

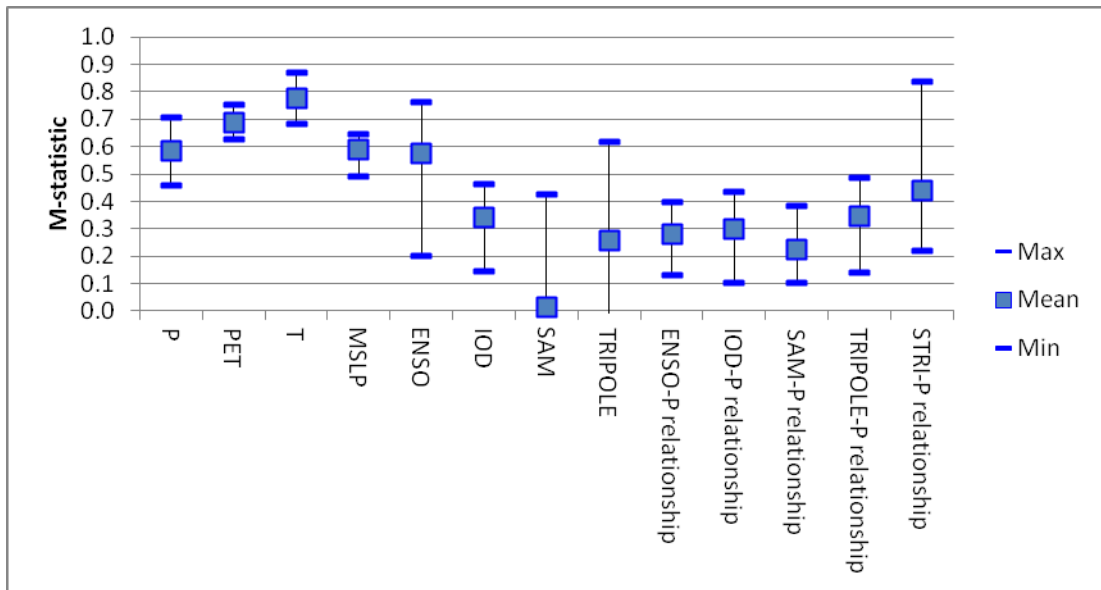


Figure 44. Range of M-statistic summarising the 25 CMIP3-GCMs ability to simulate the observed historical (1961–2000) characteristics

Figure 45 shows projected changes in annual rainfall per degree of global warming based on different sets of models (selected based on each variable’s performance). The plots indicate that:

- (i) the median estimate in all considerations indicates that future mean annual rainfall will decrease by about 5 percent for a 1 °C global warming, with models selected based on their ability to simulate ENSO and IOD indicating slightly less drying;
- (ii) there is no clear difference in the range of future rainfall projections among different considerations. The range of rainfall projections (i.e. the 90th minus 10th values) for most of the considerations is about 10 percent (for 1 °C global warming).

The same experiment, but with the best ten models selected instead of the best five models, also indicated similar results (not shown here).

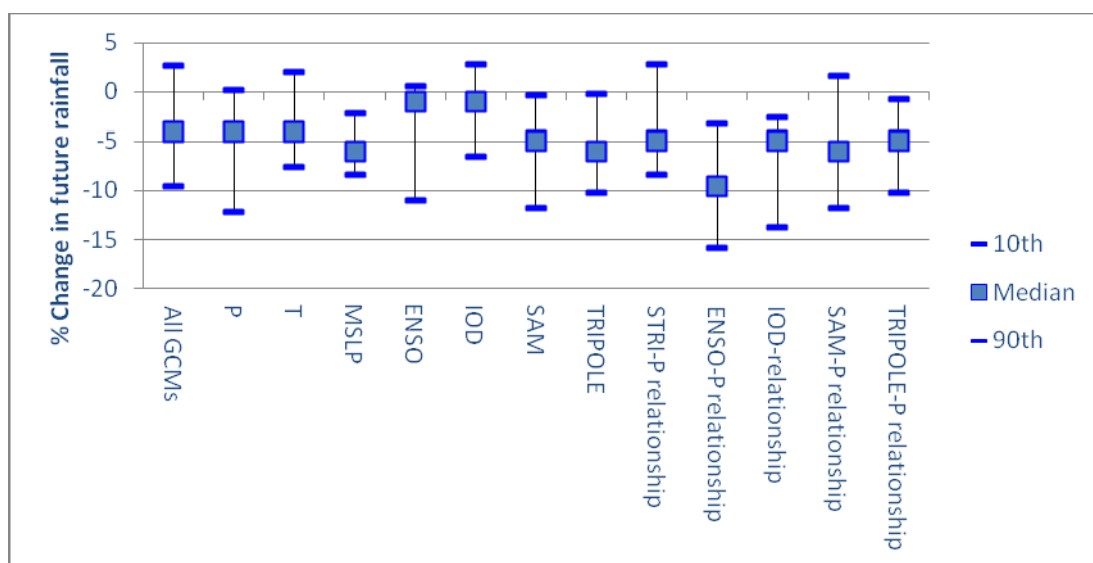


Figure 45. Range of projected change in mean annual precipitation averaged across the Murray–Darling Basin for a 1 °C global warming based on all 24 GCMs (first column) and based on the best five GCMs assessed against the different measures (columns 2 to 10)

The mean annual climate variables modelled by the new CSIRO-MK3.6 and ACCESS are shown in Figure 46, together with the observations and modelled results from the CSIRO-MK3.0 and CSIRO-MK3.5 models. Figure 47 shows two skill metrics (M-statistic and  $\Delta_{SS}$ ) for the rainfall climatology, coefficient of variation (CV) and linear trend. All four model configurations reproduce the annual mean rainfall reasonably well (M-statistic > 0.78 and  $\Delta_{SS}$  < 0.5), with CSIRO-MK3.6 showing the lowest skill. As identified previously (CSIRO, 2011), the models are less capable of simulating the inter-annual rainfall variability and trend. The CSIRO-Mk3.6 ensemble shows that the variability between the models is of similar order as the variability inherent to the model.

Figure 48 shows the spatial pattern of change in rainfall along with box-plots of the distribution of those spatial changes. All results indicate a decline in future rainfall. There is a wide range of results among the CSIRO-Mk3.6 models, with the CSIRO-MK3.0 and CSIRO-MK3.5 runs falling within this range.

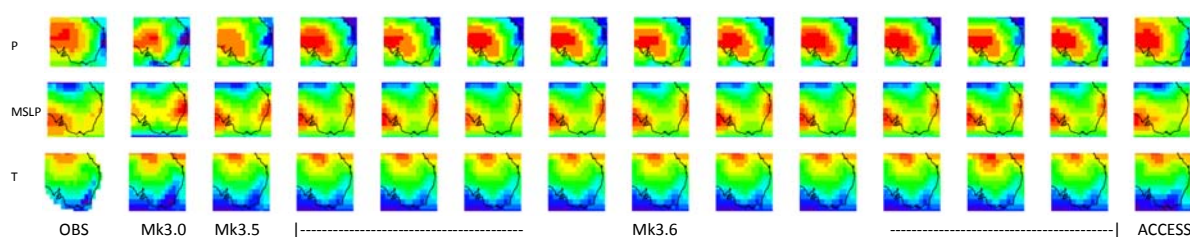


Figure 46. Annual mean rainfall, mean sea level pressure and temperature in each model along with the observed pattern for 1950–2000

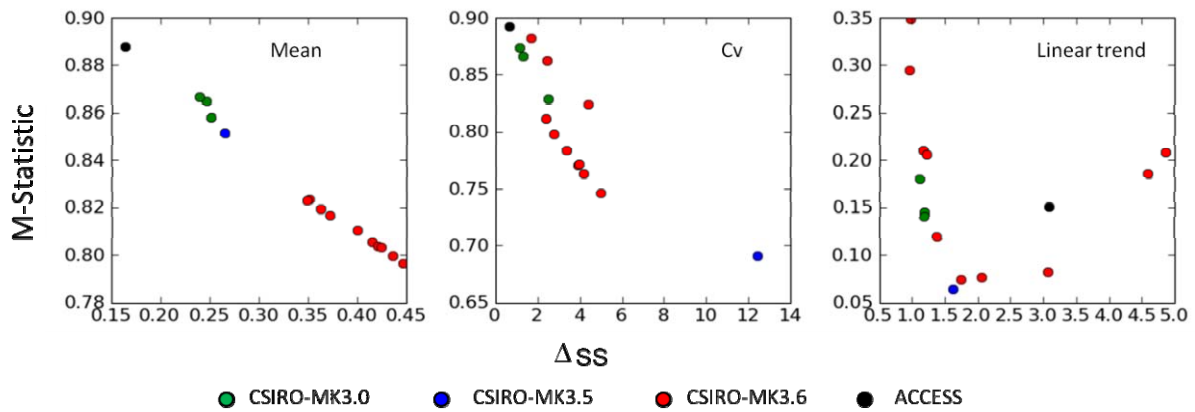


Figure 47. M-statistic and  $\Delta_{SS}$  skill scores for the mean annual rainfall, coefficient of variation of annual rainfall (CV), and linear trend of the annual rainfall simulated by each model for 1950–2000. Higher M-statistic and lower  $\Delta_{SS}$  indicate better performance

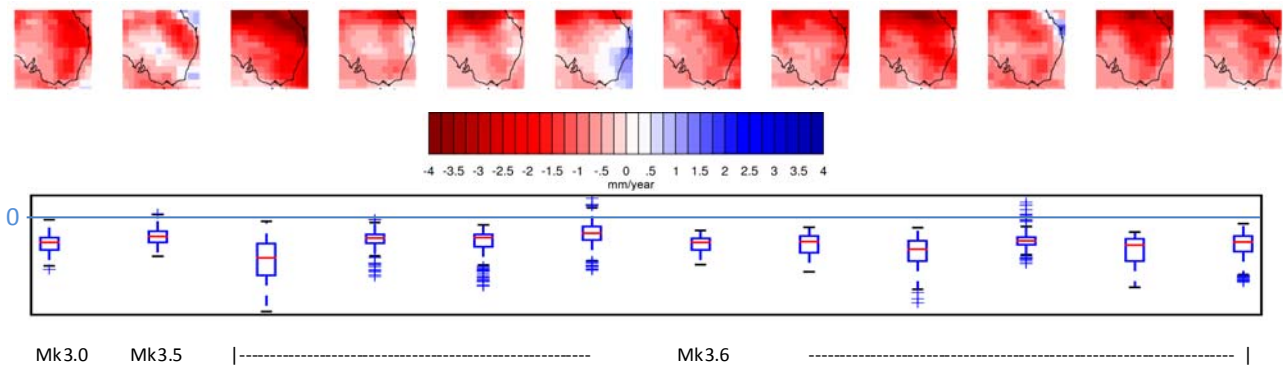


Figure 48. The projected 21st century change in rainfall over eastern Australia for each model (bottom) along with the spatial distribution of the projected changes (top)

## Activity 2

### Downscaling for hydrological modelling

#### Methods

The modelling experiments are illustrated in the flowchart in Figure 49. To assess how well the downscaling methods model climate change impact on hydrology, it is important to verify the ability of these methods in reproducing observed rainfall because the simulation of regional climate change is strongly dependent on the simulation of present conditions. Therefore, the techniques were first tested by evaluating their skills in reproducing observed rainfall characteristics for hydrological purposes during optimisation phase using the NCEP/NCAR (NNR) reanalysis dataset (Kalnay et al., 1996) (comparison 1 in Figure 49). The simulated and observed rainfall datasets were compared using a number of metrics representing characteristics of rainfall that are important for hydrological modelling, such as: seasonal and annual rainfall totals, high extremes, and number of days below selected thresholds. Then the runoff modelled by the Sacramento rainfall-runoff model using the downscaled rainfall was evaluated against the runoff modelled using observed rainfall (comparison 2 in Figure 49). After this, the same steps were repeated to evaluate the downscaling methods in application phase using CMIP3 GCM historical (20C3M) outputs (comparison 3 and 4 in

Figure 49). Lastly, the modelled changes in future rainfall and runoff were compared with the changes modelled using daily scaling method (comparison 5 and 6 in Figure 49). The description of the modelling components (shaded in grey in Figure 49) is provided below. At the time of writing, all the comparisons have been conducted for the analogue method while comparisons at points 3 to 6 (Figure 49) are still being carried out for NHMM and WRF.

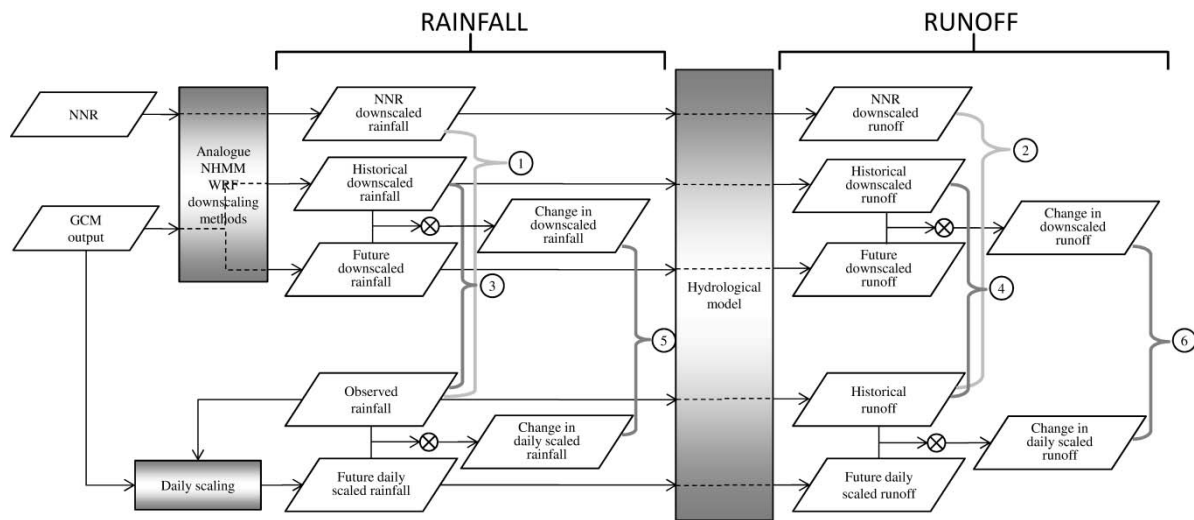


Figure 49. Flowchart showing modelling experiments. The modelling components are shaded in grey. Circles with crosses indicate calculated differences; numbered circles indicate points of comparison as referred to in the text

### Analogue downscaling method

The analogue downscaling is based on the premise that regional climate is conditioned by two factors: the large-scale climatic state and local physiographic features (Timbal et al., 2009). It derives regional or local climate information in three steps:

- (i) define a weather-state for each day using selected large-scale climate variables (or ‘predictors’) for a certain geographical domain;
- (ii) select the most similar weather-state (analogue) from the reference dataset to match the model simulated weather states for that day;
- (iii) associate the best matching analogue with the local variables (or ‘predictands’) observed on the same day.

Although the method has been used on several predictands, only rainfall was used here. Potential evapotranspiration (PET) was also used in this study but is not available from the analogue downscaling method at present. The analogue method was optimised using NNR and observations then applied using GCM simulations to provide historical and future rainfall projections across the whole SEACI region.

### NHMM statistical downscaling method

The NHMM models multi-site patterns of daily rainfall occurrence and amounts as a finite number of ‘hidden’ (i.e. unobserved) weather states (Hughes et al., 1999; Charles et al., 1999). The temporal evolution of these daily states was modelled as a first order Markov process with state-to-state transition probabilities conditioned on a small number of synoptic-scale atmospheric predictors, such as sea level pressure, geopotential heights, and measures of atmospheric moisture. Previously the NHMM has been applied to downscale site daily rainfall series in south-eastern Australia and has been found to be able to reproduce observed daily rainfall and runoff distributions reasonably well (Chiew et al., 2010; Frost et al., 2011; Fu and Charles, 2011). We explored three ways to apply NHMM to obtain statistically downscaled daily rainfall series for gridded/catchment hydrological modelling across a region in the Murray headwaters (see Figure 50) (Fu et al., submitted):

- (i) The NHMM was used to downscale rainfall to the 28 rainfall stations/sites (i.e. multi-site downscaling to 28 sites) and then post-processed to interpolate to gridded rainfall and accumulated to catchment-average rainfall;
- (ii) The NHMM was used to downscale rainfall directly to the 38 catchment-average rainfalls (i.e., multi-site downscaling to 38 catchments). This not only reduced the numbers of 'sites' for statistical downscaling, but also avoided the errors introduced when interpolating from sites to grid cells;
- (iii) The NHMM was used to downscale rainfall to the 91 0.25° grid cells (i.e., multi-site downscaling to 91 grid cells) and then accumulated to catchment-average rainfall. It is not possible to downscale directly to the 1891 0.05° grid cells because of the very high degree of spatial rainfall correlation between grid cells (Fu et al., 2011a).

The three different catchment-average daily rainfall time series, derived from the three applications of the NHMM, were then used as inputs to a calibrated 'lumped' hydrological model to assess the runoff simulations. The sites, grids and catchments are shown in Figure 50.

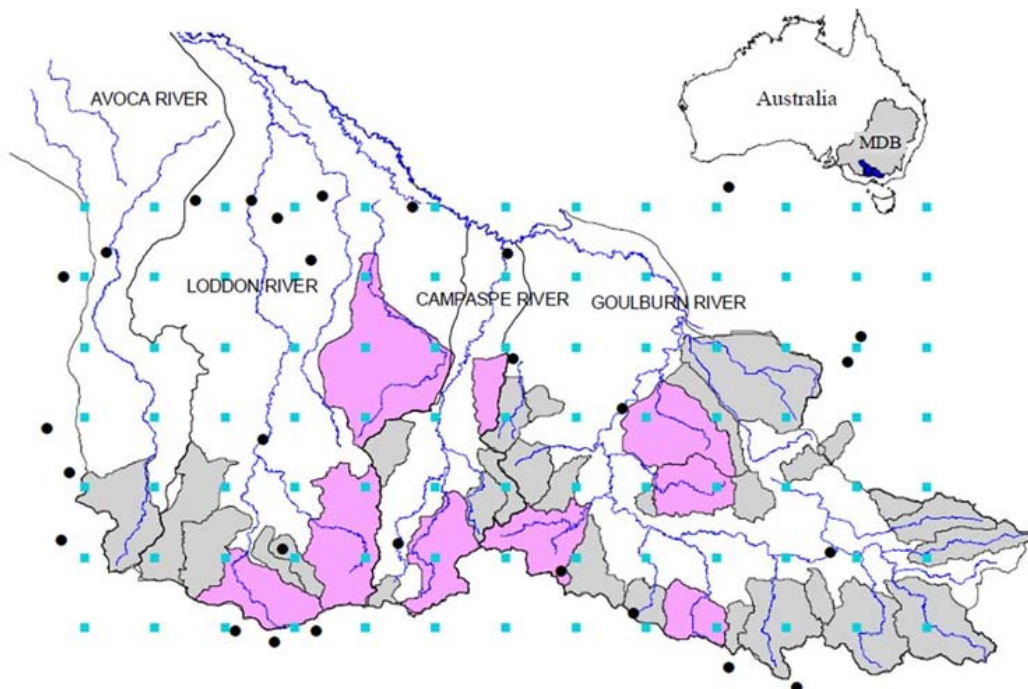


Figure 50. 28 rainfall sites (black circles), 91 grid cells (blue squares), and 38 (nine pink filled catchments are used for hydrological simulations) catchments in the Murray headwaters used for NHMM downscaling (Fu et al., submitted.)

### **WRF dynamical downscaling method**

There is an ongoing study as part of the NSW/ACT Regional Climate Modelling project (NARClIM, Evans, 2011) whose WRF hindcast runs (Evans and McCabe, 2010) are available for SEACI researchers to conduct a comparison against those from other downscaling methods. The Weather Research and Forecasting (WRF) model is a numerical weather prediction (NWP) and atmospheric simulation system which can be used to downscale climate variables from GCMs dynamically. It is a high resolution climate model run over the region of interest using the boundary conditions provided by a GCM. The core components of WRF consist of a dynamics solver and various physics schemes. During 2010–2011, 36 different combinations of physics schemes of WRF were used to simulate four different storm events over south-eastern Australia. Based on these investigations it was possible to identify schemes that performed better than others, in terms of simulating magnitude and position of rainfall and the magnitude of mass and temperature fields. These experiments were reported in Evans et al. (2011). In 2011–2012, further experiments were carried out within the NSW/ACT Regional Climate Modelling project (NARClIM, Evans, 2011). The NARClIM experiments built on

those of Evans et al. (2011) and involved further testing of parameter schemes to identify three physics scheme combinations that i) performed well across south-eastern Australia and ii) represented 'independent' simulations; independent in the sense of distances and positions of ensemble members in the output data space (concept is briefly described in Abramowitz, 2010). Due to the high computational demand of WRF modelling, long-term (60 year) hindcast experiments conducted within the context of the NSW/ACT Regional Climate Modelling (NARClIM) are expected to only become available in June 2012, and climate change experiments with a limited number of GCMs are expected to be completed within the next 12 months. The outputs from these experiments will be used to evaluate WRF for hydrological applications.

### **Hydrological model**

The hydrological model used in this study was the Sacramento lumped conceptual daily rainfall-runoff model (Burnash et al., 1973). The input data to the model are daily rainfall and potential evapotranspiration (PET), and the output is daily runoff. The Sacramento model is widely used by water agencies, research organisations and consultants for local and regional water resources assessments across south-eastern Australia. The gridded modelling at 0.05° spatial resolution was carried out for evaluation of the analogue downscaling method while lumped catchment modelling was conducted for comparison of the three downscaling methods.

The Sacramento model was first calibrated against observed streamflow data and then driven with historical and future climate data with the same optimised parameter values to obtain modelled historical and future runoff. The model was calibrated against 40 years of observed daily streamflow data from 1961 to 2000 in the 232 catchments (including the nine catchments tested with NHMM downscaling method). In the gridded application, the same parameter values were used for all the grid cells within a calibration catchment. The runoff for the other grid cells was modelled using optimised parameter values from the geographically closest grid cell which lay within a calibration catchment (Vaze et al., 2011).

To estimate future runoff, the historical PET was scaled seasonally based on seasonal scaling factors derived from the GCMs. The scaled PET was used with downscaled future rainfall to generate future runoff. As the focus of this study was on changes in future runoff, the use of this simple scaling method to estimate the change in PET was probably sufficient for this purpose as runoff is much less sensitive to changes in PET compared to rainfall.

### **Results**

We found that the analogue method can be used with hydrological models to simulate long-term runoff averages over large regions reasonably well providing a suitable inflation factor is applied (Teng et al., submitted). Without the inflation factor correction, biases are too large for direct input to hydrological models. Even with an appropriate inflation factor, the daily rainfall distribution from the analogue method is not the same as the observed distribution, and this will lead to unreliable simulations of daily runoff characteristics important for many hydrological applications.

Comparing the analogue method and the empirical scaling method on the basis of change in future runoff, averaged across the entire study region, the results are generally similar with a large majority of the GCMs showing a decline in future runoff. In those cases when there are differences, the additional climatic response produced by the analogue method appears to be a consequence of using the atmospheric moisture variable as a predictor in certain regions. Figure 52(a) compares the spatial distribution of projected change in mean annual runoff modelled using rainfall downscaled by the analogue and daily scaling method from 10 GCMs. Figure 52(b) shows the relative difference between the two methods averaged across south-eastern Australia. The range of future rainfall and runoff projections from the analogue method is smaller than that from empirical scaling. This is due to the analogue method using a single relationship between synoptic atmospheric fields and rainfall compared to as many as 10 different parameterisations from the 10 GCMs. These, combined with the fact that the analogue method models future changes at the relevant catchment scale and captures changes to a fuller range of rainfall characteristics, are the advantages of the analogue method. More research is required to confirm this and to improve the daily rainfall series produced by the analogue method for direct input into hydrological models.

This study's preliminary evaluation of three downscaling methods show that the analogue, NHMM and WRF methods are not currently able to reproduce daily rainfall characteristics well enough for direct input into hydrological models. Figure 51, which compares daily runoff distributions for eight catchments modelled using rainfall from the three downscaling methods with the runoff distributions modelled using observed rainfall from SILO (Jeffery et al., 2001), highlights this problem. (Note that the daily scaling methodology by definition reproduces the observed rainfall distribution). For the examples shown in Figure 51, although the analogue downscaled rainfall, after bias correction (i.e. applying an inflation factor), produces a mean annual runoff closest to that from the observations, it overestimates high runoff events. The mean annual runoff modelled using NHMM downscaled rainfall is considerably underestimated (Figure 51). Additionally, the NHMM statistical downscaling model is limited to applications over smaller regions because of difficulty in calibrating the model for rainfall to large numbers of grid cells.

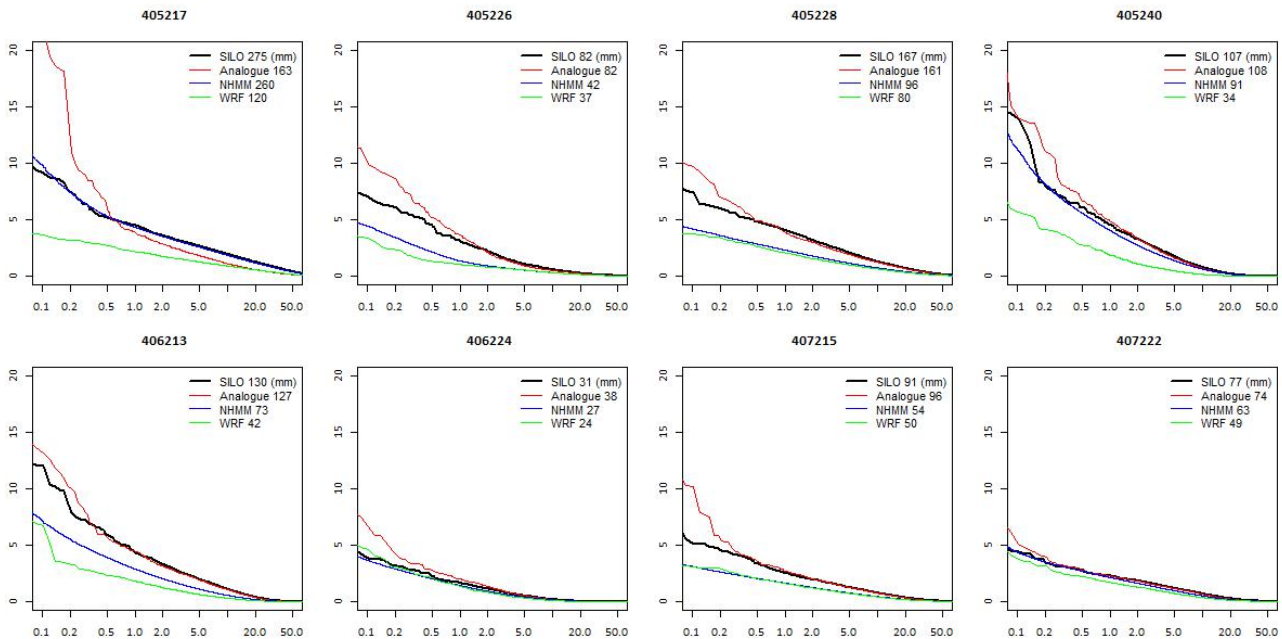


Figure 51. Daily runoff distribution (1985–2000) for eight catchments in the Murray headwaters, with hydrological modelling using daily rainfall from observation (SILO) and analogue, NHMM and WRF downscaling methods. The mean annual runoff from the various methods is shown at the end of the legend label

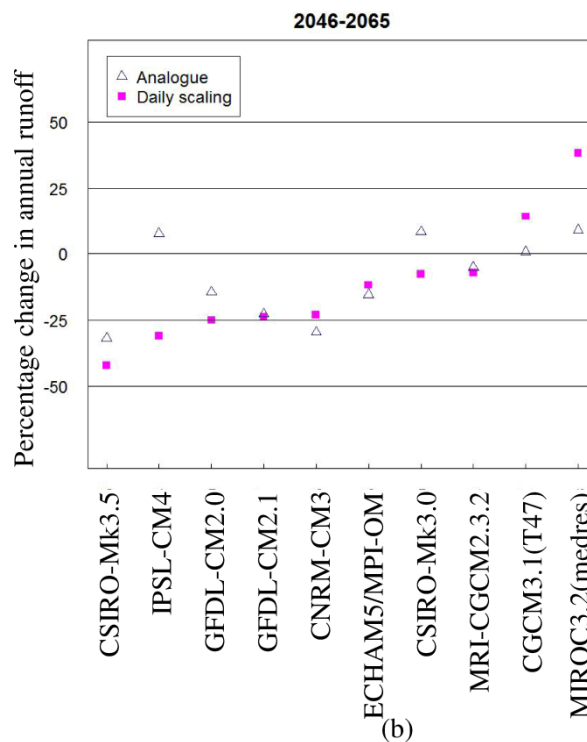
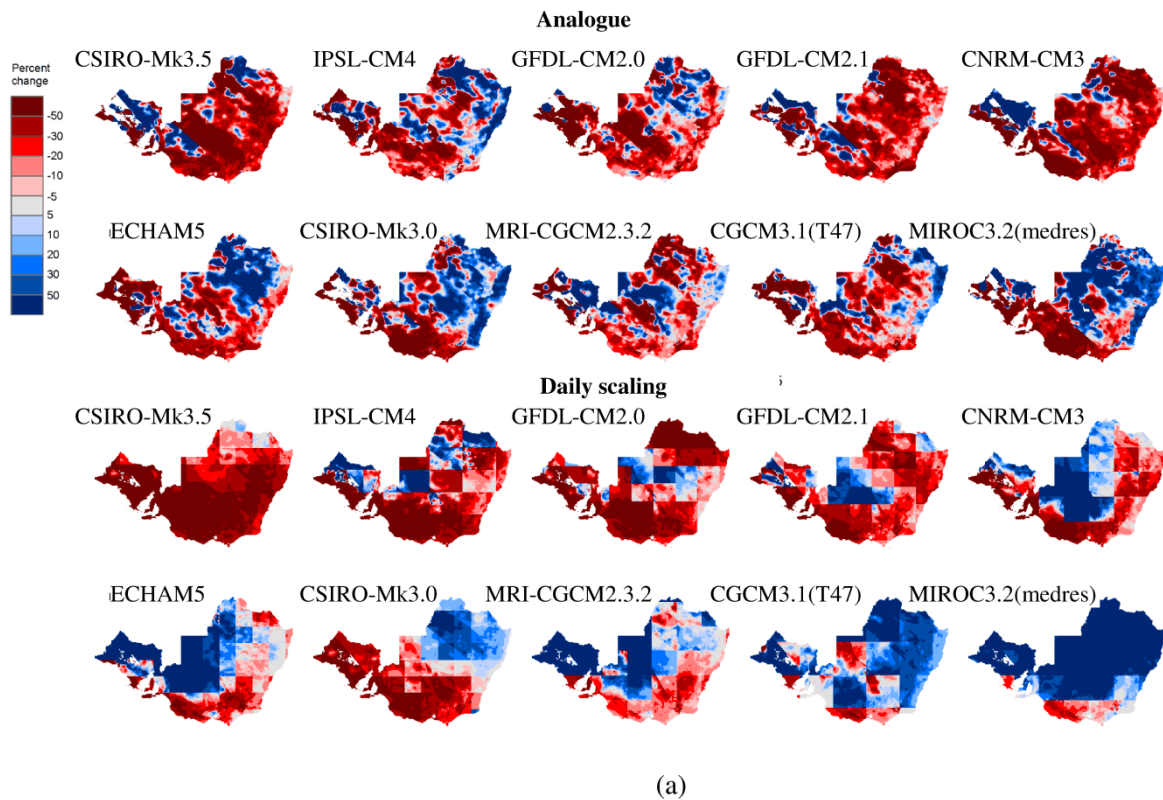


Figure 52. (a) Percentage change in future mean annual runoff for 2046–2065 according to 10 GCMs using the analogue downscaling method (top 10 plots) and the daily scaling (following 10 plots); and (b) percentage change in mean annual runoff averaged across the SEACI region (Teng et al., 2012) modelled using rainfall downscaled from 10 GCMs using the analogue downscaling method (triangles) and the daily scaling method (squares)

# Conclusions

The research activities in Project 2.1 were designed to build on results from SEACI Phase 1, and centred around (i) GCM assessment and selection for hydrological application and (ii) downscaling for hydrological modelling. Outcomes from these activities contribute towards more reliable and updated climate change projections and associated uncertainties for south-eastern Australia.

Activity 1 focused on climate projections in the SEACI region, in the context of GCM assessment and selection. The study showed that:

- Overall, the Intergovernmental Panel on Climate Change Fourth Assessment Report (CMIP3) global climate models appear to be better at simulating regional coarse-scale rainfall (and climate variables) than large-scale factors affecting SEA rainfall and their relationship with rainfall over the region. Among the indices affecting rainfall investigated in this study, the mean seasonal ENSO index is best represented by most models while the other indices are less well represented. None of the 25 models are consistently better than all the other models for all the measures, but there are a couple of models that consistently perform poorly against most measures.
- Practically all the models project a decline in precipitation across the SEACI region. However, rainfall projections based on CMIP3 models are very dependent on the measures that the models are assessed against and weighting the better models does not necessarily reduce the range of projections. Therefore, for now, climate change projections for hydrological application are probably best developed using all available CMIP3 models (apart from perhaps excluding the consistently poor ones).
- The next generation of Australian global climate models' (i.e. CSIRO-MK3.6 and ACCESS) simulations represent the annual mean state of SEA rainfall (and climate) well, but their performance on variability and trend is not as strong. The projections and the range of results are relatively similar to those of the older generation of CSIRO models (i.e. CSIRO-MK3.0 and CSIRO-MK3.5) runs.
- Like their predecessors, the CSIRO-MK3.6 and ACCESS models also suggest a decline in future rainfall across the SEACI region. However, there is a significant amount of variability among the CSIRO-MK3.6 alone, and even the CSIRO-MK3.0 and CSIRO-MK3.5 runs fall within the bounds of the CSIRO-MK3.6 ensemble. Thus, variability within runs for a single model is still a large component of uncertainty in any projections and has potentially large impacts on the magnitude of projections made.

Activity 2 focused on downscaling for hydrological modelling. Preliminary work suggested that:

- The analogue method provides more informative estimates of local rainfall compared to empirical scaling, e.g. less dependency on historical data and potential to provide process understanding in the context of rainfall change in the SEACI region. However, for the purpose of hydrological modelling, further research is required to evaluate the performance of different bias correction methods, with a view to better representing the daily rainfall distribution.
- Although the WRF simulated rainfall distributions are not good enough for direct input to hydrological models, it can produce seasonal means that are much better than what GCMs can provide. Therefore, empirical scaling from the WRF finer resolution downscaled outputs is likely to give better spatially resolved future projections than scaling based on the coarse-scale GCM models. However, this needs to be confirmed with modelling experiments over the SEACI region.
- For detailed modelling over smaller regions, the multi-site NHMM statistical downscaling model can be adjusted to provide gridded or catchment daily rainfall series. However the reason for the underestimation of the mean annual runoff modelled using the NHMM downscaled rainfall needs to be investigated further.
- Future research efforts will focus on using CMIP5 GCM simulations, along with an integrated consideration of GCMs, downscaling methods and hydrological models. This may involve, for example, weighting the results from different combinations of models based on their ability to reproduce historical streamflow characteristics.

## Links to other projects

Project 2.1 is strongly linked to Theme 1 and Project 2.2. The global climate model assessment and selection is carried out in the context of the major drivers for rainfall in SEA identified in Theme 1 and the hydrological modelling in Project 2.2. The more accurate and updated future catchment scale climate series (and associated uncertainties) from Project 2.1 were used to drive the hydrological models in Project 2.2 and elsewhere to improve prediction of climate change impact on future runoff.

## CHAPTER 5: PROJECT 2.2

### Hydroclimate impacts for south-eastern Australia

Nick Potter, Cuan Petheram, Jai Vaze, Warrick Dawes, Jin Teng, Lu Zhang, Arthur Read, Francis Chiew and Bill Wang.

## Abstract

Project 2.2 continued to build on previous studies in SEACI and elsewhere to enhance knowledge of climate-water processes and modelling. There were four activities in Project 2.2 during 2011–2012:

1. Further investigation into empirical methods for estimating the effect of rainfall and temperature on runoff in a changing climate;
2. Analysis and modelling of the rainfall-runoff response during the Millennium drought in south-eastern Australia, in particular elucidating the influence of catchment water storage and surface-groundwater connectivity on runoff and the impact of farm dams on runoff interception;
3. Assessment of the use of different objective functions and calibration periods to improve prediction of the range of streamflow characteristics during dry periods; and
4. Updating runoff projections for south-eastern Australia (SEA) through rainfall-runoff model simulations with improved future climate projections.

Outputs of the first activity indicate that results from empirical regression-based methods for estimating the effect of temperature on runoff are dependent on the spatial scale of the data used. Rainfall and temperature elasticities of runoff were estimated for increasingly larger parts of the Murray–Darling Basin, initially for the wettest part of the basin, and gradually incorporating drier and drier areas. An apparent spatial scaling effect was observed (past a spatial scale of around 100,000 km<sup>2</sup>) where temperature appears to become increasingly more important to runoff generation in larger, drier parts of the MDB. However, Budyko theory, as well as catchment scale estimates of temperature elasticity, suggests that drier regions should have smaller temperature elasticity. In the MDB, runoff generation is highly spatially variable, with most of the runoff coming from wet regions that cover less than 20 percent of the basin. So, climate elasticity of runoff or streamflow should be calculated using data in these regions only; inclusion of dry areas of a large basin can bias elasticity estimates. Rainfall elasticity of runoff appears to be robust to inclusion of dry partial areas, as rainfall and runoff occur in the same regions. In contrast, temperature variability is higher in dry regions due to relatively smaller increases in latent heat flux during dry periods compared to wet regions. This spatial disconnection between areas of runoff and temperature variability can result in biased estimates of temperature elasticity of runoff when temperature data in dry areas of a large basin are included. This is one reason why studies using MDB-averaged temperature show very large effects on runoff from temperature variability. Calculated at a catchment scale, we estimate that of the observed runoff reduction during the Millennium drought, 67 percent was due to reductions in rainfall, 4 percent was due to the higher maximum temperatures associated with this reduced rainfall, and 7 percent was due to a residual temperature increase.

Previous research in SEACI investigated the relative contributions of climatic features of the Millennium drought on runoff generation using rainfall-runoff models (Potter and Chiew, 2011). Reduced mean annual rainfall in the Campaspe river basin accounted for just over half of the runoff reduction, which is slightly smaller than the average effect calculated empirically in Activity 1. Part of this discrepancy is due to differing rainfall effects in wet and dry catchments; also smaller effects from climate variability are encountered starting from a dry baseline, compared to a baseline climate based on average conditions (as the empirically based estimates in Activity 1 show). Changes in

rainfall variability outside monthly and annual time scales accounted for 15 percent of the runoff reduction; changed seasonality of rainfall, predominantly the relatively larger reduction in autumn and winter rainfall, accounted for 11 percent; and increased potential evaporation accounted for 5 percent. The estimated effect from increased temperatures in Activity 1 was approximately double the estimate from increased potential evaporation shown in Potter and Chiew (2011). Activity 1 also showed that temperature increases can result in reductions in runoff larger than any associated effect from increased potential evaporation in wet catchments. Lower groundwater levels and farm dam interceptions also act to reduce runoff, and this was examined in Activity 2.

Results from Activity 2 indicate that runoff production is directly connected to the surface saturation of a catchment. The semi-distributed hydrological modelling shows a non-linear response to surface saturation during extremely dry periods, with rainfall replenishing the near-surface and groundwater stores rather than being converted to runoff. Simulation of runoff occurring from different climate scenarios suggests that, starting from an extremely dry catchment state, the runoff response to rainfall will return to normal or pre-drought condition after 10–20 years of average or above average rainfall. A separate modelling study also shows that adapting conceptual rainfall-runoff models to represent farm dams improved the runoff modelling slightly during the Millennium drought, suggesting a larger proportional influence of farm dams on runoff interception during droughts.

Activity 3 looked at whether calibrating against different objective functions can improve simulation of different characteristics (i.e. high and low flows) of runoff, particularly during dry periods, which are projected to increase in frequency and severity in the future. Previous research in SEACI (Vaze et al., 2010a) showed that calibrated rainfall-runoff models can be used for climate change studies where future mean annual rainfall is not more than around 15 percent drier or 20 percent wetter than the rainfall during the calibration period. For larger differences in rainfall, calibrated rainfall-runoff models can become unreliable. Model performance is generally worse when using a rainfall-runoff model calibrated over a wet period to predict runoff during a dry period. Three different objective functions were defined, namely: (1) one that gives more weight to low flows, (2) one that gives similar weight to all the flows, and (3) one that gives more weight to high and medium flows. Model performance was assessed using Nash-Sutcliffe efficiency (Nash and Sutcliffe, 1970) and bias of daily flows, as well as Nash-Sutcliffe efficiency and bias of low flows. In general, a model calibrated specifically against low flows does not necessarily perform better in simulating low flows for an independent period better than models calibrated against a high flow objective function, although in some cases, calibrating to low flows can give better simulation of low flows in another period, but at the expense of accuracy in modelling high flows. The simulation bias results for the Sacramento model showed that there was no clear under- or overestimation of flows when model parameters calibrated against wet or dry periods were used to simulate streamflow for an independent dry or wet period. The results for one particular model (GR4J) showed a slight overestimation of streamflow when model parameters calibrated against a wet period were used to simulate streamflow for a dry period. Thus bias in runoff (at least during dry periods) appears to be model dependent.

Updated runoff projections for south-eastern Australia were developed in Activity 4. Assessment of the sources of uncertainty indicated that most uncertainty in future runoff projections originates in the outputs from global climate models. However, most of the climate models indicate that the southern Murray–Darling Basin and Victoria will, on average, be drier in the future. All the climate models project a precipitation decline in winter when most of the runoff in this region occurs, translating to a considerable reduction in winter and annual runoff. Averaged over the southern half of the region (south of 33° S), mean annual precipitation is projected to reduce by 0 to 9 percent (median of 4 percent) and mean annual runoff is projected to reduce by 2 to 22 percent (median of 12 percent) for a 1 °C global warming. There is less agreement between the climate models in the north. Averaged over the northern half of the region (north of 33° S), mean annual precipitation is projected to change by –11 percent to +4 percent (median of –3 percent) and mean annual runoff is projected to change by –29 percent to +12 percent (median of –10 percent) for a 1 °C global warming.

# Background

South-eastern Australia has recently experienced a severe and prolonged drought (the Millennium drought), characterised by unprecedented declines in rainfall and runoff. Rainfall and runoff between 1997 and 2008 averaged across the southern Murray–Darling Basin and Victoria were more than 10 percent and more than 35 percent lower respectively than the long-term means. The Millennium drought occurred at the end of a 50 to 60 year trend of increasing temperatures and declining rainfall. However, the magnitude of the effects of changing temperatures on runoff is difficult to assess or quantify, as runoff is much more sensitive to changes in rainfall than other climate variables. The reduction in annual runoff in the southern part of the south-eastern Australia was much greater compared to historical droughts with similar low mean annual rainfall. South-eastern Australia experienced very heavy rainfall during 2010 and 2011, effectively ending the Millennium drought. However, autumn and winter rainfall has not returned to normal conditions (Bureau of Meteorology, 2012; see also Chapter 2: Project 1.1 of this report).

Project 2.2 continued to build on previous studies in SEACI and elsewhere to enhance knowledge on climate-water processes and modelling. The improved climate characterisation and attribution in Theme 1, improved future climate projections in Project 2.1, and improved hydrological models in Project 2.2 will lead to more accurate and updated estimates of climate change impact on catchment water yield and streamflow characteristics and associated uncertainties for south-eastern Australia.

## Objectives

### Activity 1

Finalise investigation of potential changes in the rainfall-temperature-runoff relationship and dominant hydrological processes under drier and warmer conditions.

### Activity 2

Further develop conceptual understanding of change in the rainfall-runoff relationship through the removal of anthropogenic influences and numerical experimental studies using conceptual and physically-based models.

### Activity 3

Investigate how best to adapt hydrological models to represent hydrologic non-stationarity and better simulate the range of streamflow characteristics during dry periods.

### Activity 4

Update runoff projections for SEA through rainfall-runoff model simulations with improved future climate projections.

# Activity 1

## Finalise investigation of potential changes in the rainfall-temperature-runoff relationship and dominant hydrological processes under drier and warmer conditions

There is considerable uncertainty over the effect of increasing air temperatures on water availability in south-eastern Australia. Intuitively, higher (daily maximum) air temperatures for constant annual rainfall should result in increased potential evaporation through an increase in vapour pressure deficit, which should then result in increased actual evapotranspiration and reduced runoff. This intuitive understanding has proved problematic, though, for several reasons:

- The pan evaporation paradox (Roderick et al., 2009a; 2009b), whereby pan evaporation has generally been seen to decline concurrently with increasing air temperatures, shows that the above reasoning may not be correct. This is confounded by the fact that Penman potential evaporation over 1981–2006 also increased slightly in the MDB as a whole, in contrast to the high runoff-producing areas of the MDB, and Australia as a whole (McVicar et al., 2010, Table 3). This can occur in spite of the pan evaporation paradox due to the lower rate of increase in minimum air temperatures compared to maximum temperatures, which could result in an increase of the vapour pressure deficit (Gifford, 2005; McVicar et al., 2010).
- Another factor confounding analysis is that the increasing air temperatures in south-eastern Australia have occurred concurrently with a broad scale decline in rainfall (CSIRO, 2011). Thus the assumption of stationary rainfall and soil moisture patterns underlying the intuitive explanation may also not be valid, as the reductions in rainfall and soil moisture in some parts of SEA have been unprecedented (Potter et al., 2010; CSIRO, 2011; Leblanc et al., 2012).
- Associative or causal relationships between air temperatures and sub-annual or inter-annual rainfall patterns and variability (CSIRO, 2011; Timbal and Drosowsky, 2012) can cause a reduction in the annual runoff coefficient unrelated to the causal mechanism outlined above.
- The response of runoff to changes in potential evaporation is comparatively well understood and embodied in rainfall-runoff and land surface models. However, very large sensitivities of runoff to changes in temperature have been reported recently (e.g. Cai and Cowan, 2008; Yu et al., 2010) and these seem incompatible with any associated effect from potential evaporation alone.

Research in Activity 1 during 2011–2012 sought to develop an improved conceptual understanding of rainfall-temperature-runoff relationships in south-eastern Australia and to provide greater certainty over the effect of increasing temperatures on runoff generation, based on a catchment scale data analysis.

### **Data and methods**

For this activity, we used the same 34 catchments selected during 2010–2011 (CSIRO, 2011). These catchments were selected to have long and relatively complete streamflow records. They all have at least 40 years of complete data, and less than 30 days of missing data in total between 1997 and 2008. The catchments were visually examined using Google Earth in order to rule out any effects from land use changes (forestry, large reservoirs, agriculture or bushfires), although the presence of farm dams is still an issue. Of the 34 catchments, 20 are in the southern Murray–Darling Basin, and 14 are on the northern coast of NSW (Figure 53). The median year at which the streamflow data starts is 1948–1949, and all catchments have data from 1959 onwards. Missing data were infilled using the Sacramento model, although in this activity only annually aggregated data were used.

(a)

(b)

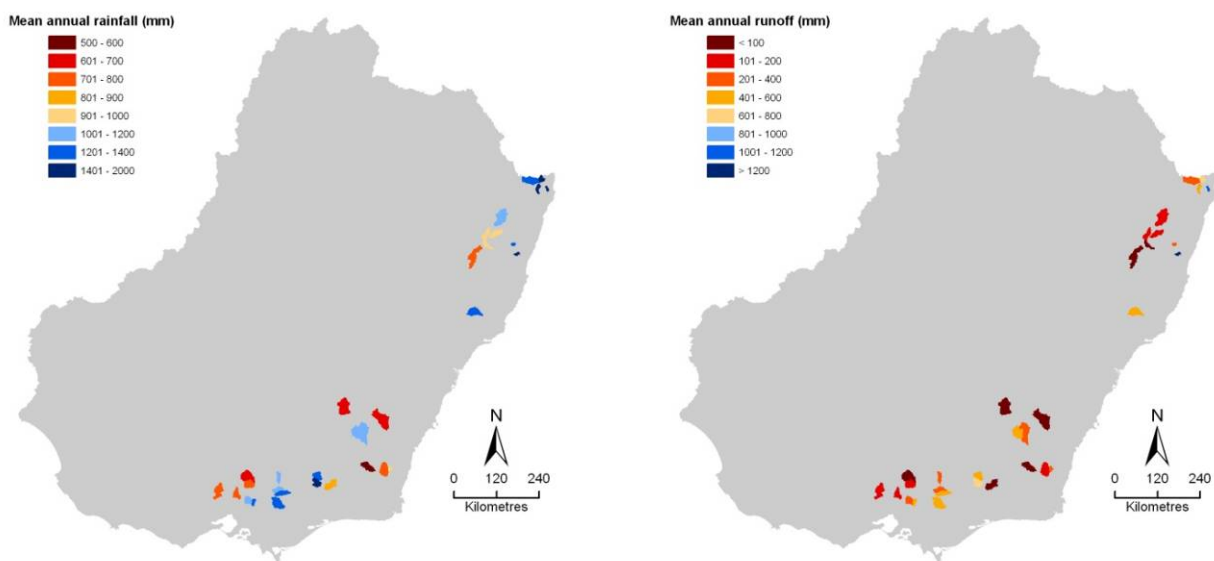


Figure 53. Mean annual rainfall (a) and runoff (b) for 34 study catchments in south-eastern Australia

The elasticities of streamflow and streamflow sensitivities are related quantities, but differ in units of measurement. We define the rainfall elasticity of streamflow,  $\eta_P$ , as the average percentage change in annual streamflow for a percentage change in rainfall, relative to the long-term means. The temperature elasticity of streamflow,  $\eta_T$ , is defined as the average percentage change in annual streamflow for a 1 °C increase in annually averaged maximum temperature. The regression-based approach to estimating elasticities, described below, calculate these in conjunction with variability in the other variable. Streamflow sensitivities are defined somewhat differently. The streamflow sensitivity to rainfall measures the change in streamflow (in mm) for a 1 mm increase in rainfall. The streamflow sensitivity to temperature is defined as the change in streamflow (in mm) for an increase in annually averaged maximum temperature corresponding to a 1 mm increase in potential evaporation, as measured by a regression between annual temperature and potential evaporation time series. In this way, the streamflow sensitivity to temperature can be compared directly to theoretical estimates based on Budyko's curve (e.g. Milly and Dunne, 2002).

The method for calculating the rainfall elasticity of streamflow and the temperature elasticity of streamflow is briefly described here, with further details available elsewhere (Potter et al., 2011; CSIRO, 2011). First, we fit a linear regression between annual percentage change in rainfall, annually averaged maximum temperature anomaly, and streamflow scaled by a Box-Cox transformation with maximum-likelihood parameter. The predicted scaled streamflow values at average rainfall and temperature were then transformed with an unbiased inverse Box-Cox transformation using the plug-in density method. The elasticities  $\eta_P$  and  $\eta_T$  were then calculated by regressing the residual streamflow at average rainfall and temperature values against rainfall and temperature anomalies. The scaling was necessary here because of the non-linear relationship between annual rainfall and annual streamflow; calculating elasticities from a multiple regression of unscaled streamflow can potentially lead to very large temperature elasticities of streamflow due to negative streamflow amounts predicted during dry years. In contrast to previously estimated elasticities (Potter et al., 2011; CSIRO, 2011), the elasticities were calculated on water years rather than calendar years, defined as starting and ending in the two months with lowest mean annual streamflow for each catchment. This is because the coherence of the rainfall-runoff relationship is stronger during a water year (Fu et al., 2011b).

Streamflow sensitivities to rainfall ( $\gamma_P$ ) and temperature ( $\gamma_T$ ) were then calculated according to the following equations:

$$\gamma_P = \eta_P \bar{Q} / \bar{P} \tag{1}$$

$$\gamma_{PET} = \eta_T \bar{Q} / \alpha_{T,PET} \tag{2}$$

The conversion factor denoted  $\alpha_{T,PET}$  is the slope of a regression between annual temperature and annual potential evaporation, with units  $\text{mm } ^\circ\text{C}^{-1}$ .

**Elasticities and sensitivities of runoff to rainfall and temperature**

The rainfall and temperature elasticities of streamflow are shown in Figure 54 with an associated 95 percent confidence interval. The catchments are ordered by increasing catchment aridity (mean annual dryness index). Ranges for the temperature elasticities that are plotted in red are statistically significant. Use of the water year (1 July to 30 June) rather than calendar year resulted in some catchments in northern NSW with predominantly summer-dominant rainfall having relatively larger rainfall elasticities and smaller temperature elasticities. Also, fewer of the temperature elasticities were statistically significant when calculated on water year data (Figure 54). The average of the temperature elasticities was  $-0.074$ , with an interquartile range of  $-0.118$  to  $-0.039$ .

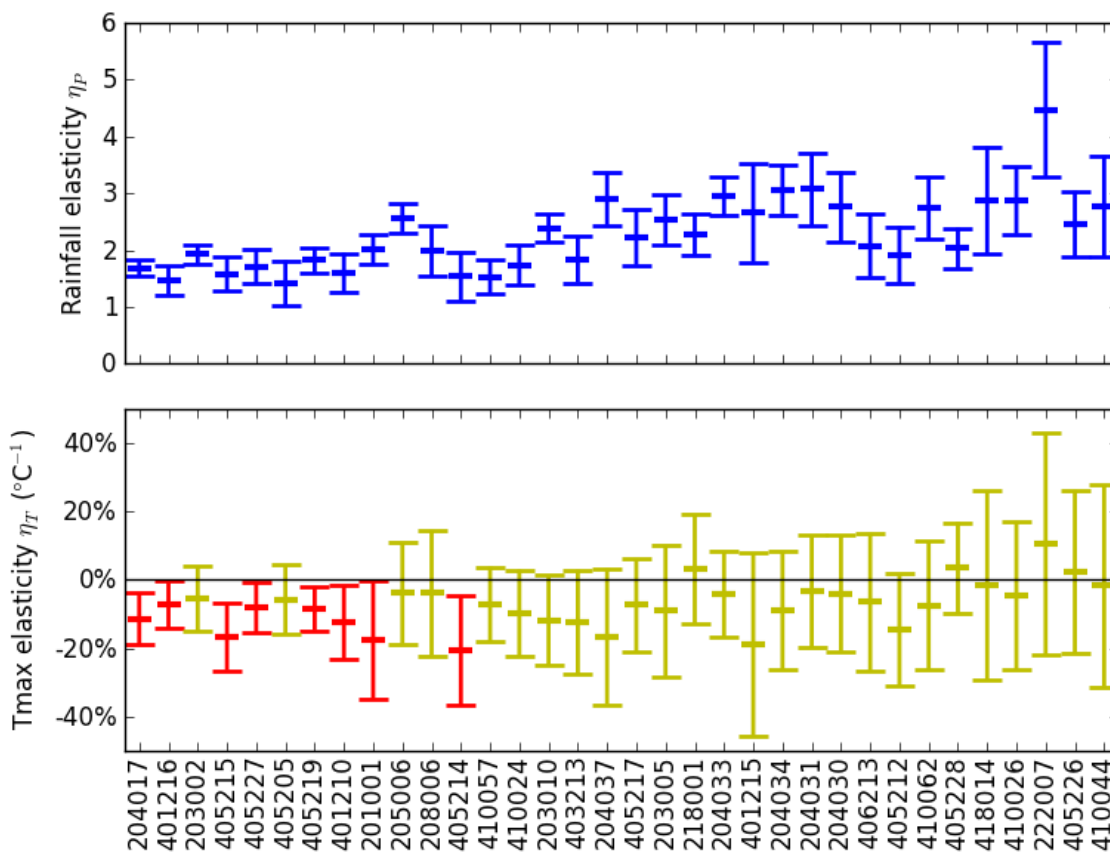


Figure 54. Rainfall elasticities of streamflow (a) and temperature elasticities of streamflow (b) for the 34 catchments in south-eastern Australia

The streamflow sensitivities to rainfall (blue dots in Figure 55) followed the theoretical sensitivity derived from Budyko’s curve (Milly and Dunne, 2002) (blue line in Figure 55). The streamflow sensitivities to temperature (orange and red dots in Figure 55) were close to the Budyko estimates for drier catchments (dryness index greater than one), but much larger than the Budyko estimates for wetter catchments. The Budyko estimates measure the effect on streamflow of changes in potential evaporation only, and so it is likely that the extra sensitivity to temperature was

due to temperature-related changes to rainfall characteristics at sub-annual scales, e.g. the occurrence of different rain-bearing systems during drier years, as well as differences in seasonality and variability of rainfall. Note that statistical significance of the temperature elasticity of rainfall (red values in Figure 54) appears to be related to this extra temperature effect (Figure 55).

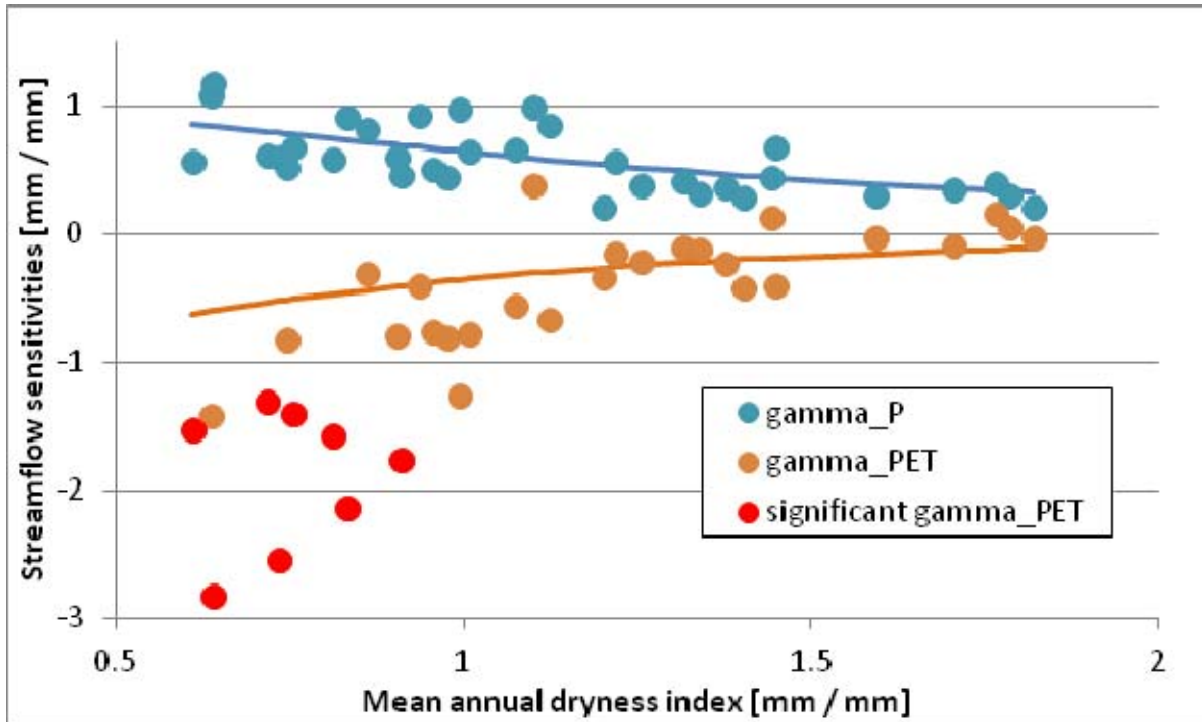


Figure 55. Runoff sensitivities to rainfall and maximum temperature. Note these are expressed as a mm change in annual runoff due to a 1 mm increase in annual rainfall, and a mm change in runoff due to an increase in annually averaged maximum temperature resulting in a 1 mm increase in potential evapotranspiration. X-axis is mean annual dryness index

For each catchment, the observed maximum temperature anomaly was split into two components:

- (i) the expected temperature anomaly, calculated as  $E(\Delta T_{\max} | \delta P_i)$  according to the linear regression:

$$\Delta T_{\max,i} = \beta \delta P_i + \varepsilon_i. \tag{3}$$

This is the temperature anomaly that is expected to occur due to decreased cloud cover associated with drought conditions (Nicholls et al., 1996; Power et al., 1998); and

- (ii) the residual temperature anomaly is  $\Delta T_{\max,i} - E(\Delta T_{\max,i} | \delta P_i)$ .

Separation of the observed temperature anomaly in this way means the effect of an observed temperature anomaly can be split into two components: the effect on runoff from the 'expected' temperature anomaly and the effect from the residual temperature anomaly (Table 5). The linear-model assumption implicitly assumes that the rate of change of runoff of a unit increase in expected temperature and of a unit increase in residual temperature anomaly is equal, namely the temperature elasticity  $\eta_T$ .

Table 5. Area-weighted estimates (mm of runoff) of the average relative effects of changes in rainfall and maximum temperatures on the study catchments during the Millennium drought (1997–2008). Bracketed values are percentage of the observed reduction during the drought compared to the pre-1997 averages

	Observed streamflow (mm)		Rainfall effect		Expected temperature effect		Residual temperature effect		Residual runoff reduction	
	pre-1997	post-1997								
<i>By region</i>										
All	286.2	155.9	-87.7	(67%)	-5.6	(4%)	-9.4	(7%)	-27.6	(21%)
MDB	259.9	133.4	-89.7	(71%)	-6.9	(5%)	-10.5	(8%)	-19.4	(15%)
non-MDB	350.1	210.3	-83.0	(59%)	-2.6	(2%)	-6.6	(5%)	-47.6	(34%)
<i>By aridity</i>										
Wettest 11	583.6	381.1	-146.8	(72%)	-12.2	(6%)	-16.3	(8%)	-27.2	(13%)
Middle 11	322.6	157.8	-108.2	(66%)	-7.7	(5%)	-15.3	(9%)	-33.5	(20%)
Driest 12	103.9	35.3	-42.5	(62%)	-0.7	(1%)	-1.6	(2%)	-23.9	(35%)

The decreased annual rainfall during the Millennium drought accounted for around two-thirds of the observed reduction in streamflow (Table 5). It accounted for more in the wetter catchments and the MDB compared to those outside the MDB (i.e. the north-eastern coastal strip of NSW, see Figure 53). The effect of higher temperatures during the Millennium drought was practically zero for the driest one-third of catchments (Table 5). Even though the temperature anomaly (and the residual temperature anomaly) was higher in these catchments compared to the wetter catchments, the effect on runoff was low, as runoff is comparatively much lower in these catchments (this is explained conceptually in the following section). Otherwise, the effect of the expected temperature increase associated with the decreased rainfall was fairly constant at around 5 percent of the observed streamflow reduction. The effect of increased residual temperatures, i.e. the effect on runoff of the observed temperature anomaly not related to the observed rainfall anomaly, was between one and two times the effect of the expected temperature increase.

The area-weighted effects of rainfall and temperature anomalies (Table 5) can be compared to the equivalent effects on an aggregated time series. That is, rainfall, streamflow and temperature were aggregated for all 34 catchments, weighted by catchment area. From the resulting climate and runoff time series, corresponding to a total area of around 16,000 km<sup>2</sup>, rainfall and temperature elasticities and the resulting rainfall and temperature effects were calculated. The combined effect from temperature calculated on the aggregated time series was 19 percent of the observed runoff reduction, compared to 12 percent from the area averaged estimates. Note that these estimates are only for post-1960s data, in contrast to the estimates from Table 5. By choosing a start date for the aggregated data that included the data from all catchments, the introduction of biases and trends was avoided. It appears that the relatively larger temperature effects calculated for the aggregated data was due to spatial scaling bias, which is the same reason why temperature elasticities calculated for large basins (e.g. the Murray–Darling Basin (Cai and Cowan, 2008; Yu et al., 2010)) can be much larger than temperature elasticities at catchment scale. This is explored in the following sections through the development of a coupled water-energy budget model, and calculating rainfall and temperature elasticities of runoff for increasingly drier partial areas of the Murray–Darling Basin.

### ***A coupled water-energy budget model for understanding rainfall-runoff-temperature relationships***

Research during 2010–2011 indicated that annually averaged maximum temperature anomalies across the study area were not uniform, and that wetter catchments, which tend to have larger temperature elasticities of streamflow (Figure 54), in fact had relatively smaller maximum temperature anomalies during the Millennium drought (Potter et al., 2011). Here we outline a conceptual model coupling water and energy budgets in order to explain this difference in temperature anomalies. The long-term water budget of a catchment is

$$\bar{P} = \bar{ET} + \bar{Q} \quad (4)$$

where  $\bar{P}$  is mean annual rainfall (precipitation),  $\bar{ET}$  is mean annual evapotranspiration and  $\bar{Q}$  is mean annual runoff for a catchment. Note that equation (4) assumes that changes in groundwater fluxes are zero, which is a common assumption when comparing the water budget of a catchment over two long time periods (i.e. decadal-scale). Likewise, the long-term energy budget is written

$$\bar{R}_n = \bar{L} + \bar{H} . \quad (5)$$

Here  $\bar{R}_n$  is the available energy flux density,  $\bar{L} = L_e \bar{ET}$  is the latent heat flux, which is evapotranspiration multiplied by the latent heat of vaporisation of water,  $L_e$ .  $\bar{H}$  is the sensible heat flux. The transfer of heat to lower layers of the earth  $G$  is generally neglected at inter-annual time scales as the annual mean of  $G$  is typically zero. The coupling between water and energy budgets is through equality of evapotranspiration and the latent heat flux.

During a drought, mean annual rainfall decreases substantially, and connected to this is an increase in incoming energy  $\bar{R}_n$  (Power et al., 1998; Jones and Trewin, 2000). For an idealised water-limited (arid) catchment, evapotranspiration is primarily controlled by rainfall, and so is expected to decrease (Figure 56). In contrast, for an idealised energy-limited (wet) catchment, evapotranspiration is primarily controlled by incoming radiation, and so can increase during a drought (Figure 57). The coupling of water and energy budgets means that we expect a decrease in latent heat flux in water-limited catchments, and an increase (or at least a relatively smaller decrease) in latent heat flux in energy-limited catchments. We propose that this relative difference in the magnitude of changes in latent heat in different catchments determines the magnitude of the maximum temperature anomaly. For otherwise equivalent turbulent diffusion and advected heat fluxes, a larger sensible heat flux will tend towards higher annually averaged maximum temperatures. Importantly, arid catchments are likely to see large temperature increases during a drought, a reduction in evapotranspiration, and a relatively small reduction in runoff, at least in volumetric terms. In contrast, humid catchments are likely to see a small temperature increase during a drought, an increase in evapotranspiration, and a large volumetric reduction in runoff.

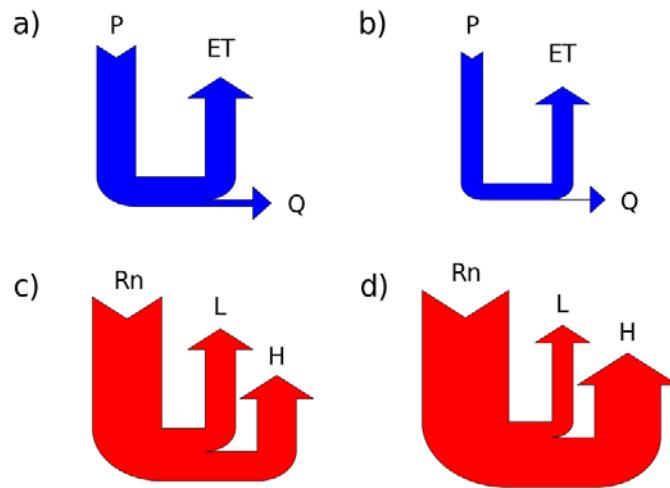


Figure 56. Water and energy budgets for a water-limited (arid) catchment: a) long-term water budget, b) drought water budget, c) long-term energy budget, and d) drought energy budget

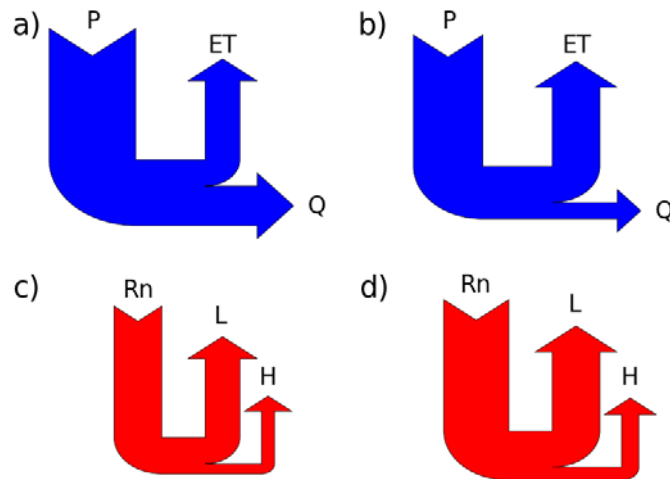


Figure 57. Water and energy budgets for an energy-limited (humid) catchment: a) long-term water budget, b) drought water budget, c) long-term energy budget, and d) drought energy budget

Figure 58 shows the strong relationship between the expected temperature anomaly for each catchment and change in evapotranspiration during the Millennium drought. Change in evapotranspiration was estimated using water balance closure, i.e. equation (4), and the expected temperature anomaly was calculated using equation (3). Residual temperature anomalies during the Millennium drought appear to be only weakly related to change in evapotranspiration. Observed temperature anomalies (being the sum of expected and residual temperature anomalies) are also related to change in evapotranspiration, but relatively less so than the expected temperature anomalies. A similar relationship between observed temperature anomalies and change in evapotranspiration during the Millennium drought was also seen using evapotranspiration estimates using the CABLE model (Chapter 3: Project 1.2); as well as the Bureau of Meteorology high-quality temperature data and Budyko-curve estimates for change in evapotranspiration (as the Bureau of Meteorology data are point-based and do not correspond directly with gauged catchments).

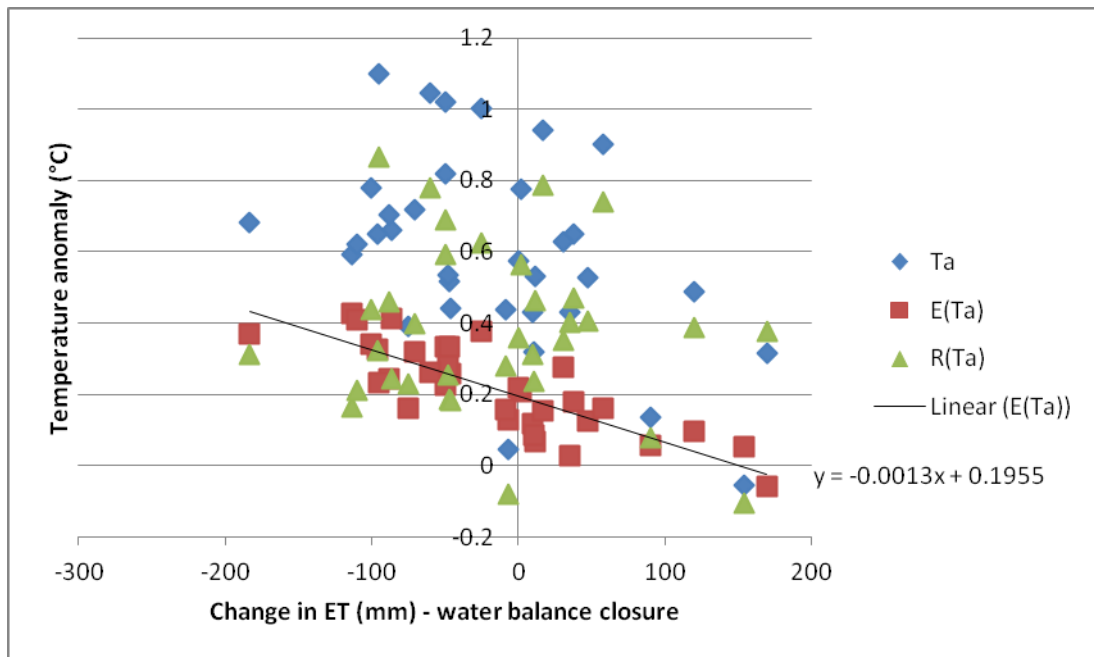


Figure 58. Change in actual evapotranspiration against observed, expected and residual temperature anomalies (Ta; E(Ta); R(Ta)) since 1997 for 34 catchments in SE Australia

**A spatial scaling effect for temperature elasticities**

To explore the relatively larger temperature effect from aggregated data compared to area averaged data discussed below Table 5, we calculated rainfall and temperature elasticities for increasingly drier partial areas of the Murray–Darling Basin. That is, we ranked all 40,467 grid cells in the MDB by decreasing mean annual runoff. Then, we defined a given partial area (for a given number of grid cells) as the number of grid cells with the highest mean annual runoff (Figure 59). Thus a larger partial area entirely included a smaller partial area. Note that these partial areas are not catchments, nor are they necessarily contiguous grid cells. Calculating elasticities on increasing partial areas thus gave a series of elasticities on increasingly drier basin areas.

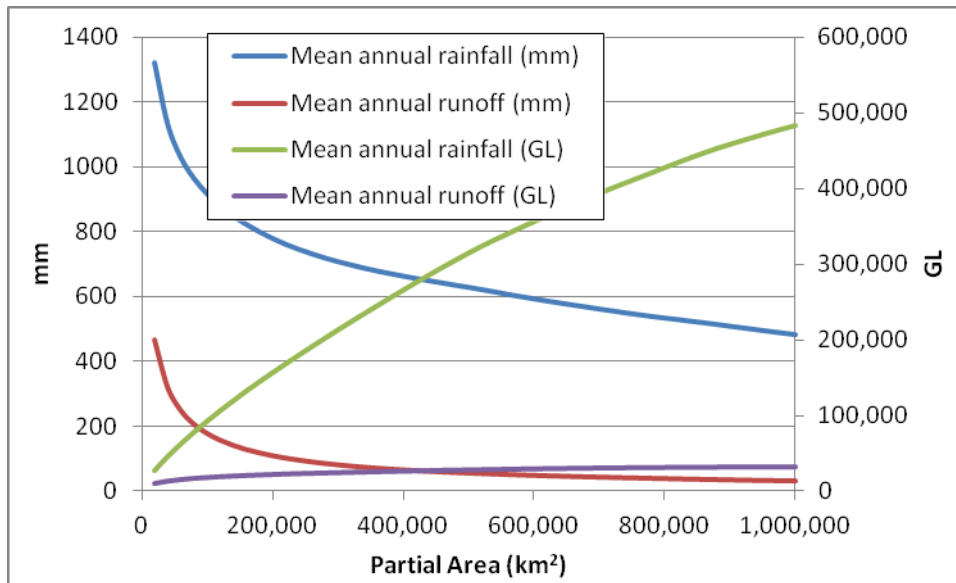


Figure 59. Mean annual rainfall and runoff (mm and GL) for increasingly drier partial areas of the MDB

Figure 60a shows the estimated rainfall and temperature elasticities of runoff for increasing partial areas of the MDB. The rainfall elasticities initially increase with increasing area and dryness, similarly to the catchment scale estimates in Figure 54a. However, in contrast to the catchment estimates, the partial area rainfall elasticities begin to decrease at a partial area of a just over 100,000 km<sup>2</sup>. When the rainfall elasticities were converted to sensitivities (Figure 60b), they followed the theoretical sensitivities based on Budyko theory (Milly and Dunne, 2002) very closely, suggesting that the decrease in rainfall elasticities is a spatial scaling effect: whereas rainfall elasticities calculated for a small to medium sized catchment with mean annual rainfall of 500 mm would be close to 4 or 5 (Chiew, 2006), the rainfall elasticity for the entire MDB calculated here of 1.8 is similar to median-based estimates calculated elsewhere (e.g. Fu et al., 2011b).

In contrast, the temperature elasticities initially decrease in absolute terms to almost zero (similarly to the decrease in catchment scale estimates in Figure 54b), and then begin an almost linear increase at around 50,000 km<sup>2</sup>, which corresponds approximately to a dryness index of one. When the corresponding partial area sensitivities to temperature were compared to the theoretical sensitivities from Budyko theory (Figure 60b), it was evident that the increasing partial area sensitivities to temperature are inconsistent with the theory, which suggests that runoff sensitivity to temperature should decrease with increasing catchment aridity. The conceptual coupled water-energy budget model developed above also suggests that temperature should be increasingly less related to runoff production for increasingly drier partial areas of any basin, as temperature anomalies in an arid catchment are related primarily to changes to evapotranspiration, rather than changes to runoff. Indeed, proceeding to the limiting case, i.e. including an extremely dry area that receives rainfall but creates no annual runoff, the temperature elasticity should decrease, rather than increase, as we are including temperature variability wholly disconnected from runoff production. And yet, Figure 60c shows that whereas the proportion of the observed runoff reduction in the Murray–Darling Basin explained by the reduction in annual rainfall during the Millennium drought stabilised with increasing partial area at just over half of the runoff reduction, the proportion of the observed runoff reduction explained by the temperature anomaly steadily increased with increasing partial area.

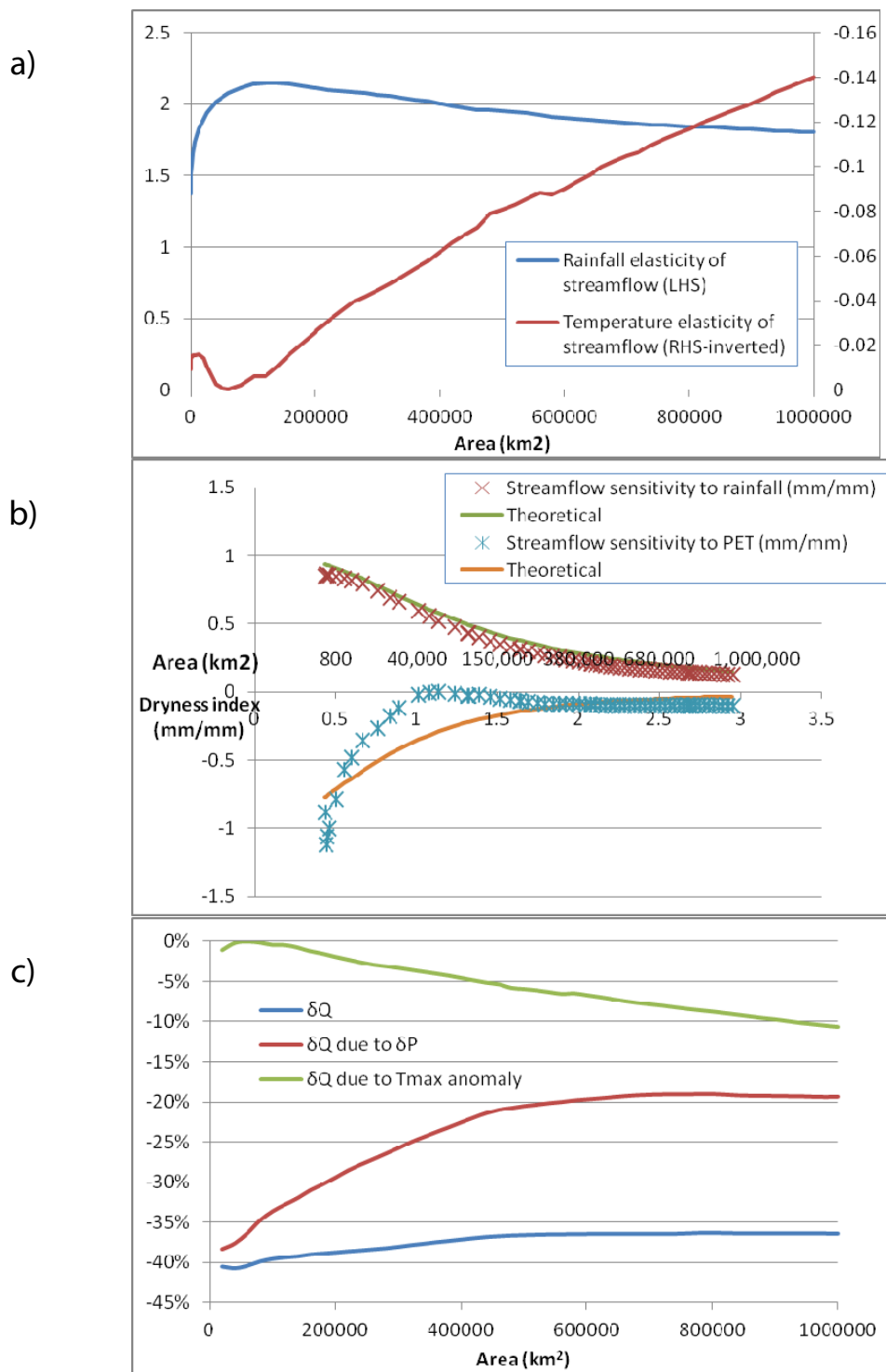


Figure 60. Rainfall and temperature elasticities of runoff (a) – note the reversed right hand axis; sensitivities to rainfall and potential evaporation (b); and proportion of the observed runoff reduction ( $\delta Q$ ) in the MDB explained by the reduction in rainfall and the temperature anomaly during the Millennium drought (c) for increasing partial area of the Murray–Darling Basin

## Activity 2

### **Further develop conceptual understanding of change in the rainfall-runoff relationship through the removal of anthropogenic influences and numerical experimental studies using conceptual and physically-based models**

Research during 2010–2011 suggested that farm dams and potential non-stationarities in hydrological processes during the Millennium drought may introduce biases in rainfall-runoff modelling (Petheram et al., 2011; CSIRO, 2010). It has been suggested that changes in dominant hydrological processes due to the very dry conditions have acted to change the rainfall-runoff relationship during the Millennium drought too. For example, a lowered water table in response to continued very low rainfall could lead to surface-groundwater disconnection in a normally connected system. This can lead to significant seepage losses at the streambed, as well as changes to surface saturation in runoff generation areas of the catchment, ultimately decreasing gauged streamflow. Furthermore, farm dams act to reduce streamflow by intercepting and storing surface runoff, and so change the catchment rainfall-runoff relationship at the gauge outlet. This has implications for the calibration of rainfall-runoff models, particularly when comparing modelled runoff response between time periods in which there has been a change in the number, volume or usage of farm dams.

However, data constraints and uncertainty make assessment of these non-stationarities problematic. Conceptual rainfall-runoff models based on soil moisture accounting generally have a coarse representation of groundwater, and typically no connection between surface infiltration and groundwater stores. However, detailed groundwater modelling requires extensive spatial data for soils and regolith, making medium-scale catchment estimates subject to significant uncertainty. Further, although the location of farm dams can be captured using remote-sensing data, changes over time in the number and volume of farm dams are known with less certainty (Nathan and Lowe, 2011). The volume of individual farm dams is also unknown and is typically estimated using regionalised relationships, although this does not appear to have too great an effect on estimates of the impact of farm dams (Nathan et al., 2005). The level and timing of extractions from farm dams are obviously of critical importance, and these must also be approximated in the absence of detailed information on irrigation practices (Lowe et al., 2005).

There were two parts to Activity 2. The first was modelling of a typical catchment in southern south-eastern Australia, using the physically-based, spatially explicit, and dynamic model TOPOG, described by Vertessy et al. (2000), in order to examine potential changes in dominant hydrological processes that may not be modelled well with conceptual rainfall-runoff models. The second was development of a farm dam component to SIMHYD, and spatial analysis of remotely sensed farm dam information for south-eastern Australia.

### ***Investigation of potential changes in dominant hydrological processes during the Millennium drought in south-eastern Australia***

The objectives of this part of the project were to:

- I. quantify spatially any changes in saturated areas before and during the period 2000–2009, corresponding to the impact of the Millennium drought in the study catchment,
- II. investigate how depth to water table affects runoff generation, and
- III. estimate the time required to return to pre-drought water yield levels under average and wet climate sequences.

TOPOG (Vertessy et al., 2000), is a physically-based, spatially explicit model, with both dynamic water and carbon balance model components. TOPOG is ideally suited to addressing the issues of changes in yield and spatial distribution of saturated areas embodied in Objectives 1 and 3. For Objective 2 it must be noted that depth to water table is not a single catchment attribute but that some of the behaviour may be addressed using total catchment storage as a surrogate, i.e. under the steady-state assumption that there is an underlying single-valued relationship between total storage and the extent and depth of the water table.

### **Methods and catchment description**

The primary method of reducing computational effort modelling a three-dimensional land surface in TOPOG is a contour-based topographic analysis that defines one-dimensional land elements that connect in a linear additive manner from highest to lowest elevation. In principle this is the same as determining single or multiple flow directions from a regular grid, if each grid cell is then modelled in the correct order and the inputs and outputs are routed as calculated. The advantage of using a contour-based approach is that elements align in a natural manner, distributed according to the shape of the land surface and the density of discrete contours. The concurrent disadvantage is that in general high slope areas get higher density while low slope areas get lower density, which is usually not where the hydrological action of interest occurs. This is addressed by using a variable set of contour levels, rather than a constant contour interval, so that flatter areas are represented by closer contours, and tops of hills which might not be of much interest have wider spaced contours.

The study catchment (Brankeet Creek at Altona, 405251) was chosen as a catchment in south-eastern Australia with a representative large reduction in runoff. Criteria for selection were good surface streamflow records, sufficient bore data to show a declining water table during the Millennium drought, and being small enough to be realistically represented with TOPOG. Brankeet Creek is located in the Goulburn River catchment at approximately  $-36.92^{\circ}$  S  $145.81^{\circ}$  E. The boundary encompasses  $121 \text{ km}^2$  with elevation ranging from 320 to 970 m, with an average slope of  $5.2^{\circ}$ . The catchment still has 60 percent remnant tree cover, mostly in the higher elevation northern areas. The streamflow record is excellent with daily average flow from 18/10/1973 to present (only downloaded to 14/12/2011). ASRIS is not useful for determining soil type here, although it is classified entirely as a sodosol. This soil type is strongly duplex, with a sandy clay loam A-horizon between 0.5 and 1.0m thick before an abrupt change to a B-horizon of lower conductivity medium to medium heavy clay. Total regolith thickness is variable and not well described.

Performing the topographic analysis on Brankeet Creek proved difficult. As a whole the catchment is larger and more complex than usual for TOPOG simulations so the topographic analysis failed at several points where contour lines proved inadequate to describe the shape of the land surface. The catchment was successfully completed in three separate pieces, then the output files stitched together to form a single catchment for subsequent simulation. Dynamic leaf area index was modelled using feedbacks between the availability of water, light, temperature and nutrients, as they affect assimilation of carbon and photosynthesis. Assimilation feeds on to canopy conductance and transpiration via Penman-Monteith, while the reduction in leaf area index was handled through mortality and respiration rates (Hatton et al., 1992; Wu et al., 1994; Zhang and Dawes, 1998).

### **Fitted streamflow**

The primary function of the TOPOG modelling was to reproduce daily streamflow, and any changes in behaviour of monthly or annual streamflow due to climatic influences. TOPOG can be run with or without activating streams – water flowing from elements that are adjacent to a stream is included in streamflow for that day and removed from further down gradient routing. Figure 61 shows streamflow modelling with streams activated, to remove water immediately it reaches a stream side element. For this simulation the Nash-Sutcliffe efficiency was  $NSE=0.55$  daily (13937 records),  $NSE=0.78$  monthly (459 records) and  $NSE=0.93$  yearly (39 records). The same simulation was performed without stream side water removal, *i.e.* overland flow cascades over the land surface only, and the  $NSE$  were lower at  $NSE=0.53$  daily,  $NSE=0.76$  monthly and  $NSE=0.78$  yearly.

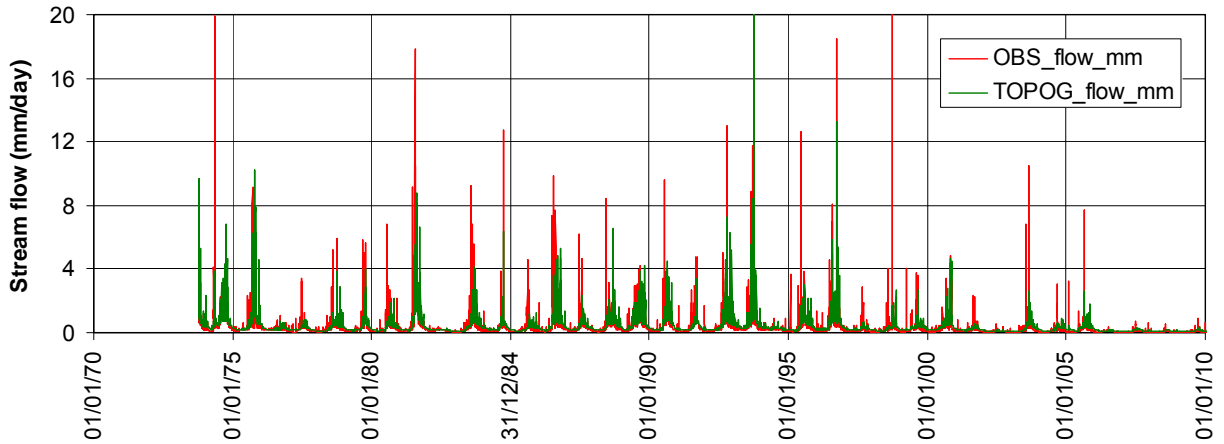


Figure 61. Daily observed and streamflow prediction from TOPOG; stream option activated

It is difficult to see specific differences between the stream and no-stream options on a full flow graph, so Figure 62 shows just the second half of 1993. The with-stream trace is always lower than the no-stream trace due to the fact that removal of water via the stream reduces saturation areas that are otherwise generated due to all water requiring transport through, or over, the soil. This is most visible under low flow conditions in November 1993, for example, where the observed and with-stream trace both slowly decline, while the no-stream trace has several spikes when rain falls but is otherwise falling at a higher rate.

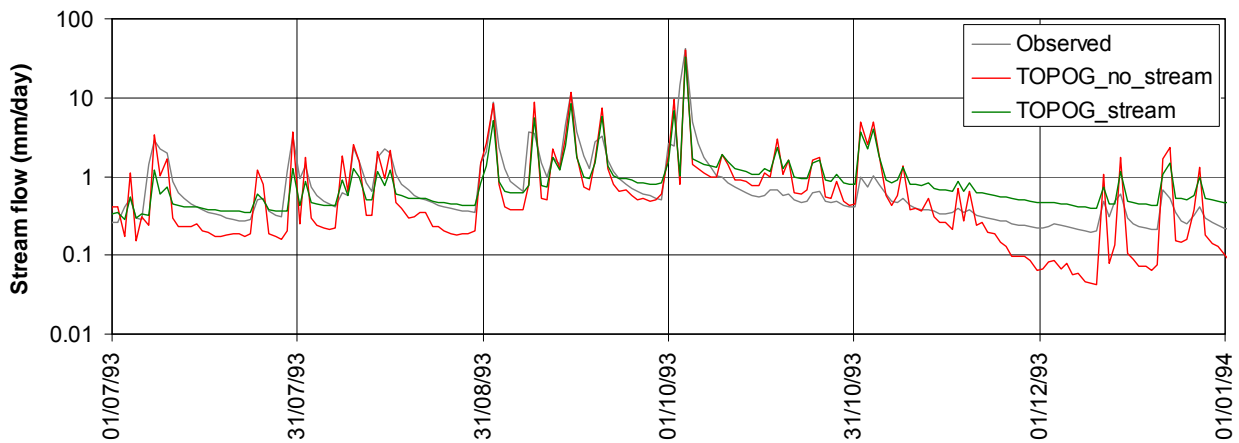


Figure 62. Daily observed and predicted streamflow with and without stream option in TOPOG. Y-axis has logarithmic scale to show better differentiation of individual lines

Figure 63 shows the very good correspondence between TOPOG simulated streamflow and observations on an annual basis. It also illustrates one of the problems with TOPOG – that large elements at the bottom of the catchment get very wet then leak slowly. Brankeet Creek was perennial according to observation from 1973 to 2003. Following this the stream experienced varying times of zero flow annually. TOPOG on the other hand leaks at a slow rate less than 0.1 mm/day, but over summer and autumn this can add up to 20 mm of flow when the stream would otherwise be dry; see flow between 2005 and 2009 in Figure 63.

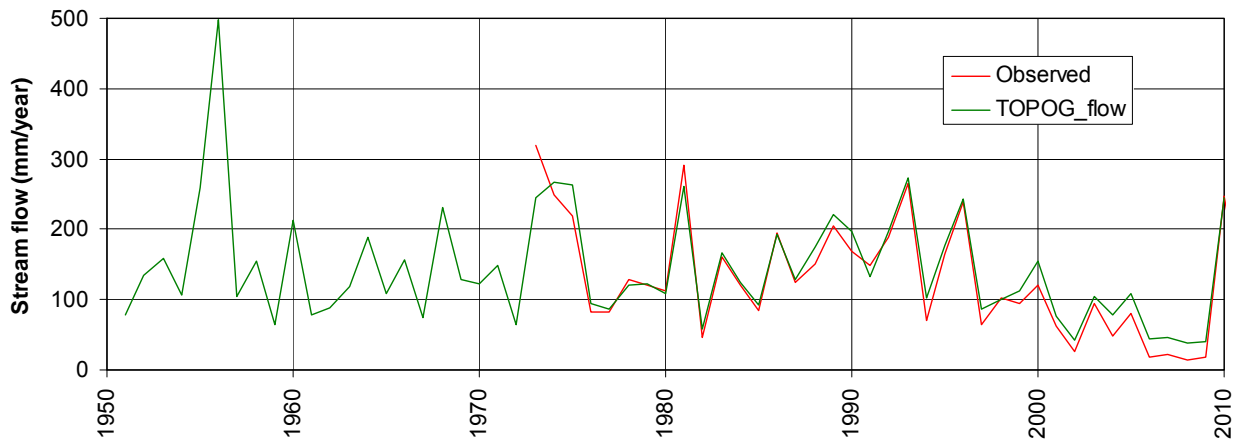


Figure 63. Annual summary of streamflow; simulations start 1951 while observations start 1973

Summarising the SILO climate data (Jeffrey et al., 2001) for the catchment centroid, we can see patterns forming (Table 6). While the 1950s was the wettest decade, and the 2000s the driest, the intervening 40 years are remarkably consistent in all climatic variables, with the exception of a steady rise in shortwave solar radiation. There was a stark contrast in the 2000s, where maximum and minimum temperature both had large increases, vapour pressure deficit was also elevated, average rainfall dropped 22 percent and average streamflow by 57 percent from the previous half century; the runoff ratio halved. The last three lines of Table 6 compare the measured period from 1974 to 2000 with the Millennium drought period from 2001 to 2009, and with the decade to 2011 which included two recent wet years.

Table 6. Climate data summary for Brankeet Creek including streamflow where available. Note that streamflow from 1951 to 1973 is estimated from a quadratic relationship between annual rainfall and runoff

Time Period	Tmax (°C)	Tmin (°C)	VPD (mb)	Rainfall (mm)	Radiation (kJ/m <sup>2</sup> /d)	Streamflow (mm)	Runoff Ratio
1950s	17.5	6.3	4.4	1179.5	15821	175.1	
1960s	17.5	6.5	5.1	1026.6	15647	126.9	
1970s	17.5	6.4	4.8	1053.8	15803	142.2	13.5%
1980s	17.7	6.3	5.0	1061.2	16190	154.7	14.6%
1990s	17.4	6.5	4.6	1070.2	16275	145.4	13.6%
2000s	18.1	6.9	5.3	845.3	16475	63.4	7.5%
1974–2000	17.5	6.4	4.8	1062.6	16121	148.0	13.9%
2001–2009	18.2	6.9	5.4	760.2	16563	42.9	5.6%
2001–2011	18.0	6.9	5.2	867.7	16423	66.9	7.7%

### Catchment relationships

We examined the observed streamflows and TOPOG modelling results to distil any relationships between variables. Figure 64 shows the plot of observed annual rainfall versus runoff, and the least-squares regressions for linear and quadratic (through the origin) functions. The linear fit is very good and provides the most basic form of streamflow

prediction: approximately 25 percent of rainfall above an annual threshold of 516 mm becomes streamflow. The quadratic fit has only a slightly higher R<sup>2</sup>, which emphasises the apparent tightness of the streamflow relationship.

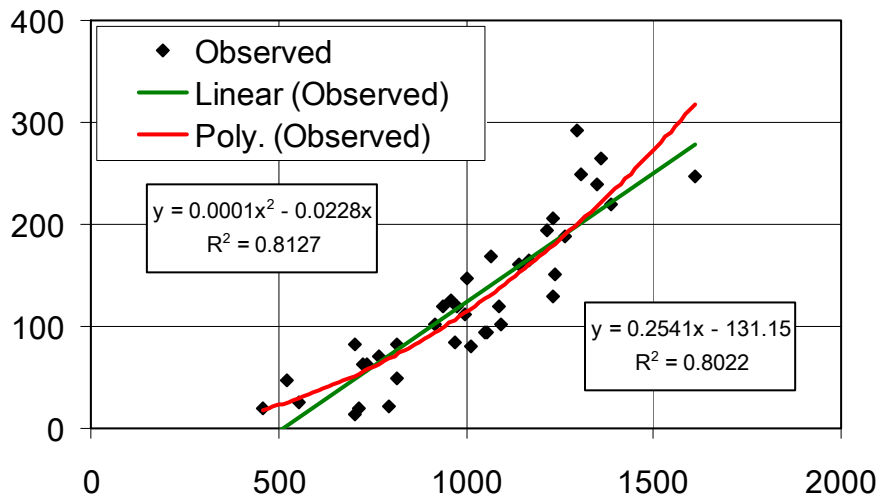


Figure 64. Observed relationship between annual rainfall (x-axis; mm) and streamflow (y-axis; mm), Brankeet Creek, 1973–2011

Removing the Millennium drought rainfall and runoff data from the relationship in Figure 64 reduced the correlation strength, and reduced the values of the fitted coefficients. Although this suggests they may be part of the same population, there also seems to be some catchment memory or change in behaviour. For example, during the period prior to 2000, rainfall between 700 and 800 mm produced 60 to 80 mm of runoff while during the Millennium drought the same rainfall range resulted in 15 to 25 mm of runoff. Similarly rainfall around 1000 mm changed from 90 to 150 mm of runoff pre-2000 to 80 to 100 mm post-2000.

The observed annual streamflow shown in Figure 63 decreased at a rate of 3.6 mm/year/year over the full period of record, and at a rate of 4.2 mm/year/year from 1973 to 2009; over the same periods annual rainfall decreased by 7.2 and 11.4 mm/year/year. These rates consider some steady fall while the actual climate records in Table 6 suggest more of a step change between 2001 and 2009; it remains to be seen if this is a temporary change.

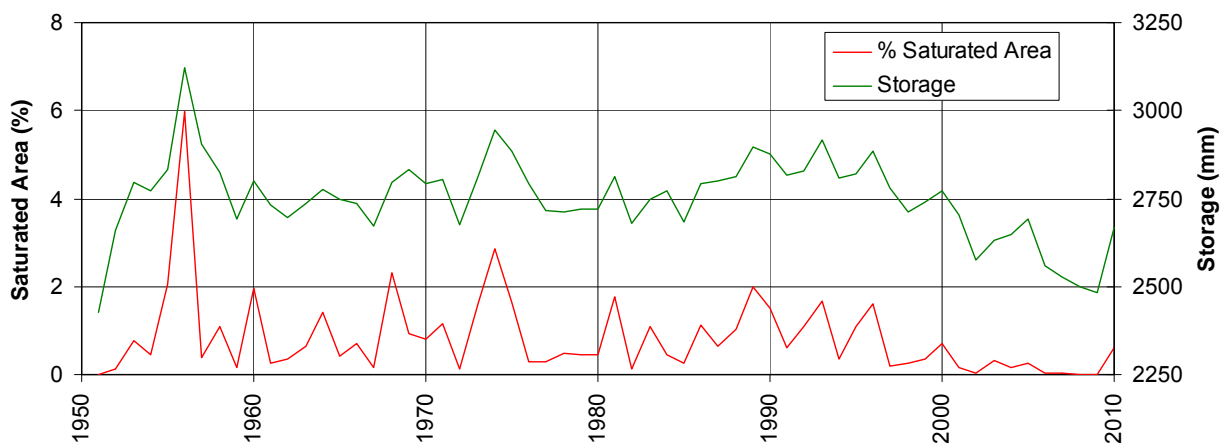


Figure 65. Annual average TOPOG catchment storage and percentage saturated area

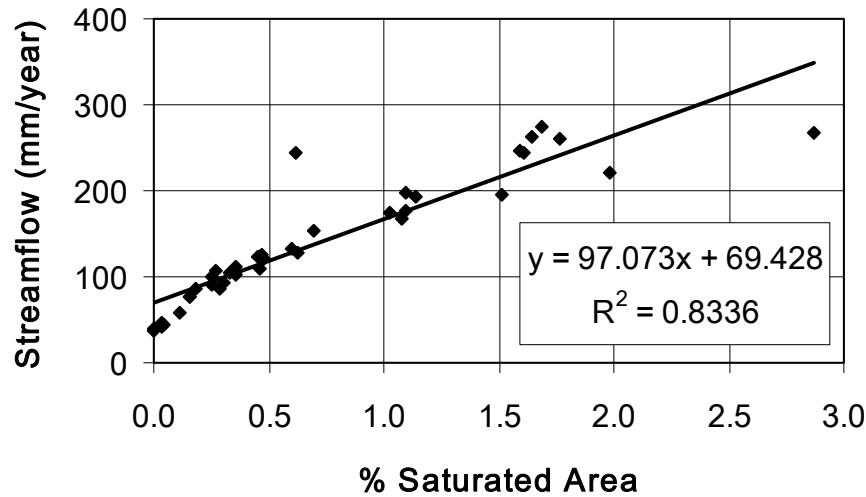


Figure 66. Annual average TOPOG modelled catchment saturated area versus streamflow, 1974–2011

Figure 65 and Figure 66 show the storage, percent catchment saturation and streamflow estimates. In Figure 65 the similarities between storage and percentage saturated area are clear, with the saturated area collapsing in the late 2000s close to, or equal to, zero from 2006 to 2009. In a very bucket-like manner it is seen in Figure 66 that annual runoff is closely linked with average saturated area, and although the timing of rainfall that creates saturation must vary from year to year and cause the scatter on the graph, it seems to be a second order effect compared to the average area.

### Wet and dry periods

Consideration was given to how the catchment responds to wet and dry periods. The observed rainfall was summarised in 10 year blocks from 1974 to 2011 and compared to the long-term average. The results are listed in Table 7.

Table 7. Average rainfall for decades between 1974–83 and 2002–11

Time Period	Average Rainfall (mm)	Classification
1974–2011	1006.2	
2000–2009	793.0	Lowest
1977–1986	1009.7	Average
1981–1990	1061.2	Median
1987–1996	1140.0	Highest

Three periods were selected for further simulation – lowest, median and highest rainfall decades. The ‘average’ decade was not considered, as that implies a smooth change process, and the median rainfall is nearly as far above the average as the highest is above median. The three decadal records were repeated for 50 more years each to form three long climatic sequences. Each simulation was started from the same dry initial condition and allowed to run; results are listed by decade in Table 8.

Table 8. Decadal average streamflow (mm/a), % saturated area and catchment-average leaf area index for three historic climate series

Years	Low Rainfall, 793 mm/year			Median Rainfall, 1061 mm/year			High Rainfall 1140 mm/year		
	Flow	%Sat	Leaf area index	Flow	%Sat	Leaf area index	Flow	%Sat	Leaf area index
01 – 10	36.7	0.03	2.44	110.6	0.56	2.62	117.9	0.63	2.70
11 – 20	53.2	0.08	2.99	154.0	1.00	3.11	160.3	1.06	3.15
21 – 30	57.7	0.07	3.07	163.3	1.03	3.19	171.2	1.12	3.23
31 – 40	59.4	0.07	3.10	168.8	1.04	3.22	175.8	1.14	3.26
41 – 50	60.9	0.07	3.10	172.8	1.05	3.23	178.5	1.16	3.27
51 – 60	62.0	0.07	3.10	175.7	1.06	3.24	180.5	1.18	3.28

From the details in Table 8 it can be seen that most of the variation was in the first 20 years, with much smaller changes thereafter. With both water and carbon changing dynamically, there was no dynamic equilibrium in any of the cases even after six complete rainfall cycles, i.e. identical flow and leaf area index for subsequent cycles. According to the simulations in Table 8, a return to the pre-drought average runoff of around 150 mm would occur between 10 and 20 years for the high and median rainfall climate sequences. To minimise the number of confounding effects, the simulations were also run with constant leaf area index appropriate to each climate series. In this case, annual average flow and saturated area equilibrated a little faster, changing little from decade to decade. However, total flow was also much lower – a consequence of constant leaf area and rooting distribution.

### **A closer comparison of 1990 and 2003**

Here two years were compared in more detail using the full dynamic climate and leaf area index as fitted earlier. These two years were selected because

- (i) they receive approximately the same annual rainfall amount,
- (ii) their rainfall is close to the long-term catchment-average rainfall,
- (iii) the year 1990 was at the start of the wettest decade since the 1950s, and
- (iv) the year 2003 was within the Millennium drought period.

Table 9 presents the annual summary data of observed and simulated catchment streamflow, along with average saturated area, leaf area index and total stored water in 20 m of regolith. At the annual level it is clear that 2003 started in a drier state with about 8 percent less stored water which resulted in a simulated reduction in streamflow of 47 percent; actual observed reduction was 45 percent.

*Table 9. Annual summary of water balance and leaf area index for comparison years 1990 and 2003*

Year	Rainfall (mm)	Observed Flow (mm)	Simulated Flow (mm)	% Saturated Area	Average leaf area index	Stored Water (mm)
1990	1065.3	169.6	196.1	1.51	3.22	2874
2003	1057.6	93.6	103.6	0.33	2.97	2632

Table 10 presents the same information as Table 9, but broken down to a monthly time step so more detail can be seen.

Table 10. Monthly simulated water balance and leaf area index for the years 1990 and 2003

Month	Rainfall (mm)	Simulated Flow (mm)	% Saturated Area	Leaf area index	Storage (mm)
Jan-1990	7.2	7.4	0.00	3.63	2805.0
Feb-1990	65.9	5.8	0.01	3.66	2765.6
Mar-1990	20.0	5.7	0.00	3.57	2717.4
Apr-1990	127.6	5.7	0.11	3.48	2725.5
May-1990	54.8	6.1	0.24	3.37	2762.0
Jun-1990	127.7	7.1	0.33	3.17	2786.8
Jul-1990	234.1	25.3	1.92	2.93	2946.2
Aug-1990	196.1	48.4	5.46	2.76	3040.0
Sep-1990	100.2	36.4	6.24	2.70	3072.8
Oct-1990	88.4	26.9	3.37	2.84	3046.4
Nov-1990	24.1	12.9	0.38	3.12	2968.2
Dec-1990	19.2	8.4	0.04	3.41	2854.3
Jan-2003	44.7	2.9	0.00	3.46	2500.7
Feb-2003	16.1	2.4	0.00	3.32	2460.5
Mar-2003	11.7	2.6	0.00	3.19	2448.3
Apr-2003	114.8	2.6	0.00	3.09	2483.0
May-2003	98.1	3.1	0.00	3.07	2537.0
Jun-2003	127.2	4.8	0.00	2.94	2600.5
Jul-2003	152.5	8.8	0.18	2.76	2657.2
Aug-2003	170.5	20.5	0.48	2.63	2762.3
Sep-2003	79.1	22.0	1.58	2.56	2826.5
Oct-2003	75.6	15.9	1.33	2.62	2811.1
Nov-2003	50.8	9.5	0.31	2.83	2764.3
Dec-2003	116.5	8.5	0.08	3.16	2736.4

One of the stark differences between the rainfall in 1990 and 2003 is that approximately 100 mm more fell in December of 2003 than 1990, with a similar but reversed difference in July. This combined with the fact that 2003 started out about 200 mm drier in terms of stored water, led to the start of significant streamflow delayed by a month; in 1993 flow jumped from 7.1 mm in May to 25.3 mm in July while in 2003 flow jumped from 8.8 mm in July to 20.5 mm in August. Such a delay in the increase of streamflow and saturated area will reduce the effectiveness of subsequent rainfall as more is used for storage or evaporation than would be otherwise. For example, from October

to December 1990 there was 131.7 mm of rain resulting in 48.2 mm of streamflow, while in the corresponding period in 2003 there was 242.9 mm of rainfall but only 33.9 mm of streamflow.

TOPOG also allows us to examine the state of each catchment element at any point in simulation time. Spatial water balance dumps were taken on the first of each month during 1990 and 2003 and the state of the water table within elements examined. Table 11 lists the number of catchment elements, which is not directly related to area on the ground, to a range of water table depths and a category where the entire column is unsaturated, i.e. no water table exists.

The water level breakdown in Table 11 provides much the same insights as the water balance in Table 10. In the year 1990 there are significant areas of shallow water table and some of saturation through the late summer and autumn while these are absent in the year 2003. In the earlier time there is also much less area with no water table and more with some water table, even if it is deep and below 10 metres in depth. The extra rainfall in December 2003 appeared only to maintain areas with deep existing water tables, rather than provide much runoff or streamflow, while the latter period in 1990 had substantial areas with shallow to moderately deep water tables, less than 5 m deep.

Looking at total storage from Table 10, the year 1990 was an average rainfall year and the initial and final month storages were quite similar, being 49 mm wetter at the end. In the case of the year 2003 which had average long-term rainfall in a dry period, there was substantial wetting up as the year ended 236 mm wetter than it started. Clearly not all of this can be attributed to the 116 mm of rain that fell in December, and even taking this into account, the catchment stored more water over the year in 2003 than in 1990.

Table 11. Number of land elements with various depths of water table for the years 1990 and 2003

Month	WT 0 – 1 m	WT 1 – 2 m	WT 2 – 5 m	WT 5 – 10 m	WT > 10 m	No WT
Jan-1990	22	79	36	89	1530	1111
Feb-1990	5	52	77	81	1445	1207
Mar-1990	5	41	84	76	1398	1263
Apr-1990	4	27	97	71	1358	1310
May-1990	8	34	86	67	1373	1299
Jun-1990	11	31	83	65	1729	948
Jul-1990	19	27	76	67	2678	0
Aug-1990	51	15	66	75	2660	0
Sep-1990	91	19	32	92	2633	0
Oct-1990	106	13	28	100	2620	0
Nov-1990	100	24	26	99	2612	6
Dec-1990	52	68	25	92	1645	985
Jan-2003	1	6	43	68	969	1780
Feb-2003	1	5	41	70	916	1834
Mar-2003	0	3	42	65	836	1921
Apr-2003	0	2	42	63	780	1980
May-2003	1	4	36	61	844	1921
Jun-2003	3	8	25	64	2368	399
Jul-2003	3	13	23	61	2767	0
Aug-2003	8	11	28	59	2761	0
Sep-2003	22	2	41	54	2748	0
Oct-2003	24	2	45	52	2744	0
Nov-2003	26	8	38	55	2740	0
Dec-2003	23	13	36	55	2435	305

### **Modifying SIMHYD to include a farm dam component**

The presence of farm dams and reported recent increases in the number and capacity of farm dams in south-eastern Australia is likely to have an effect on the rainfall-runoff relationship. The relative effect of farm dams on catchment runoff is suggested to be higher during dry periods (Nathan and Lowe, 2011). Here we propose a method for estimating and potentially removing the effect of farm dams on catchment streamflow signals, through modification of a rainfall-runoff model.

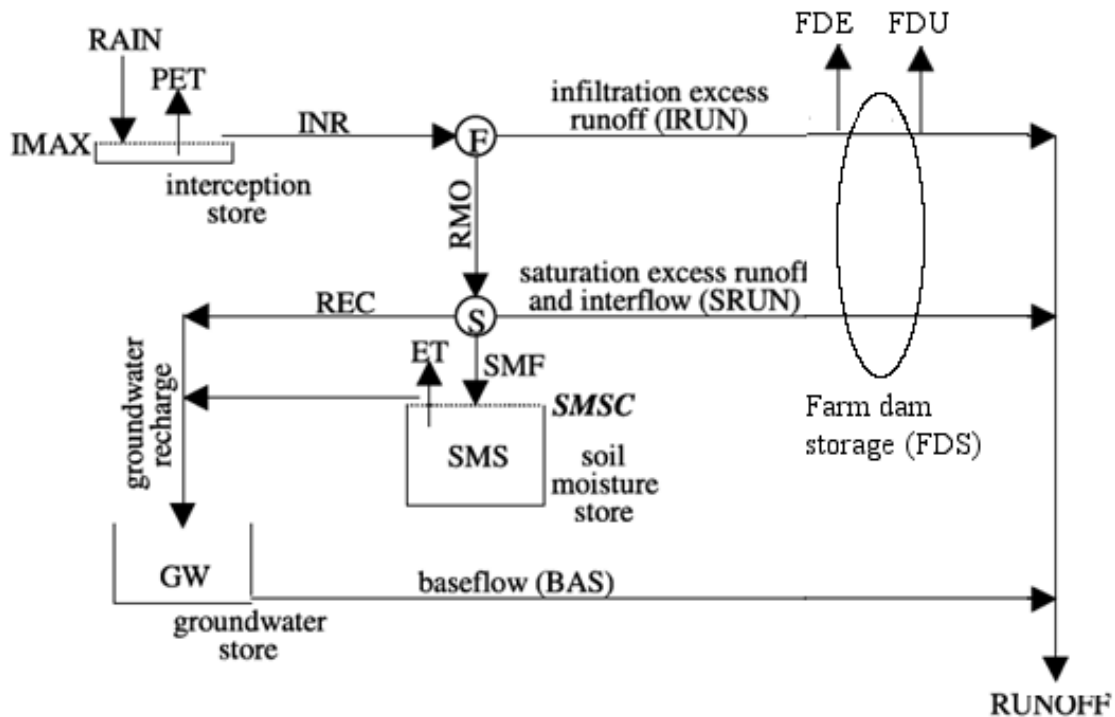


Figure 67. Modification of SIMHYD to include a farm dam component

SIMHYD is a conceptual rainfall-runoff model, typically applied at catchment scale. In the original model there are three catchment aggregated water storages: an interception store, soil moisture store and a groundwater store (Figure 67). Runoff occurs through three pathways: infiltration-excess runoff (IRUN), which occurs when potential infiltration (INR) exceeds the infiltration capacity of the soil; interflow and saturation-excess runoff (SRUN), which is a function of the soil moisture store (SMS); and baseflow, which is a linear recession from the groundwater store (GW). SIMHYD has seven parameters to be calibrated. The farm dam component consists of a farm dam water store (FDS), which intercepts IRUN and SRUN. Four extra parameters are needed: catchment farm dam storage capacity (in mm), farm dam contributing area, farm dam surface area, and farm dam maximum annual usage.

Taken at catchment scale, each additional farm dam storage is modelled as an aggregated store. Each individual farm dam has a contributing area that can be ascertained from analysis of the DEM of a catchment (see below). When modelled at catchment scale, these contributing areas are summed to provide an aggregate contributing area. The maximum runoff interception of the catchment farm dam storage is limited by the contributing area (e.g. if the contributing area is three-quarters of the total catchment area, the maximum farm dam interception is three-quarters of IRUN and SRUN). Evaporation from the farm dam storage is assumed to occur at the rate of potential evaporation. The actual rate of farm dam evaporation depends on the aggregated surface area of farm dams.

Farm dam usage is perhaps the most difficult to model. This is obviously not a natural process, and depends on many unknown factors, such as the type of dam and its volume, as well as agricultural decisions. Lowe et al. (2005) suggest that the annual demand factor (i.e. the water extracted annually as a proportion of total capacity) from farm dams is dependent on the type of farm dam. The median annual demand factor for farm dams from land-holder surveys in Victoria was 0.83. Extractions from farm dams are assumed in the first instance to be constant throughout the year, governed by an annual demand factor parameter; seepage is assumed to be zero.

Parameters for the models were calibrated using the Shuffled Complex Evolution method. The objective function was bias-penalised Nash-Sutcliffe efficiency (Viney et al., 2009). The calibration period was 1975–1996, and the validation period was 1997–2008. There were two separate calibrations for the model with the farm dam component included. In the first instance, we calibrated all eleven parameters (notated SIMHYDFD); also, we calibrated ten parameters with the farm dam storage capacity fixed to a preliminary estimate of remotely sensed catchment farm dam storage capacity.

Figure 68 shows the exceedance probabilities for Nash-Sutcliffe efficiency during the validation period (1997–2008) from the 34 catchments in south-eastern Australia studied in Activity 1. The Nash-Sutcliffe efficiencies for the SIMHYDFD model (all parameters calibrated) are mostly a little higher than the efficiencies for the SIMHYD model. When the farm dam capacity parameter was fixed, the SIMHYDFD model performed well for some of the better modelled catchments, but worse for others. Looking at the model bias (Figure 69), we see that most of the catchments modelled with SIMHYD have a small positive bias during the validation period, with a few having large negative biases. Including a farm dam component in SIMHYD seems to reduce negative bias fairly well, along with modest reductions in positive bias. This suggests that including a farm dam component in SIMHYD would result in a more accurate modelled runoff response during dry periods. Better spatial mapping of farm dam contributing areas and connectivity is expected to improve modelling results (see below).

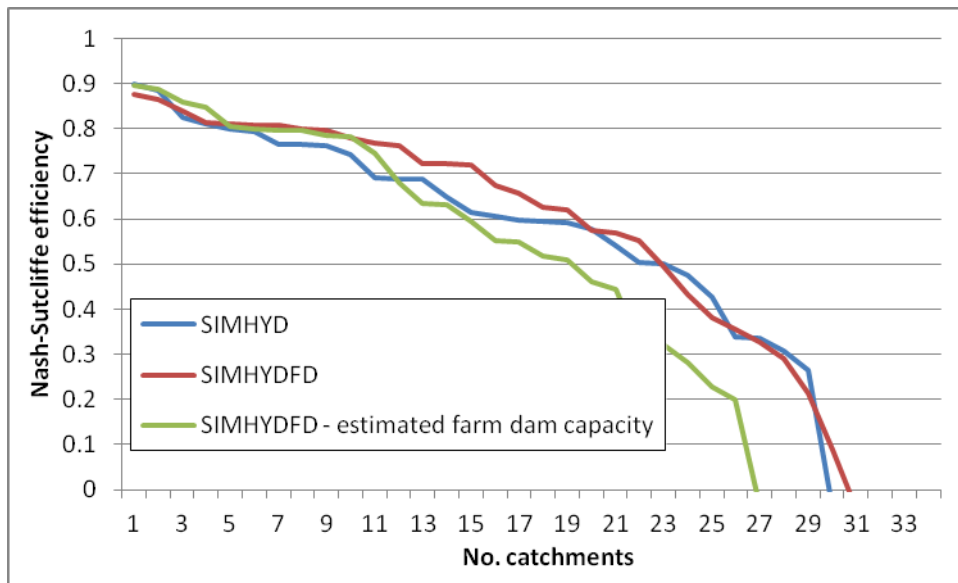


Figure 68. Number of catchments exceeding Nash-Sutcliffe Efficiency scores during the validation period (1997–2008)

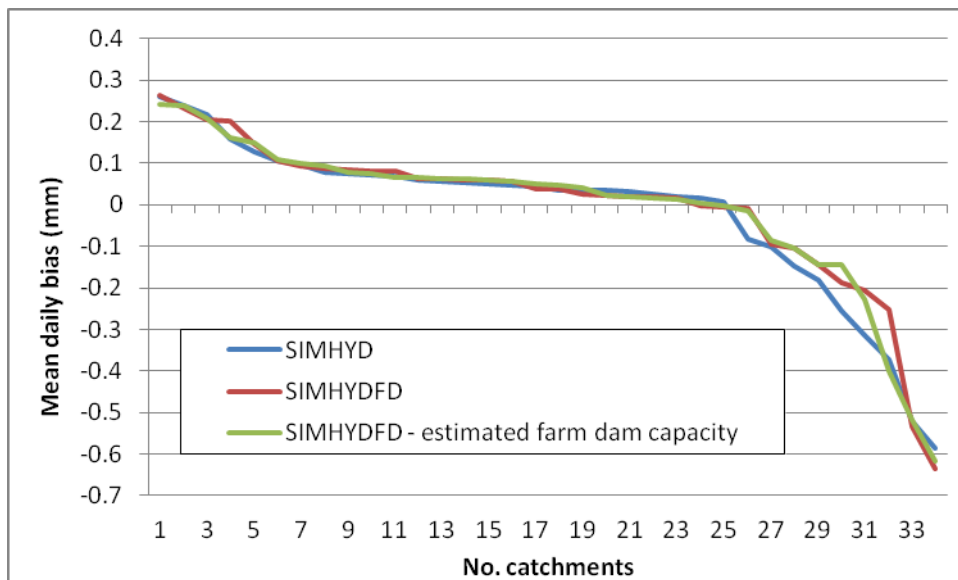


Figure 69. Number of catchments exceeding mean daily runoff bias (modelled minus observed) during the validation period (1997–2008)

The farm dam component described here provides a very coarse representation of farm dams in catchments. Future work will look at relaxing some of the inherent assumptions in the above model. A more realistic representation of

farm dam usage is one potential avenue for improvement. Aggregating farm dams to a catchment store ignores non-linearities in inflows, demand, spills, evaporation and changes in surface area. One option to overcome this could be parameterising changes in farm dam surface area, and hence the rate of evaporation, with changes in total storage (to model the drying out of smaller farm dams before larger dams). Resolving this by modelling with sub-catchments with individually aggregated farm dam stores is another option. This would also provide better representation of spatial heterogeneity of inflows. Improvements are also foreseeable with more realistic modelling of farm dam usage.

### ***Spatial data for farm dams in south-eastern Australia***

Farm dams are spatially distributed throughout a catchment. The impact of any particular dam on runoff is dependent on its usage, size and position in the catchment. By using spatial analysis techniques we are able to estimate the last two of these factors. The position is important for determining inflows, both through the dam's contributing area and spatial variability of rainfall/runoff inputs.

Geoscience Australia (2008) has mapped dams in the Murray–Darling Basin based on imagery from 2005. The resulting data products include a point dataset for very small dams (<1000 m<sup>2</sup>) and a polygon dataset for larger dams. The polygon-based datasets provide an estimate of the surface area of the dam, which, along with a broad estimate of the depth and bank slope, can be used to provide a rough estimate of the volume of the dam (see e.g., Shaikh et al., 2011). Surface area and volume of point dams can be estimated using probability distributions (Nathan et al., 2005). The location information from both datasets can be used to extract the catchment and its area for each dam by using a suitable digital elevation model. The recently released one-second SRTM Derived Hydrological Digital Elevation Model (DEM-H) (Geoscience Australia, 2011) is the most suitable product available for this task. It covers all of the SEACI catchments being analysed, has a high level of detail at the hill-slope scale and is drainage enforced to ensure main stream lines follow the correct path.

Despite all datasets being of a high spatial resolution, minor relative position errors between the digital elevation model and the dam mapping occur which can result in errors in the identification of the contributing area of the dam. If these errors result in small dams being placed on large streams then the errors are large. It should be possible to automatically identify the most extreme cases of this occurring but it is likely that some manual intervention will be required. Examples of these errors can be seen in Figure 70, where a contributing area from a small dam extends across the southern edge of the region. In contrast, the sub-catchment in the south-western corner is real as there is a larger reservoir located on the stream-line in this catchment.

Dams can be nested in a catchment such that when the upper one spills it flows to a lower one. The digital elevation model lets us capture this connectivity to produce a graph network structure of the flow path through the dams in the catchment to the outlet. This structure will enable modelling to be performed at the finest dam level or with an aggregation of dam catchments to a simplified representation to investigate sensitivity to the effect of dams. This connectivity is not explicitly shown in Figure 70 but is implied by the presence of smaller dam catchments within larger dam catchments.

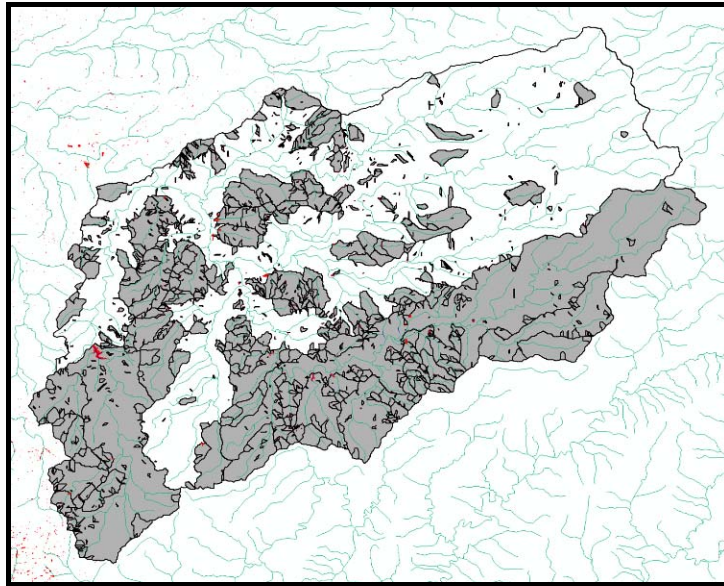


Figure 70. Farm dams (red) and their catchments (grey) for an example catchment in south-eastern Australia

The volume, surface area and contributing area of individual dams estimated from this method will allow constraints to be applied to a rainfall-runoff model with farm dam components such as the one proposed above. It is expected that this will reduce uncertainty in model calibration, and allow for more realistic representations of farm dams. Further, the network topology will allow for the identification and modelling of sub-catchments. In this way, it is envisaged that the spatial variability of farm dams in catchments will be resolved by modelling progressively smaller sub-catchments with a farm dam rainfall-runoff model.

## Activity 3

### **Investigate how best to adapt hydrological models to represent hydrologic non-stationarity and better simulate the range of streamflow characteristics during dry periods**

Often, conceptual rainfall-runoff models simulate dry years and low flow events poorly because calibration processes are typically biased to high flow events. Changing the bias to low flow events usually results in a reduction in skill at simulating high flow events. This activity examined the effects of using different objective functions and calibration periods to simulate runoff response during wet and dry periods.

#### **Data and methods**

The ten study catchments are located in the winter rainfall dominated region of Victoria, and the catchment areas vary between 540 km<sup>2</sup> and 1240 km<sup>2</sup> (Figure 71). The catchments are largely unregulated with no major storages or irrigation schemes, as determined from knowledge of the drainage systems, advice from state water agencies and interpretation of spatial images. All ten catchments have a very small number of farm dams which have minimal impact on streamflow.

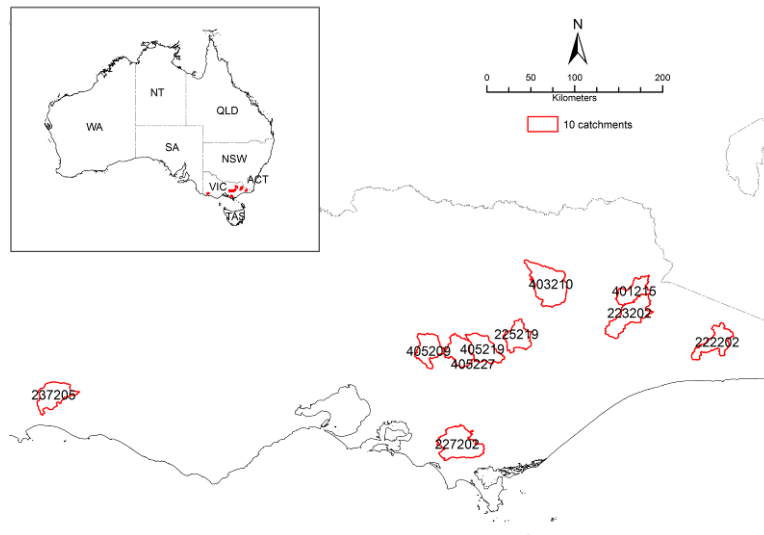


*Figure 71. Location of the ten catchments used in this activity*

The climate data were derived from the SILO Data Drill (Jeffrey et al., 2001) which provides surfaces of daily climate data for 0.05° grids (approximately 5 km x 5 km) across Australia, interpolated from point measurements made by the Australian Bureau of Meteorology.

The daily potential evaporation is calculated from the 0.05° climate data (incoming solar radiation, maximum and minimum temperature and actual vapour pressure) using Morton’s wet environment (or equilibrium evaporation or areal potential evaporation) algorithms (Morton, 1983). The potential evaporation used here is conceptually the upper limit of actual evaporation in the rainfall-runoff models. The streamflow data were collated as part of the Catchment Water Yield Estimation Tool (CWYET) project and were checked for errors to be usable in large-scale hydrological modelling (Vaze et al., 2010b). The main checks for errors include plotting time series and scatter plots of monthly rainfall and streamflow (and runoff coefficient) to identify inconsistency in the data and checking for recording errors (spikes in data, same data value for a long period, etc.).

Two conceptual daily rainfall-runoff models: Sacramento (Burnash et al., 1973) and GR4J (Perrin et al., 2003) were used in this study. The models are typical of lumped conceptual rainfall-runoff models, with interconnected storages and algorithms that mimic the hydrological processes used to describe movement of water into and out of storages. The input data into the models were daily rainfall and potential evaporation, and the models simulate daily runoff. Both the models have been widely used in Australia, Europe and the USA, including for regionalisation studies to predict runoff in ungauged catchments and for climate impact and land use change studies (Gan and Burges, 2006; Vaze and Teng, 2011; Oudin et al., 2008). The Sacramento model has 18 parameters and only 13 of these are calibrated (with five set to fixed values), and all the four parameters for the GR4J model were calibrated in this study.

The ten catchments used in this study have 30 years of continuous streamflow data (1978–2007) that was split equally into three ten year periods (P1: 1978–1987; P2: 1988–1997; P3: 1998–2007) for modelling (Table 12). The first two periods (P1 and P2) had average or above average mean annual rainfall and runoff and the last 10 years’ (P3) rainfall and runoff was significantly lower than P1 and P2. The mean annual rainfall for the ten catchments varied between 701 mm and 1466 mm with a median of 1126 mm for period P1, between 676 mm and 1451 mm with a median of 1137 mm for period P2 and between 639 mm and 1224 mm with a median of 1010 mm for period P3. There is only a median difference of 2 percent in mean annual rainfall between periods P1 and P2 (both periods have above average to average rainfall) with period P3 rainfall 10 percent lower than P1 and 12 percent lower than P2. The differences in rainfall between the three periods for the ten catchments are amplified in observed runoff with period P3 runoff 27 percent and 36 percent lower than for periods P1 and P2 respectively. The two hydrological models were calibrated for each of the three ten year periods using three objective functions. A one year warm-up period was used at the start of the calibration period.

Table 12. Modelling experiments carried out in this activity

Modelling experiment	Calibration period	Simulation period
Experiment 1	P1 (1978–1987)	P2 (1988–1997), P3 (1998–2007)
Experiment 2	P2 (1988–1997)	P1 (1978–1987), P3 (1998–2007)
Experiment 3	P3 (1998–2007)	P1 (1978–1987), P2 (1988–1997)

In the model calibration, the model parameters for both models were optimised to maximise three objective functions (OF1: *NSE* lower half of flow duration curve (FDC)-bias, OF2: *NSE* daily log flow-bias, OF3: daily *NSE*-bias) for the three periods (P1, P2, P3). The *NSE* lower half of FDC-bias objective function is a combination of ranked lower 50 percent of flows with an additional bias constraint on total volume and the *NSE* log flow-bias objective function is a combination of log of daily flows with an additional bias constraint on total volume. The *NSE*-bias objective function is a weighted combination of daily Nash-Sutcliffe (Nash and Sutcliffe, 1970) efficiency and a logarithmic function of bias and is given by

$$\text{Obj3} = NSE - 5|\ln(1 + B)|^{2.5}, \quad (6)$$

where *NSE* is the Nash-Sutcliffe efficiency of daily streamflow and *B* is the bias (total modelled error divided by observed total streamflow) (Viney et al., 2009). The coefficients of this equation control the severity and shape of the bias constraint penalty and they are chosen such that the models are calibrated predominantly to optimise *NSE* while ensuring a low bias in the total streamflow. The three objective functions used in this study are formulated such that in the model calibration, OF1 gives more weight to low flows; OF2 gives similar weight to all the flows whereas OF3 gives more weight to high and medium flows.

The modelling was undertaken at 0.05° grid cells to allow a better representation of the spatial patterns and gradients in the rainfall compared to a lumped catchment modelling approach. The daily runoff for each catchment in the model calibration (and simulation) was obtained by aggregating the modelled daily runoff for all the 0.05° grid cells in the catchment. The Shuffled Complex Evolution global optimisation method (Duan et al., 1993) followed by a local optimisation method (Rosenbrock, 1960), with multiple starting parameter sets, were used to calibrate the models.

The calibrated models for each of the three periods were used to simulate streamflow for the other two periods to investigate: (i) how the models calibrated for a wet periods (P1 and P2) perform on an independent wet (P2 and P1) and dry (P3) periods as well as how the models calibrated for a dry period (P3) perform on independent wet periods (P1 and P2), and (ii) to determine whether a model calibrated using a particular objective function which puts more weight on high or low flows is more suitable for simulating that particular flow characteristic in an independent simulation period. The performance of the two models in calibration and the calibrated models ability to simulate streamflow for the other two periods for high and low flows was assessed using four metrics: (1) daily *NSE*; (2) bias; (3) *NSE* of lower 30 percent of three day cumulative FDC; and (4) bias of lower 30 percent of daily FDC. The performance of the models against the four metrics used here provides an assessment of the ability of the models to simulate different streamflow characteristics that the models are calibrated against using the three objective functions.

## Results

The model calibration and simulation results for the ten catchments and the three objective functions for the Sacramento model are shown in Figure 72, and for GR4J in Figure 73. The performance of the Sacramento model in calibration and simulation against the four metrics is presented as box and whisker plots. The top row of plots are for daily *NSE* with the first three panels showing the simulation results for period P1 (1978–1987) when using calibrated parameters from periods P1, P2 and P3 respectively. As such, the first panel of plots shows the calibration results for P1 whereas the next two panels show the simulation results for P1 when using calibrated model parameters from periods P2 and P3. The three box and whiskers within each panel represent the three objective functions (first, second and third box and whisker showing results for OF1, OF2 and OF3 respectively). The next three panels (4, 5, 6)



The calibration results for daily bias for all three periods P1, P2 and P3 (Figure 73, second row, panels 1, 5, 9) show that the Sacramento model calibrated using all the three objective functions has very low bias. This is to be expected as we used total volumetric bias constraint within all three objective functions. The simulation results for the Sacramento model for period P1 when using model parameters calibrated for periods P2 and P3 (second row, panels 2, 3) show that the model parameters calibrated using all the three objective functions overestimate streamflow for P1 by about 10 percent.

The observed rainfall and streamflow in period P2 was slightly higher than that in period P1 whereas the rainfall and streamflow in period P3 was substantially lower than that in P1. The simulation results for period P2 when using calibrated model parameters for period P1 (second row, panel 4) showed that the model parameters calibrated using all three objective functions underestimated streamflow for P1 by about 10 percent. The simulation results for period P2 when using calibrated model parameters for period P3 (second row, panel 6) showed that the model parameters calibrated using OF1 underestimated streamflow for P1 (median of -4 percent) whereas model parameters calibrated using OF2 and OF3 overestimated streamflow for P1 (median of 3 percent and 1 percent respectively).

The simulation results for period P3 when using calibrated model parameters for period P1 (second row, panel 7) showed that model parameters calibrated using all the three objective functions underestimated streamflow for P1 by more than 10 percent. When using P2 calibrated model parameters to simulate streamflow for period P1, OF1 calibrated model parameters overestimated streamflow for P1 (median of 4 percent), OF2 calibrated model parameters underestimated streamflow for P1 (median of 6 percent) and calibrated model parameters from OF3 overestimated streamflow for P1 in some catchments and underestimated in others (median of 0 percent).

The simulation bias results for Sacramento showed that there was no clear under- or overestimation of flows when model parameters calibrated against wet (P1 and P2) or dry (P3) periods were used to simulate streamflow for an independent dry or wet period. The results for the GR4J model (Figure 73) showed a slight overestimation of streamflow when model parameters calibrated against a wet period were used to simulate streamflow for a dry period and a slight underestimation when model parameters calibrated against a dry period were used to simulate streamflow for a wet period. The results for GR4J model were in agreement with the findings of Coron et al. (2012). The difference in results between Sacramento and GR4J were in agreement with the findings of Vaze et al. (2010a) who showed that this consistent over or underestimation of flows when moving from drier/wetter calibration period to a wetter/drier simulation period can be model dependent.

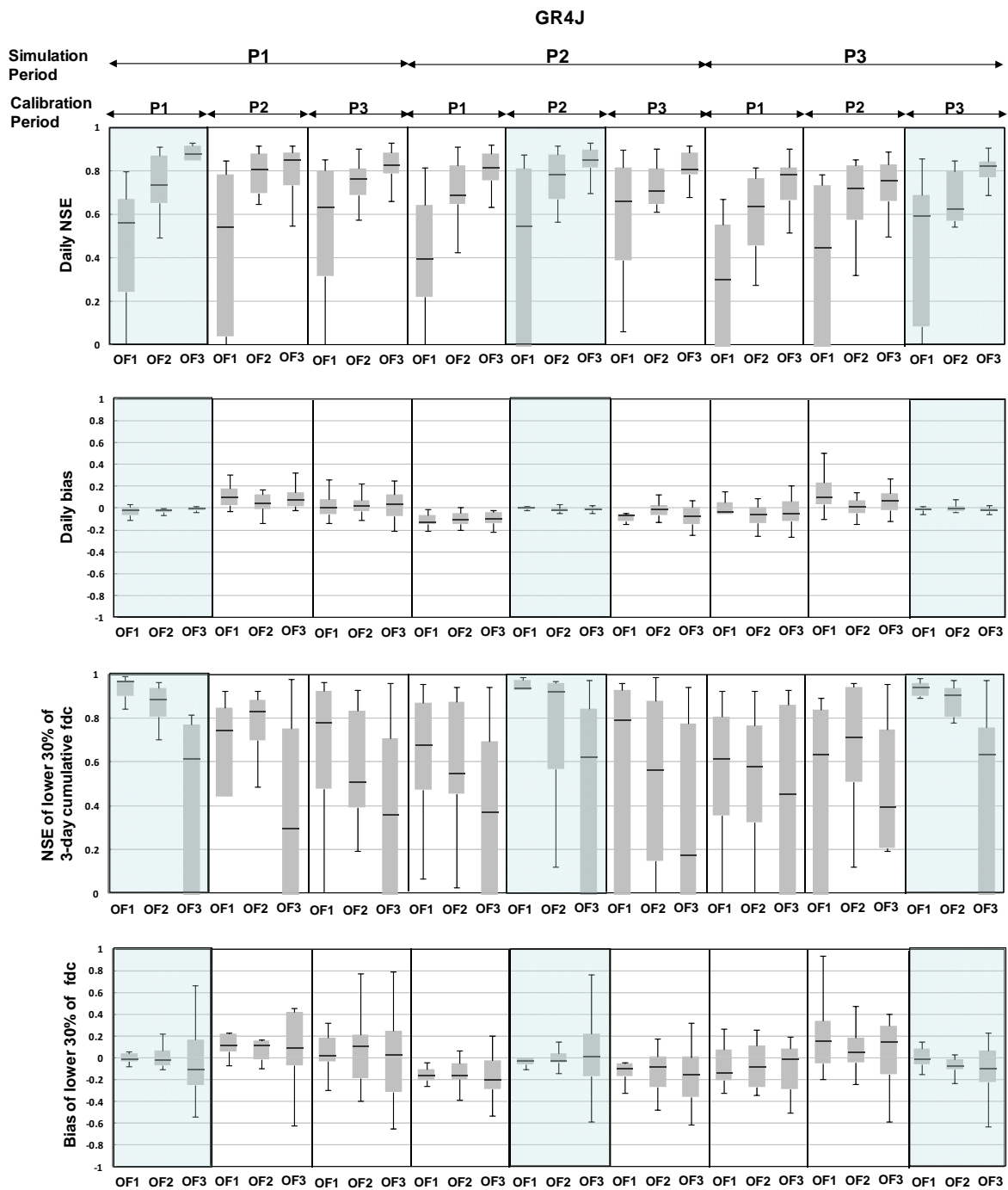


Figure 73. Calibration and simulation results for the GR4J model

The calibration results for *NSE* of lower 30 percent of 3-day cumulative FDC for all the three periods P1, P2 and P3 (Figure 2, third row, panels 1, 5, 9) show that the Sacramento model calibrated using OF1 performed extremely well for all the three periods (median value of 0.99 for all three periods). The calibration results for *NSE* of lower 30 percent of 3-day cumulative FDC for OF2 were reasonably good with median values of 0.94, 0.92 and 0.96 for P1, P2 and P3 respectively. The calibration results for OF3 were poorer than those for OF1 and OF2 with median values of 0.33, 0.61 and 0.62 for P1, P2 and P3 respectively. This is to be expected as OF3 puts more weight on medium to high flows; OF2 puts similar weight to all the flow values whereas OF1 puts all the weight towards the lower half of the FDC and disregarded medium and high flows. The simulation results for *NSE* of lower 30 percent of 3-day cumulative FDC for the Sacramento model for period P1 when using model parameters calibrated for period P2 (third row, panel 2) show

that the model parameters calibrated using OF3 performed better than those calibrated using OF1 and OF2. When using the calibrated model parameters from P3 to simulate streamflow for P1, OF2 calibrated parameters performed the best (median value of 0.84), the simulation results for OF1 were reasonable (median value of 0.48) with the simulation results for OF3 (median value of 0.19) substantially poorer than those from OF1 and OF2. Similar to the results for P1, there was no consistency in the simulation *NSE* of lower 30 percent of 3-day cumulative FDC results for the other two periods (P2 and P3) with different objective functions performing better for different periods. The simulation *NSE* of lower 30 percent of 3-day cumulative FDC results for the Sacramento model indicate that a model calibrated specifically against low flows does not necessarily perform better in simulating low flows for an independent period not used in model calibration. The results for the GR4J model were different from those from Sacramento as the results show that when GR4J was calibrated against low flows (OF1 and to some extent OF2), it performed better in simulating low flows over an independent period compared to the simulation when using a high flow objective function (OF3).

The calibration results for bias of lower 30 percent of FDC for all the three periods P1, P2 and P3 (Figure 2, bottom row, panels 1, 5, 9) show that the Sacramento model calibrated using OF1 perform extremely well with a median bias of about 0 percent with little to no over or underestimation. The results for OF2 were reasonably good with a slight overestimation for periods P1 and P3. The results for OF3 were poorer than those from OF1 and OF2 for P1 and P2. The performance of OF1 is expected to be good in calibration as the model parameters are optimised to reproduce the lower half of FDC with a total volumetric constraint. The simulation results for period P1 when using model parameters calibrated for period P2 (bottom row, panel 2) show that the model parameters calibrated using all the three objective functions overestimated streamflow for the lower 30 percent of FDC by 15 percent to 30 percent. When using the P3 calibrated model parameters, OF1 underestimated the flows whereas OF2 and OF3 both overestimated the flows with the median bias for OF1 and OF2 lower than that for OF3. The simulation results for period P2 when using calibrated model parameters from P1 showed that all three objective functions underestimated the lower 30 percent of P2 flows by about 20 percent. When using P3 calibrated model parameters for P2, OF1 and OF2 underestimated the flows whereas the median bias for OF3 was close to 0 percent with the flow being underestimated in some catchments and overestimated in others. The simulation results for P3 when using calibrated model parameters from P1 for all the three objective functions underestimated the lower 30 percent of flows. When using P2 calibrated model parameters, the lower 30 percent of P3 flows were overestimated for OF1 and OF2 and underestimated when using OF3. The simulation results for the Sacramento model for bias of the lower 30 percent of FDC when using the three objective functions do not provide any indication that models specifically calibrated to reproduce low flows can simulate low flows for an independent period better than models calibrated against a high flow objective function.

## Activity 4

### **Update runoff projections for SEA through rainfall-runoff model simulations with improved future climate projections**

Climate change projections were updated using improved methods for determining the impacts of a changing climate on future water availability. This included assessing the source of the large uncertainties in future projections of runoff. Much of this uncertainty was found to originate in the outputs from global climate models, with lesser amounts attributable to the choice of downscaling technique and hydrological model used (Teng et al., 2012).

The projected change in future mean annual precipitation and runoff across south-eastern Australia for a 1 °C global warming is shown in Figure 74. The median IPCC AR4 (IPCC, 2007) projection is a 1 °C warming by 2030 relative to 1990 and 2 °C warming by 2060 relative to 1990. The future climate (precipitation and potential evaporation) scenarios were obtained using the pattern scaling and daily scaling methods where the change in seasonal means are estimated from global climate model simulations for 2001–2100 and the historical climate data were scaled to reflect the changes in the seasonal means and daily precipitation distribution (Chiew et al., 2009). The scenarios were informed by simulations from 15 global climate models. The future daily precipitation and potential evaporation series were used to run a conceptual daily rainfall-runoff model (SIMHYD), using parameter values calibrated against

historical data. The hydrological modelling therefore only considered the runoff response to changes in the future climate.

The large range in the future runoff projections mainly reflects the uncertainty in the future projections of annual and seasonal precipitation. Nevertheless, the large majority of climate models indicate that the southern Murray–Darling Basin and Victoria will, on average, be drier in the future. All the climate models project a precipitation decline in winter when most of the runoff in this region occurs, translating to a considerable reduction in winter and annual runoff. The projections of precipitation decline in the cool season (late autumn and winter) which is consistent with expected changes in large-scale atmospheric and oceanic drivers of precipitation in this region in a warmer world. Averaged over the southern half of the region (south of 33° S), mean annual precipitation is projected to reduce by 0 to 9 percent (median of 4 percent) and mean annual runoff is projected to reduce by 1 to 24 percent (median of 12 percent) for a 1 °C global warming. There is less agreement between the climate models in the north. Averaged over the northern half of the region (north of 33° S), mean annual precipitation is projected to change by –12 percent to +4 percent (median of –3 percent) and mean annual runoff is projected to change by –30 percent to +14 percent (median of –10 percent) (Post and Moran, 2011). The projected decline, as well as the range of uncertainty, is larger for larger amounts of warming, and although not scaling exactly linearly (Post et al., 2011) is roughly twice as large for a 2 °C global warming.

Because of the very large variability in Australian river flows, the changes in the long-term average identified here are relatively small compared to this variability. The future climate will still be one that produces long wet and dry periods, but the projected decline in the long-term average in south-eastern Australia means that water resources systems will need to be able to cope with more frequent and potentially more severe and longer droughts. The projections in Figure 74 are best interpreted as changes relative to a long-term baseline climate. The use of a long-term baseline (including, where available, palaeo-hydroclimate data) is important to characterise the large variability over different time scales, whilst the projections here predict how these climate and runoff characteristics may change in a warmer climate.

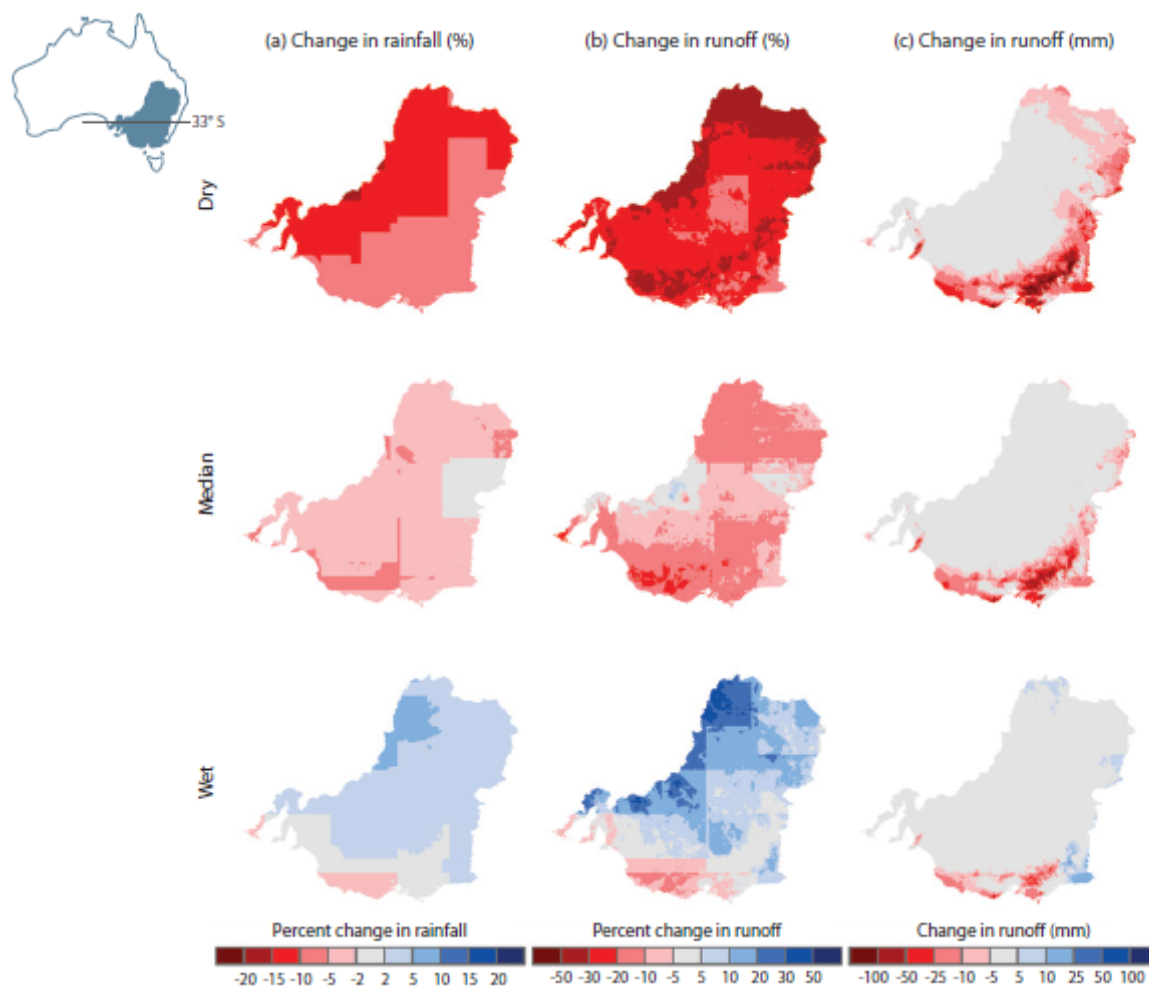


Figure 74. Projected median and range (10th and 90th percentiles) of change for (a) mean annual precipitation (% change); (b) mean annual runoff (% change); and (c) mean annual runoff (mm change) for a 1 °C global warming

## Conclusions

The effect of increasing temperatures on runoff in south-eastern Australia was assessed using a catchment scale empirical method, as well as continental projections of future runoff informed by global climate models. The results suggest that regression-based empirical methods should be performed at catchment scale; regression-based methods can potentially result in spatial scaling biases at larger scales (i.e. basin scale). In particular, year to year variability in annual temperatures appears to have a greater effect on runoff with increasing spatial scale, but this effect is apparently incompatible with Budyko theory of water and energy budgets in different climate zones. The effect of increases in annually averaged maximum temperatures is dependent on the aridity of the catchment, with relatively larger effects in wetter catchments.

Catchment response to drought conditions was assessed in Activity 2 with TOPOG, a dynamic and physically-based spatially explicit model. Use of TOPOG allows for modelling of saturated areas within catchments shows that runoff production is closely linked, and mostly linearly related, to saturated area. During the Millennium drought in the study catchment, catchment storage and saturated area dropped below any previous level in the past 60 years. Modelled results indicate that when the average saturated area of a catchment is very low, runoff response becomes non-linear. Rainfall in a catchment during a very dry period acts to replenish catchment storages rather than produce

runoff. Based on simulations of alternative climate sequences starting from a very dry initial condition, the replenishment of catchment water storage in order to generate an average runoff response would take between 10 and 20 years of median or above average rainfall.

One possible source of model bias is the effect of farm dams. A modification to SIMHYD was proposed, in which farm dam storage is taken as an extra reservoir at the catchment outlet, intercepting surface runoff and interflow. The inclusion of this farm dam component showed modest improvements in modelled (validated) runoff. Improvement to this component is warranted, particularly the representations of evaporation and usage, and spatial data has been analysed for use in constraining model parameters, and for providing network structure of sub-catchments and their upstream dams.

Activity 3 evaluated the ability of commonly used hydrological models at simulating streamflow under variable climate conditions for different streamflow characteristics. The simulation results for the Sacramento model showed that model parameters calibrated using an objective function which gives more weight to medium and high flows are suitable for simulating streamflow for an independent period with a reasonably good calibration. Also, objective functions that put more weight on low flows are not suitable for simulating streamflow for an independent period if the metric of interest is daily streamflow. In some cases calibrating to low flows can give better simulation of low flows in another period, but at the expense of accuracy in modelling high flows. The simulation bias results for the Sacramento model show that there is no clear under- or overestimation of flows when model parameters calibrated against wet or dry periods are used to simulate streamflow for an independent dry or wet period. The results for the GR4J model showed a slight overestimation of streamflow when model parameters calibrated against a wet period were used to simulate streamflow for a dry period. Thus bias in runoff during dry periods appears to be model dependent.

Updated runoff projections for south-eastern Australia were developed in Activity 4. Assessment of the sources of uncertainty indicates that most uncertainty in future runoff projections originates in the outputs from global climate models. However, most of the climate models indicate that the southern MDB and Victoria will, on average, be drier in the future, with a reduction in mean annual runoff of 2 to 22 percent (median reduction of 12 percent) for a 1 °C global warming. All the climate models project a precipitation decline in winter when most of the runoff in this region occurs, translating to a considerable reduction in winter and annual runoff. There is less agreement between the climate models in the north with a range of future runoff in the future, with a projected change in mean annual runoff of -29 percent to +12 percent (median of -10 percent) for a 1 °C global warming.

## Links to other projects

Project 2.2 is closely related to and used contextual information from the projects in Theme 1. Development and testing of rainfall and temperature sensitivities in Activity 1 were compared and tested against CABLE model outputs from Project 1.2. Future rainfall and runoff simulations under future climate projections (Activity 4) were developed closely with Project 2.1.

## CHAPTER 6: PROJECT 3.1

### Advancing seasonal predictions for south-eastern Australia

Eun-Pa Lim, Harry Hendon, Guo Liu and Griffith Young

## Abstract

Record high spring rainfall in eastern Australia in 2010 was assessed against historical relationships for 1960–2009. The record rainfall in 2010 is determined to have occurred largely as a result of an extraordinary La Niña event. Although the bulk of the rainfall can be attributed to the La Niña event, trends in sea-surface temperature to the north of Australia were assessed to have contributed about 10 percent of the total rainfall anomaly averaged across eastern Australia. Regionally in the northern portions of eastern Australia the contribution from the trend in SST accounts for 25 percent of the rainfall in 2010. The behaviour of the Southern Annular Mode (SAM), which exhibited record high polarity in spring 2010, was assessed to have contributed about 8 percent of the area-mean eastern Australian rainfall but upwards of 50 percent regionally in central NSW. To the degree that the rainfall was a result of the La Niña, the record rainfall in spring 2010 was largely predictable given the demonstrated capability to predict SST variations associated with El Niño/La Niña. However, even after accounting for the behaviour of the SAM and SST trends, the rainfall received in 2010 was at the upper limit of what would typically be expected for a La Niña event of the magnitude that occurred in 2010. Thus, we concede that the 2010 event was unusual at least from the perspective of a linear attribution. For instance, the additional rainfall that was received because La Niña was operating on a warmer basic state due to the SST trend to the north of Australia would not be accounted for. Ongoing model studies are addressing this issue.

Seasonal prediction of the 2010 rainfall anomaly was demonstrated to a lead time of 3 months with the POAMA2.4 model. Forecast skill derives from a good capability to predict the La Niña SST anomalies in the tropical Pacific, as well as those in the Indian Ocean associated with the negative Indian Ocean Dipole (IOD) event. Interestingly, SAM appears to be a source of longer lead predictability because of the strong boundary forcing provided by the La Niña but atmospheric initial conditions (the index of SAM was already high throughout late winter and spring 2010) also appear to provide some predictability.

## Background

After a 15 year dry period beginning in the late 1990s (referred to as the Millennium drought), south-eastern Australia (SEA) experienced its wettest recorded spring in 2010. Wet conditions continued into the summer of 2010/11. The enormity of the spring/summer rainfall resulted in excess of 80 percent capacity water storage in the Murray–Darling Basin by the end of 2010. This project focused on understanding the causes of the extreme wet conditions in spring/summer 2010/11, with an eye towards understanding predictability of such extreme wet events. This study was conducted in light of the probable role of climate change in promoting the Millennium drought but noting that spring season rainfall is notoriously variable because it is the season when El Niño/La Niña exerts its greatest control on rainfall variability in SEA. The cause of the record wet conditions has been presumed to be the strong La Niña event that developed in mid-2010, however, it is an open question as to whether the enormity of the rainfall was commensurate with the magnitude of the La Niña event and if other factors were at play, including the recent warming trends in the seas surrounding Australia. By identifying the causes of the record wet conditions, this project assessed the potential to predict extreme wet periods such as spring 2010.

# Objectives

Assess possible roles of El Niño – Southern Oscillation (ENSO), IOD, SAM and the warming trend in the oceans to the north of Australia for producing extreme wet conditions in 2010.

Evaluate POAMA forecasts for the behaviour of large-scale climate drivers and SEA during spring 2010 and explore the forecast sensitivity to atmospheric and land surface initial conditions.

# Methods

- Characterise the observed anomalies of sea-surface temperatures (SST) and sea level pressure (SLP) and assess their relationship with rainfall in 2010 in comparison to past behaviour. Document the role of key drivers of climate variability in SEA using indices such as El Niño/La Niña and the Southern Annular Mode. Attribute causes of extreme rainfall by reconstruction of rainfall anomalies using key SST and SAM indices. Assess the impact of trends in these indices by doing the reconstruction with and without the trend.
- Evaluate hindcasts (1960–2009) and predictions (2010) from POAMA of the key drivers of climate variability in SEA (i.e., ENSO, IOD, SAM) and evaluate predictions of SEA rainfall for 2010 based on the capability to predict these drivers. Explore prediction of other extreme wet years.
- Conduct forecast experiments for spring 2010 to determine sensitivity to atmosphere and land surface initial conditions. Three different experiments were designed: 1) initialise POAMA2.4 (hereafter, POAMA) forecasts with 2010 SST and land surface conditions but random atmosphere conditions to see the impact of atmosphere initial conditions, 2) initialise POAMA forecast with 2010 SST and atmospheric initial conditions but use random land surface conditions to see the impact of land surface initial conditions, and 3) initialise POAMA with 2010 atmosphere and land surface conditions but random ocean conditions to understand the predictability of 2010 SAM based on ENSO.

# Results

## Understanding the spring rainfall of 2010 and its predictability

Australia as a whole and especially eastern Australia in 2010 experienced its wettest spring (September to November) since 1900 (Figure 75). Mean rainfall across the country was 125 percent of average, with the country-wide average of 163 mm breaking the previous record of 140 mm set in 1975. Wet conditions were widespread across the country and SEA except for the south-east coastal region of Gippsland. The enormity of the subsequent rainfall in spring 2010, especially in the Murray–Darling Basin which received more than double its long-term mean spring rainfall (235 mm compared to a long-term mean of 114 mm), was reflected in the impact on water storage in the Murray–Darling Basin; at the start of 2010 storage was 26 percent of the total capacity of 35 000 GL but exceeded 80 percent of capacity by December 2010. The extreme wet conditions in the east of Australia extended (and even intensified in some regions) into austral summer 2010/11, when devastating floods occurred in parts of New South Wales and Queensland in December 2010 and early January 2011 and the state of Victoria experienced by far its wettest summer on record. The initial focus of this study was on the wet conditions during spring because spring rainfall is usually more important and predictable than summer rainfall. However, we will make some preliminary assessments of causes and predictability of summer rainfall in 2011.

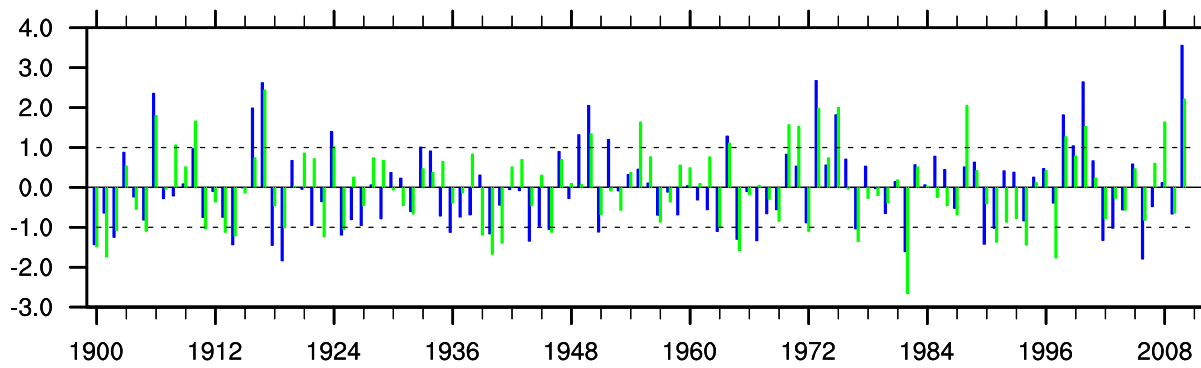


Figure 75. Standardised eastern Australian area averaged rainfall anomaly (east of 135° E; blue) and the SOI (green) calculated with respect to the 30 year reference period 1961–1990 (Jones et al., 2009)

A number of factors contributed to the record spring rainfall in SEA in spring/summer 2010/11. Importantly and foremost, 2010 experienced the strongest La Niña event in the past 50 years, as judged by the magnitude of the positive swing in the Southern Oscillation Index (SOI; Figure 75) and the appearance of strong negative SST anomalies in the equatorial central Pacific and positive anomalies in the western Pacific (Figure 76a). The magnitude of these cold/warm SST anomalies was captured by strong negative loading on the first empirical orthogonal function of tropical Pacific SST (Figure 77a), which showed the strongest negative loading since 1960. Additionally, the cold La Niña conditions in the Pacific were shifted westward compared to the location of their El Niño counterparts, which was reflected by a strong loading on the second empirical orthogonal function of tropical Pacific SSTs (Figure 77b). This westward shift of the cold anomalies in the Pacific during La Niña is known to increase the impact of the El Niño – Southern Oscillation (ENSO) on Australian rainfall (Wang and Hendon, 2007). The Indian Ocean Dipole was also strongly negative due to warm SSTs in the eastern Indian Ocean (Figure 76a) and was depicted by the strong negative loading on the Dipole Mode Index (DMI) in Figure 77c. A negative IOD should also contribute to increased rainfall across southern portions of Australia (e.g. Cai et al., 2011). SSTs to the north of Australia, which also promote increased rainfall in north-eastern Australia, were also high (Figure 76a), and were quantified by the near-record loading on the north Australia SST index (SSTnAU: mean SST over 110–160° E, 10° S–equator; Figure 77d). The coincidence of all of these features in the SST is perhaps not surprising since a negative IOD with positive SST anomalies to the north of Australia and a westward shift of the SST anomalies in the Pacific relative to El Niño typically occur during La Niña conditions (Figure 76b) but they all were large and provided the ‘perfect’ set of conditions to promote high rainfall in eastern Australia in 2010 (Figure 76c).

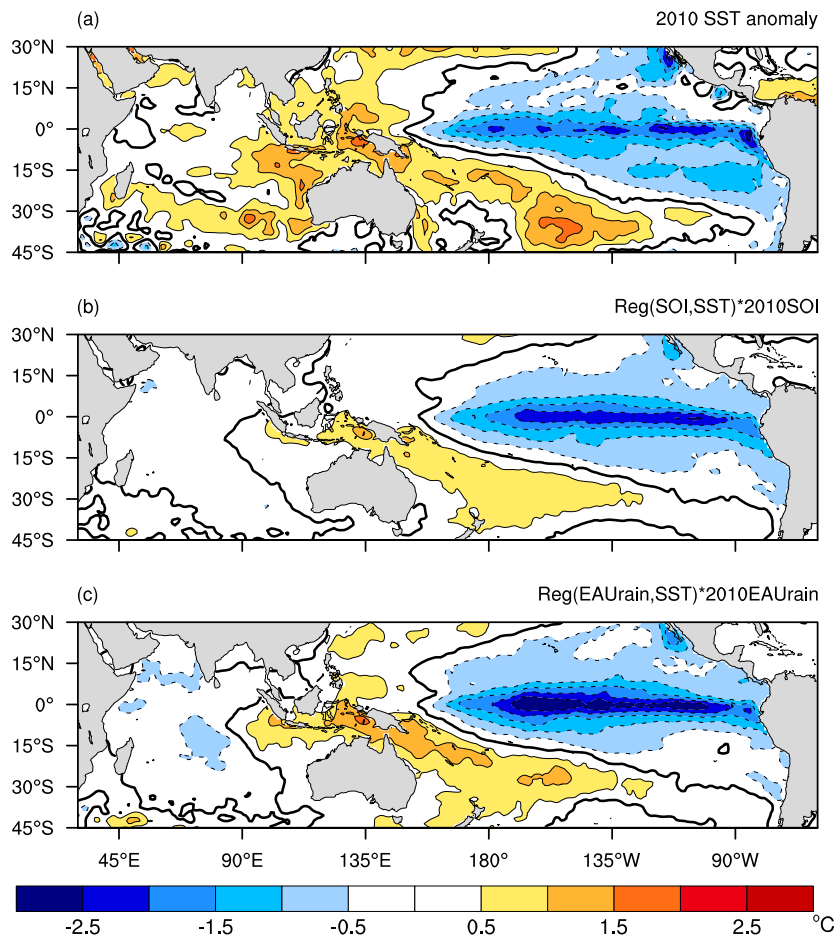


Figure 76. (a) Seasonal mean sea-surface temperature (SST) anomaly for September, October, November 2010 based on the Hurrell SST analysis (Hurrell et al., 2008), (b) reconstruction of September, October, November 2010 SST anomaly based on regression of SST onto the SOI index for 1960–2009 and then scaled by the magnitude of 2010 SOI in September, October, November, and (c) as in (b) but regression of SST onto a time series of eastern Australian rainfall (mean rainfall east of 135E) for 1960–2009 and then scaled by the magnitude of the observed eastern Australian rainfall anomaly in September, October, November 2010

Although La Niña conditions in the tropical Indo-Pacific were well established in 2010, inspection of the sea level pressure anomaly for 2010 (Figure 78a) indicated that south of Australia experienced higher than normal surface pressure rather than the usual lower than normal surface pressure that should accompany La Niña conditions (Figure 78b). This discrepancy is accounted for by the behaviour of the Southern Annular Mode, which was a record-positive in spring 2010 (Figure 77e). The high phase of SAM is associated with a poleward shift of the extra-tropical jet stream and results in anomalous easterly flow across sub-tropical Australia. During springtime, these anomalous easterlies are associated with increased rainfall across much of sub-tropical eastern Australia (Hendon et al., 2007). The dominance of the SAM for the extra-tropical mean sea level pressure anomaly in 2010 is demonstrated in Figure 78c, which shows that the 2010 SLP anomaly reconstructed based on the historical relationship with the SAM index. Importantly, high SLP to the south of Australia during this extreme La Niña event is accounted for by the behaviour of the SAM. Reconstruction of the rainfall using SST and SAM indices (discussed further below) indicates that the record high SAM contributed approximately 8 percent of the total springtime rainfall anomaly in eastern Australia, up to 20 percent of the anomaly in SEA, and up to 50 percent of the regional rainfall on the central eastern seaboard.

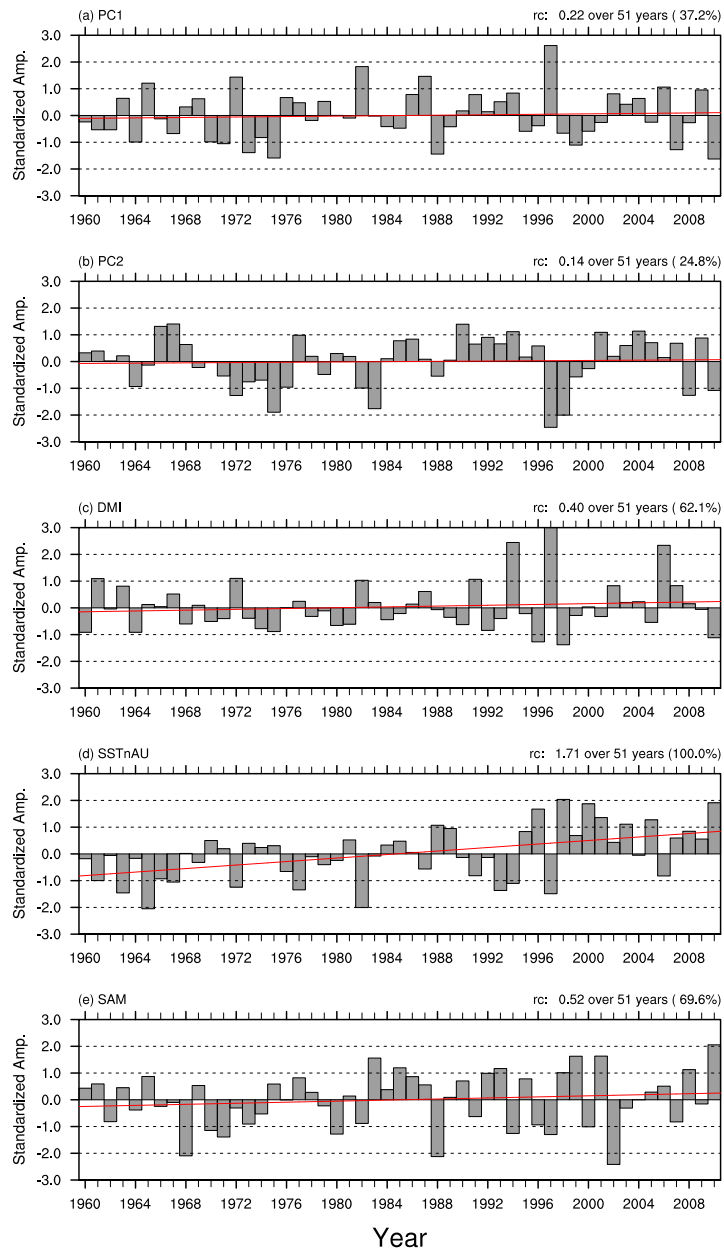


Figure 77. Time series (grey bars) of (a) SST PC1, (b) SST PC2, (c) the DMI, (d) SSTnAU and (e) the SAM index overlaid with trend lines (red) computed over the period of 1960–2010. The total change attributed to the trend over the 51 years is indicated along with its statistical significance of the trend on the upper right of each graph

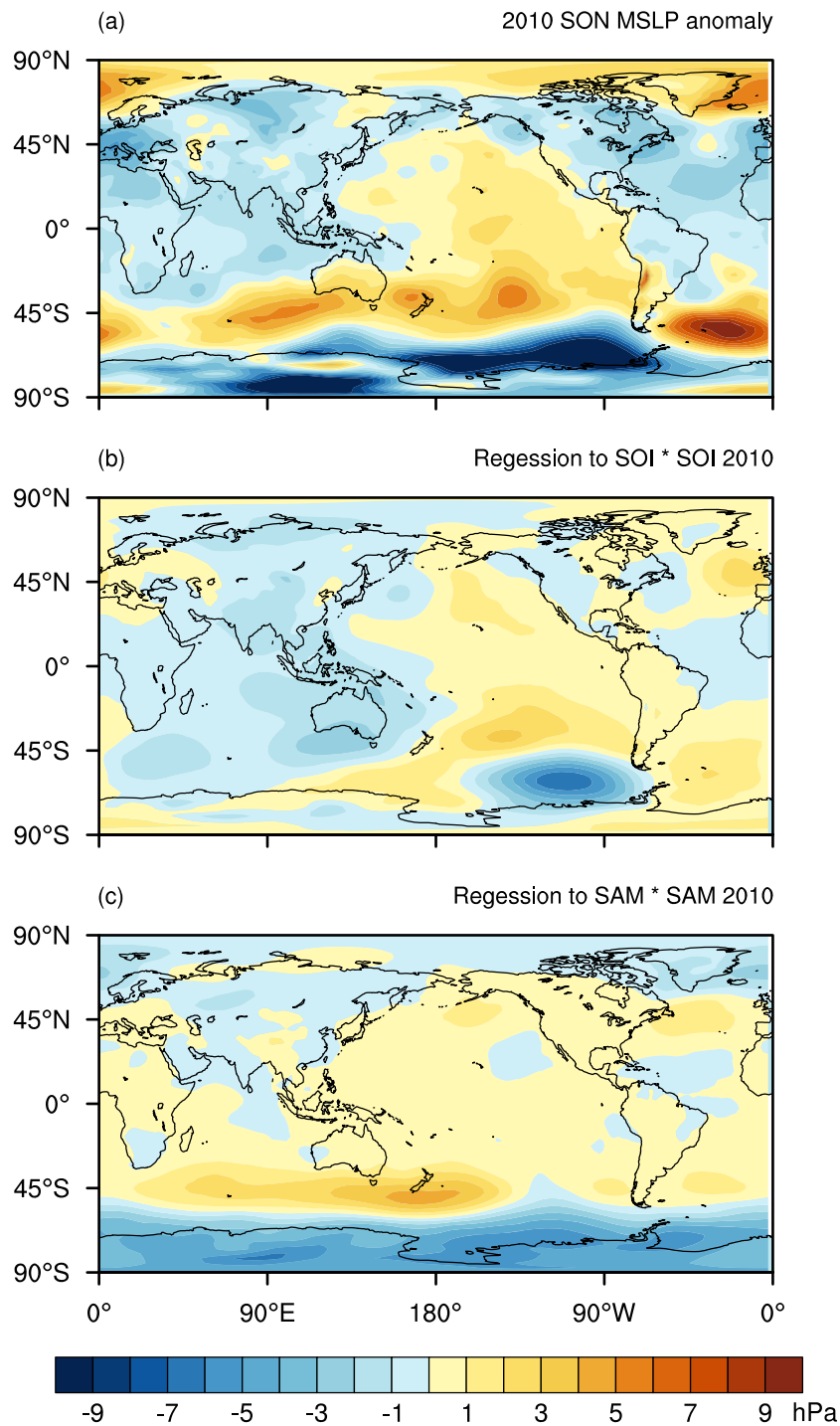


Figure 78. (a) Global MSLP anomaly in 2010 September, October, November (SON) from NCEP reanalyses. (b) Reconstruction of 2010 September, October, November MSLP anomaly based on the regressed relationship with the SOI during 1960–2009 and then scaled by the SOI anomaly in September, October, November 2010. (c) As in (b) except for regression onto the SAM. Colour shading interval is 1 hPa

Further investigation into the role of the SAM indicated the profound impact it can have on the climate conditions in SEA that are experienced during El Niño and La Niña. The magnitude and even the sign of the surface pressure anomaly over and to the south of Australia during El Niño/La Niña depends on the state of SAM (Figure 79). Lowest

pressures occur during La Niña when SAM is low (upper right Figure 79), while high SAM during La Niña as occurred in 2010 yields the opposite sign (lower right Figure 79). A similar, though not quite as dramatic, impact occurs for El Niño events (left hand column in Figure 79): high SAM magnifies the El Niño induced high pressure over southern Australia while low SAM largely mitigates it. This large impact of the state of SAM on the surface pressure pattern during El Niño/La Niña events translates to a similar profound impact on Australian rainfall (Figure 80). Low SAM during La Niña greatly reduces wet conditions across central eastern Australia, while high SAM during La Niña results in the wettest conditions there (Figure 80 right column). A similar impact occurs during El Niño, with strongest dry conditions in central eastern Australia occurring during El Niño with low SAM, while the occurrence of high SAM during El Niño almost mitigates dry conditions in the central east (Figure 80 left column). To the degree that SAM is unpredictable, the seasonal behaviour of SAM contributes importantly to inter-El Niño variations of the climate anomalies that are experienced across SEA.

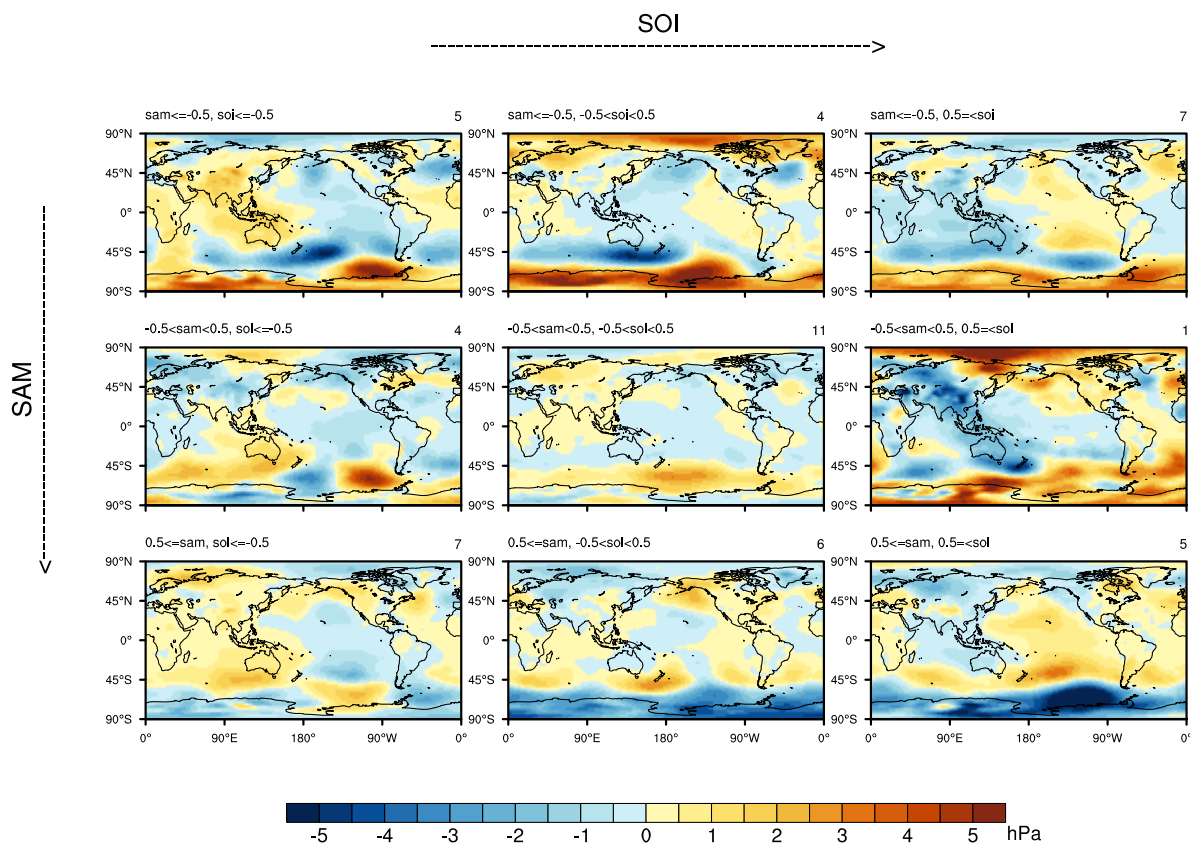


Figure 79. Composites of MSLP anomalies in September, October, November for negative ( $\leq -0.5$ ), neutral ( $-0.5 < < 0.5$ ) and positive ( $\geq 0.5$ ) events of SOI and SAM. MSLP data are from NCEP-NCAR reanalyses 1960–2010. Colour shading indicates MSLP anomalies with 0.5 hPa interval. The number of samples in each category is shown in the upper right of each map

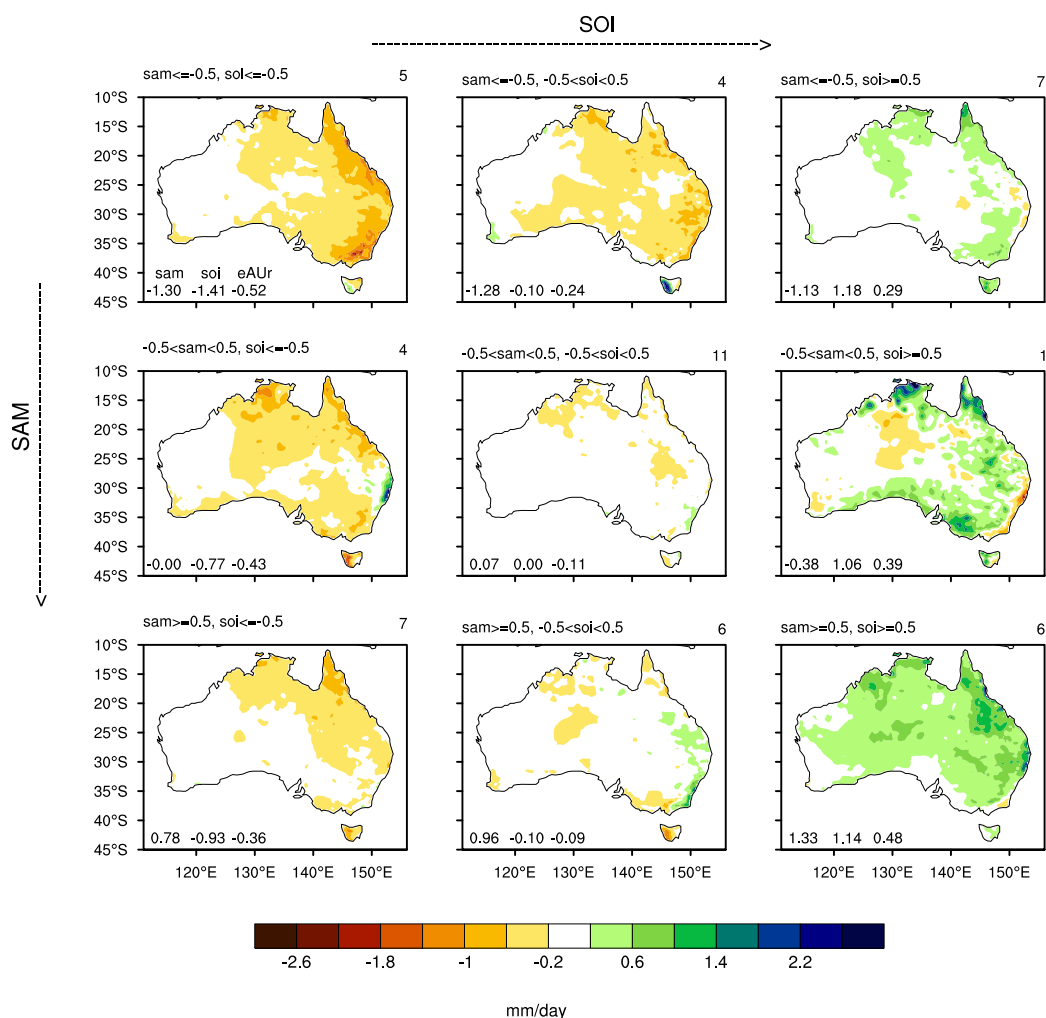


Figure 80. Composites of rainfall anomalies in September, October, November for negative ( $\leq -0.5$ ), neutral ( $-0.5 < < 0.5$ ) and positive ( $\geq 0.5$ ) events of SOI and SAM. Rainfall anomalies are from the AWAP analyses 1960–2010. Colour shading indicates rainfall anomalies with 0.4 mm/day shading interval. The number of samples in each category is shown in the upper right of each map. The mean amplitudes of standardised SAM and SOI and raw eastern Australia area averaged rainfall for each category are displayed at the bottom left in each map

In order to provide insight into the predictability of the 2010 spring rainfall and to ascertain the degree to which the rainfall was commensurate with what should have fallen based on historical relationships with SST and the SAM, we reconstructed rainfall with a multiple linear regression using as predictors the key SST indices and the SAM index displayed in Figure 77. We also reconstructed the SOI using the SST indices in order to ascertain whether the large positive swing in the SOI should have been anticipated by the occurrence of La Niña conditions. The regression relations were cross-validated using leave-one-out technique. The time series of observed and reconstructed SOI and eastern Australian rainfall are displayed in Figure 81. The explained variance of the reconstruction for the observed SOI over the period 1960–2009 is very high ( $r^2=0.86$ ), indicating that the Southern Oscillation is largely determined by the variations of SST associated with ENSO. The magnitude of the reconstructed SOI anomaly for 2010 was very close to the observed, indicating that the large positive excursion of the SOI in 2010 was commensurate with the magnitude of the La Niña event as judged by the anomalous state of tropical SST. The contribution of the trend in SST, in particular the warming SST to the north of Australia (the trend in the SST indices is indicated by the red lines in Figure 77) to the magnitude of the SOI in 2010 was found to be approximately 9 percent.

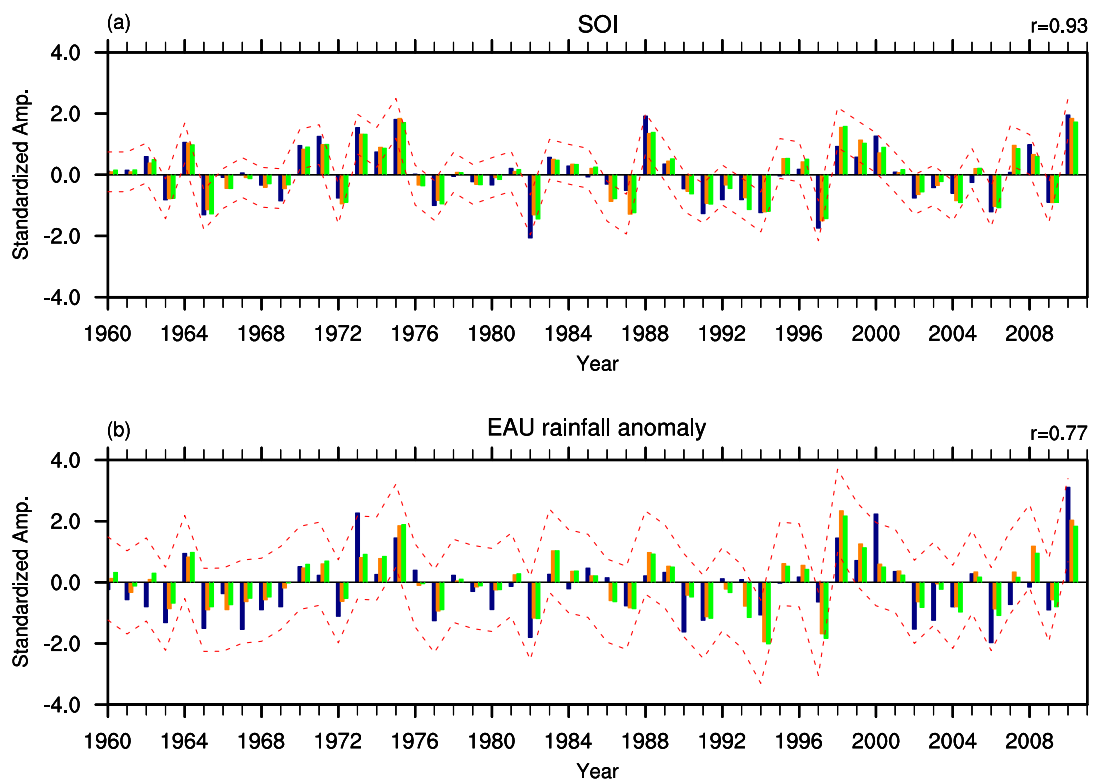


Figure 81. Observed (blue bars) and predicted (orange and green bars) time series of SOI and eastern Australia area averaged rainfall (EAU) in September, October, November. (a) Prediction of SOI was made using multiple linear regression onto SST PC1, PC2, DMI and SSTnAU index including trend (orange) and detrended (green). Predictions/regressions were formed with leave-one-out cross-validation. The correlation of the prediction including the trend with the observed values (using cross validation) is displayed in upper right of the panel. Red dotted lines indicate 95% prediction interval. (b) As in (a) except for eastern Australia rainfall predicted using SST PC1 and PC2, the DMI, SSTnAU and the SAM indices. Prediction of eastern Australia area averaged rainfall was made in the same manner as that of SOI but with the SAM index as an additional predictor

Reconstruction for eastern Australian rainfall using the SST indices and the SAM index was also successful, although the explained variance of the observed rainfall times series for the period 1960–2009 was lower than for the SOI ( $r^2=0.56$  compared to 0.86), indicating the challenge of accounting for a noisy process like rainfall. Nonetheless, the reconstructed anomaly for 2010 (Figure 81b), although being some 40 percent weaker than observed, fell within the error bars of what should have occurred for a La Niña event with the magnitude observed in 2010. Hence, we conclude that the extreme rainfall for eastern Australia in 2010 was largely accounted for by the extreme magnitude of the La Niña event, in conjunction with the record-positive excursion of the SAM. The trend in SST to the north of Australia was assessed to have contributed about 10 percent of the total anomaly in eastern Australia rainfall. As mentioned above, about 8 percent of the reconstructed rainfall was due to the SAM. Regionally, the SAM contribution approached 50 percent in central NSW. This component due to the SAM is potentially not predictable because the SAM is viewed to be largely an internal process to the atmosphere. However, as discussed below, the association of SAM with La Niña, especially extreme La Niña events such as 2010, may be a source of seasonal climate predictability.

The regional reconstruction of rainfall (using the same predictors as for area-mean rainfall) also largely encompassed the observed rainfall anomaly in 2010 for most of SEA, but in portions of central inland NSW and Queensland significantly more rain fell than would have been anticipated by the historical relationship with SST and the SAM. Whereas the contribution of the warming trend in SST to the north of Australia to the area-mean rainfall in 2010 was determined to be of the order of 10 percent (discussed above), it was assessed to have contributed up to 25 percent of the observed rainfall in the northern portion of the MDB. In other words, up to 25 percent more rainfall occurred

regionally in central NSW/Queensland than has typically occurred for past La Niña events of this magnitude, because of the warming SSTs to the north of Australia. However, as discussed further below, the SST trend was assessed to have acted to suppress rainfall in the southern part of SEA while increasing rainfall to the north (hence the contribution to the area-mean rainfall anomaly was only 10 percent). The mechanism by which the trend in SST acts to enhance rainfall to the north and suppress rainfall in SEA needs to be determined.

The contribution to the total rainfall anomaly by the individual predictors is provided in the top row of Figure 82, which displays the individual regression coefficients multiplied by their predictor values in 2010. A cursory examination of Figure 82 suggests that all of the predictors played a prominent role in generating the rainfall anomaly in eastern Australia in 2010. The relative contribution, in descending order, would appear to be the SAM, SSTnAU (especially for the northern portions of Australia), SST PC1, SST PC2, and the IOD (primarily for the south-east). However, because the predictors are not completely independent, contributions from covariance of the predictors are spread between the associated regression coefficients. In particular, SSTnAU and the DMI covary with SST PC1 and to a lesser degree, with SST PC2, which reflects that the positive IOD and cold SST to the north of Australia tend to develop during El Niño (and vice versa for La Niña). In order to highlight the independent contributions of SSTnAU and the DMI to rainfall beyond their covariation with SST PC1 and PC2, we formed the bivariate regression using SST PC1 and PC2, and then formed the regression of rainfall onto the DMI, SSTnAU and SAM holding SST PC1 and PC2 fixed (lower row of Figure 82). Comparing with the top row of Figure 82, it is immediately apparent that the contribution by SST PC2 in the bivariate regression is nearly identical to that from the full multiple regressions because there is little covariation of PC2 with the other predictors and no covariation with PC1. However, the coefficient for PC1 from the bivariate regression (Figure 82f) now shows much larger loading than does the multiple regression (Figure 82a) because all of the contribution due to the covariation of SSTnAU and the DMI with SST PC1 is now included.

The remaining three panels of Figure 82 are the partial regressions onto the DMI, SSTnAU and the SAM after removing the covarying component due to SST PC1 and PC2. The independent contribution of the DMI in 2010 is now, importantly, revealed to be very small (Figure 82h, but still positive across SE as would be expected for a negative IOD event). In contrast, the independent contribution of SSTnAU (Figure 82i) is only reduced by about 50 percent compared to what was inferred by the multiple regression (Figure 82d). In other words, about 50 percent of the contribution to the rainfall anomaly in 2010 by SSTnAU is due to the variation of SSTnAU that is independent of La Niña. This independent contribution accounts for up to 25 percent of the regional anomaly in north-eastern Australia. Because of the relatively small covariation of the SAM with SST PC1, the independent contribution of the SAM (Figure 82j) is nearly identical to that implied by the multiple regression (Figure 82e).

Comparing the top and bottom rows of Figure 82 leads to the conclusion that the major contribution to the rainfall anomaly across eastern Australia in 2010 was the occurrence of La Niña (which includes the occurrence of a negative IOD event as encompassed by a negative DMI and positive SSTs to the north of Australia as embodied in positive SSTnAU), a westward shift of the La Niña SST anomalies (as embodied by a negative loading onto SST PC2), and a strong positive SAM (especially for the central east coast). The variation of SSTnAU that is independent of the occurrence of the La Niña event accounts for about half of the total contribution by SSTnAU (Figure 82). This independent contribution is due primarily to the trend in SSTnAU, which itself accounts for about half of the magnitude of the SSTnAU anomaly in 2010 (the other half being due to La Niña; not shown).

These results for September, October, November 2010 are summarised in Hendon et al. (submitted)

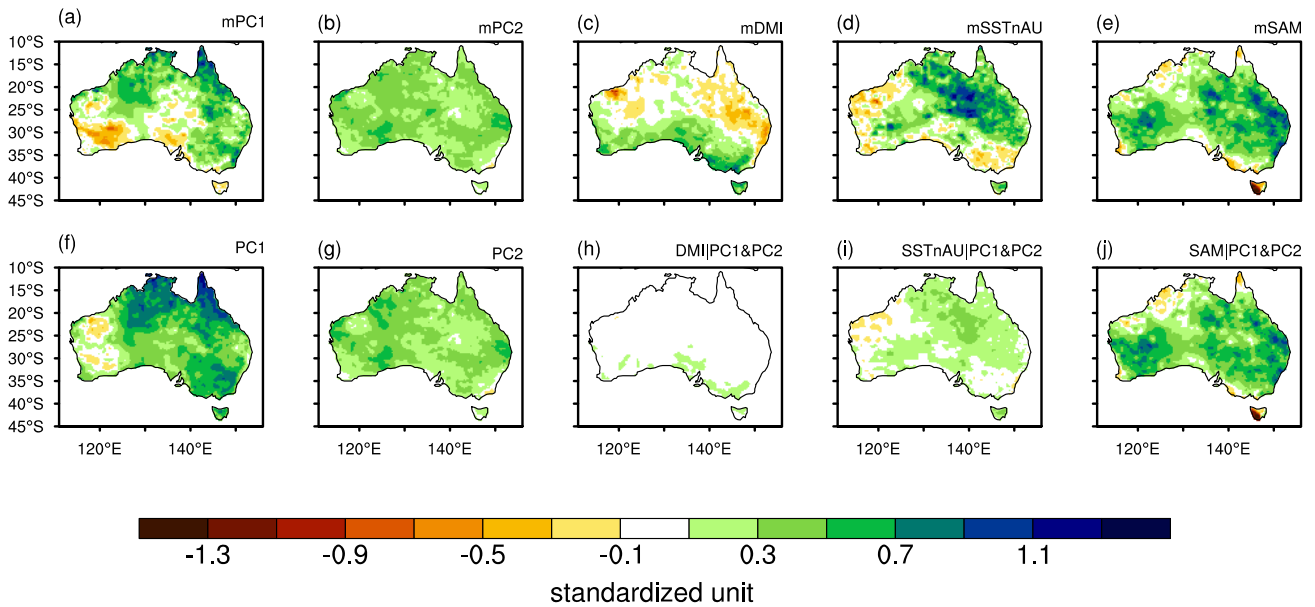


Figure 82. Top row (a) to (e): Values of the individual multiple linear regression coefficients when multiplied by the magnitudes of each predictor in September, October, November 2010. Bottom row (f) to (g): Values of the bivariate regression coefficients in 2010 for (f) PC1 and (g) PC2. The partial regression coefficients after removing the influence of SST PC1 and PC2 are shown for (h) DMI, (i) SSTnAU, and (j) the SAM. Colour shading interval is 0.2

We also reconstructed the SOI and area-mean rainfall for summer 2010/11 with the same predictors in order to understand the extreme wet conditions in summer 2010/11 (Figure 83). The explained variance of the reconstructed SOI and eastern Australian rainfall in summer were much lower than those in spring ( $r^2 = 74$  percent for SOI and  $r^2 = 20$  percent for rainfall as compared to 86 percent and 50 percent in spring, respectively), which reflects the much weaker impact of ENSO on summer rainfall with larger uncertainty as compared to spring. In this regard, the extreme wet conditions in SEA in summer 2010/11 were highly unusual but still within the error bars of what would have been historically expected based on La Niña events of the magnitude of 2010/11 (the error bars are large due to the weak signal). Also, Figure 83b indicates that trend in predictors for the summer season, (primarily due to SST north of Australia), has a drying effect on eastern Australia, which is the opposite of its role in spring rainfall. Therefore, the causes of the extreme rainfall in 2010/11 summer cannot be attributed to the same causes of that in 2010 spring, and further investigation is necessary to better understand the 2010/11 summer rainfall episode.

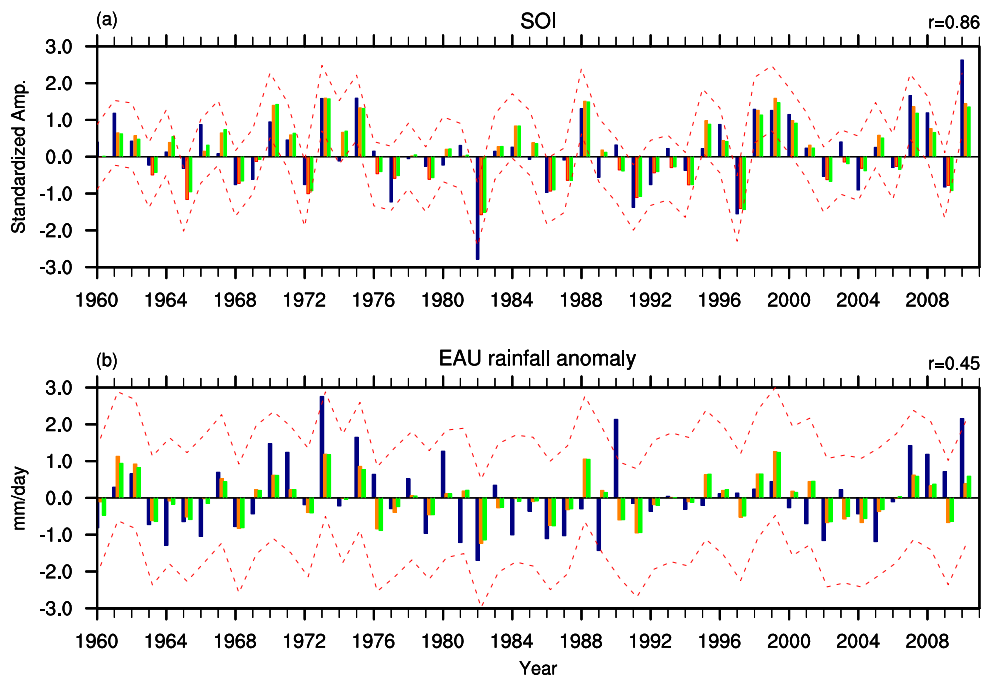


Figure 83. The same as Figure 81 except for December, January, February

### Assessing predictions of spring 2010

The strong 2010 La Niña and associated record wet conditions over Australia provided a challenging but excellent opportunity to test the performance of POAMA2 seasonal forecasts. Credible forecasts for wet conditions in south-eastern Australia for spring 2010 were provided by the POAMA2 system to a lead time of about 6 months. Predictions for a 0 and 3 month lead time are shown in Figure 84. These high rainfall forecasts were a result of POAMA2 correctly predicting the strong La Niña conditions in the Pacific Ocean and a very strong positive SAM (Figure 84), all of which made major contributions to the record wet spring as discussed earlier.

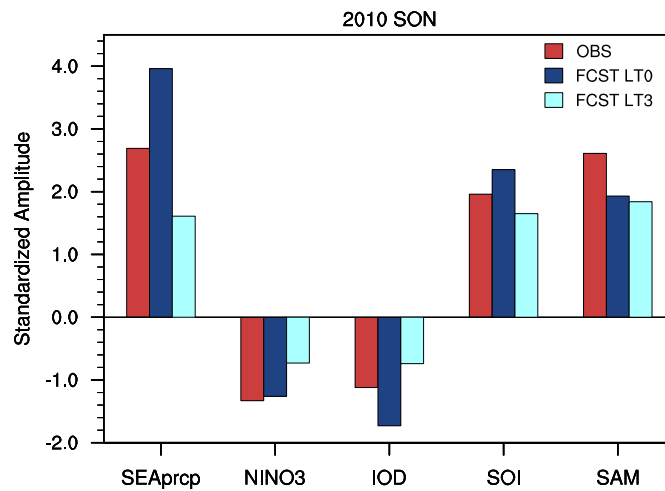


Figure 84. Observed (red bars) and predicted (lead time 0 months in dark blue, lead time 3 months in light blue) anomalies of various climate indices for spring 2010. From left to right: south-eastern Australia rainfall index (rainfall averaged over south-eastern Australia), and the NINO3, IOD, SOI and SAM indices. Magnitudes of the indices are in respective standard deviations

The roles of atmosphere and land surface initial conditions for the wet forecasts for 2010 spring were examined by redoing the forecasts but with random atmosphere or land surface initial conditions. The observed initial land surface condition for 2010 spring forecasts was wetter than normal in Victoria but drier than normal in most of eastern Australia reflecting impacts of the Millennium drought (Figure 85). Figure 85b suggests that neither atmosphere nor land surface initial conditions influence the predictions of the SOI and the SST anomalies associated with the La Niña event (including the negative IOD event), which is expected because the predictability of ENSO is largely derived from ocean initial conditions. However, forecasts initialised with random atmospheric conditions have significantly reduced amplitudes for SAM and SEA rainfall. This highlights the importance of realistic atmospheric initial conditions for seasonally predicting the extremity of atmospheric events at a short lead time. It also indicates some predictability of the SAM derived solely from the atmospheric initial condition. Prediction of the SAM was sensitive to the initial land conditions probably because land surface temperature and its contrast with the surrounding ocean temperature matters for storm tracks and therefore for SAM. However, the benefit of realistic land initial conditions was marginal for predicting SEA rainfall in 2010 spring.

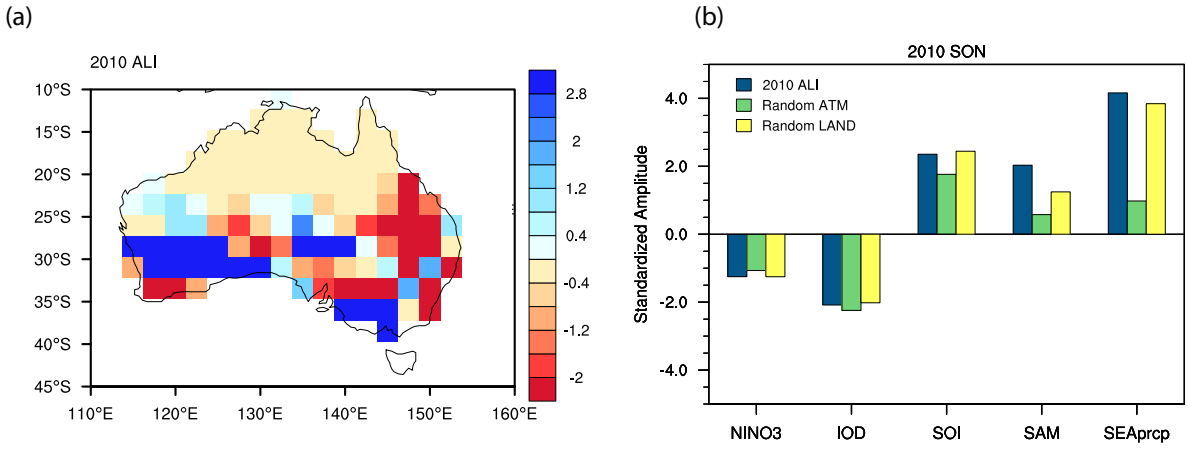


Figure 85. (a) Initial land surface wetness anomaly for 1 September 2010. Shading interval is 0.4 mm, (b) Lead time 0 predictions of standardised anomalies of key climate drivers and SEA rainfall from POAMA24 (blue bars), the experiment with randomised atmospheric initial conditions (green bars) and the experiment with random land surface initial conditions (yellow bars)

An additional forecast experiment was conducted with 2010 atmosphere and land surface conditions but with random ocean conditions. This experiment was designed to assess the role of boundary forcing for prediction of the SAM. That is, did the boundary forcing provided by the strong La Niña of 2010 contribute to the large magnitude of the SAM. The results showed that when the ocean initial conditions were scrambled but the observed initial atmospheric conditions in 2010 were used, a positive SAM was still predicted in the first month of the forecast, but no SAM signal was found in the second and third months (orange bars in Figure 86). In contrast, the strong positive SAM was maintained in the second and third months for forecasts that were initialised with the observed ocean state (red bars in Figure 86). Therefore, our result suggests that the strong positive amplitude of SAM in spring 2010 was predictable as a result of strong positive SAM in the atmospheric initial conditions for the shortest lead times and as a result of the strong La Niña condition for the longer lead times. Hence, seasonal predictability of the SAM is indicated even though SAM is generally regarded as a relatively fast internal process in the atmosphere.

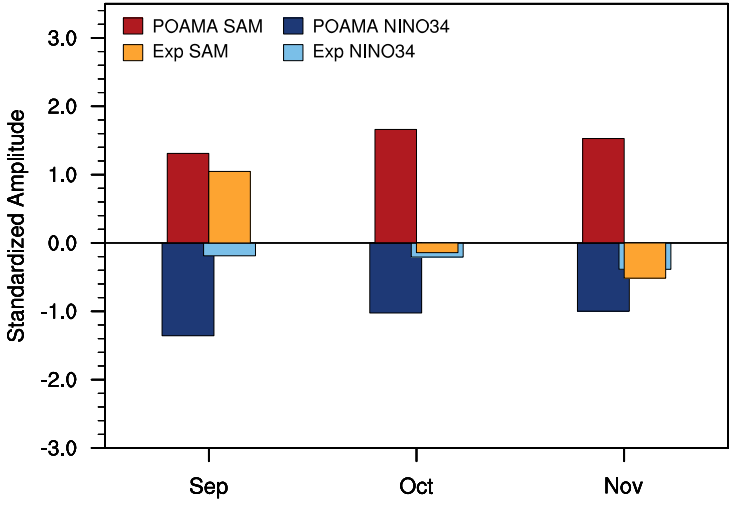


Figure 86. SAM (red and orange bars) and NINO3 (dark and light blue bars) predicted from POAMA and the forecast experiment initialised with random ocean conditions. The atmosphere and land surface for both POAMA and the experiment were initialised with observed 2010 conditions

Finally, the ability of POAMA to predict other extreme rainfall events in spring was assessed. Based on the standardised mean rainfall over eastern Australia (east of 135E; EAUprcp), we made rainfall composites of six historical wet springs (EAUprcp  $\geq$  1stddev) and eight historical dry springs (EAUprcp  $\leq$  -1) (Figure 87; see the figure caption for the list of the wet and dry years). The composites demonstrate that POAMA can skilfully predict the magnitudes and spatial patterns of the extreme wet and dry rainfall anomalies up to lead times of 2 months.

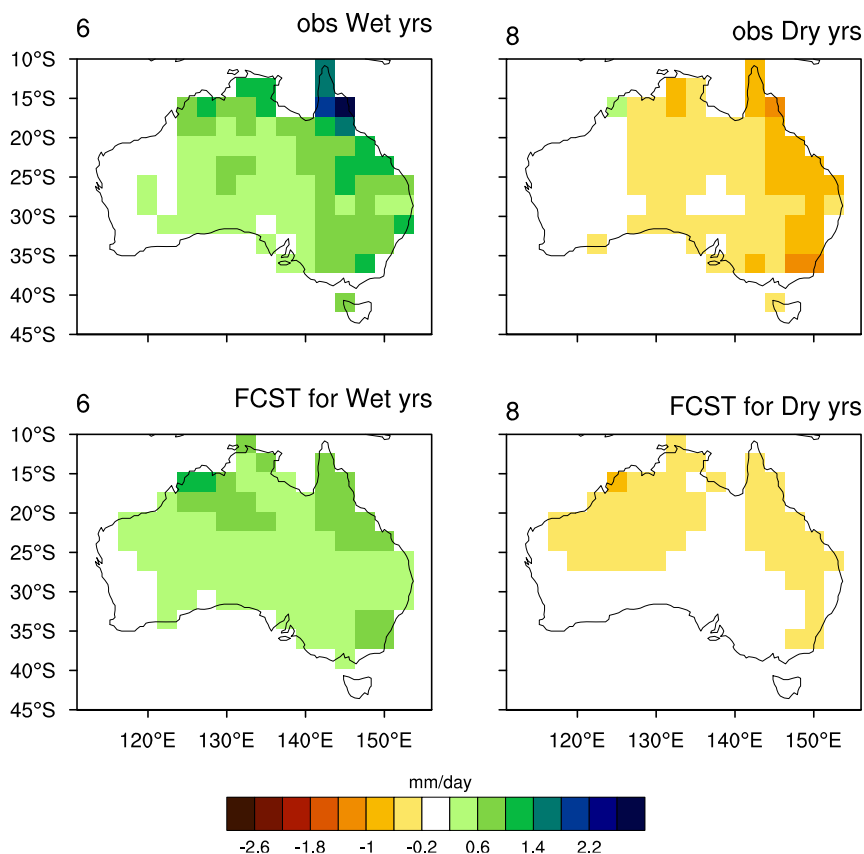


Figure 87. Composites of observed (upper panels) and 2 month lead POAMA forecast (lower panels) September, October, November rainfall anomalies in extreme wet years (1964,1973,1975,1998,2000, 2010) and extreme dry years (1963,1965,1967,1977,1982,1990,2002,2006) in eastern Australia. The numbers on the upper left corners indicate the number of sample years. The colour shading interval is 0.4 mm/day

## Conclusions

Record high spring rainfall in eastern Australia in 2010 is assessed to have occurred largely as a result of a record-strength La Niña event. The occurrence of a strong La Niña event on the back of the Millennium drought is a reminder of the highly variable climate experienced in eastern Australia during spring when El Niño/La Niña impacts are their greatest. To the degree that the rainfall was tied to La Niña, the record rainfall in spring 2010 was largely predictable given the demonstrated capability to predict SST variations associated with El Niño/La Niña. However, the rainfall received in 2010 was at the upper limit of what would typically be expected for a La Niña event of the magnitude as occurred in 2010, so we have to admit the possibility that the 2010 event was unusual (or that we have not captured a key process in our reconstruction model).

Although the primary contribution to rainfall was the strong La Niña, significant contributions were made by a) the strong positive excursion of the SAM (accounting for 8 percent of the area-mean eastern Australian rainfall and regionally up to 50 percent in central NSW) and b) the upward trending SST to the north of Australia (10 percent of the mean eastern Australia rainfall and up to 25 percent of the regional rainfall in inland southern Queensland and NSW). The SAM component is presumably largely unpredictable while any component due to the trend or ENSO should be predictable using initialised coupled climate models.

Based on this empirical study that uses historical relationships, we cannot rule out a larger role of the upward trending SSTs to the north of Australia than the approximate 10 percent contribution that we have diagnosed here. For instance, the magnitude of the La Niña event itself may have been amplified by the presence of upward trending SSTs to the north of Australia. Further, our analysis is linear. So, for instance, the additional rainfall that was received because La Niña was operating on a warmer basic state due to the SST trend would not be accounted for. Ongoing modelling studies are addressing these possibilities.

Seasonal prediction of the 2010 rainfall anomaly was demonstrated to a lead time of 3 months with POAMA. Forecast skill derives from a good capability to predict the La Niña SST anomalies in the tropical Pacific, as well as those associated with the negative Indian Ocean Dipole event. Interestingly, SAM appears to be a source of longer lead predictability, presumably because of the strong boundary forcing provided by the La Niña event but also derived from the atmospheric initial condition (extreme high SAM at the initial time all through late winter and spring 2010). Complementary work has identified a strong control of the polar vortex ozone hole on subsequent development of the SAM in early spring (Son et al., submitted), which thus suggests an additional source of shorter lead (0–1 month) predictability if the stratosphere is properly resolved and initialised.

## Links to other projects

This project has a strong link to Project 1.1 by providing new insights into the mechanism of spring time climate variability in SEA, especially the strong role that the SAM plays during extremes of El Niño and La Niña. Projected changes in the SAM in the late spring/early summer seasons as a result of anthropogenic forcing thus need to be carefully assessed because of this capability of the SAM to affect ENSO impacts (as well as providing direct impacts on SEA climate). That the bulk of the rainfall in 2010 resulted from a strong La Niña event that occurred after a 15 year dry spell is a reminder that strong internal variability of the climate system will not disappear any time soon, and noting that it can both exacerbate (e.g., an occurrence of a strong El Niño event) or mitigate impacts of recent climate change.

## CHAPTER 7: PROJECT 3.2

### Hydrological application of seasonal predictions

QJ Wang, Prafulla Pokhrel and David Robertson

## Abstract

Seasonal streamflow forecasts are useful for the planning and allocation of water resources. The Bureau of Meteorology's seasonal streamflow forecasting service is underpinned by the Bayesian joint probability (BJP) modelling approach, developed through SEACI and Water Information Research and Development Alliance (WIRADA) research.

The operational BJP forecast model uses predictors related to catchment wetness and climate condition. Catchment wetness is represented by antecedent streamflow or rainfall, and climate condition by lagged climate indices. To further improve the BJP forecast model (which is currently used operationally by the BoM), SEACI research investigated the use of outputs from dynamical hydrological and climate models as predictors to represent catchment wetness and climate condition, as well as the use of multiple models to produce merged forecasts. Forecasts using three new methodologies were developed and compared with results from the operational BJP model. A total of four methods were therefore considered:

1. The operational BJP model.
2. Incorporating WAPABA model output: Predictions of streamflow in the upcoming season (under mean seasonal climate conditions) made by the Water Partition and Balance (WAPABA) monthly hydrological model were added as a candidate predictor in the BJP forecast model. This prediction reflects the influence of the initial catchment condition only. This WAPABA variant of the forecast model produces more skilful forecasts than the current operational BJP model for most of the catchments tested in eastern Australia.
3. Merging forecasts from multiple models: As the choice of the best climate index for use in the operational BJP model can be subject to sample error, an alternative is to use multiple models each with a different climate index. A Bayesian model averaging technique was used to merge forecasts from multiple models. The merged forecasts are more skilful in many situations. Importantly, the merged forecasts also appear to moderate the errors of poorly forecast events relative to those made using only the best climate index.
4. Incorporating POAMA output: Forecast rainfall and climate indices from the Predictive Ocean Atmosphere Model for Australia (POAMA) were used as predictors to establish additional BJP models. Forecasts from these models were then merged together and further merged with forecasts from models from Method 3. The use of POAMA forecasts leads to some improvement in streamflow forecasts but only for a few catchments and in some seasons.

## Background

Seasonal forecasts of streamflows are valuable for water resources management. The seasonal streamflow forecasting service provided by the Australian Bureau of Meteorology is underpinned by the Bayesian joint probability modelling approach, developed through SEACI and WIRADA research.

The BJP modelling approach uses two sources of predictability to produce forecasts: catchment wetness and future climate conditions. Candidate predictors used to represent catchment wetness are antecedent rainfall and

streamflow totalled over the most recent 1 to 3 months. Candidate predictors used to represent future climate conditions are 13 observed climate indices over the most recent 1 to 3 months. Final predictors used in the BJP model are selected according to model predictive performance in cross validation on historical data.

The candidate predictors used in the operational BJP model are simple to apply, but forecast skill may be improved by using other predictors that reflect more the evolution of physical processes occurring in catchment or climate systems. Furthermore, it may be advantageous to use multiple models rather than just the 'best' model, which can be contentious to decide based on only a short data series.

## Objectives

- Assess the benefit of incorporating dynamic hydrological and climate model outputs into the BJP modelling approach.
- Assess the benefit of merging forecasts from multiple models to improve seasonal forecasts.

## Methods

A total of 20 sites located in eastern Australia were included in this study (see Figure 88).

For each site, a forecast of the next season streamflow total was made at the start of each month over a hindcast period. The following methods were investigated:

### **Method 1: Operational BJP model**

Candidate predictors used to represent catchment wetness were antecedent rainfall and streamflow totalled over the most recent 1 to 3 months. Candidate predictors used to represent future climate conditions were 13 observed climate indices over the most recent 1 to 3 months. Final predictors used in the BJP model were selected according to model predictive performance in cross validation on historical data. For further information, see Wang et al. (2009), Wang and Robertson (2011) and Robertson and Wang (2012).

### **Method 2: Incorporating WAPABA model output**

The WAPABA model is a monthly water balance model recently developed by Wang et al. (2011). After model calibration, the model was first run to the start of a forecast season using observed climate forcing to initialise the model states. The model was then run to generate a prediction of the next season's streamflow under the climatological mean condition for the season. In cross validation, the WAPABA model was calibrated by using all historical data except 5 years (forecast year plus four years after).

The WAPABA prediction was used as a predictor in the BJP model to represent the influence of the initial catchment condition on the next season streamflow. Observed streamflow of the previous month was also included as a predictor to assimilate real-time data.

Candidate predictors used to represent future climate conditions were the same as in Method 1. The best predictor was selected according to model predictive performance in cross validation on historical data. For further information on Method 2, see Robertson et al. (submitted).

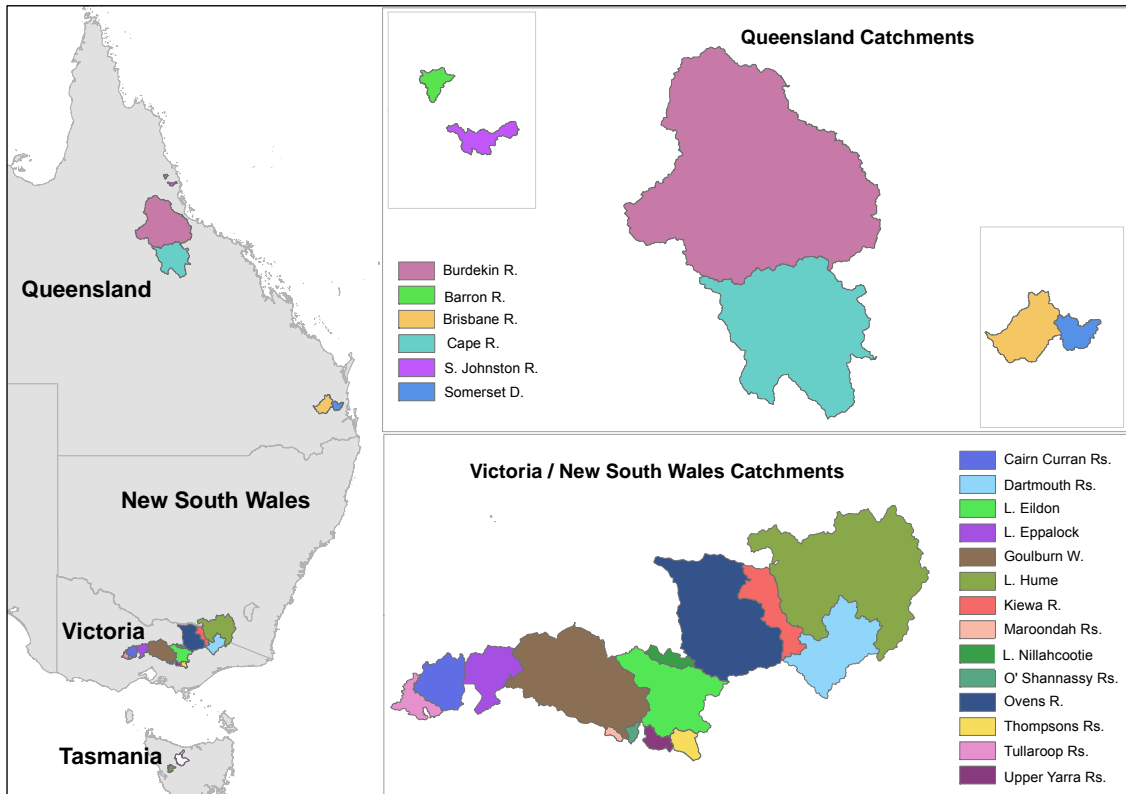


Figure 88. Location of the 20 catchments used in the study

### Method 3: Merging forecasts from multiple models

Here all the models used in Method 2 to select the best predictor to represent future climate conditions were considered, not just the final best performing model. A Bayesian model averaging technique was applied to merge forecasts from the multiple models. This technique is described in Wang et al. (in press).

### Method 4: Incorporating POAMA output

In addition to the multiple models in Method 3, additional BJP models were constructed using POAMA forecasts of rainfall and climate indices as predictors to represent future climate conditions. The forecast climate indices were derived from the forecast sea-surface temperature. Seasonal streamflow forecasts of these additional BJP models were merged together and further merged with the models in Method 3.

Forecast performance by the four methods was evaluated through cross validation. Incremental improvements in forecast skill were quantified.

## Results

Method 2 was shown to produce more skilful forecasts than Method 1 for most catchments and seasons (Figure 89a). A more detailed analysis (documented in Robertson et al., submitted) showed that the greatest increases in forecast skill tend to be (1) when the catchment is wetting up but antecedent streamflows have not responded to antecedent rainfall; (2) when the catchment is drying and the dominant source of antecedent streamflow is in transition between surface runoff and base flow; and (3) when the initial catchment condition is near saturation intermittently throughout the historical record.

Method 3 was shown to produce more skilful forecasts than Method 2 for many seasons and catchments (Figure 89b). The average gain in skill was 2.7 percent, but the gain was as high as 20 percent in some catchments, while any loss in skill was less than 5 percent. Most of the improvement was achieved by moderating the errors of the worst forecasts, as shown in Figure 90 of skill score calculated across all the catchments but for individual seasons over time.

Improvement of Method 4 over Method 3 was mostly marginal (Figure 89c). The average gain in skill was less than 1.2 percent but for a few catchments and seasons, the improvement was significant. The improvements were higher for catchments located in Upper Murray region and Central Victoria, for the months of March, April, May; June, July, August; and July, August, September.

The overall forecast skill achieved by Method 4 is shown in Figure 91. Forecast skill varies considerably with catchments and seasons. In general, the skill scores were higher (as high as 50 percent) for forecasts made during winter months in Queensland and spring months in Victorian catchments. The forecast skill was low for forecasts made during the summer months in Queensland and autumn months in Victoria. The forecast skill mostly depends on the contribution of the initial catchment condition and therefore the skill was higher in seasons and catchments for which the runoff was dominated by contributions from slow responding mechanisms (with correspondingly longer catchment memory).

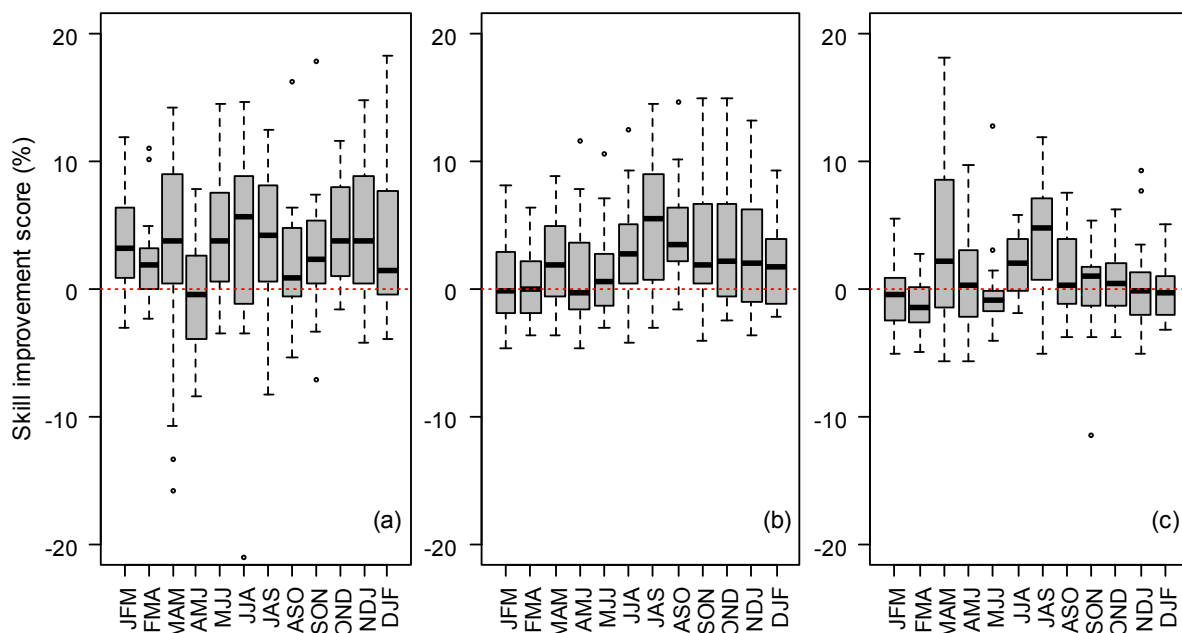


Figure 89. Skill improvement in percentage for 12 overlapping seasons (a) Method 2 over Method 1, (b) Method 3 over Method 2, and (c) Method 4 over Method 3. The skill improvement score used is based on root mean squared error in probability (RMSEP)

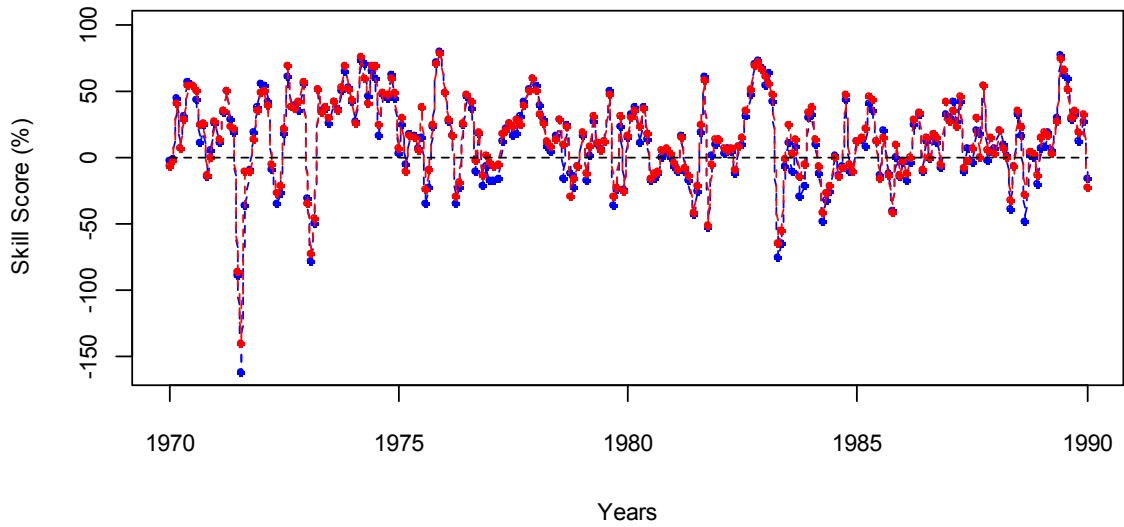


Figure 90. Skill score calculated across all the catchments but for individual seasons over time. Blue is for Method 2 and red for Method 3. The skill score used is based on root mean squared error in probability (RMSEP)

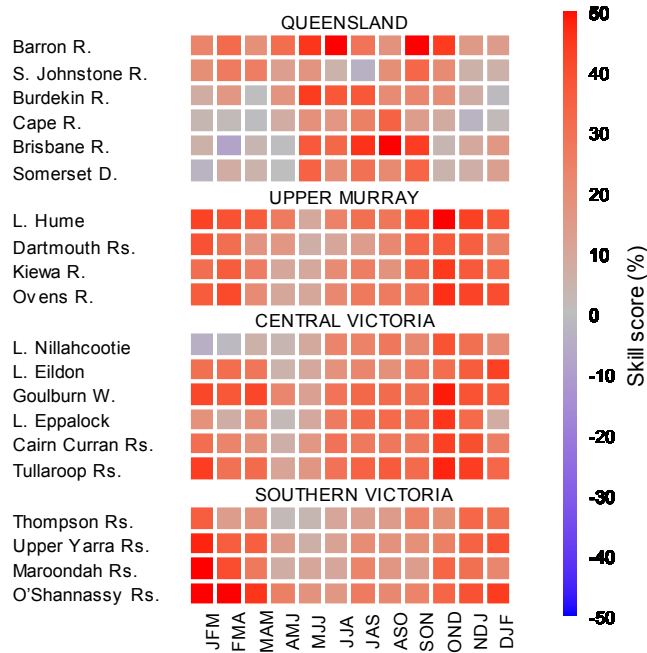


Figure 91. Overall skill score achieved using Method 4 relative to climatology for the 12 overlapping seasons (columns) and 22 catchments (rows). The skill score used is based on root mean squared error in probability (RMSEP)

## Conclusions

- The current operational implementation of the BJP modelling approach for seasonal streamflow forecasting uses antecedent streamflow, rainfall and climate indices as candidate predictors. The predictor combination that gives the 'best' predictive performance in cross validation on historical data is used for operational forecasting.
- Dynamical hydrological and climate models capture the evolution of various physical processes occurring in catchment and climate systems. Incorporating output from the dynamical models into the BJP model has the potential to improve forecast skill of the current operational model.
- In this study, we found that seasonal streamflow forecast skill was significantly improved by incorporating the output of a monthly water balance model into the BJP model. In contrast, forecast skill was improved only for a few seasons and catchments when incorporating the output of a dynamical climate model (POAMA).
- A multiple model approach allows for model uncertainty and for combining the strengths of different models. In this study, we found that forecast skill is improved in many situations by merging forecasts from multiple models through Bayesian model averaging. Importantly, the merged forecasts appear to moderate the errors of the worst forecasts when using only the best model.

## Links to other projects

This project and WIRADA Project 4.2 (Seasonal to long-term water forecasting and prediction) represent a joint effort in developing seasonal streamflow forecasting methods and tools for adoption by the Bureau of Meteorology and key water management agencies in Australia.

The project has a strong linkage with Project 3.1 in two ways. The first is the use of dynamic climate model predictions for streamflow forecasting. The second is the use of the Bayesian joint probability method for calibration of climate model predictions to overcome bias and reliability problems and for combining dynamic modelling with empirical modelling to improve rainfall predictions.

The project also draws on results from Project 1.1, especially results on climate drivers.

## CHAPTER 8: NEXT STEPS

Research has progressed well in the third and final year of Phase 2 of SEACI. The outcomes of the research carried out in this third year have been combined with those of the previous two years to produce an overarching Synthesis Report (CSIRO, 2012).

Due to a realignment of their research funding strategies, the Commonwealth Department of Climate Change and Energy Efficiency (DCCEE) have chosen not to provide direct funding for a third phase of SEACI. In an unrelated issue, the Murray–Darling Basin Authority (MDBA) have received a major funding cut from the New South Wales Government and are also unable to provide funding for a third phase of SEACI. Negotiations are currently underway with the Victorian Department of Sustainability and the Environment (DSE) to set up a Victorian Climate Initiative (VicCI) in order to continue to carry out some of the areas of research identified in this report.

## LIST OF SEACI PUBLICATIONS FOR 2011/12

### Project 1.1

- Cai W and Cowan T (In press.) Southeast Australia autumn rainfall reduction: A climate-change induced poleward shift of ocean-atmosphere circulation. *Journal of Climate*. (In press.)
- Cai W and Li Y (Submitted) The influence of climate drivers on the inflow to the Murray–Darling Basin. (Submitted to *Journal of Hydrometeorology*.)
- Cai W, van Rensch P, Cowan T and Hendon H (In press.) An asymmetry in the IOD and ENSO teleconnection pathway and its impact on Australian climate. *Journal of Climate* (In press.)
- Cai W, van Rensch P and Cowan T (2011) Influence of Global-Scale Variability on the Subtropical Ridge over Southeast Australia. *Journal of Climate*, 24, 6035–6053. doi:10.1175/2011JCLI4149.1.
- Leblanc M, Tweed S, van Dijk A and Timbal B (2012) A review of historic and future hydrological changes in the Murray–Darling Basin, *Global and Planetary Change* 80–81 (2012) 226–246 doi:10.1016/j.gloplacha.2011.10.012
- Lucas C, Nguyen H and Timbal B (Submitted.) An observational analysis of Southern Hemisphere tropical expansion. (Submitted to *Journal of Geophysical Research*.)
- Nguyen H, Timbal B, Smith I, Evans A and Lucas C (Submitted.) The Hadley Circulation in Reanalyses: climatology, variability and change. (Submitted to *Journal of Climate*.)
- Smith I and Timbal B (2010) Links between tropical indices and southern Australia rainfall, *International Journal of Climatology*, doi:10.1002/joc.2251.
- Timbal B and Drosowsky W (2012) The relationship between the decline of South Eastern Australia rainfall and the strengthening of the sub-tropical ridge, *International Journal of Climatology*, doi:10.1002/joc.3492.
- Timbal B and Fawcett R (Submitted.) An historical perspective on South Eastern Australia rainfall since 1865. (Submitted to *Journal of Climate*.)
- Timbal B and Hendon H (2011) The role of tropical modes of variability in the current rainfall deficit across the Murray–Darling Basin, *Water Resources Research* 47, W00G09.
- Whan K, Timbal B and Lindsay J (Submitted.) A CART analysis of the joint impact of the sub-tropical ridge intensity and position on South Eastern Australia rainfall. (Submitted to *International Journal of Climatology*.)

## Project 2.1

Chiew FHS, Prosser I and Post DA (2012) On climate variability and climate change and impact on water resources, 19th International Congress on Modelling and Simulation, Perth, Australia, 12–16 December 2011.

Evans J, Ekstrom M and Ji F (2011) Evaluating the performance of a WRF physics ensemble over South-East Australia. *Climate Dynamics*. doi:10.1007/s00382-011-1244-5.

Frost AJ, Charles SP, Timbal B, Chiew FHS, Mehrotra R, Nguyen KC, Chandler RE, McGregor JL, Fu G, Kirono DGC, Fernandez E and Kent DM (2011) A comparison of multi-site daily rainfall downscaling techniques under Australian conditions, *Journal of Hydrology* 408, 1–18, doi:10.1016/j.jhydrol.2011.06.021.

Kent DM, Kirono DGC, Timbal B and Chiew FHS. (2011) Representation of the Australian sub tropical ridge in the CMIP3 models, *International Journal of Climatology*, doi:10.1002/joc.3406.

Kirono D, Kent D, Chiew FHS, Teng J (2012) Consistent assessment of global climate model simulation for hydrological applications in south eastern Australia, 19th International Congress on Modelling and Simulation, Perth, Australia, 12–16 December 2011.

Teng J, Chiew FHS, Timbal B, Vaze J, Wang Y, Wang B, Evans A, Kent D, Kirono D and Post DA (2012) Assessing historical and future runoff modelled using rainfall from the analogue downscaling method, 19th International Congress on Modelling and Simulation, Perth, Australia, 12–16 December 2011.

## Project 2.2

Petheram C, Potter N, Vaze J, Chiew F and Zhang L (2012) Towards better understanding of changes in rainfall-runoff relationships during the recent drought in south-eastern Australia, 19th International Congress on Modelling and Simulation, Perth, Australia, 12–16 December 2011.

Potter NJ and Chiew FHS (2011) An investigation into changes in climate characteristics causing the recent very low runoff in the southern Murray–Darling Basin using rainfall-runoff models, *Water Resources Research*, 47, W00G10, 12pp.

Potter N, Petheram C and Zhang L (2012) Sensitivity of streamflow to rainfall and temperature in south-eastern Australia during the Millennium drought, 19th International Congress on Modelling and Simulation, Perth, Australia, 12–16 December 2011.

Post DA and Moran RJ (2012) Provision of usable projections of future water availability for south-eastern Australia: the South-Eastern Australian Climate Initiative (SEACI). Practical Responses to Climate Change National Conference, 1–3 May 2012, Canberra, Australia.

## Project 3.1

Charles A, Hendon HH, Wang QJ, Robertson D, and Lim EP (In press.) Comparison of techniques for the calibration of coupled model forecasts of Murray–Darling Basin seasonal mean rainfall, CAWCR Technical Report.

Lim EP, Hendon HH, Langford S and Alves O (2012) Improvements in POAMA2 for the prediction of major climate drivers and south eastern Australia rainfall. *CAWCR Technical Report No. 051*.

## Project 3.2

Pokhrel P, Robertson DE and Wang QJ (2011) Improving statistical streamflow forecasts using the output of dynamic hydrological and climate models: Application to 23 catchments in eastern Australia. CSIRO: Water for a Healthy Country National Research Flagship.

Robertson DE, Wang QJ and Pokhrel P (2011) Improving statistical seasonal streamflow forecasts using the output of dynamic hydrological and climate models. WIRADA Water Information Research and Development Alliance: Science Symposium Program, Melbourne, Australia, 1–5 August 2011. CSIRO: Water for a Healthy Country National Research Flagship.

Robertson DE and Wang QJ (2012) A Bayesian approach to predictor selection for seasonal streamflow forecasting, *American Meteorological Society*, 13, doi:10.1175/JHM-D-10-05009.1.

Robertson DE and Wang QJ (Submitted.) Seasonal forecasts of unregulated inflows into the Murray River, Australia. (Submitted to *Water Resources Management*.)

Wang QJ, Schepen A, Robertson DE and Hawthorne S (2011) Hierarchical Bayesian model averaging of statistical and dynamical models for improved seasonal rainfall forecasts, WIRADA Water Information Research and Development Alliance : Science Symposium Program, Melbourne, Australia, 1–5 August 2011. CSIRO: Water for a Healthy Country National Research Flagship.

## REFERENCES

- Abramowitz G (2010) Model independence in multi-model ensemble prediction. *Australian Meteorological and Oceanographic Journal*, 59, 3–6.
- Allen RJ, Sherwood SC, Norris JR and Zender CS (2012) Recent Northern Hemisphere tropical expansion primarily driven by black carbon and tropospheric ozone. *Nature*, 485, 350–354. doi:10.1038/nature11097.
- Allen RJ and Sherwood SC (2011) The impact of natural versus anthropogenic aerosols on atmospheric circulation in the Community Atmospheric Model. *Climate Dynamics*, 36, 1959–1978. doi:10.1007/s00382-010-0898-8.
- Ashcroft L, Karoly D and Gergis J (Submitted.) Temperature variations of southeastern Australia, 1860–2009. (Submitted to *Australian Meteorological and Oceanographic Journal*.)
- Bureau of Meteorology (2012) Australia's wettest two year period on record; 2010–2011. Special Climate Statement 38, [www.bom.gov.au/climate/current/statements/scs38.pdf](http://www.bom.gov.au/climate/current/statements/scs38.pdf).
- Burnash RJC, Ferral RL and McGuire RA (1973) A Generalised Streamflow Simulation System – Conceptual Modelling for Digital Computers. Joint Federal and State River Forecast Center, Sacramento, Technical Report, 204 pp.
- Cai W and Cowan T (2008), Evidence of impacts from rising temperature on inflows to the Murray–Darling Basin. *Geophysical Research Letters*, 35, L07701, doi:10.1029/2008GL033390.
- Cai W and Cowan T (In press.) Southeast Australia autumn rainfall reduction: A climate-change induced poleward shift of ocean-atmosphere circulation. *Journal of Climate* (In press.)
- Cai W, van Rensch, Cowan T and Hendon H (2011a) Teleconnection pathways for ENSO and the IOD and the mechanism for impacts on Australian rainfall. *Journal of Climate*, 24, 3910–3923. doi:10.1175/2011JCLI4129.1
- Cai W, van Rensch P and Cowan T (2011b) Influence of global-scale variability on the subtropical ridge over southeast Australia. *Journal of Climate*, 24, 6035–6053.
- Cai W, Cowan T, and Sullivan A (2009) Recent unprecedented skewness towards positive Indian Ocean Dipole occurrences and its impact on Australian rainfall. *Geophysical Research Letters*, 36, L11705, doi:10.1029/2009GL037604.
- Cai W, Sullivan A and Cowan T (2009) Rainfall teleconnection with Indo-Pacific Variability in the WCRP CMIP3 models, *Journal of Climate*, 22, 5046–5071.
- Charles SP, Bates BC and Hughes JP (1999) A spatio-temporal model for downscaling precipitation occurrence and amounts. *Journal of Geophysical Research – Atmospheres* 104(D24), 31657–31669.
- Chiew F and Prosser I (2011) Climate and Water. In: *Water – Science and Solutions for Australia* (Editor: IP Prosser), CSIRO Publishing, pp. 29–46.
- Chiew FHS, Teng J, Vaze J, Post DA, Perraud JM, Kirono DGC and Viney NR (2009) Estimating climate change impact on runoff across south-east Australia: method, results and implications of modelling method. *Water Resources Research*, 45, W10414.
- Chiew FHS, Kirono DGC, Frost AJ, Charles SP, Timbal B, Nguyen KC and Fu G (2010) Comparison of runoff modelled using rainfall from different downscaling methods for historical and future climates. *Journal of Hydrology*, 387, 10–23.

- Chiew FHS, Prosser IP and Post DA (2011) On climate variability and climate change and impact on water resources. In: MODSIM2011 (Editors: F Chan, D Marinova and RS Anderssen), 19th International Congress on Modelling and Simulation, Modelling and Simulation Society of Australia and New Zealand, December 2011, pp. 3553–3559, [www.mssanz.org.au/modsim2011/I6/chiew.pdf](http://www.mssanz.org.au/modsim2011/I6/chiew.pdf).
- Collins WJ, Bellouin N, Doutriaux-Boucher M, Gedney N, Halloran P, Hinton T, Hughes J, Jones CD, Joshi M, Liddicoat S, Martin G, O'Connor F, Rae J, Senior S, Sitch S, Totterdell I, Witshire A and Woodward S (2011) Development and evaluation of an Earth-System model HadGEM2. *Geoscientific Model Development*, 4, 1051–1075, doi:10.5194/gmd-4-1051-2011.
- Coron L, Andréassian V, Perrin C, Lerat J, Vaze J, Bourqui M and Hendrickx F (2012). Crash testing hydrological models in contrasted climate conditions: an experiment on 216 Australian catchments. *Water Resources Research*, 48, 5, doi:10.1029/2011WR011721.
- CSIRO (2008). Water Availability in the Murray–Darling Basin: A report from CSIRO to the Australian Government. CSIRO, Canberra, Australia.
- CSIRO (2010a) Climate variability and change in south-eastern Australia: A synthesis of findings from Phase 1 of the South Eastern Australian Climate Initiative (SEACI). May 2010, Canberra, Australia, 30 pp, [www.seaci.org](http://www.seaci.org).
- CSIRO (2010b) South Eastern Australian Climate Initiative Program Annual Report 2009/10. November, 2010, Canberra, Australia, 101 pp, [www.seaci.org](http://www.seaci.org).
- CSIRO (2011) South Eastern Australian Climate Initiative Program Annual Report 2010/11. October, 2011, Canberra, Australia, 142 pp, [www.seaci.org](http://www.seaci.org).
- CSIRO (2012) Climate and Water Availability in south-eastern Australia: A synthesis of findings from Phase 2 of the South Eastern Australian Climate Initiative (SEACI). September, 2012, Canberra, Australia, 41 pp, [www.seaci.org](http://www.seaci.org).
- Dai A (2006) Recent climatology, variability and trends in global surface humidity. *Journal of Climate*, 19, 3589–3606. doi:10.1175/JCLI3816.1.
- Drosowsky W (2005) The latitude of the subtropical ridge over eastern Australia: The L index revisited. *International Journal of Climatology*, 25, 1291–1299, 10.1002/joc.1196.
- Duan QY, Gupta VK and Sorooshian S (1993) Shuffled complex evolution approach for effective and efficient global minimization. *Journal of Optimization Theory and Applications*, 76(3), 501–521.
- Evans JP (2011) CORDEX – An international climate downscaling initiative, MODSIM2011 International Congress on Modelling and Simulation. Modelling and Simulation Society of Australia and New Zealand and International, Perth, Australia, 12–16 December 2011.
- Evans J, Ekstrom M and Ji F (2011) Evaluating the performance of a WRF physics ensemble over South-East Australia. *Climate Dynamics*. doi:10.1007/s00382-011-1244-5.
- Evans JP and McCabe MF (2010) Regional climate simulation over Australia's Murray–Darling basin: A multitemporal assessment. *Journal of Geophysical Research*, doi:10.1029/2010JD013816
- Fowler HJ, Blenkinsop S and Tebaldi C (2007) Linking climate change modelling to impact studies: recent advances in downscaling techniques for hydrological modelling. *International Journal of Climatology*, 27, 1547–1578.
- Frost AJ, Charles SP, Timbal B, Chiew FHS, Mehotra R, Nguyen KC, Chandler RE, McGregor JL, Fu G, Kirono DGC, Fernandez E and Kent DM (2011) A comparison of multi-site daily rainfall downscaling techniques under Australian conditions. *Journal of Hydrology*, 408, 1–18.

- Fu GB and Charles SP (2011) Statistical downscaling of daily rainfall for southeastern Australia. In: Hydro-climatology: Variability and change (Proceedings of symposium JH02 held during IUGG2011 in Melbourne, Australia, July 2011), IAHS Publ. 344, 69–74.
- Fu GB, Charles SP, Chiew FHS and Teng J (2011a). Statistical Downscaling of Daily Rainfall for Hydrological Impact Assessment. In Chan F, Marinova D and Anderssen RS (eds.) MODSIM2011, 19th International Congress on Modelling and Simulation, Perth, Australia, 12–16 December 2011, pp. 2803–2809. ISBN: 978-0-9872143-1-7.
- Fu G, Chiew FHS, Charles SP and Mpelasoka F (2011b), Assessing precipitation elasticity of streamflow based on the strength of the precipitation-streamflow relationship. In Chan F, Marinova D and Anderssen RS (eds.) MODSIM2011, 19th International Congress on Modelling and Simulation. Modelling and Simulation Society of Australia and New Zealand, December 2011, pp. 3567–3572. [www.mssanz.org.au/modsim2011/l6/fu.pdf](http://www.mssanz.org.au/modsim2011/l6/fu.pdf).
- Fu GB, Charles SP, Chiew FHS, Teng J, Frost AJ, Liu W and Kirshner S (Submitted) Modelling runoff with statistically downscaled daily site, gridded and catchment rainfall series. (Submitted to *Journal of Hydrology*).
- Gan TY and Burges SJ (2006), Assessment of soil-based and calibrated parameters of the Sacramento model and parameter transferability. *Journal of Hydrology*, 320, 117–131, doi:10.1016/j.jhydrol.2005.07.008.
- Geoscience Australia (2008) Mapping the Growth, Location, Surface Area and Age of Man Made Water Bodies, including Farm Dams, in the Murray–Darling Basin. Available at: [www2.mdbc.gov.au/nrm/Risks\\_to\\_Shared\\_Water\\_Resource/risks\\_to\\_shared\\_water\\_resources/man\\_made\\_water\\_bodies\\_including\\_farm\\_dams\\_in\\_the\\_murray-Darling\\_Basin\\_report.html](http://www2.mdbc.gov.au/nrm/Risks_to_Shared_Water_Resource/risks_to_shared_water_resources/man_made_water_bodies_including_farm_dams_in_the_murray-Darling_Basin_report.html)
- Geoscience Australia (2011) 1 second SRTM Derived Hydrological Digital Elevation Model (DEM-H) version 1.0, available at [www.ga.gov.au/meta/ANZCW0703014615.html](http://www.ga.gov.au/meta/ANZCW0703014615.html).
- Gifford RM, Farquhar G, Roderick M and Nicholls N (eds.) (2005) Pan evaporation: An example of the detection and attribution of trends in climate variables. Proceedings of a workshop held at the Shine Dome, Australian Academy of Sciences, Canberra, 22–23 November 2004. Available at [www.science.org.au/natcoms/nc-ess.html](http://www.science.org.au/natcoms/nc-ess.html).
- HadGEM2 Development Team (2011) The HadGEM2 family of Met Office Unified Model climate configurations, *Geoscientific Model Development*, 4, 723–757, doi:10.5194/gmd-4-723-2011.
- Hatton TJ, Walker J, Dawes WR and Dunin FX (1992) Simulation of hydroecological responses to elevated CO<sub>2</sub> at the catchment scale. *Australian Journal of Botany*, 40, 679–696.
- Haverd V, Böhm M and Raupach MR (2010) The effect of source distribution on bulk scalar transfer between a rough land surface and the atmosphere. *Boundary-Layer Meteorology* 135, 351–368.
- Haverd V, Cuntz M, Griffith DWT, Keitel C, Tadros C, Twining J (2011) Measured deuterium in water vapor concentration does not improve the constraint on the partitioning of evapotranspiration in a tall forest canopy, as estimated using a soil vegetation atmosphere transfer model. *Agricultural and Forestry Meteorology*, 151 645–654. <http://dx.doi.org/10.1016/j.agrformet.2011.02.005>.
- Haverd V, Lovell JL, Cuntz M, Jupp DLB, Newnham GJ and Sea W (2012) The Canopy Semi-analytic Pgap and Radiative Transfer (CanSPART) model: Formulation and application. *Agricultural and Forest Meteorology*, 160, 14–35, doi:10.1016/j.agrformet.2012.01.018.
- Hendon HH, Lim E-P, Arblaster J and Anderson D (Submitted) Causes and predictability of the record wet spring Australia 2010. (Submitted to *Monthly Weather Review*).
- Hughes JP, Guttorp P and Charles SP (1999) A non-homogeneous hidden Markov model for precipitation occurrence. *Journal of the Royal Statistical Society, Series C–Applied*, 48(1), 15–30.
- Hurrell JW, Hack JJ, Shea D, Caron JM and Rosinski J (2008) A New Sea Surface Temperature and Sea Ice Boundary Dataset for the Community Atmosphere Model. *Journal of Climate*, 21, 5145–5153. doi:10.1175/2008JCLI2292.1.

- IPCC (2007) *Climate Change 2007: The Physical Science Basis. Contribution of Working Group I to the Fourth Assessment Report of the Intergovernmental Panel on Climate Change*. Cambridge, UK, Cambridge University Press.
- Jeffrey SJ, Carter JO, Moodie KB and Beswick AR (2001) Using spatial interpolation to construct a comprehensive archive of Australian climate data. *Environmental Modelling and Software*, 16,309–330.
- Jones BA and Trewin BC (2000) On the relationships between the El Niño–Southern Oscillation and Australian land surface temperature. *International Journal of Climatology*, 20, 697–719.
- Jones DA, Wang W and Fawcett R (2009) High quality spatial climate data sets for Australia, *Aust. Met. Oceanogr. J.*, 58, 233–48
- Kalnay E, Kanamitsu M, Kistler R, Collins W, Deaven D, Gandin L, Iredell M, Saha S, White G, Woollen J, Zhu Y, Leetmaa A, Reynolds R, Chelliah M, Ebisuzaki W, Higgins W, Janowiak J, Mo KC, Ropelewski C, Wang J, Jenne R and Joseph D (1996) The NCEP/NCAR 40-year reanalysis project. *Bulletin of the American Meteorological Society* 77 (3), 437–471.
- Kang SM, Polvani LM, Fyfe JC and Sigmond M (2011) Impact of polar ozone depletion on subtropical precipitation. *Science*, 332, 951–954. doi:10.1126/science.1202131.
- Kent DM and Kirono DGC (2012) A preliminary look at the hydroclimate of Southeastern Australia in the next generation of Australia Global Circulation Model simulations, AMOS 18th National Conference, Connections in the Climate System, UNSW, 31 Jan – 3 Feb 2012, Australia.
- Kent DM, Kirono DGC, Timbal B and Chiew FHS (2011) Representation of the Australian sub-tropical ridge in the CMIP3 models. *International Journal of Climatology*. doi:10.1002/joc.3406.
- Kirono DGC, Kent DM, Chiew FHS, Teng J (2011) Consistent assessment of global climate model simulation for hydrological application in south eastern Australia. In Chan F, Marinova D and Anderssen RS (eds.) MODSIM2011, 19th International Congress on Modelling and Simulation. Modelling and Simulation Society of Australia and New Zealand, December 2011, pp. 2754–2760. ISBN: 978-0-9872143-1-7. [www.mssanz.org.au/modsim2011/F5/kirono.pdf](http://www.mssanz.org.au/modsim2011/F5/kirono.pdf)
- Leblanc M, Tweed S, Van Dijk A and Timbal B (2012) A review of historic and future hydrological changes in the Murray–Darling Basin. *Global and Planetary Change*, 80–81, 226–246.
- Lohmann U and Feichter J (2005) Global indirect aerosol effects: a review. *Atmospheric Chemistry and Physics*, 5, 715–737.
- Lowe L, Nathan R and Morden R (2005) Assessing the impact of farm dams on streamflows, Part II: Regional characterisation. *Australian Journal of Water Resources*, 9, 13–25.
- Lucas C (2010) A high-quality humidity database for Australia. CAWCR Technical Report No. 024, 162 pp. (Available from: [www.cawcr.gov.au/publications/technicalreports.php](http://www.cawcr.gov.au/publications/technicalreports.php))
- Lucas C, Nguyen H and Timbal B (Submitted.) An observational analysis of Southern Hemisphere tropical expansion. (Submitted to *Journal of Geophysical Research*.)
- Marshall GJ and Connolley WM (2006) Effects of changing Southern Hemisphere winter sea-surface temperatures on Southern Annular mode strength. *Geophysical Research Letters*, 33, L17717. doi:10.1029/2006GL026627.
- McLandress C, Shepherd T, Scinocca J, Plummer D, Sigmond M, Jonsson A and Reader C (In press.) Separating the dynamical effects of climate change and ozone depletion: Part 2. Southern hemisphere troposphere. *Journal of Climate*. (In press.)

- McVicar TR, Donohue RJ, O'Grady AP and Li LT (2010) The effects of climatic changes on plant physiological and catchment ecohydrological processes in the high-rainfall catchments of the Murray–Darling Basin: A Scoping Study. CSIRO: Water for a Healthy Country National Research Flagship, 95 pp.
- Milly PCD and Dunne KA (2002) Macroscale water fluxes. 2. Water and energy supply control of their interannual variability. *Water Resources Research*, 38, 1206, doi:10.1029/2001WR000760.
- Ming Y and Ramaswamy V (2009) Nonlinear climate and hydrological responses to aerosol effects. *Journal of Climate*, 22, 1329–1339. doi:10.1175/2008JCLI2362.1.
- Ming Y and Ramaswamy V (2011) A model investigation of aerosol-induced changes in tropical circulation. *Journal of Climate*, 24, 5125–5133.
- Morton FI (1983) Operational estimates of areal evapotranspiration and their significance to the science and practice of hydrology, *Journal of Hydrology*, 66, 1–76, doi:10.1016/0022-1694(83)90177-4.
- Nash JE and Sutcliffe JV (1970) River flow forecasting through conceptual models. Part 1: A discussion of principles. *Journal of Hydrology* 10, 282–290.
- Nathan R and Lowe L (2011) Discussion Paper: The hydrologic impact of farm dams. Available at [www.engineersaustralia.org.au/water-engineering/publications](http://www.engineersaustralia.org.au/water-engineering/publications).
- Nathan R, Jordan P and Morden R (2005) Assessing the impact of farm dams on streamflows, Part I: Development of simulation tools. *Australian Journal of Water Resources*, 9, 1–11.
- Nguyen H, Timbal B, Smith I, Evans A and Lucas C (Submitted.) The Hadley Circulation in Reanalyses: climatology, variability and change. (Submitted to *Journal of Climate*.)
- Nicholls N, Lavery B, Frederiksen C, Drosowsky W and Torok S (1996) Recent apparent changes in relationships between the El Niño–Southern Oscillation and Australian rainfall and temperature. *Geophysical Research Letters*, 23, 3357–3360.
- Oort AH and Yienger JJ (1996) Observed interannual variability in the Hadley circulation and its connection to ENSO. *Journal of Climate*, 9, 2751–2767.
- Oudin L, Andreassian V, Perrin C, Michel C and Le Moine N (2008) Spatial proximity, physical similarity, regression and ungauged catchments: A comparison of regionalisation approaches based on 913 French catchments. *Water Resources Research*, 44, W03413, doi:10.1029/2007WR006240.
- Perrin C, Michel C and Andreassian V (2003) Improvement of a parsimonious model for streamflow simulations. *Journal of Hydrology*, 279, 275–289.
- Petheram C, Potter NJ, Vaze J, Chiew FHS and Zhang L (2011) Towards better understanding of changes in the rainfall–runoff relationships during the recent drought in south-eastern Australia. In Chan F, Marinova D and Anderssen RS (eds.) MODSIM2011, 19th International Congress on Modelling and Simulation. Modelling and Simulation Society of Australia and New Zealand, December 2011, pp. 3622–3628. [www.mssanz.org.au/modsim2011/l6/petheram.pdf](http://www.mssanz.org.au/modsim2011/l6/petheram.pdf).
- Pierce DW, Barnett TP, Santer BD, Glecker PJ (2009) Selecting global climate models for regional climate change studies. *PNAS* 106, 8441–8446.
- Polvani LM, Waugh DW, Correa GJP and Son S-W (2011) Stratospheric ozone depletion: The main driver of twentieth-century atmospheric circulation changes in the Southern Hemisphere. *Journal of Climate*, 24, 795–812. doi:10.1175/2010JCLI3772.1.

- Post DA, Teng J, Chiew FHS, Wang B, Vaze J and Marvanek S (2011) Non-linearity of the runoff response across south-eastern Australia to increases in global average temperature, in Franks SW, Boegh E, Blyth E, Hannah DM and Yilmaz KK (eds.). *Hydro-climatology: Variability and Change*, IAHS Publication 344. IAHS Press, Wallingford, UK: 188–194.
- Post DA and Moran RJ (2011) Practical application of climate-induced projected changes in water availability to underpin the water planning process in Victoria, Australia, in Chan F, Marinova D and Anderssen R S(eds.) MODSIM 2011 International Congress on Modelling and Simulation, 12–16 December 2011, Perth, Australia, pp 3629–3635.
- Potter NJ and Chiew FHS (2011) An investigation into changes in climate characteristics causing the recent very low runoff in the southern Murray–Darling Basin using rainfall-runoff models. *Water Resources Research*, 47, W00G10, doi:10.1029/2010WR010333.
- Potter NJ, Chiew FHS and Frost AJ (2010) An assessment of the severity of recent reductions in rainfall and runoff in the Murray–Darling Basin. *Journal of Hydrology*, 381, 52–64, doi:10.1016/j.jhydrol.2009.11.025.
- Potter NJ, Petheram C and Zhang L (2011) Sensitivity of streamflow to rainfall and temperature in south-eastern Australia during the Millennium drought. In Chan F, Marinova D and Anderssen RS (eds.) MODSIM2011, 19th International Congress on Modelling and Simulation. Modelling and Simulation Society of Australia and New Zealand, December 2011, pp. 3636–3642. [www.mssanz.org.au/modsim2011/16/potter.pdf](http://www.mssanz.org.au/modsim2011/16/potter.pdf).
- Power SB and Kociuba G (2011) What caused the observed twentieth-century weakening of the Walker Circulation? *Journal of Climate*, 24, 6501–6514. doi:10.1175/2011JCLI4101.1.
- Power S, Tseitkin F, Torok S, Lavery B, Dahni R and McAvaney B (1998) Australian temperature, Australian rainfall and the Southern Oscillation, 1910–1992: coherent variability and recent changes. *Australian Meteorological Magazine*, 47, 85–101.
- Ramanathan V, Crutzen PJ, Kiehl JT and Rosenfeld D (2001) Aerosols, climate and the hydrological cycle. *Science*, 294, 2119–2124.
- Rayner, N. A., D. E. Parker, E. B. Horton, C. K. Folland, L. V. Alexander, D. P. Rowell, E. C. Kent, and A. Kaplan, (2003) Global analyses of sea surface temperature, sea ice, and night marine air temperature since the late nineteenth century. *J. Geophys. Res.*, 108, 4407, doi:10.1029/2002JD002670.
- Reichler T, Dameris M and Sausen R (2003) Determining the tropopause height from gridded data. *Geophysical Research Letters*, 30, 2042–2046. doi:10.1029/2003GL018240.
- Robertson DE and Wang QJ (2012) A Bayesian approach to predictor selection for seasonal streamflow forecasting, *Journal of Hydrometeorology*, 13, 155–171.
- Robertson DE, Pokhrel P and Wang QJ (Submitted.) Improving statistical forecasts of seasonal streamflows using hydrological model output. (Submitted to *Hydrology and Earth System Sciences*.)
- Roderick ML, Hobbins MT and Farquhar GD (2009a) Pan evaporation trends and the terrestrial water balance. I. Principles and observations. *Geography Compass*, 3, 746–760, doi:10.1111/j.1749-8198.2008.00213.x.
- Roderick ML, Hobbins MT and Farquhar GD (2009b) Pan evaporation trends and the terrestrial water balance. II. Energy balance and interpretation. *Geography Compass*, 3, 761–780, doi:10.1111/j.1749-8198.2008.00214.x.
- Rosenbrock HH (1960) An automatic method for finding the greatest or least value of a function, *Computer Journal*, 3, 175–184.
- Seidel DJ and Randel WJ (2006) Variability and trends in the global tropopause estimated from radiosonde data. *Journal of Geophysical Research*, 111, D21101. doi:10.1029/2006JD007363.

- Seidel DJ and Randel WJ (2007) Recent widening of the tropical belt: Evidence from tropopause observations. *Journal of Geophysical Research*, 112, doi:10.1029/2007JD08861.
- Shaikh M, Whyte J and Pobre L (2011) Desktop surveillance of farm dams – areas covered by Parkes and Braidwood 1:100,000 scale maps, NSW Office of Water, Sydney, available at [www.water.nsw.gov.au/ArticleDocuments/34/monitor\\_catchment\\_desktop\\_surveillance\\_farm\\_dams.pdf.aspx](http://www.water.nsw.gov.au/ArticleDocuments/34/monitor_catchment_desktop_surveillance_farm_dams.pdf.aspx).
- Skamarock WC, Klemp JB, Dudhia J, Gill DO, Barker DM, Duda M, Huang XY, Wang W and Powers JG (2008) A description of the Advanced Research WRF version 3. NCAR Technical Note, NCAR, Boulder, CO, USA.
- Son S-W, Tandon NF, Polvani LM and Waugh DW (2009) Ozone hole and southern hemisphere climate change. *Geophysical Research Letters*, 36, L15705. doi:10.1029/2009GL038671.
- Son S-W and others (2010) Impact of stratospheric ozone on Southern Hemisphere circulation change: A multimodel assessment. *Journal of Geophysical Research*, 115, D00M07, doi:10.1029/2010JD014271.
- Son S-W, Purich A, Hendon HH and Kim, B-M (Submitted.) Weather from the ozone hole. (Submitted to *Science*.)
- Stachnik JP and Schumacher C (2011) A comparison of the Hadley circulation in modern reanalyses, *Journal of Geophysical Research*, 116, D22102, doi:10.1029/2011JD016677.
- Staten PW, Rutz JJ, Reichler T and Lu J (2011) Breaking down the tropospheric circulation response by forcing. *Climate Dynamics*, doi:10.1007/s00382-011-1267-y.
- Teng J, Chiew FHS, Timbal B, Wang Y, Vaze J and Wang B (Submitted) Assessment of an analogue downscaling method for modelling climate change impact on runoff. (Submitted to *Journal of Hydrology*).
- Teng J, Vaze J, Chiew FHS, Wang B and Perraud JM (2012) Estimating the relative uncertainties sourced from GCMs and hydrological models in modelling climate change impact on runoff. *Journal of Hydrometeorology*, 13, 122–139.
- Timbal B and Hendon H (2011) The role of tropical modes of variability in recent rainfall deficits across the Murray–Darling Basin. *Water Resources Research*, 47, doi:10.1029/2010WR009834.
- Timbal B, Fernandez E and Li Z (2009) Generalization of a statistical downscaling model to provide local climate change projections for Australia. *Environmental Modelling & Software*, 24(3), 341–358, doi:10.1016/j.envsoft.2008.07.007.
- Timbal R and Drosowsky W (2012) The relationship between the decline of Southeastern Australian rainfall and the strengthening of the subtropical ridge. *International Journal of Climatology*, doi:10.1002/joc.3492.
- Timbal B and Fawcett R (In press.) An historical perspective on South Eastern Australia rainfall since 1865, *Journal of Climate*. (In press.)
- Vaze J, Chiew FHS, Perraud J-M, Viney NR, Post DA, Teng J, Wang B, Lerat J, and Goswami M (2010b) Rainfall-runoff modelling across southeast Australia: Datasets, models and results. *Australian J. Water Res.* 14 (2), 101–116.
- Vaze J, Post DA, Chiew FHS, Perraud J-M, Viney NR and Teng J (2010a) Climate non-stationarity – Validity of calibrated rainfall-runoff models for use in climate change studies. *Journal of Hydrology*, 394, 447–457, doi:10.1016/j.jhydrol.2010.09.018.
- Vaze J, Chiew FHS, Perraud J, Viney N, Post DA, Teng J, Wang B, Lerat J and Goswami M (2011) Rainfall-runoff modelling across southeast Australia: datasets, models and results. *Australian Journal of Water Resources*, 14(2), 101–116.
- Vaze J and Teng J (2011) Future climate and runoff projections across New South Wales, Australia – results and practical applications. *Hydrological Processes*, 25, 18–35, doi:10.1002/hyp.7812.

- Vecchi GA and Soden BJ (2007) Global warming and the weakening of the tropical circulation. *Journal of Climate*, 20, 4316–4340.
- Vertessy R, Connell L, Morris J, Silberstein R, Heuperman A, Feikema P, Mann L, Komarzynski M, Collopy J, and Stackpole D (2000) Sustainable hardwood production in shallow watertable areas. RIRDC Publication No. 00/163, Water and Salinity Issues in Agroforestry, No. 6, 105pp.
- Viney NR, Perraud J, Vaze J, Chiew FHS, Post DA and Yang A (2009) The usefulness of bias constraints in model calibration for regionalisation to ungauged catchments. In Anderssen RS, Braddock RD and Newham LTH (eds.), 18th World IMACS Congress and MODSIM09 International Congress on Modelling and Simulation. July 2009, pp. 3421–3427. [http://mssanz.org.au/modsim09/17/viney\\_17a.pdf](http://mssanz.org.au/modsim09/17/viney_17a.pdf).
- Wang C (2007) Impact of direct radiative forcing of black carbon aerosols on tropical convective precipitation. *Geophysical Research Letters*, 34:L05709. doi:10.1029/2006GL028416.
- Wang G and Hendon HH (2007) Sensitivity of Australian rainfall to inter-El Nino variations. *Journal of Climate*, 20, 4211–4226.
- Wang QJ, Schephen A and Robertson DE (In press.) Merging Seasonal Rainfall Forecasts from Multiple Statistical Models through Bayesian Model Averaging, *Journal of Climate* (In press).
- Wang QJ and Robertson DE (2011) Multisite probabilistic forecasting of seasonal flows for streams with zero value occurrences, *Water Resources Research*, 47, 10.1029/2010wr009333.
- Wang QJ, Pagano TC, Zhou SL, Hapuarachchi HAP, Zhang L and Robertson DE (2011) Monthly versus daily water balance models in simulating monthly runoff, *Journal of Hydrology*, 404, 166–175.
- Wang QJ, Robertson DE and Chiew FHS (2009) A Bayesian joint probability modelling approach for seasonal forecasting of streamflows at multiple sites. *Water Resources Research*, 45, 10.1029/2008WR007355.
- Wang XL (2008) Penalized maximal F test for detecting undocumented mean shift without trend change. *Journal of Atmospheric and Oceanic Technology*, 25, 368–384, doi:10.1175/2007JTECHA982.1.
- Wang XL and Feng Y (2010) RHtestsV3 User Manual. Atmospheric Science and Technology Directorate, Science and Technology Branch, Environment Canada, Toronto.
- Wang XL, Wen QH and Wu Y (2007) Penalized maximal t test for detecting undocumented mean change in climate data series. *Journal of Applied Meteorology and Climatology*, 46, 916–931, doi:10.1175/JAM2504.1.
- Watterson IG (2008) Calculation of probability density function for temperature and precipitation change under global warming. *Journal of Geophysical Research* 113: D12106, doi:10.1029/2007JD009254.
- Webb LB, Whetton PH, Bhend J, Darbyshire R, Briggs PR and Barlow EWR (2012) Earlier wine grape ripening driven by climate warming and drying and management practices. *Nature Climate Change* 2, 259–264, doi:10.1038/NCLIMATE1417
- Whan K, Timbal B and Lindesay J (In press.) Linear and non-linear statistical analysis of the impact of sub-tropical ridge intensity and position on south-east Australian rainfall. *International Journal of Climatology* (In press.).
- Willett KM, Gillett NP, Jones PD and Thorne PW (2007) Attribution of observed surface humidity changes to human influence. *Nature*, 449, 710–713. doi:10.1038/nature06207.
- Wu H, Rykiel Jr EJ, Hatton TJ and Walker J (1994) An integrated rate methodology (IRM) for multi-factor growth rate modelling. *Ecological Modelling*, 73, 97–116.
- Yu J, Fu G, Cai W and Cowan T (2010) Impacts of precipitation and temperature changes on annual streamflow in the Murray–Darling Basin. *Water International*, 35, 313–323, doi:10.1080/02508060.2010.484907.

Zhang L and Dawes WR (1998) WAVES – An integrated energy and water balance model. CSIRO Land and Water Technical Report No 31/98, Canberra, 24pp.

For more information:

Email [seaci@csiro.au](mailto:seaci@csiro.au)

Visit [www.seaci.org](http://www.seaci.org)



**Australian Government**

**Department of Climate Change  
and Energy Efficiency**

**Bureau of Meteorology**

